UNIVERSITÀ DEGLI STUDI DI PADOVA

DEPARTMENT OF PHYSICS AND ASTRONOMY "GALILEO GALILEI"

MASTER DEGREE IN PHYSICS

Final dissertation

STUDY OF THE TRIGGER SYSTEM PERFORMANCE OF THE ICARUS T600 DETECTOR AT FERMILAB EXPOSED TO THE BOOSTER AND NUMI NEUTRINO BEAMS

Thesis supervisor
Dr. Alberto GUGLIELMI

Thesis co-supervisor
Prof. Daniele GIBIN

Candidate
Riccardo TRIOZZI

Academic Year 2022–2023

Abstract

The ICARUS T600 detector is a high-granularity Liquid Argon Time Projection Chamber (LArTPC), located at a 600 m baseline along the Booster Neutrino Beam (BNB) at Fermilab. ICARUS operates at shallow depth as the far detector of the Short Baseline Neutrino program, based on three LArTPCs installed at different distances from the BNB target, and aiming to perform a definitive search on the existence of eV-scale sterile neutrinos with world-leading sensitivity in both the ν_e-appearance and ν_μ-disappearance channels. Moreover, ICARUS foresees a rich stand-alone program on ν-Ar cross-sections and on the search for a Neutrino-4-like anomaly at the BNB and with the off-axis Neutrinos from the Main Injector (NuMI) beam. In this work, an online trigger system is developed to select the physical events, initially based on the detection with PMTs of scintillation light in liquid Argon with PMTs inside the BNB and NuMI proton beam extraction spills. A PMT-majority trigger logic was defined based on data-driven Monte Carlo calculations with neutrinos and cosmic muons and then tested on real data from the most recent ICARUS physics run. Data confirms the Monte Carlo hints and reports a full event recognition efficiency above ~ 200 MeV of deposited energy, identifying inefficiencies for low-energy neutrino events and short muon tracks crossing the detector corners. To optimize the trigger, a study was conducted with cosmic muons using so-called adder boards, performing the analog sum of adjacent PMT signals and providing complementary information on the total scintillation light signal, to be combined with the multiplicity logic. An update to the ICARUS trigger system is proposed on the basis of Monte Carlo calculations and is preliminarily tested with cosmic ray data, predicting an improvement to the recognition of low-energy neutrino interactions and of cosmic muons crossing the detector during the ~ 1 ms drift of ionization electrons in the TPCs.

Contents

Introduction

Neutrinos are among the most abundant particles in the Universe and are generated in the Sun, from the interaction of cosmic rays and the atmosphere, in nuclear reactors, and at accelerators. The discovery of neutrino "oscillations", hence the fact that they are massive, is still the most striking signal of physics beyond the Standard Model of Particle Physics, which predicts neutrinos to be massless. Despite a well-established model for oscillations among the three ν_e, ν_μ, and ν_τ "active" flavors of neutrinos, several anomalies have been collected at short baselines, possibly hinting at the existence of additional "sterile" neutrino states. Most notably, anomalies were reported at accelerators (LSND, MiniBooNE), at Gallium-based experiments (GALLEX, SAGE, BEST), and at nuclear reactors. Recently, the Neutrino-4 experiment at reactor observed a clear short-baseline oscillation signal hinting at a sterile neutrino, with a predicted mass of interest for explaining dark matter in the Universe. Indeed, a global picture highlights strong tensions in the results, with no definitive indication of sterile neutrinos, requiring a single program aiming at a $> 5\sigma$ sensitivity on multiple short-baseline oscillation channels with a single experiment.

The ICARUS T600 detector is a 760 ton large-scale Liquid Argon Time Projection Chamber (LArTPC), operating as the far detector of the Fermilab Short Baseline Neutrino (SBN) program, based on three LArTPC detectors at different baselines along the Booster Neutrino Beam (BNB) and performing a definitive search for eV-scale sterile neutrinos by exploring both ν_μ-disappearance and ν_e-appearance in BNB. Moreover, ICARUS is collecting off-axis neutrinos from the Neutrinos at the Main Injector (NuMI) neutrino beam, performing a stand-alone search for a Neutrino-4-like anomaly and a ν-Ar cross-section study in the energy range of future long-baseline LArTPC-based experiments. The LArTPC technology represents a strong advantage for ICARUS and SBN, enabling for mm-scale three-dimensional event imaging and calorimetric reconstruction. It allows to clearly distinguish between photon and electron-induced electromagnetic showers and reject the neutral-current interaction background to an unprecedented level. An online trigger is needed to recognize beam neutrino interactions and to tag cosmic ray activity during the $\sim$ 1 ms drift of ionization electrons in the TPCs, enhancing cosmic background rejection in the data analysis.

The goal of this work is to develop an optimal trigger logic, initially based on the recognition of the prompt scintillation light signal in the TPCs with PMTs. The performance of the trigger based on PMT-multiplicity will be thoroughly assessed with data-driven dedicated Monte Carlo calculations and with recently collected ICARUS cosmic ray data. A possible update of the trigger using "adder boards" to collect part of the total event light signal collected by PMTs is proposed and will be preliminarily evaluated.

The structure of this work follows:

- chapter 1 provides an overview of the current knowledge on neutrinos, their interactions, and the oscillation phenomenon, and of the most notable anomalies reported at short baselines;
- chapter 2 describes the ICARUS T600 detector and its three sub-systems, the liquid Argon Time Projection Chamber, the light collection system, and the cosmic ray tagger, and its current program at Fermilab within the Short Baseline Neutrino project;
- in chapter 3, I develop a data-driven Monte Carlo simulation framework to study the collection of scintillation light in liquid argon with BNB neutrinos and cosmic rays, and its applications to define an optimal trigger based on a PMT-majority logic;
- chapter 4 describes the chosen ICARUS trigger deployment and presents the software used to reconstruct events in the TPC, along with the selection procedures I developed to mitigate reconstruction issues and ensure a reliable evaluation of the trigger efficiency, to serve as input for ICARUS physics analyses;
- in chapter 5, I propose a possible trigger layout for combining adder boards with the established PMT-majority logic, and I present promising results on the projected trigger improvements, both with low-energy neutrino interactions and cosmic rays during the ionization electron drift in the TPC.

1

Active and Sterile Neutrinos

This Chapter contains:

1.1 Neutrinos

The history of neutrinos traces back to 1930 when W. Pauli proposed their existence, describing a new light-weighted neutral particle with a $1/2$ spin [1]. Earlier in 1927, C. D. Ellis and W. A. Wooster observed the energy spectrum of electrons emitted from Bismuth-210 nuclei in a beta-decay process [2], which was thought to convert a neutron into a proton-electron couple. The spectrum was found to be continuous and not compatible with the discrete spectrum predicted by the well-understood energy conservation for a two-body decay, in which the electron would always have a well-defined energy value. Therefore, Pauli theorized neutrinos as a "desperate remedy" to provide an explanation for the apparent non-conservation of energy and angular momentum in nuclear beta decays [1]. In 1933, Enrico Fermi later incorporated the neutrino in his effective theory of beta decay, in which he describes the beta decay of a neutron with the direct coupling of the neutron with a proton, an electron, and a neutrino [3]. The Fermi theory described the process as

a three-body decay characterized by a continuous energy spectrum satisfying the energy and angular momentum conservation. The Fermi effective interaction constant $G_F = 1.166 \cdot 10^{-5}$ GeV^{-2} was far too small to foresee the observation of the neutrino and justified calling this type of interaction *weak*. Only 26 years after their theorization, in 1956 a team led by F. Reines and C. L. Cowan was able to observe electron antineutrinos produced by the Savannah River reactor through the inverse beta decay process, $\overline{\nu}_e + p \rightarrow n + e^+$, in a water target and detecting the two gamma rays from the outgoing positron annihilation with a liquid scintillator [4].

In the meanwhile, the muon was discovered [5], and it was not clear whether neutrinos produced along electrons were the same as those produced with muons. In 1962, L. M. Lederman, M. Schwarz, and J. Steinberger confirmed the existence of the muon neutrino with a distinct flavor with respect to electron neutrinos [6]. The experiment at the Brookhaven Alternating Gradient Synchrotron (AGS) used proton-Beryllium collisions to produce pion and kaons, which decay in-flight to muons and neutrinos, $(\pi^-, K^-) \rightarrow \mu^- + \overline{\nu}_\mu$. By using a spark chamber, they were able to detect outgoing muons from neutrino interactions, but no electron-like events, proving the existence of a second type of neutrino.

In 1989, the ALEPH detector at the e^+e^- Large Electron Positron (LEP) collider at CERN exploited measurements of the Z-boson decay width to confirm the existence of only three neutrino families, ruling out the possibility of a fourth (active) neutrino flavor at the 98% confidence level [7]. The tau neutrino, the third flavor of neutrino, was finally detected in 2000 by the DONUT (Direct Observation of the Nu Tau) experiment at Fermilab [8], 25 years after the discovery of the tau lepton.

1.1.1 Neutrinos in the Standard Model

The Standard Model (SM) of Particle Physics is a quantum field theory that describes particles and their electromagnetic, weak, and strong nuclear interactions [9]. In this model, neutrinos are massless neutral leptons and are characterized only by left chirality, as verified in the Goldhaber experiment in 1957 [10]. Chirality is identical to helicity for massless particles and is hence defined as the projection of spin onto the direction of momentum, $h = \mathbf{S} \cdot \mathbf{p}/|\mathbf{p}|$. They don't carry color or electromagnetic charges but carry weak isospin, hence they only interact via the weak force.

The Standard Model unifies the electromagnetic and the weak interactions described by the V-A theory, by introducing massive $W^\pm$ and Z^0 boson mediators respectively for the Charged-Current (CC) and Neutral-Current (NC) interactions, as discovered by C. Rubbia with the UA1 experiment at the CERN S$p\overline{p}$S accelerator [11]. In particular, the Standard Model describes three flavors of neutrinos, ν_e, ν_μ and ν_τ, defined by the charged lepton they couple to in charged-current weak interactions.

Interactions Neutrinos may undergo several types of interactions, and energy is crucial in determining their phenomenology. Figure 1.1 presents the Feynman diagrams of the most important processes both for the CC and NC channels for the muon-flavor neutrino (interactions for other flavors of neutrinos are akin). Specifically, for l-flavor Charged-Current (CC) neutrino interactions the main processes are given by:

- the Quasi-Elastic (QE) channel, which is the dominant one in the $\mathcal{O}(1\text{ GeV})$ energy range: a neutrino or anti-neutrino scatters off a nucleon, producing a nucleon and the corresponding lepton or anti-

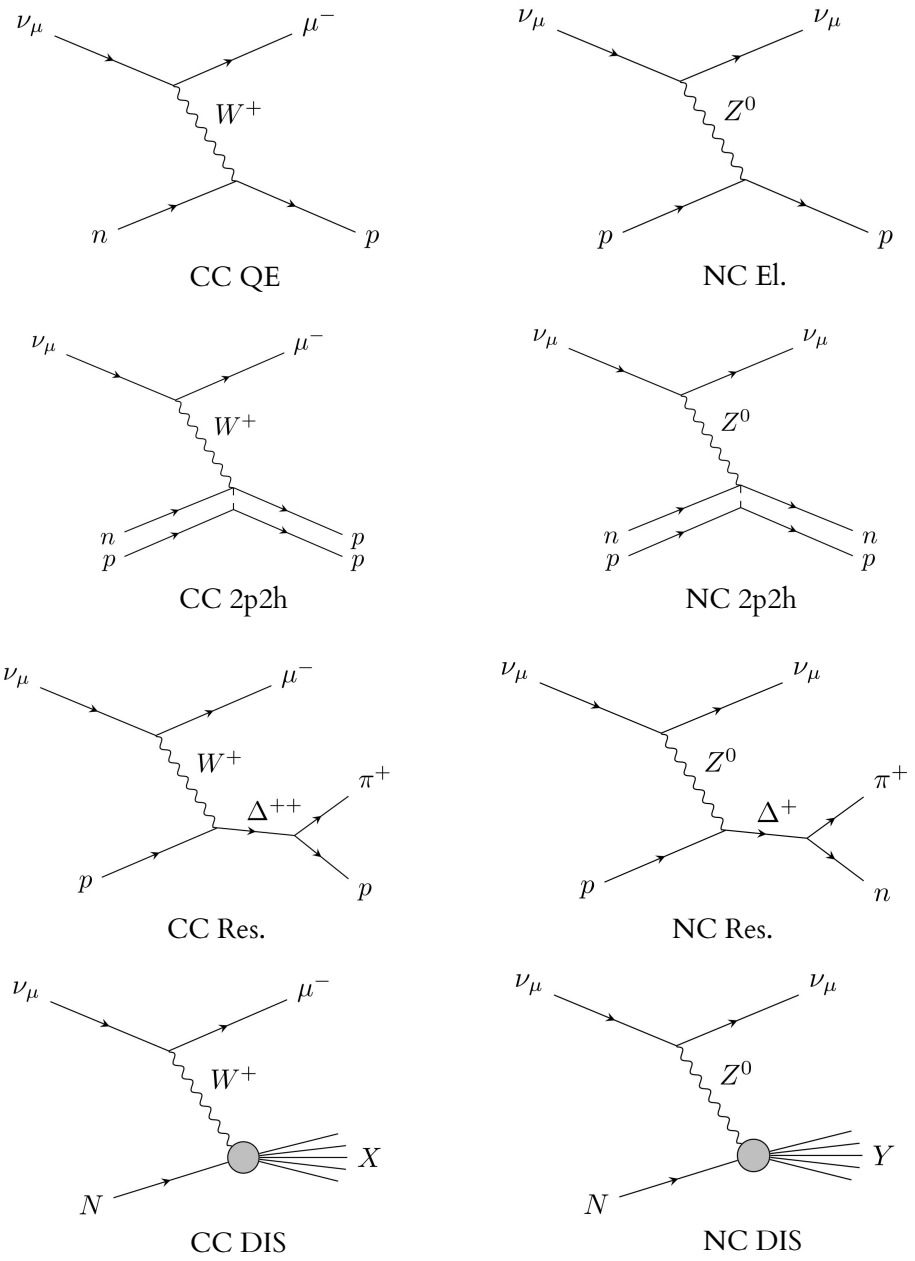

Figure 1.1: Schematic and Feynman diagrams of dominant neutrino interactions processes in the $\mathcal{O}(1\text{ GeV})$ energy range, taken from [12].

lepton, e.g.,

$$\nu_l + n \to l^- + p\,, \quad \overline{\nu}_l + p \to l^+ + n\,; \tag{1.1}$$

- the n-particle n-hole (npnh) process, consisting of a neutrino interacting with a single or more bound nucleons inside the nucleus; e.g., for the 2p2h process,

$$\nu_l + (n+p) \to l^- + (p+p)\,; \tag{1.2}$$

- pion production processes. Specifically, such processes can be *resonant*, when the scattering pro-

duces an excited intermediate heavy resonance (e.g., Δ^{++}), which promptly decays (usually into pion-nucleon pairs). For instance:

$$\nu_l + p \xrightarrow{\Delta^{++}} l^- + \pi^+ + p \,. \tag{1.3}$$

Note that when the transferred momentum is low, the neutrino interacts with the nucleus as a whole, producing pions, ρ mesons, and photons: this is the *coherent* pion production process, which also contributes to the production of pions;

- Deep Inelastic Scattering (DIS), the dominant process for neutrino energies of $\mathcal{O}(10\,\text{GeV})$ and higher: an energetic neutrino scatters off of quarks in nuclei, leading to a hadron shower (hadronization). For instance:

$$\nu_l + N \to l^- + X \,, \tag{1.4}$$

in which X is the charged-current hadron shower.

Similarly, for Neutral-Current (NC) interactions, some of the most important neutrino interaction processes are: quasi-elastic scattering, with a neutrino scattering off of a nucleon without changing the nature of the involved particles, e.g., $\nu_l + n \to \nu_l + n$; *n*p*n*h processes like $\nu_l + (n+p) \to \nu_l + (n+p)$; resonant (or coherent) pion-production processes, e.g., $\nu_l + p \xrightarrow{\Delta^{++}} \nu_l + \pi^+ + n$; NC deep inelastic scattering, $\nu_l + N \to \nu_l + Y$, with Y being the NC hadron shower.
More information on interactions between neutrinos and matter can be found in [13]. Finally, Figure 1.2 depicts the global dataset on neutrino and anti-neutrino charged-current scattering cross-sections on a nucelon, with respect to the underlying interaction modes. As previously anticipated, the leading channel for energies of $\mathcal{O}(1\,\text{GeV})$ is the quasi-elastic scattering, while at increasing energies the DIS becomes dominant. Note that the 2p2h cross-section has large theoretical uncertainties and is not shown.

1.1.2 Neutrino Mixing and Oscillations

Neutrinos are among the most abundant particles in the Universe and are generated extensively in nature and artificially through several processes:

- neutrinos with MeV-scale energies are produced in the Sun from the *pp* chain and CNO cycle reactions, responsible for the energy production in the core of the Sun;
- atmospheric neutrinos originate from interactions between cosmic rays and nuclei in the atmosphere, in a broad GeV to TeV energy region;
- nuclear reactors emit electron anti-neutrinos isotropically from the beta decay of unstable fissioning isotopes like ^{238}U and ^{239}Pu, with energies peaking at around 3 MeV and extending up to 8 MeV;
- neutrinos can be produced at accelerators, with collisions of accelerated protons on a target, generating mesons that are selected, focused, and decay into neutrinos. Neutrinos from beams have energies spanning from roughly 0.1 GeV to 100 GeV.

Several experiments at reactors and accelerators at CERN, Fermilab, and BNL since the 1970s investigated

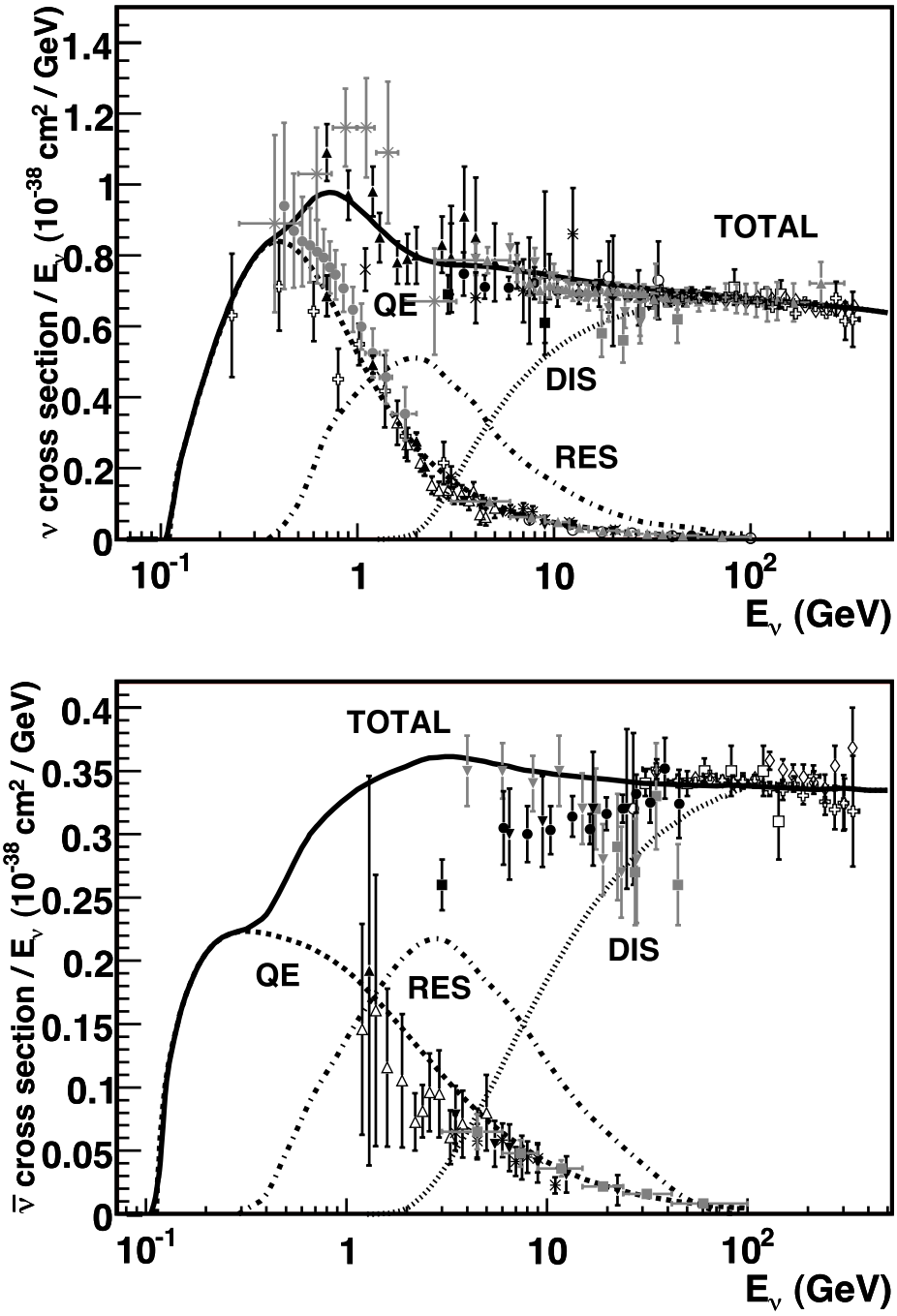

Figure 1.2: Total neutrino (top) and anti-neutrino (bottom) per nucleon Charged-Current (CC) cross sections over neutrino energy with respect to neutrino energy. The various contributing processes are shown. By increasing energies, the main interaction channels are Quasi-Elastic (QE) scattering, resonant interactions (Res.), and Deep Inelastic Scattering (DIS). Taken from [14].

the intrinsic properties of neutrinos, and in particular searched for $\nu_\alpha \to \nu_\beta$ "oscillation" signals to study the flavor lepton number conservation [15]. The neutrino oscillation phenomenon, namely the fact that neutrinos can change their flavor while traveling through time and space, implies that neutrinos have to be massive, and can be described in the mass basis. In the two neutrino flavors approximation, the probability of neutrino oscillations from the α-flavor to the β-flavor is

$$P(\nu_\alpha \to \nu_\beta) = \sin^2(2\theta)\sin^2\left(\frac{\Delta m^2 L}{4E_\nu}\right) , \tag{1.5}$$

in which E_ν is the neutrino energy, L is the baseline or the distance between source and detector, $\sin^2(2\theta)$ characterizes the amplitude of the oscillation, and $\Delta m^2 = m_2^2 - m_1^2$ is the difference between the squared masses of the two neutrino mass states. Experiments are hence able to provide allowed regions or exclusion curves of oscillation parameters with respect to the $(\sin^2 2\theta,\ \Delta m^2)$ plane.

In 1968, a radiochemical experiment led by R. Davis deep underground in the Homestake Mine, United States, observed a deficit in the neutrinos from the decay of ^{8}B in the Sun [16]. The solar neutrinos were detected through the capture reaction on a tetrachloroethylene target, $\nu_e + {}^{37}\mathrm{Cl} \to e^- + {}^{37}\mathrm{Ar}$, and the observed rate was roughly 3 times lower than expected according to the Standard Solar Model ("solar neutrino anomaly"). In 1986, the Irvine-Michigan-Brookhaven (IMB) and Kamiokande experiments observed a deficit in the muon neutrino component expected from the atmospheric neutrino flux [17, 18] ("atmospheric neutrino anomaly"). Atmospheric neutrinos originate from interactions between cosmic rays and nuclei in the atmosphere, leading to the production of mesons, decaying mainly through $\pi^\pm \to \mu^\pm + \nu_\mu(\overline{\nu}_\mu)$; neutrinos are also produced in secondary muon decays, $\mu^\pm \to e^\pm + \nu_e(\overline{\nu}_e) + \overline{\nu}_\mu(\nu_\mu)$, leading to an expected flavor ratio of $(\nu_e + \overline{\nu}_e)/(\nu_\mu + \overline{\nu}_\mu) = 1/2$.

The solution to the "atmospheric neutrino anomaly" came from the Super-Kamiokande experiment in 1998 [19], detecting atmospheric neutrinos from the signature Cherenkov rings produced by the corresponding charged leptons in charged-current interactions with ultra-pure water. The rate of neutrinos coming from below, namely the ones that traveled through Earth, was smaller than the rate of neutrinos from above the experiment. This result provided the first evidence of the neutrino oscillation phenomenon: neutrinos that traveled a longer distance changed their flavor along the way. Super-Kamiokande reported a good agreement between data and the neutrino oscillation interpretation of the observed "disappearance" of ν_μ, estimating the parameters $\sin^2 2\theta > 0.82$ and $5\cdot10^{-4} < |\Delta m^2| < 6\cdot10^{-3}$ eV^2 at the 90% confidence level [19]. In 1999, the Chooz experiment reported no evidence of oscillation for a parameter region defined by $|\Delta m^2| > 7\cdot10^{-4}$ eV^2 at the 90% confidence level, collecting $\overline{\nu}_e$ from a nuclear reactor at a 1 km baseline through the inverse beta decay reaction on a liquid scintillator target, $\overline{\nu}_e + p \to e^+ + n$ [20]. This result suggested that the ν_μ deficit as detected in Super-Kamiokande was likely not due to an oscillation to the ν_e-flavor. The ν_μ-disappearance signal from Super-Kamiokande was further confirmed by its successor experiment, KEK to Kamioka (K2K), using a GeV-scale beam of ν_μ neutrinos directed at the Super-Kamiokande far detector, with a 250 km baseline. K2K observed 56 beam ν_μ candidates over an expectation of $80.1^{+6.2}_{-5.4}$ events, consistent with neutrino oscillations with a maximal $\sin^2 2\theta = 1$ mixing strength and $|\Delta m^2| = (1.5 - 3.9)\cdot10^{-3}$ eV^2 [21]. The ν_μ oscillation measurement was refined by the MINOS experiment at Fermilab, exposed to the NuMI beam of ~ 2 GeV muon neutrinos at a 735 km baseline. MINOS reported 215 events compared to an expectation of

446 ± 14.4 events, consistent with the ν_μ-disappearance via oscillations with $|\Delta m^2| = 2.75^{+0.44}_{-0.26} \cdot 10^{-3}$ eV^2 and $\sin^2 2\theta > 0.87$ at the 68% confidence level [22]. The final unequivocal evidence of ν_μ oscillating to the ν_τ-flavor was reported by the OPERA experiment at LNGS, which detected 5 ν_τ candidates over a background of 0.25 events in the CERN Neutrinos to Gran Sasso (CNGS) ν_μ beam, at a baseline of 735 km and neutrino energies around ~ 17 GeV [23].

The "solar neutrino anomaly" was solved in a similar fashion in 2001 by the Sudbury Neutrino Observatory (SNO) [24] using a heavy water Cherenkov detector, sensitive to the solar neutrinos from the ^{8}B decay. SNO measured the neutral-current neutrino interaction rate and found it to be consistent with the expected value predicted by the Standard Solar Model. While the neutral-current rate is independent of the flavor, the charged-current rate depends on it and the deficit in the ν_e-flux observed by SNO was found to be compatible with the measurement from the Homestake experiment. The neutrinos oscillate among different flavors while traveling from the Sun to Earth, hence solar ν_e neutrinos are converting to the ν_μ and ν_τ flavors. In particular, solar neutrino experiments like SNO, the Gallium Experiment (GALLEX) [25], and the Soviet-American Gallium Experiment (SAGE) [26] originally reported a mass splitting of the order of $\Delta m^2 \sim 10^{-5}$ eV^2 and a $\sin^2 2\theta \sim 0.3$ oscillation amplitude.

Three-flavor Neutrino Mixing In the Standard Model of Particle Physics, neutrinos do not couple with the Higgs field and hence do not acquire mass terms. Indeed, the aforementioned experimental shreds of evidence of neutrino oscillations imply that neutrinos have to be massive. The mechanism that assigns a mass term to neutrinos is still unknown and several theoretical interpretations were formulated [27]. So far, neutrinos were described through the eigenstates of the so-called flavor basis, given by ν_e, ν_μ, and ν_τ. Being massive, they can also be described in the mass basis, with eigenstates ν_1, ν_2, and ν_3. In particular, the flavor eigenstates undergo weak interactions and are detectable by experiments, while mass eigenstates dictate the time propagation of neutrinos. The two bases are linked by a rotation, defined by the unitary Pontecorvo-Maki-Nakagawa-Sakata (PMNS) lepton-mixing matrix U_{PMNS} [28], hence the flavor states are expressed as a linear combination of mass states and vice versa,

$$|\nu_\alpha\rangle = \sum_k U^*_{\alpha k} |\nu_k\rangle \ , \quad |\nu_k\rangle = \sum_\alpha U_{\alpha k} |\nu_\alpha\rangle \ , \tag{1.6}$$

in which $\alpha = e, \mu, \tau$ indicates the flavor, $k = 1, 2, 3$ indicates the mass state, and $U^*_{\alpha k}$ are the components of the PMNS matrix, which can be described with three *mixing* angles and one complex phase. The typical parametrization of the PMNS matrix is:

$$U_{\text{PMNS}} = \begin{pmatrix} 1 & 0 & 0 \\ 0 & c_{23} & s_{23} \\ 0 & -s_{23} & c_{23} \end{pmatrix} \times \begin{pmatrix} c_{13} & 0 & s_{13} e^{-i\delta} \\ 0 & 1 & 0 \\ -s_{13} e^{i\delta} & 0 & c_{13} \end{pmatrix} \times \begin{pmatrix} c_{12} & s_{12} & 0 \\ -s_{12} & c_{12} & 0 \\ 0 & 0 & 1 \end{pmatrix} , \tag{1.7}$$

where θ_{12}, θ_{23}, and θ_{13} are the three real mixing angles, $c_{ij} = \cos\theta_{ij}$ and $s_{ij} = \sin\theta_{ij}$, δ is the Dirac Charge Parity (CP) violating phase. Majorana CP-violating phases α_1, α_2 can be included by multiplying Equation 1.7 by a fourth matrix $\text{diag}(e^{i\alpha_1/2}, e^{i\alpha_2/2}, 1)$, to describe possible ν-$\overline{\nu}$ oscillations.

Neutrino Oscillations The time evolution of the neutrino mass eigenstates in a vacuum [29] is

$$|\nu_k(t)\rangle = e^{-iE_k t}\,|\nu_k(0)\rangle \ , \tag{1.8}$$

in which $|\nu_k(0)\rangle = |\nu_k\rangle$ and $k = 1,2,3$. Considering Equation 1.6, the time evolution of the $\alpha = e,\mu,\tau$ flavor eigenstates can be written as:

$$|\nu_\alpha(t)\rangle = \sum_k U^*_{\alpha k} e^{-iE_k t}\,|\nu_k\rangle = \sum_\gamma \left(\sum_k U^*_{\alpha k} e^{-iE_k t} U_{\gamma k}\right)|\nu_\gamma\rangle \ . \tag{1.9}$$

The probability of measuring a neutrino in the definite flavor state $|\nu_\beta\rangle$ at a given time t, having been in the definite initial state of α-flavor $|\nu_\alpha\rangle$ is

$$\begin{aligned} P_{\alpha\to\beta}(t) = |\,\langle\nu_\beta|\nu_\alpha(t)\rangle\,|^2 &= \sum_{k,j} U^*_{\alpha k} U_{\beta k} U_{\alpha j} U^*_{\beta j} \exp\left(-i\frac{\Delta m^2_{kj} L}{2E}\right) = \\ &= \delta_{\alpha b} - 4\sum_{k>j} \mathrm{Re}(U^*_{\alpha k} U_{\beta k} U_{\alpha j} U^*_{\beta j}) \sin^2\left(\frac{\Delta m^2_{kj} L}{2E}\right) \\ &+ 2\sum_{k>j} \mathrm{Im}(U^*_{\alpha k} U_{\beta k} U_{\alpha j} U^*_{\beta j}) \sin\left(\frac{\Delta m^2_{kj} L}{2E}\right) \ , \end{aligned} \tag{1.10}$$

in which the phase of the oscillation is expressed as $E_k - E_j = \Delta m^2_{kj}/2E$, with E neutrino energy and $\Delta m^2_{kj} = m^2_k - m^2_j$ mass squared difference between the $|\nu_k\rangle$ and $|\nu_j\rangle$ mass eigenstates, where $E_k = \sqrt{\mathbf{p}^2 + m^2_k}$ can be expanded to $E_k = E + m^2_k/2E$ since $|\mathbf{p}| \gg m_k$ and E tends to $|\mathbf{p}|$. The first term in Equation 1.10 corresponds to not having oscillations. The second term represents three-flavor oscillations with an amplitude given by $\mathrm{Re}(U^*_{\alpha k} U_{\beta k} U_{\alpha j} U^*_{\beta j})$ and a $\Delta m^2_{kj} L/2E$ phase, depending on the mass splitting among different mass eigenstates and on the L/E ratio, with L distance between neutrino source and detector (baseline). The third term accounts for the impact of CP violation: the CP-violating phase δ can be measured by quantifying the difference of oscillation probabilities between neutrinos and anti-neutrinos, namely $P(\nu_\alpha \to \nu_\beta)$ and $P(\overline{\nu}_\alpha \to \overline{\nu}_\beta)$.

So far, neutrino oscillations were discussed in a vacuum, where all neutrino flavors interact equally. Indeed, the so-called Mikheyev-Smirnov-Wolfenstein (MSW) matter effect [30–32] involves neutral and charged-current coherent scatterings of neutrinos off electrons or nucleons in a medium. While neutral-current scattering impacts all flavors equally, charged-current coherent scattering occurs only for electron neutrinos off electrons in matter. This effect leads to a modification of oscillation probabilities, crucial when considering oscillation experiments at long baselines, e.g., solar neutrinos traveling from the Sun to Earth or atmospheric neutrinos traversing the Earth before being detected.

Neutrino Mass Ordering Note that the squared mass differences Δm^2_{12} and Δm^2_{13} measured by several oscillation experiments are linked by $\Delta m^2_{32} = \Delta m^2_{31} - \Delta m^2_{21}$. Experimental evidence from atmospheric neutrino experiments like Super-Kamiokande found that $|\Delta m^2_{32}| \sim |\Delta m^2_{31}| \sim 10^{-3}$ eV^2, but the sign of this so-called "atmospheric mass splitting" is currently unknown. This splitting is roughly two orders of magnitude higher than the so-called "solar mass splitting", $\Delta m^2_{21} \sim 10^{-5}$ eV^2, originally reported by solar neutrino experi-

ments like SNO, GALLEX, and SAGE. Since the sign of the atmospheric splitting was not determined, the third mass eigenstate can be either smaller or larger than the first two. The two possible scenarios are pictured in Figure 1.3: a Normal Mass Ordering (NMO) implies that m_3^2 is larger than m_1^2 and m_2^2; in the Inverted Mass Ordering (IMO), m_3^2 is instead the smaller absolute mass out of the three mass eigenstates. Moreover, note that the CP-violating phase δ has not been determined yet, and it will impact the flavor composition of the mass eigenstates.

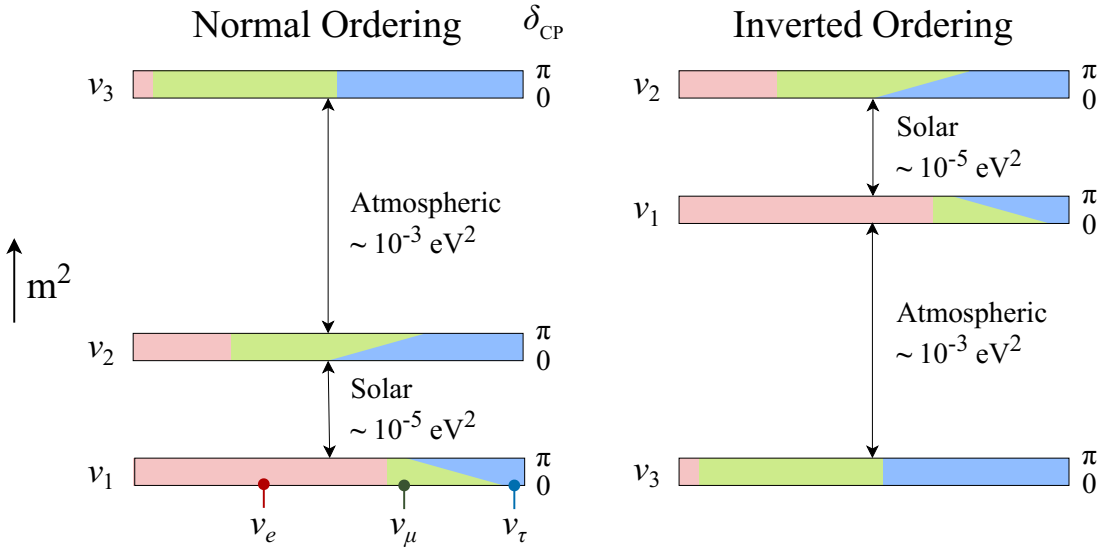

Figure 1.3: Representation of the two Normal Ordering and Inverted Ordering scenarios for the neutrino mass orderings, based on the sign of the atmospheric mass splitting, which is roughly 300 times larger than the solar splitting. The contribution of the three neutrino flavors to each mass eigenstate is highlighted, for two possible values of the CP-violating phase δ.

1.1.3 Status of Oscillation Experiments

Oscillation experiments are a crucial tool to determine the PMNS matrix. Consider the parametrization of the PMNS matrix from Equation 1.7: each parameter can be accessed by exploiting different neutrino sources to vary the baseline and the energy, hence the L/E ratio. Moreover, oscillation experiments are classified into "appearance" experiments, where the oscillation probability from a neutrino $|\nu_\alpha\rangle$ to a different flavor $|\nu_\beta\rangle$ is tested, and "disappearance" experiments, where the probability $P(\nu_\alpha \to \nu_\alpha) = 1 - \sum_{\beta \neq \alpha} P(\nu_\alpha \to \nu_\beta)$ is measured, hence the decrease in the flux of a specific neutrino flavor in the source. Note that typically an experiment is sensitive to a mass splitting around $\Delta m^2 \sim E/L$. Figure 1.4 shows how from 1998 until now different experiments helped improve the precision of oscillation parameters, the three mixing angles, the two mass squared differences, and the complex CP-violating phase. Recent global analyses improved the precision on the parameters to the percent level, and experiments are hence entering the so-called "precision era" for neutrino physics.

Solar Neutrino Experiments Several solar neutrino oscillation experiments exist to detect the neutrinos produced in the Sun, for which the L/E ratio allows mainly the mixing between the ν_1 and ν_2 states and the dominant oscillations are dictated by θ_{12} and Δm_{12}^2. As a result, solar neutrino experiments are sensitive

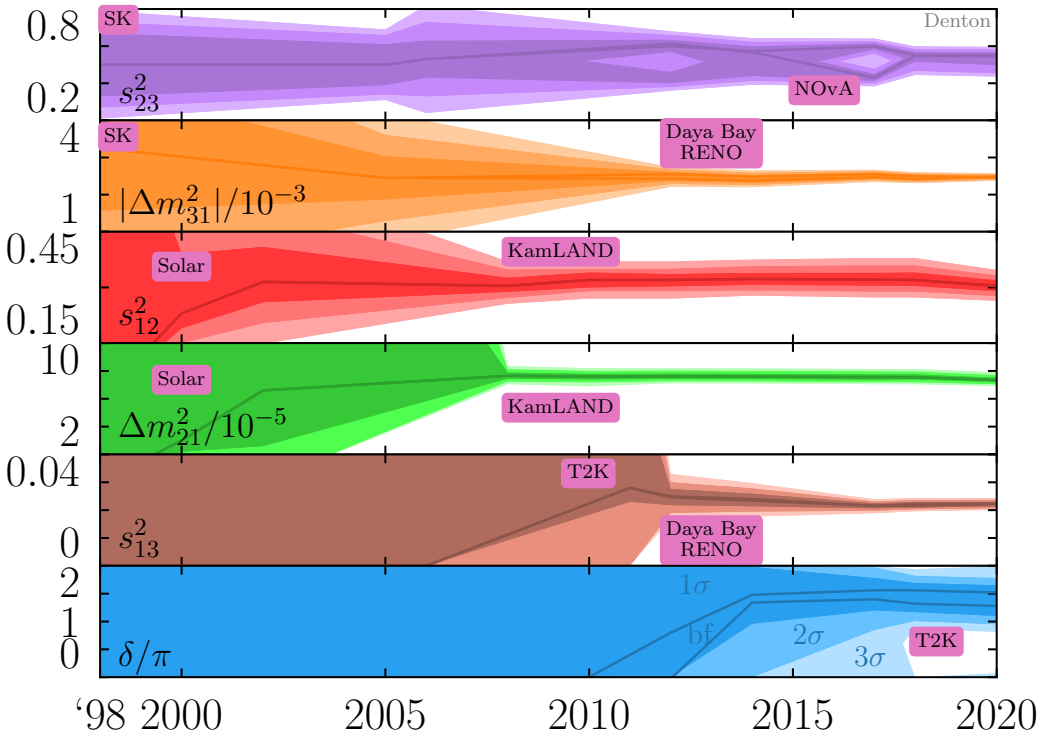

Figure 1.4: Experimental limits on the six neutrino oscillation parameters from 1998 till now. Some of the experiments that helped increase the precision of the parameters are highlighted. Taken from [33].

mostly to the parameters in the third matrix of the decomposed PMNS matrix from Equation 1.7 ("solar sector"). As previously mentioned, the Chlorine-based Homestake experiment [16] was the first to detect neutrinos from the Sun, and the corresponding "solar neutrino anomaly" was later resolved by the SNO experiment [24]. The dominant parameters are estimated to be $\sin^2 2\theta_{12} = 0.270 - 0.341$ and $\Delta m^2_{21} = (6.82 - 8.03) \cdot 10^{-5}$ eV^2 at the 3σ level and were constrained by Gallium-based experiments like the Soviet-American Gallium Experiment (SAGE) [26] and the Gallium Experiment (GALLEX) [25], by Cherenkov experiments like Super Kamiokande [34], SNO [35] and Borexino [36], and by KamLAND [37].

Atmospheric Neutrino Experiments The L/E ratio for neutrinos produced in the atmosphere implies that atmospheric neutrino experiments can access with good sensitivity the θ_{23} and Δm^2_{23} parameters, hence the first matrix of the PMNS decomposition from Equation 1.7 ("atmospheric sector"). First results were provided by the Super Kamiokande experiment from ν_μ-disappearance data [38] and recently they were combined with the IceCube DeepCore results from 2018 [39]. Resulting parameter values show that $|\Delta m^2_{32}| \sim 2.5 \cdot 10^{-3}$ eV^2 and $\sin^2 \theta_{23} \sim 0.5$, depending on the neutrino mass ordering.

Accelerator Experiments Precise measurements of neutrino oscillations can be made with neutrino beams, with the advantage that the detector can be placed at a precise baseline L according to a certain average neutrino energy E, yielding more control over the oscillation observables. In particular, accelerator experiments operate both in the appearance and disappearance channels with two detectors: a near detector collects neutrinos close to the source before the oscillation develops, while the far detector observes the oscillated

energy spectrum of neutrinos.

The first neutrino oscillation searches at accelerators at long baselines ($L/E < 10^3$ km/GeV) were carried out with the K2K and MINOS experiments, exploring the ν_μ-disappearance channel and the Δm^2_{31}, Δm^2_{32} and θ_{13} oscillation parameters linked to the atmospheric sector with GeV-scale muon neutrino beams. Current experiments include the successor of K2K, T2K, based on the far Super Kamiokande detector at a 295 km baseline [40, 41], and NOνA as the successor of MINOS, studying neutrino oscillations with the NuMI beam at an 810 km baseline [42]: both experiments focus on the ν_μ-disappearance and ν_e-appearance channels to constrain Δm^2_{32}, θ_{32}, θ_{31}, and also the CP-violating phase $\delta_{\rm CP}$. In particular, both experiments have reported a slight preference in data for the normal ordering of neutrino masses and T2K prefers a $\delta_{\rm CP} \sim 3\pi/2$ phase [43], while the best fit from NOνA points at around $\delta_{\rm CP} \sim \pi/2$ [44].

Reactor Experiments Nuclear reactors emit electron anti-neutrinos with fission reactions in their core with energies at the MeV-scale, typically detected in disappearance experiments through the inverse beta-decay, $\overline{\nu} + p \to e^+ + n$. Reactor experiments at medium baselines are sensible to the θ_{13} mixing angle, which remained unmeasured for a long time. The Chooz experiment first searched for the $\overline{\nu}_e$ disappearance at reactors and a 1 km baseline, but found no evidence of oscillation and excluded the $\sin^2 2\theta_{13} > 0.10$ parameter region [20]. Its successor, Double Chooz, found an observed-to-predicted ratio of $\overline{\nu}_e$ events equal to $0.944 \pm 0.016_{\rm stat.} \pm 0.040_{\rm syst.}$: this deficit was interpreted in terms of neutrino oscillations and suggested a non-zero value of θ_{13}, finding that $0.017 < \sin^2 2\theta_{13} < 0.16$ at the 90% confidence level [45]. Eventually, the θ_{13} mixing angle was accurately measured by combining the datasets from Double Chooz [46], Daya Bay [47], and the Reactor Experiment for Neutrino Oscillation (RENO) [48], yielding a best-fit value of $\theta_{13} \sim 9^\circ$.

Moreover, the Kamioka Liquid Scintillator Anti-Neutrino Detector (KamLAND) investigated the solar sector by collecting neutrinos from nuclear reactors at an average baseline of 180 km, being able to constrain the θ_{12} and Δm^2_{12} parameters [49].

1.2 Short-baseline Neutrino Anomalies

The discovery of neutrino oscillations and non-zero neutrino masses represents today the main experimental evidence of physics beyond the Standard Model. Being some of their fundamental properties still unknown, neutrinos are naturally one of the main portals toward new physics beyond the Standard Model. Despite the well-established three-flavor neutrino mixing picture, several anomalies have been collected so far at short baselines ($L/E < 10$ m/MeV), hinting at the existence of additional neutrino states.

The LSND experiment found an excess of $\overline{\nu}_e$ events in a $\overline{\nu}_\mu$ neutrino beam with a 3.8σ significance [50]. In the ν_e-disappearance channel, the GALLEX and SAGE Gallium-based experiments originally found a deficit in the rates from Mega-Curie radioactive sources used for calibrating the solar neutrino experiments with an $R = 0.84 \pm 0.05$ observed-to-expected ratio [25, 26], recently confirmed at 4σ by the BEST experiment [51]. In the $\overline{\nu}_e$-disappearance channel, nuclear reactor experiments at short baselines found a deficit in the $\overline{\nu}_e$ rates initially amounting to $R = 0.934 \pm 0.024$, but dependent on uncertainties on the neutrino spectrum and much discussed [52].

Short-baseline neutrino anomalies serve as a first possible hint at additional neutrino states, originally hypothesized by B. Pontecorvo in a 1957 seminal paper [53]. Indeed, measurements of the Z-boson decay width at LEP constrain the number of neutrino states actively interacting via the weak force to three [7]: additional neutrino states would be compatible with past neutrino measurements only if "sterile", hence interacting only through the gravitational force.

LSND Anomaly The Liquid Scintillator Neutrino Detector (LSND) at the Los Alamos Meson Physics Facility (LAMPF) collected data from 1993 to 1998 and observed an anomalous excess of $\overline{\nu}_e$ in an almost pure $\overline{\nu}_\mu$ beam with energies of $\mathcal{O}(50\ \text{MeV})$ and at a baseline of 30 m [50]. The source of $\overline{\nu}_\mu$ were μ^+-s decaying at rest and produced by 800 MeV protons on beam target. The $\overline{\nu}_e$ signals are detected through the inverse beta decay interaction with protons, $\overline{\nu}_e + p \to n + e^+$: event signatures are given by the positron, resulting in prompt Cherenkov and scintillation light signals, and by the neutron undergoing capture and producing a delayed 2.2 MeV photon. The light is collected by 1,220 8-inch PhotoMultiplier Tubes (PMTs). The backgrounds in this search are false $\overline{\nu}_e$ signatures due to accidental coincidences between a positron-like and a neutron-like signal and $\overline{\nu}_e$ interactions from μ^- or π^- decays in the source. An excess of roughly $87.9 \pm 22.4 \pm 6.0$ $\overline{\nu}_e$ events over the expected background was observed, with a significance of 3.8σ. The excess as a function of L/E compared to the expected beam backgrounds is shown in Figure 1.5(a).
Figure 1.5(b) shows the allowed parameter region in the $(\sin^2 2\theta,\ \Delta m^2)$ plane from LSND, interpreting the event excess as a hint for neutrino oscillations. Several experiments investigated the LSND anomaly, including KARMEN [54], BNL E776 [55], CDHSW [56], CHORUS [57], NOMAD [58] and MINOS [59].

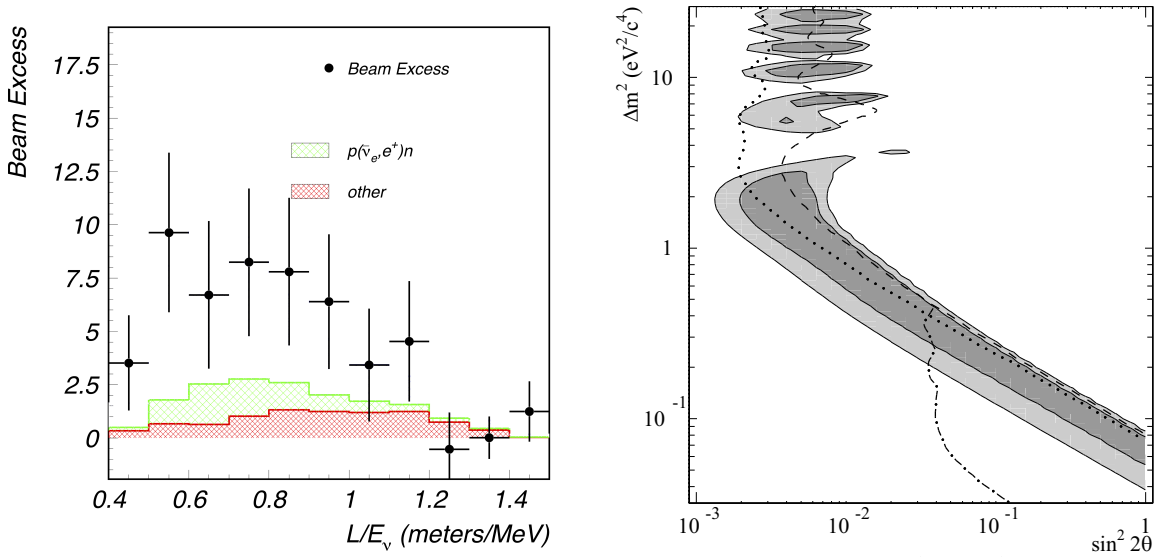

(a) (b)

Figure 1.5: (a) Excess of $\overline{\nu}_e$ in a $\overline{\nu}_\mu$ beam as observed by LSND, compared to the predicted backgrounds. Beam-unrelated backgrounds are already subtracted. (b) 90% and 99% likelihood regions in the $(\sin^2 2\theta,\ \Delta m^2)$ plane from the LSND anomaly, along with 90% C.L. limits from the KARMEN (dashed), BNL E776 (dotted), and the Bugey reactor (dot-dashed) experiments. Taken from [50].

The MiniBooNE experiment collected data at Fermilab from 2002 until 2019 exposed to the Booster ν_μ Neutrino Beam (BNB), to address the $\overline{\nu}_e$ short-baseline anomalous excess reported by LSND [60] with a spherical detector filled with 450 tons of pure CH_2 mineral oil and located at a baseline of 541 m. Since the neutrino energies peak at roughly 500 MeV, MiniBooNE is characterized by a similar L/E with respect to the LSND experiment, being sensitive to the same oscillation parameters. The detector featured 1,520 PMTs to detect scintillation and Cherenkov light, focusing mainly on charged-current quasi-elastic ν_e and ν_μ interactions. The signatures for those events are Cherenkov light rings projected onto the PMTs: while the muon creates a sharp ring, a less massive electron scatters and showers, generating a fuzzy Cherenkov ring. Besides the intrinsic $\sim 0.5\%$ $\nu_e + \overline{\nu}_e$ beam contamination, event backgrounds come from NC interactions with a single photon or a π^0 in the final state, decaying into photons and producing Cherenkov rings hard to be distinguished from the single-ring signature of genuine ν_e or $\overline{\nu}_e$ events (Figure 1.6). MiniBooNE reported an event excess concentrated in the low energy $200 < E_\nu^{\mathrm{QE}} < 475$ MeV region at 4.8σ (Low Energy Excess, LEE, Figure 1.6), combining data from both the neutrino and anti-neutrino BNB modes. The MiniBooNE LEE anomaly is below the sensitive L/E region of LSND.

In 2013, the ICARUS experiment, based on the innovative Liquid Argon Time Projection Chamber (LArTPC) technology, identified four electron neutrino candidates out of the expected 6.4 ± 0.9 ν_e events from the CERN Neutrinos to Gran Sasso (CNGS) ν_μ beam, restricting the LSND oscillation signals in a narrow parameter region where all experimental results were in agreement. This result also strongly limits the MiniBooNE LEE anomaly, "suggesting an instrumental or otherwise unexplained nature of the low energy signal" [61]. More recently, the MicroBooNE experiment addressed the MiniBooNE anomaly with the same Booster Neutrino Beam and a similar baseline, but using the LArTPC technology, pioneered by the ICARUS experiment. No excess of low-energy ν_e candidates was found, refusing at $> 97\%$ C.L. the hypothesis that ν_e charged-current interactions are fully responsible for the MiniBooNE LEE anomaly [62].

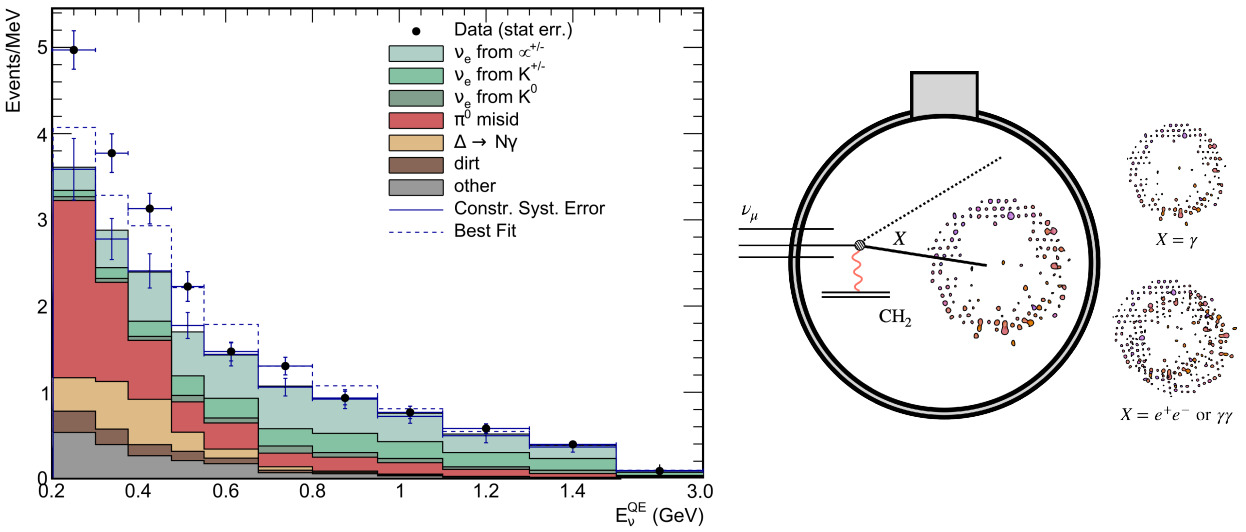

Figure 1.6: (left) Neutrino energy distribution at MiniBooNE for Charged-Current (CC) Quasi-Elastic (QE) ν_e events in neutrino mode. The dashed curve shows the best fit to data considering two-neutrino short-baseline oscillations. The significance of the Low-Energy Excess (LEE) with the full MiniBooNE datasets amounts to 4.8σ. (right) Examples of Cherenkov rings detected by MiniBooNE's PMTs.

Gallium Anomaly The Gallium Experiment (GALLEX) [25] and the Soviet-American Gallium Experiment (SAGE) [26] observed a deficit of events in radioactive source experiments aimed at characterizing the solar neutrino detection efficiency through the inverse beta decay on Gallium, i.e. $\nu_e + {}^{71}\mathrm{Ga} \rightarrow e^- + {}^{71}\mathrm{Ge}$. GALLEX used an intense artificial ${}^{51}\mathrm{Cr}$ radioactive source inside the detector, emitting electron neutrinos through the electron capture process, $e^- + {}^{51}\mathrm{Cr} \rightarrow {}^{51}\mathrm{V} + \nu_e$. Similarly, SAGE performed source experiments with ${}^{51}\mathrm{Cr}$ and ${}^{37}\mathrm{Ar}$. Substantial deficits were observed in the observed rates with respect to the rates calculated from the well-measured activity of the sources and different cross-sections for the detection process. Recently, the Baksan Experiment on Sterile Transitions (BEST) explored the results reported by GALLEX and SAGE with a similar design and detection technique and reported an even larger deficit, hence confirming the anomaly [51]. The ratios of observed and predicted rates as a function of the average neutrino path lengths are reported in Figure 1.7. The two BEST values show the ratio in the two nested ${}^{71}\mathrm{Ga}$ volumes of the experiment, corresponding to 0.5 m and 1.1 m average path lengths. Data from the three experiments can be fitted with a constant average ratio of $R = 0.80 \pm 0.04$ [63].

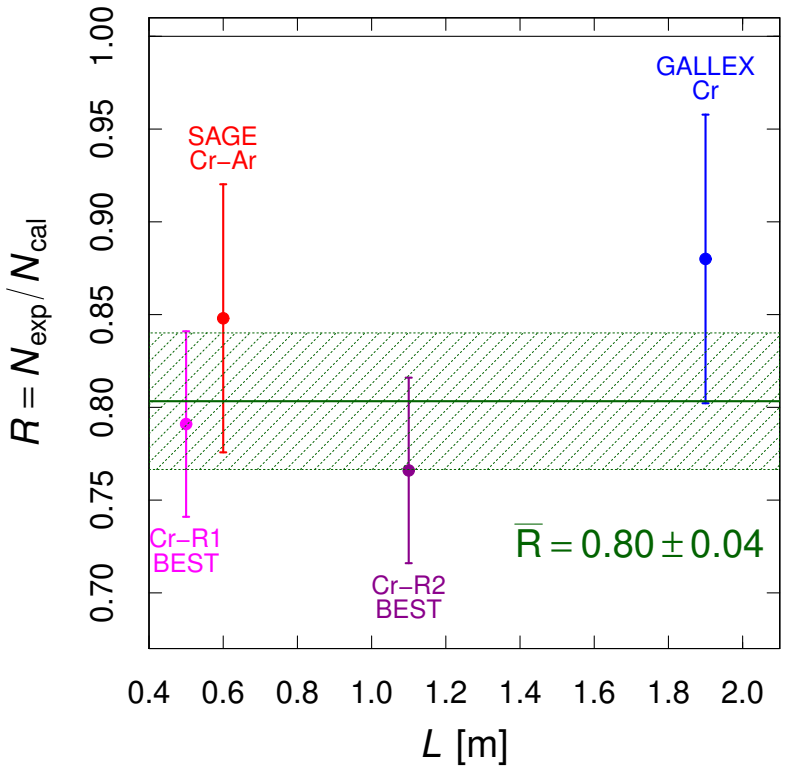

Figure 1.7: Ratios of observed and predicted ν_e event rates in source experiments at the GALLEX, SAGE, and BEST Gallium-based experiments. Taken from [63].

Anomalies at Reactor Experiments Nuclear reactor experiments at distances smaller than roughly 100 m from the reactor core at ILL-Grenoble, Savannah River, and Bugey, measured the rate of $\overline{\nu}_e$ to be slightly lower than expected, with a $R = 0.976 \pm 0.024$ ratio ("reactor anti-neutrino anomaly") [52]. By including measurements from the longer-baseline Chooz and KamLAND reactor experiments, the average deficit increases and leads to a $R = 0.943 \pm 0.023$ ratio deviating from unity at the 98.6% confidence level [52]. If this deficit is due to neutrino mixing, it could be explained by an energy-independent suppression of the

$\overline{\nu}_e$ flux at $\mathcal{O}(10\text{ m})$ distances, hinting at an additional (sterile) neutrino state with a mass splitting at the $\mathcal{O}(1\text{ eV}^2)$ scale. The reactor anomaly has been long discussed, due to difficulties in calculating the expected anti-neutrino flux, accounting for the several involved nuclear reactions.

Recently, the Neutrino-4 experiment [64] measured the flux and spectrum of reactor anti-neutrinos as a function of the distance from the core of the SM-3 reactor in Dimitrovgrad, Russia, and gave evidence of short-baseline neutrino oscillations in the $\overline{\nu}_e$-disappearance channel with a clear $L/E = 1-3$ m/MeV modulation. The main component of the Neutrino-4 detector is its highly-segmented inner vessel, which is divided into 50 sections, ten rows by five sections each with a $0.225 \times 0.225 \times 0.85$ m^3 size and filled with liquid scintillator, yielding a total 1.8 m^3 volume of scintillator. The detector can be moved along with its steel passive shielding into various positions in the $6-12$ m range with respect to the reactor's core. Considering a detection efficiency of roughly 30%, the detector expected roughly 300 anti-neutrino events per day at an average baseline of 8 m. The detection technique is the Inverse Beta Decay (IBD) of electron anti-neutrinos on protons, producing a positron and a prompt light signal, and a neutron undergoing capture on Gadolinium atoms, present at a 0.1% concentration in the liquid scintillator. The light signals are detected by PMTs. The experiment carried out a spectrum-independent data analysis based on the ratio $R_{ik} = S_{ik}/\frac{1}{K}\sum_k^K S_{ik}$ with $S_{ik} = (N_{ik} \pm \Delta N_{ik})L_k^2$: the numerator is the rate of anti-neutrino events in the i-th energy range and at the k-th distance, considering the correction to the geometric factor L^2; the denominator is the rate of anti-neutrino events with the same energy, but averaging it over all the sampled distances. Since the oscillation effect is averaged out in the denominator, in the no-oscillation case the ratio should yield the unity. The result of the Neutrino-4 analysis on $2016-2021$ data is reported in Figure 1.8.

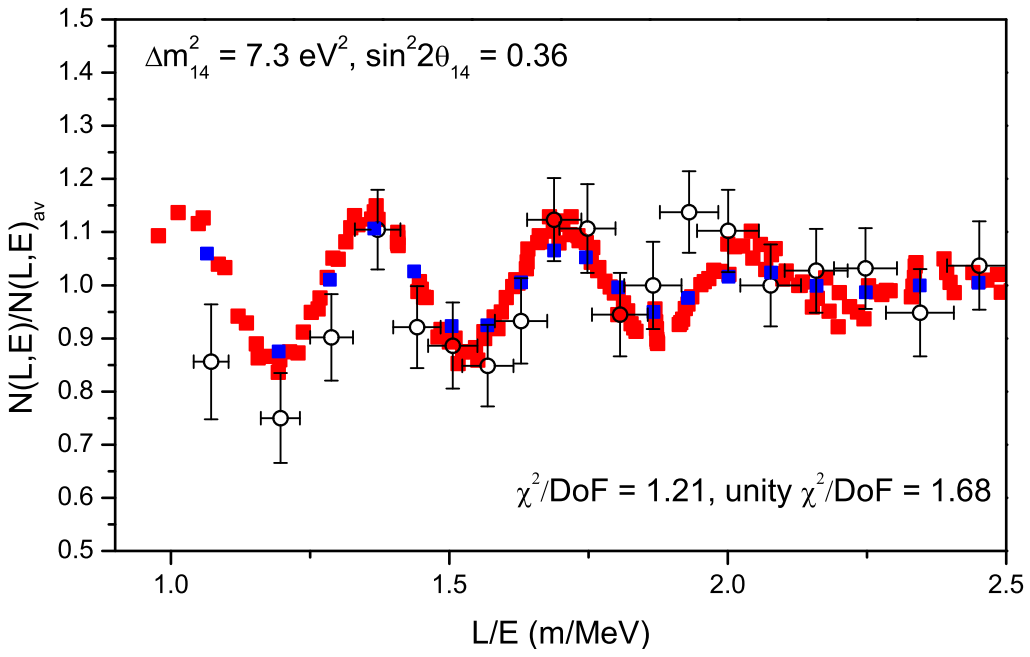

Figure 1.8: Trend of the R_{ik} ratio (for reference, see text) of $\overline{\nu}_e$ events as a function of L/E_ν for the neutrino sample, given by the ON-OFF reactor data in the Neutrino-4 experiment. Taken from [64].

The main background in the Neutrino-4 experiment is given by fast neutrons from cosmic rays. The scattering of fast neutrons on protons mimics the IBD process: the recoil proton imitates the IBD positron prompt

signal, while the capture of the scattered neutron on Gadolinium is similar to the corresponding delayed process in the IBD. Indeed, the first and last detector rows were used as an "active" shielding to address the fast neutron background, thus yielding a 1.42 m^3 fiducial volume for the detector. It was estimated by Neutrino-4 that background fluctuations uncorrelated with the reactor flux are taken care of through the subtraction of reactor-ON and reactor-OFF data, and the surviving cosmic background contribution is of the order of $\mathcal{O}(0.1\%)$ with respect to the neutrino signal.

1.2.1 Sterile Neutrino Models

The short-baseline neutrino anomalies reported at accelerators, radioactive source experiments with Gallium detectors, and at nuclear reactors could be interpreted as short-baseline oscillations, induced by an additional neutrino mass state ν_4 with a mass splitting of $\Delta m^2_{41} = \mathcal{O}(1\ \mathrm{eV}^2)$, inducing fast oscillations not detected by experiments at longer baselines. As already mentioned, any additional neutrino state is compatible with the measurements at LEP on the Z-boson decay width [7] only if "sterile", hence not interacting through the weak force. Clearly, a fourth sterile neutrino would not be detectable directly, but its presence should induce oscillations through the three active neutrino states.

To accommodate for N additional sterile neutrino states, the PMNS matrix from Equation 1.7 can be extended to a $(3+N)\times(3+N)$ matrix. In the simplest $3+1$ sterile neutrino model, there is one additional flavor state ν_s and a fourth mass state ν_4. To maintain consistency with past three-neutrino oscillation measurements, the sterile-flavor neutrino ν_s contribution to the ν_1, ν_2, ν_3 mass states should be small, hence the heavier ν_4 mass state is composed primarily of ν_s. Figure 1.9 represents the mass splittings and flavor mixing in the $3+1$ sterile neutrino model.

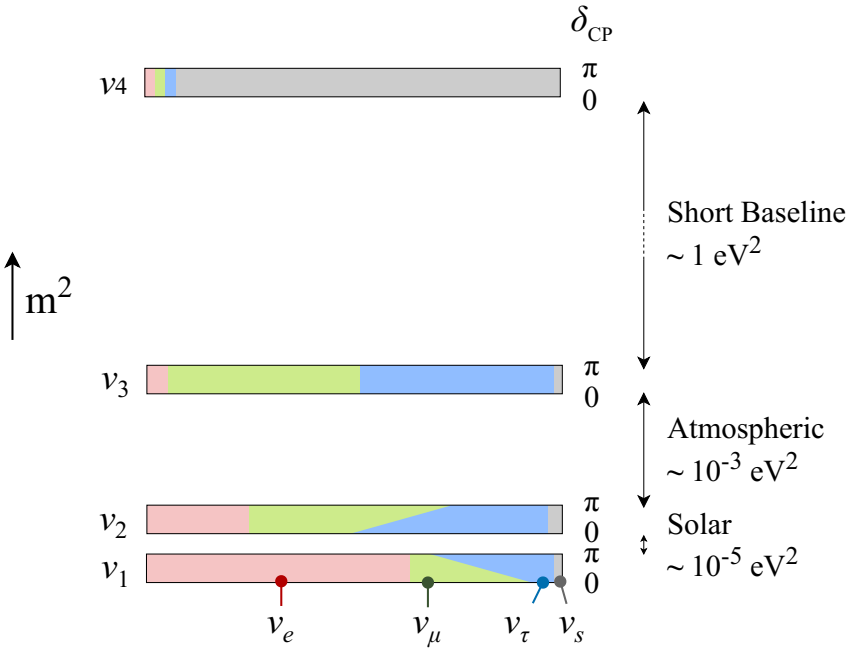

Figure 1.9: Representation of the neutrino mass splittings and flavor mixing for the $3+1$ sterile neutrino model. Mass splittings in the Normal Ordering scenario are shown not to scale.

From short-baseline experimental evidence, the mass splitting Δm^2_{41} should be much bigger than the pre-

viously discussed Δm^2_{31} and Δm^2_{32} mass splittings and the oscillation probabilities at short baselines can be approximated by the two-flavor oscillation case:

$$P(\nu_e \to \nu_e) = 1 - 4(1 - |U_{e4}|^2)|U_{e4}|^2 \sin^2(1.27 \cdot \Delta m^2_{41} L/E_\nu) \,, \tag{1.11}$$

$$P(\nu_\mu \to \nu_\mu) = 1 - 4(1 - |U_{\mu 4}|^2)|U_{\mu 4}|^2 \sin^2(1.27 \cdot \Delta m^2_{41} L/E_\nu) \,, \tag{1.12}$$

$$P(\nu_\mu \to \nu_e) = 4|U_{\mu 4}|^2|U_{e4}|^2 \sin^2(1.27 \cdot \Delta m^2_{41} L/E_\nu) \,, \tag{1.13}$$

respectively for the ν_e and ν_μ-disappearance and ν_e-appearance channels. Thus, each channel corresponds to an "effective" mixing angle: e.g., for the ν_e-appearance case the effective mixing strength is defined as $\sin^2 2\theta_{\mu e} = 4|U_{\mu 4}|^2|U_{e4}|^2$.

1.2.2 Status and Perspectives

Several other experiments have recently emerged to tackle neutrino anomalies and a global picture highlights tensions in the results, with no definitive indication of the existence of sterile neutrinos, nor of their non-existence. The majority of short-baseline experiments focused on the $\nu_\mu \to \nu_e$ appearance channel, ν_μ-disappearance and ν_e-disappearance and analogous anti-neutrino channels.
As already mentioned, one of the strongest short-baseline anomalies was found by the LSND in the $\overline{\nu}_e$-appearance channel: the signal can be interpreted in terms of short-baseline $\overline{\nu}_\mu \to \overline{\nu}_e$ oscillations in the $3+1$ sterile neutrino model, favoring a mass splitting $\Delta m^2_{14} = 0.2 - 2$ eV^2 and an oscillation strength of $\sin^2(2\theta_{\mu e}) \sim 0.003$ [50]. Similarly, in the ν_e-apperance channel, the MiniBooNE LEE anomaly can be modeled with the $3+1$ picture and the best-fit of data points to $(\Delta m^2_{14}, \sin^2 2\theta_{\mu e}) = (0.043 \text{ eV}^2,\ 0.807)$. It is worth mentioning that the best fit using the $3+1$ sterile neutrino model does not fully match the MiniBooNE data (see Figure 1.6). Recall that the LEE anomaly has been extensively discussed and both the ICARUS at LNGS and MicroBooNE experiments rejected the ν_eCC nature of the MiniBooNE anomalous excess. Indeed, the allowed regions from LSND and MiniBooNE are in overall agreement, as shown in Figure 1.10. On the other hand, the KARMEN experiment, with a liquid scintillator detector similar to LSND and at a 17 m baseline, found no evidence of oscillation in the $\overline{\nu}_e$-appearance channel, hence excluding part of the LSND and MiniBooNE allowed regions in the $(\sin^2 2\theta_{\mu e},\ \Delta m^2_{41})$ plane [54]. Similarly, CHORUS [57] and NOMAD [58] did not observe $\nu_\mu \to \nu_e$ oscillations at a baseline of 625 m with neutrinos at ~ 20 GeV energies at CERN, excluding the $\Delta m^2_{41} > 10$ eV^2 parameter region. As already mentioned, ICARUS in 2013 [65] and OPERA later in 2015 [66] provided strong limits on the LSND and MiniBooNE allowed regions with the analysis of neutrinos from the CNGS beam at Gran Sasso, defining a narrower allowed region around $(\Delta m^2_{14}, \sin^2 2\theta_{\mu e}) = (0.5 \text{ eV}^2, 0.005)$ in which there is a 90% C.L. overall agreement among different experiments.

The Gallium Anomaly, originally found by the GALLEX [25], SAGE [26], and recently confirmed by BEST [51], can be interpreted in terms of short-baseline neutrino oscillations in the ν_e-disappearance channel, using the $3+1$ sterile neutrino framework. There is a clear indication of a large value of $\sin^2 2\theta_{ee} \sim 0.14$ for a mass splitting $\Delta m^2_{14} > 0.6$ eV^2 at the $> 2\sigma$ level, needed to produce an oscillation amplitude that is sufficient to explain the observed deficit. Indeed, the Gallium-based results are in tension with results from

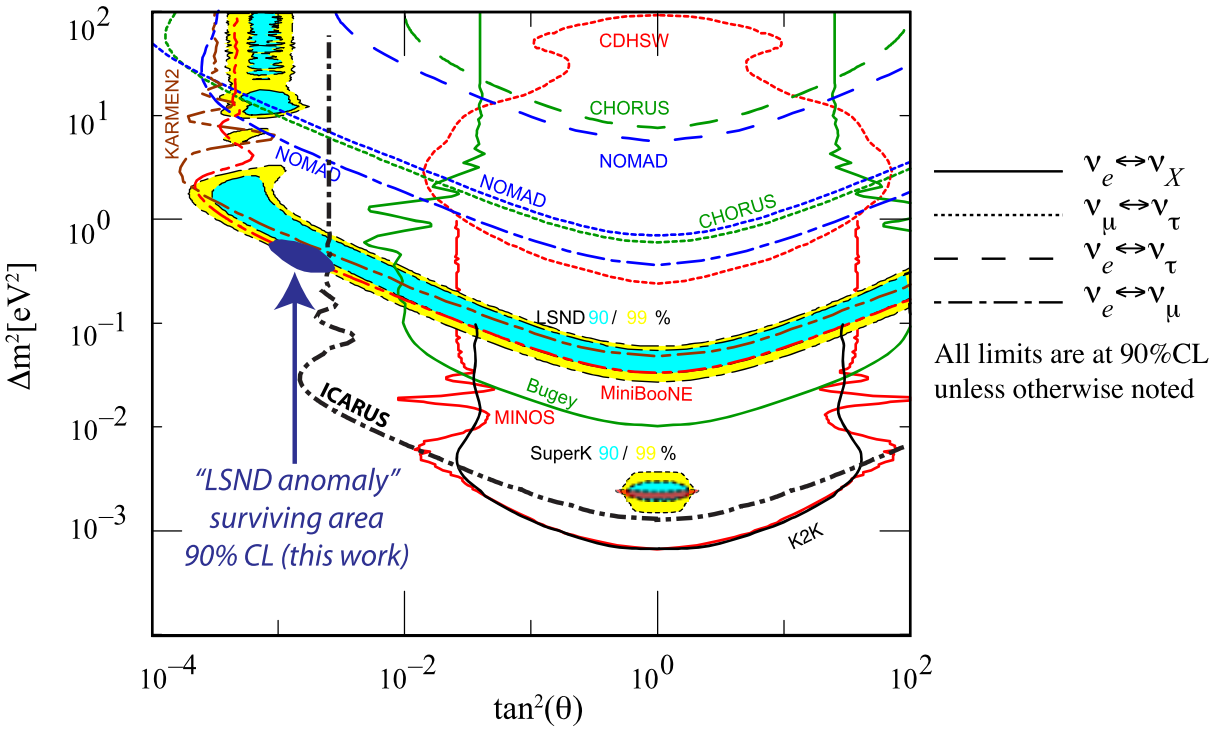

Figure 1.10: Comparison of the best-fit regions from the LSND short-baseline anomaly and exclusion curves from published results, most notably KARMEN, NOMAD, and ICARUS. The "surviving area" of the LSND anomaly where there is overall agreement at 90% C.L. is highlighted. Taken from [65].

LSND and MiniBooNE, which measured the ν_e cross-section on Carbon through $\nu_e + {}^{12}\mathrm{C} \to {}^{12}\mathrm{N} + e^-$ at different baselines but with similar neutrino spectra [67]. The ν_e-C cross-sections in LSND and MiniBooNE were found to be compatible, hence partially excluding signs of ν_e-disappearance.

Again, tension arises also in the $\overline{\nu}_e$-disappearance channel, dominated primarily by reactor experiments where the $\overline{\nu}_e$ spectra usually peak at a few MeV and the baselines are $\mathcal{O}(10\ \mathrm{m})$. As already anticipated, the Neutrino-4 experiment [64] recently found evidence of a strong short-baseline oscillation signal at $6-12$ m baselines with a sensitivity of roughly 3σ, increasing to 5.8σ when including the GALLEX, SAGE, and BEST data [68]. The $3+1$ best fit on Neutrino-4 data hints at a mass splitting of $\Delta m^2_{14} = 7.30 \pm 0.13_{\mathrm{stat.}} \pm 1.16_{\mathrm{syst.}}\ \mathrm{eV}^2$ and a strength $\sin^2 2\theta_{ee} = 0.36 \pm 0.12_{\mathrm{stat.}}$, which is essentially not compatible with results from other reactor-based experiments. A slight preference for the $3+1$ sterile oscillation hypothesis was also found in the DANSS experiment, yielding a mass splitting $\Delta m^2_{41} \sim 1.4\ \mathrm{eV}^2$ and a mixing strength $\sin^2 2\theta_{ee} \sim 0.05$ [69]. At the same time, no evidence of oscillations was found in the Bugey [70], NEOS [71], PROSPECT [72], and STEREO [73] experiments. Note that the search for short-baseline oscillations at reactors is influenced by uncertainties related to reactor anti-neutrino fluxes: those are mitigated by using segmented detectors (Neutrino-4, DANSS, PROSPECT, STEREO) or by using ratios between detectors at different baselines (Bugey, NEOS). Figure 1.11 shows a collection of constraints on ν_e and $\overline{\nu}_e$-disappearance data.

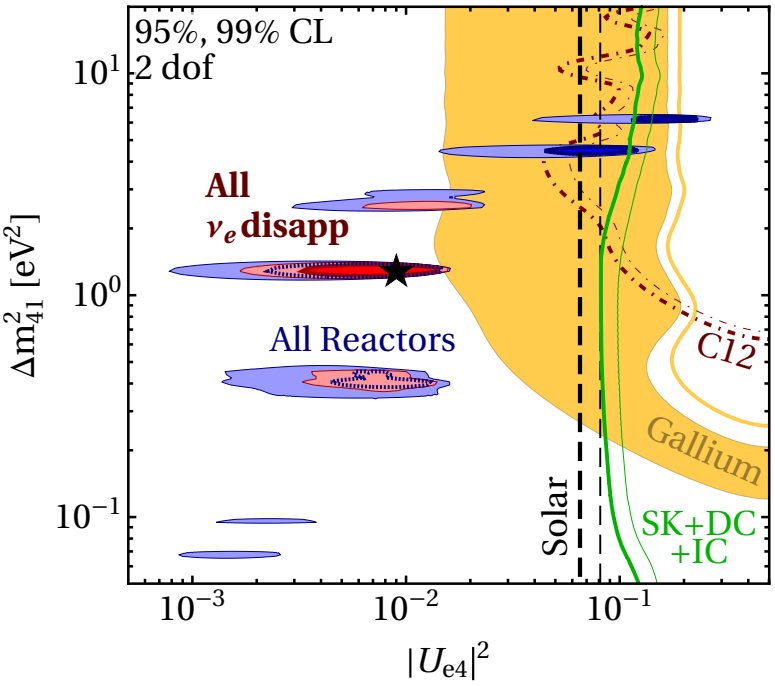

Figure 1.11: Dark-shaded regions and thick curves refer to 95% C.L. allowed regions or exclusion curves, while light-shaded regions and thin curves refer to the 99% C.L. Red and blue regions are allowed by ν_e and reactor $\overline{\nu}_e$-disappearance measurements. The yellow region is allowed by the Gallium Anomaly. The dashed red curve is the exclusion curve from ν_e-Carbon cross-sections as measured by the LSND and MiniBooNE experiments. Solar exclusion curves from Super Kamiokande and IceCube data are also shown. Taken from [74].

Finally, no oscillation signals were observed yet in the ν_μ and $\overline{\nu}_\mu$-disappearance channels, tackled mainly by short-baseline accelerator experiments using a primarily ν_μ or $\overline{\nu}_\mu$ beam, like in MiniBooNE, CDHS, and MINOS [74]. Contributions came also from Super Kamiokande and IceCube.

Perspectives Overall, the sterile neutrino picture appears complex and highlights several tensions. Figure 1.12 shows the combination of global appearance-disappearance data in the $(\sin^2 2\theta_{\mu e},\ \Delta m^2_{41})$ plane, resulting in the ν_e and $\overline{\nu}_e$-appearance data being excluded by the combined ν_e, $\overline{\nu}_e$, ν_μ, and $\overline{\nu}_\mu$-disappearance data.

Future precision experiments such as the Short Baseline Neutrino (SBN) program at Fermilab are expected to provide a definitive answer to the sterile neutrino puzzle, having access to both the ν_e-appearance and ν_μ-disappearance channels at the same time with an expected sensitivity of 5σ, by comparing neutrino spectra at different distances from the Booster Neutrino Beam target. SBN and its far detector, ICARUS, will be described thoroughly in the upcoming chapters.

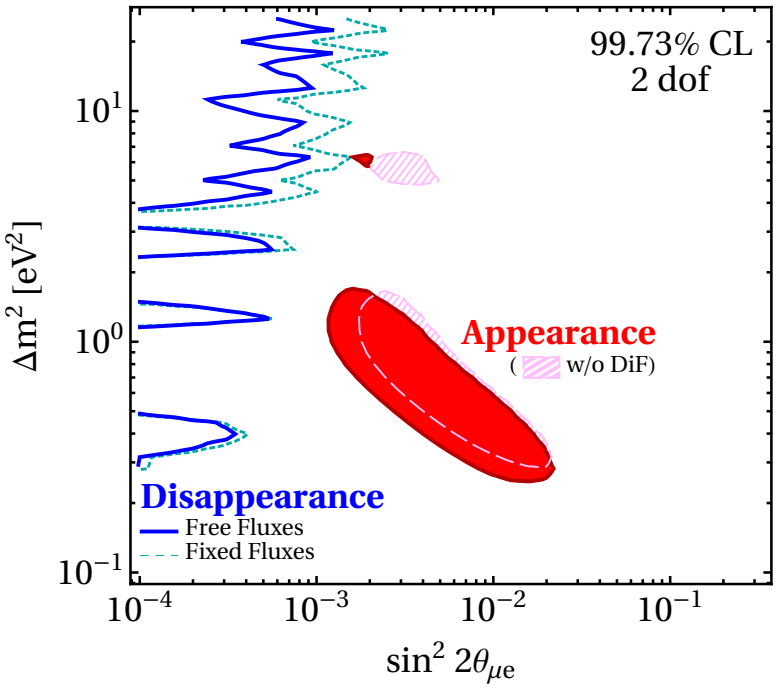

Figure 1.12: Allowed regions at 3σ from ν_e and $\overline{\nu}_e$-appearance data, with (red) and without (pink) LSND neutrino data from decay-in-flight of pions. Exclusion curve from combined ν_e, $\overline{\nu}_e$, ν_μ, and $\overline{\nu}_\mu$-disappearance data, with (solid) and without (dashed) fixed reactor fluxes. Taken from [74].

2

The ICARUS Detector at the Fermilab SBN Program

This Chapter contains:

2.1 ICARUS at Fermilab

The ICARUS (Imaging Cosmic And Rare Underground Signals) T600 detector [75, 76] is the first large-scale Liquid Argon Time Projection Chamber (LArTPC) detector ever realized and regularly taking data. Figure 2.1 presents a schematic of the detector in its basic components, which will be thoroughly presented in the upcoming sections. ICARUS consists of a warm vessel containing two adjacent identical ICARUS T300 modules, also indicated as West (W) and East (E) modules with respect to the direction of Fermilab's Booster Neutrino Beam (BNB). Each module has a volume of $3.6 \times 3.9 \times 19.6$ m^3 and consists of a cryostat housing two LArTPCs separated by a common central cathode. Between the insulation warm vessel and the aluminum containers of the T300 modules, a set of heat exchangers filled with LN_2 acts as a cold shield and prevents the heat coming from the external thermal insulation to reach the LAr containers. Thermal insulation is provided by 60 cm thick polyurethane foam panels maintaining the cryostats bulk temperature uniform and stable at 89 K.

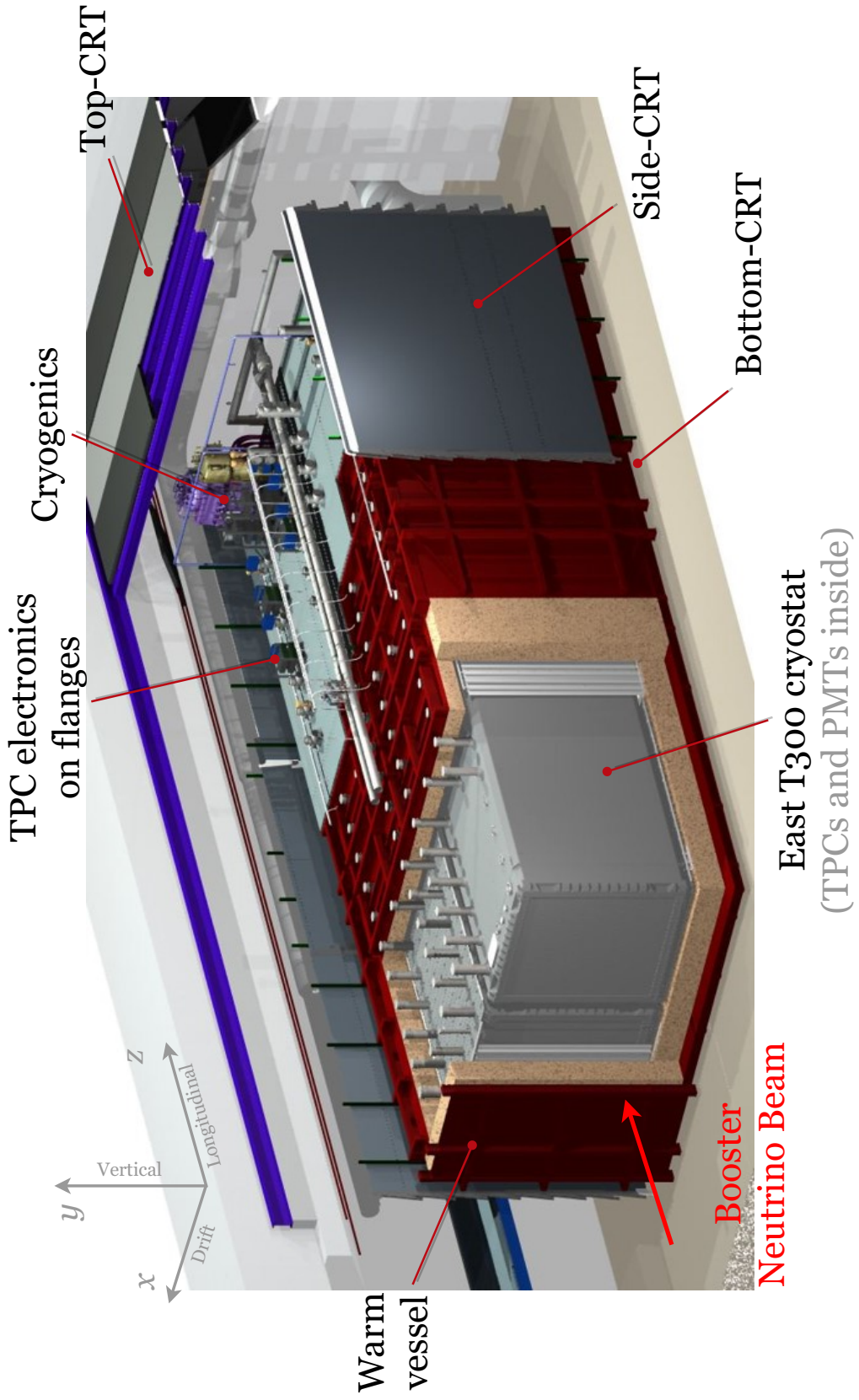

Figure 2.1: Schematic of the ICARUS T600 detector at Fermilab, with its basic components. The insulated warm vessel houses the two ICARUS T300 modules and is surrounded by the Cosmic Ray Tagger (CRT) system. On top of the vessel, one can find the TPC electronics and the proximity cryogenics.

The ICARUS collaboration successfully carried out a 3-year long run from 2010 to 2013 in the deep underground INFN Gran Sasso laboratory in Italy, collecting approximately 3,000 neutrinos from the CERN to Gran Sasso (CNGS) neutrino beam in the $10-30$ GeV energy range, and also recording cosmic rays and atmospheric neutrino interactions [76, 77]. ICARUS demonstrated the superior detection capabilities of the liquid argon TPC technology, with an exceptionally high argon purity level crucial for enabling physics studies with large-scale LArTPC detectors, hence paving the way for future similar experiments, e.g., the Deep Underground Neutrino Experiment (DUNE) [78, 79]. Furthermore, in 2013 a search for an LSND-like anomalous signal was carried out with ICARUS at LNGS data [65] and led to strongly limiting the region of allowed parameters for the LSND and MiniBooNE anomalies (for reference, see section 1.2).

From 2015 until 2017, an intense overhauling activity of the ICARUS detector was carried out at CERN and at the Legnaro National Laboratories (Padova, Italy) [75, 76], improving the readout electronics, the cryostats and the purification systems, and developing a more efficient light collection system. The apparatus eventually arrived at Fermilab (U.S.A.) and was installed at a shallow depth to operate as the far detector within the Short Baseline Neutrino (SBN) program [75], collecting data with the Booster Neutrino Beam and the Neutrinos at the Main Injector (NuMI) neutrino beams to address the light sterile neutrino hints mostly from LSND and MiniBooNE. An in-depth description of SBN can be found in section 2.2.

The PMT, TPC, and CRT sub-systems were commissioned from early 2021 until June 2022, when the deployment of the concrete overburden was completed. In the commissioning phase or Run0, ICARUS collected event statistics corresponding to $27.8 \cdot 10^{18}$ and $52.0 \cdot 10^{18}$ POT with BNB and NuMI respectively. This first sample was used to develop, test and tune the event reconstruction algorithms.

The ICARUS Run1 started on June 9th, 2022, and lasted until the usual Fermilab summer beam-shutdown on July 10th, 2022, and approximately $41 \cdot 10^{18}$ and $68 \cdot 10^{18}$ POT were collected with BNB and NuMI.

The ICARUS Run2 started on December 20th, 2022, and lasted until July 14th, 2023. Figure 2.2 shows the delivered and collected POT with BNB and NuMI throughout Run2. The collected-over-delivered POT efficiency is estimated to be $> 95\%$. Globally, the collected event statistics for physics analyses corresponds to $2.5 \cdot 10^{20}$ and $3.5 \cdot 10^{20}$ POT respectively for BNB and NuMI, more than a third of the total expected statistics.

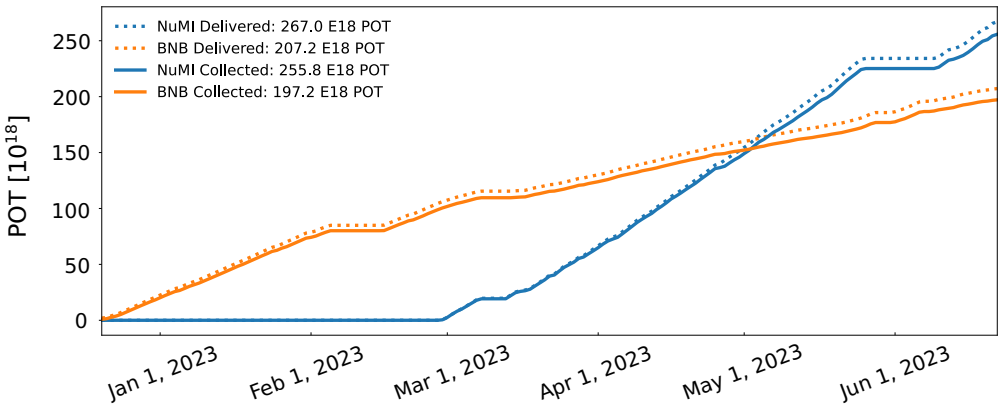

Figure 2.2: Delivered and collected Protons on Target (POT) for both the Booster and NuMI neutrino beams, throughout the ICARUS Run2 (December 20th, 2022 - July 14th, 2023).

2.1.1 Liquid Argon Time Projection Chamber

The ICARUS T600 detector consists of a large cryostat containing two identical T300 modules, and each module houses two liquid argon Time Projection Chambers separated by a common vertical cathode. The LArTPC imaging technology was originally conceived by C. Rubbia in 1977 [80] to fulfill the need for a device capable of combining the huge amount of information on the topology of a neutrino event typical of a bubble chamber but with the larger mass, timing, and flexibility of an electronic detector. Many years of research and development by the ICARUS collaboration [81] culminated with the ICARUS detector initially operating at the INFN Laboratori Nazionali del Gran Sasso (LNGS).

The principle of operation of a LArTPC [82] is pictured in Figure 2.3. The interaction between a neutrino and the liquid argon produces charged ionizing particles, that while propagating in the medium ionize and excite argon atoms. Produced electrons drift in the Liquid Argon (LAr) medium within the Time Projection Chamber (TPC) due to an electric field along the drift direction, induced by a potential difference between the cathode plane and the anode. The maximum drift distance of the ICARUS LArTPCs is 1.5 m, corresponding to approximately 1 ms electron drift time, for the nominal 500 V/cm electric drift field. In particular, the cathode consists of an array of nine panels made of pierced stainless steel, allowing for a 58% optical transparency between the two adjacent drift regions. The anode of each TPC is constituted by three overlapped planes (3 mm apart from each other) of sensing wires with a 3 mm pitch, respectively: Induction-1, Induction-2, Collection. In ICARUS, the first Induction-1 wire plane has horizontal wires split into two 9 m long wires. The second Induction-2 plane has wires at 60° degrees with respect to the horizontal direction, while the third Collection plane has them at $-60°$. Each stainless steel wire has a diameter of 150 μm and a variable length, depending on its orientation, and overall there are 13,312 wires per TPC, namely 53,248 in the T600 detector, consisting of four TPCs.

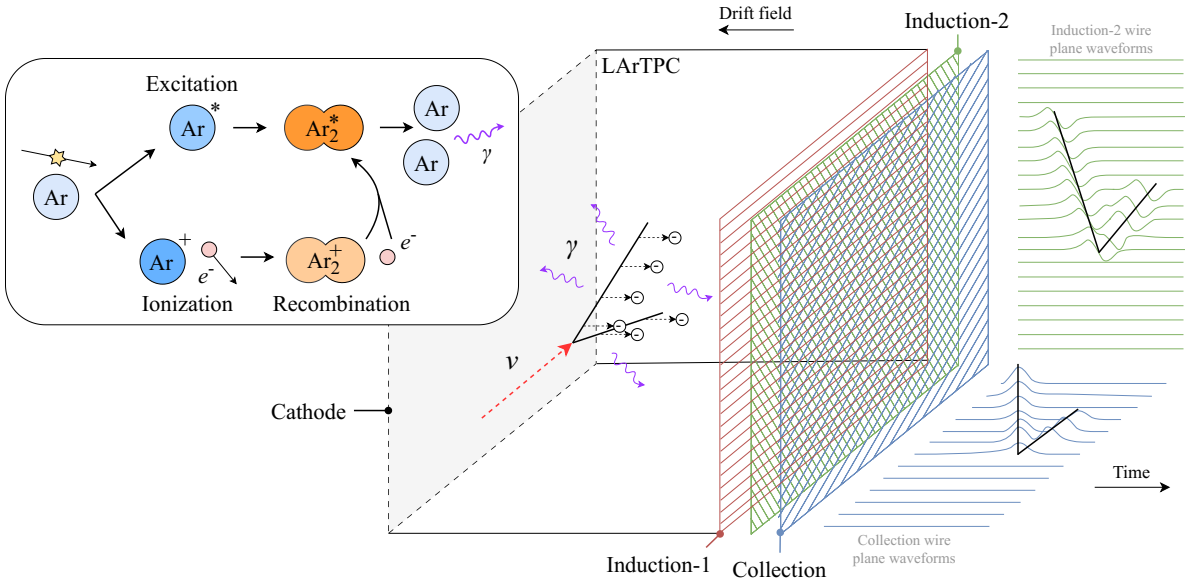

Figure 2.3: Working principle of the LArTPC technology. An incoming neutrino interacts with an Ar atom, producing charged ionizing particles: Ar^+ ions drift toward the cathode plane on the left and e^- drift towards the anode, represented by the three Induction-1, Induction-2, Collection wire planes. Scintillation light is produced and propagates inside the TPC.

Due to ionization, pairs of e^- and Ar^+ produced in the liquid Argon drift towards respectively the anode and cathode of the TPCs. Roughly 42,000 ionization electrons are produced per MeV from ionizing particles crossing the active volume of the detector. An appropriate voltage biasing between different wire planes enables full transparency of the Induction-1 and Induction-2 wire planes, where drifting electrons induce small bipolar current signals, while Collection wires collect the full charge as unipolar signals. Considering the nominal drift electric field $E = 500$ V/cm between Induction-1 and cathode, good transparency is obtained when $E_2 \geq F \cdot E_1$, $E_1 \geq F \cdot E$, in which E_1 and E_2 are respectively the field values in the Induction-1 to Induction-2 and Induction-2 to Collection gaps [77]. The range of the required field-scaling factor is $F = 1.2 - 1.5$, and the three wire planes are biased at the $(-250\text{ V}, -30\text{ V}, 250\text{ V})$ potentials respectively. The charge signal in the Collection view is proportional to the deposited energy of the event, allowing for calorimetric reconstruction of particle energies. Note that every wire is read out as a single channel. From the recorded wire signals it is possible to reconstruct the ionization pattern, namely the 3-dimensional location where each ionization electron was produced, with a resolution of $\mathcal{O}(1\text{ mm}^3)$. The position in the vertical-longitudinal yz plane perpendicular to the drift direction is determined from the signals in the three wire planes. The x drift coordinate of the ionization electron is derived from the timing information. In fact, the scintillation light produced by the event constitutes a prompt signal and is used in conjunction with beam information to assign a time t_0 to the interaction. Given the time t the electron arrived at the anode wires, by knowing the drift velocity v_D it is possible to derive the x-coordinate, $x = v_D \cdot (t - t_0)$.

When a charged ionizing particle crosses the liquid Argon, two processes concur to the production of scintillation light:

- excitation of Argon atoms, leading to the formation of excited Ar_2^* molecules, which decay producing scintillation photons:
$$Ar^* + Ar \rightarrow Ar_2^* \rightarrow Ar + Ar + \gamma\,;$$

- recombination of ionized Argon atoms with an electron [83]. In particular, this process requires an electron cloud surrounding the ionized Ar^+ atom:
$$Ar^+ + Ar \rightarrow Ar_2^+ e^- \rightarrow Ar_2^* \rightarrow Ar + Ar + \gamma\,,$$
and its light yield depends on the energy loss of the ionizing particle and on the electric field. The contribution from this process is inversely proportional to the electric field strength.

Both processes lead to the emission of approximately 20,000 monochromatic Vacuum-Ultra-Violet (VUV) photons per MeV, with a $\lambda \sim 128$ nm wavelength. The emitted light presents fast $\tau \sim 6$ ns and slow $\tau \sim 1.5$ μs decay components with a relative intensity depending on the stopping power characterizing the ionizing particle. Note that the liquid argon is transparent to the scintillation light, which propagates inside the TPC volume with negligible attenuation. The scintillation photons can be then detected by a light detection system that is immersed in the liquid Argon behind the wire planes and faces into the detector volume: this is crucial for determining the absolute timing of events and for positioning tracks along the drift coordinate, for triggering purposes, and possibly for calorimetry. In ICARUS, the light is detected by

means of PhotoMultiplier Tubes (PMTs): more on this can be found in subsection 2.1.2.

Why liquid Argon? Argon was indicated as the ideal target material [80] because of its remarkable properties. It is a noble gas, it does not attach electrons and only a minimal part of the energy from charged particles traversing the detector is absorbed by Argon atoms and not re-emitted. The high density of 1.4 g/cm^3 yields a fairly high interaction probability for neutrinos and a high electron mobility. Furthermore, the radiation length of $X_0 = 14$ cm of liquid Argon allows the fine sampling mm-scale calorimetry of a LArTPC and to discriminate precisely between electron and photon-induced activities along the particle propagation path. Once an interaction vertex is identified, the gap between the vertex and the starting point of an electromagnetic shower is a photon signature. Additionally, when the photon converts to produce a positron-electron pair, the ionization pattern in the first centimeters will be consistent with two Minimum Ionizing Particles (MIPs) developing an electromagnetic shower, which can be easily distinguished from the single-MIP deposit of an electron (Figure 2.4). This would identify with high efficiency electron neutrino events, rejecting to an unprecedented level the Neutral-Current (NC) background in the study of neutrino oscillations.

Finally, note that in highly purified liquid Argon free electrons from ionization can be efficiently transported

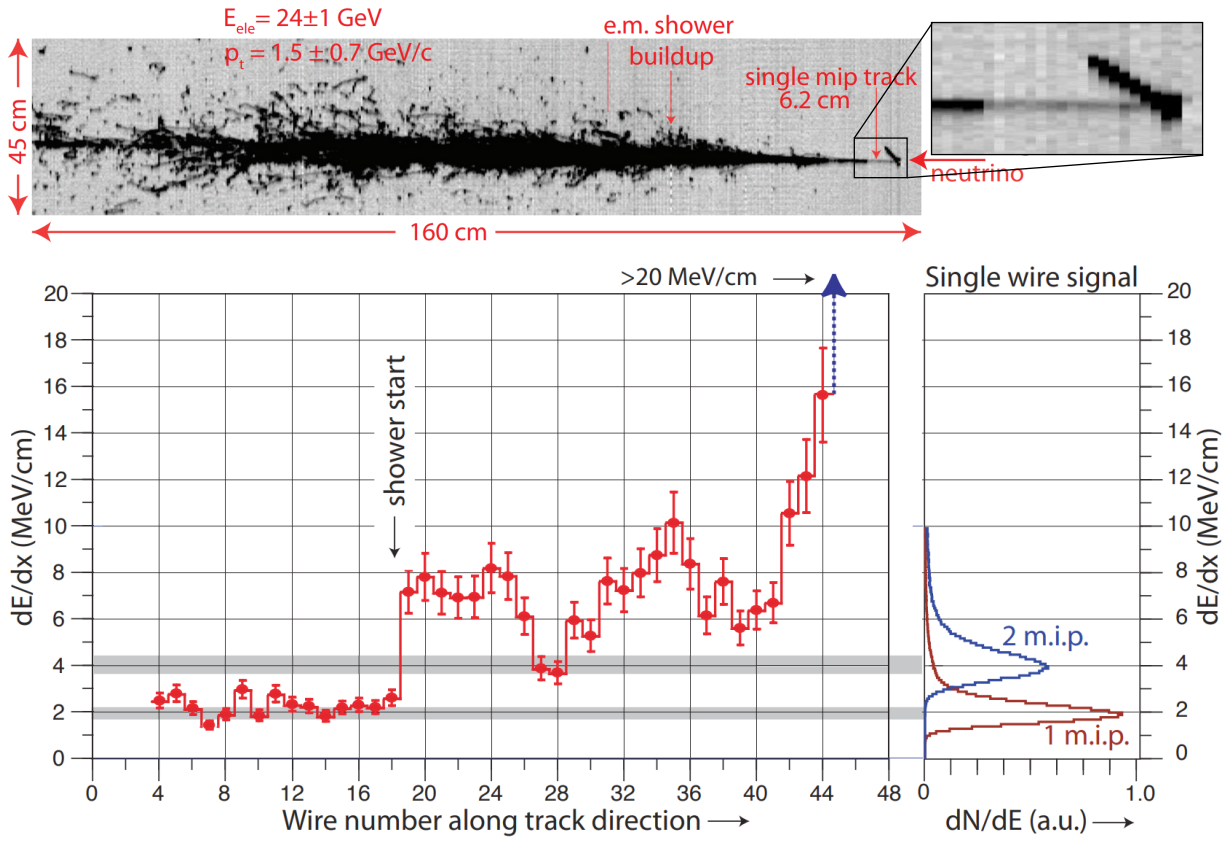

Figure 2.4: (top) ν_e Charged-Current (CC) Quasi-Elastic (QE) event from the ICARUS at LNGS run in the 2-dimensional Collection view. (Bottom) Evolution of the ionization density dE/dx in the first wires, with the marked shower onset. The expected dE/dx signal for 1 and 2 Minimum Ionizing Particles (MIPs) are also shown. Taken from [84].

over macroscopic distances of $\mathcal{O}(\mathrm{m})$, with the fundamental requirement that electro-negative impurities (mainly O_2, H_2O, CO_2) are kept at extremely low concentrations. Considering an electron drift velocity of

$v_D \sim 1.6$ m/ms, to obtain a 3 ms electron lifetime (namely, roughly a 5 m free electron attenuation length), the concentration of the O_2-equivalent electronegative impurities has to be as low as 100 parts per trillion (ppt) [85]. Already during the ICARUS at LNGS run, an exceptionally high 16 ms electron lifetime was reached in 2013, corresponding to a 20 ppt O_2-equivalent LAr contamination and demonstrating the feasibility of larger-scale LAr-TPC detectors, with drift distances up to 5 m [76]. To this aim, four Argon gas recirculation units (two per T300 cryostat) continuously draw the Argon flowing from the gas phase on top of the LAr containers, purify, re-condense, and inject back the Argon in the LAr containers. Moreover, two liquid Argon recirculation units (two per T300 cryostat) provide forced circulation, with a cryogenic pump, of the Argon coming from the cryostats through a set of purifiers before injecting it back into the cryostats. In particular, convective motions induced by heat losses from the modules' walls ensure a fast and complete LAr mixing, minimizing fluctuations of LAr density, temperature, and purity.

ICARUS TPC Deployment The TPC electronics [76, 86] had to be designed to independently read out 53,248 wire channels, considering high data rates due to the shallow depth ICARUS operates at, while maintaining the ICARUS at LNGS architecture, allowing for a continuous triggerable multi-buffered waveform recorder for each wire. In particular, the flat signal cables from the TPC wires are grouped in bundles of 18 cables and routed through 96 chimneys on top of the ICARUS T600 detector. On top of the chimneys, ultra-high vacuum feed-through flanges are used to transmit the TPC wire signals to the front-end electronics, contained in a mini-crate mounted on the flanges. The interface between the wire signals from the TPC and the front-end electronics is given by custom-made Decoupling and Biasing Boards (DBBs), housed in the feed-through flanges (see Figure 2.5, left). The Decoupling and Biasing Boards were designed to house two isolated 32-channel banks, to allow for providing bias voltage to each bank independently and preventing any parallel noise contribution to the wires readout linked to leakage currents. The DBBs are expected to function in Argon gas and operate up to 300 V, and are installed inside the cryostats below the vacuum flanges in unreachable positions. Specifically, the 53,248 ICARUS T600 wires are connected to 1,664 32-channel flat cables and served by 856 DBBs on 96 flanges, hence 9 DBB cards serving 576 channels are installed on each flange. All the boards were tested with a static test at bench to guarantee the integrity of the boards and an HV test at bench to exclude unwanted currents generated by the voltage biasing [86].
The front-end electronics are housed in the custom-designed CAEN A2795 motherboards, integrating both the analog and digital electronics for the TPC signal processing (see Figure 2.5, center). Eight amplifiers are mounted on a single amplifier board, and eight boards fit in each one of the 8 connectors of the CAEN A2795 board, for a total of 64 channels per board. A dedicated filter reduces the RMS serial noise, while preserving the area of the filtered signal in the pass-band, linked to the charge information. The filter interfaces each amplifier with its serial 12-bit, 400 ns sampling time ADC. Data buffering, digital processing, and transmission are performed with a programmable Altera Cyclone 5 GX FPGA. Nine A2795 boards are housed in each mini-crate (see Figure 2.5, right). The electronics chain is identical for all the wire planes. Note that a 10 Hz throughput is guaranteed by carrying out transactions over an optical 1.25 Gb/s serial link. Each mini-crate is powered by a linear DC Low Voltage Power Supply (LVPS) module, whose design is set by the requirement of extremely low noise, needed to preserve the front-end electronics performance.

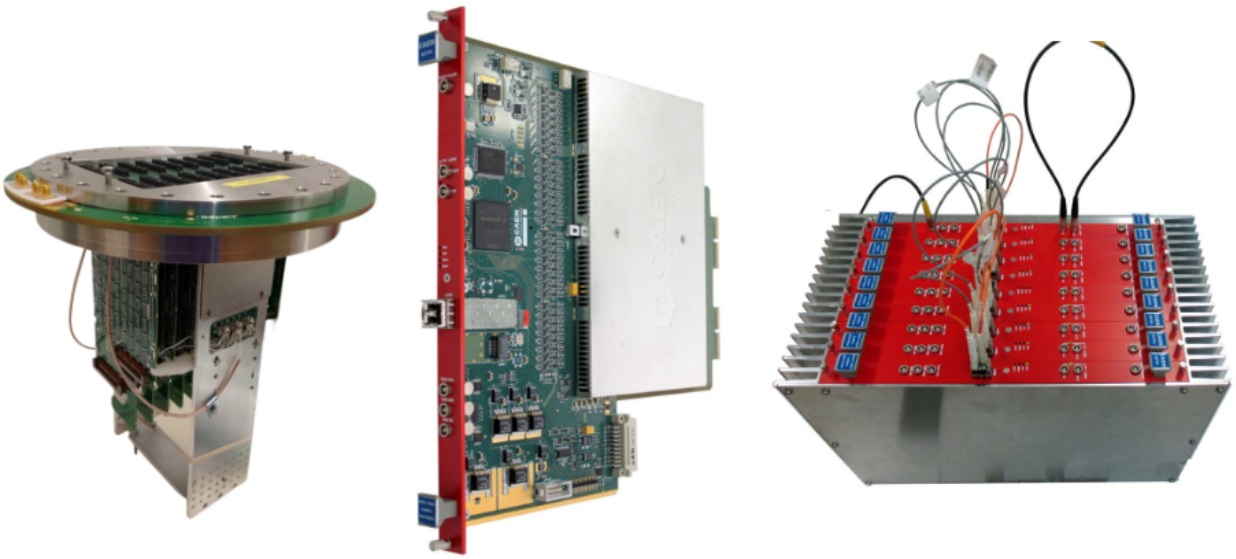

Figure 2.5: (left) Assembled feed-through flange with nine Decoupling and Biasing Boards, with biasing cables. (center) CAEN A2795 custom motherboard, housing 64 amplifiers, ADC, FPGA, and optical link. (right) A mini-crate, containing nine A2795 boards, serving 576 channels.

2.1.2 Light Collection System

As already mentioned, when a charged particle crosses the LArTPC volume, Vacuum-Ultra-Violet (VUV) scintillation photons with a $\lambda \sim 128$ nm wavelength are emitted from the decay of Ar_2^* molecules, produced from the excitation of Argon atoms or recombination of electron-ion pairs. The high scintillation light yield of liquid Argon ensures the production of roughly 20,000 photons per MeV at the nominal drift field[i], corresponding to 15 expected photo-electrons per MeV in each TPC. This light constitutes a prompt signal characterizing an ionizing event, crucial for absolute timing of events, triggering purposes, and cosmic background rejection. The ICARUS scintillation Light Collection System (LCS) [76, 87] consists of 360 8-inch Hamamatsu R5912-MOD PhotoMultiplier Tubes (PMTs), mounted in groups of 90 PMTs per TPC, about 5 mm behind the wire planes and facing towards the active volume of the LArTPCs (see Figure 2.6). The ICARUS T600 PMTs feature bialkali photocathodes on Platinum undercoating to guarantee high performance at cryogenic temperatures and relatively high pressures as expected with their immersion in liquid Argon. Moreover, a 200 $\mu g/cm^2$ layer of Tetra-Phenyl Butadiene (TPB) wavelength shifter was deposited by evaporation on the PMT windows, to ensure sensitivity to VUV photons, yielding a 12% quantum efficiency [88]. The PMTs can be calibrated in time with a laser system based on a Hamamatsu PLP10 laser diode, emitting laser pulses with $\lambda = 405$ nm and an FWHM of 60 ps, delivered to single PMTs via optical fibers [89].

The design of the ICARUS Light Collection System was driven by several requirements:

- a good sensitivity to interactions in the liquid Argon down to energies of $\mathcal{O}(100$ MeV$)$;

[i] The average scintillation light yield of liquid Argon increases to about 40,000 photons per MeV in the absence of a drift field, due to recombination.

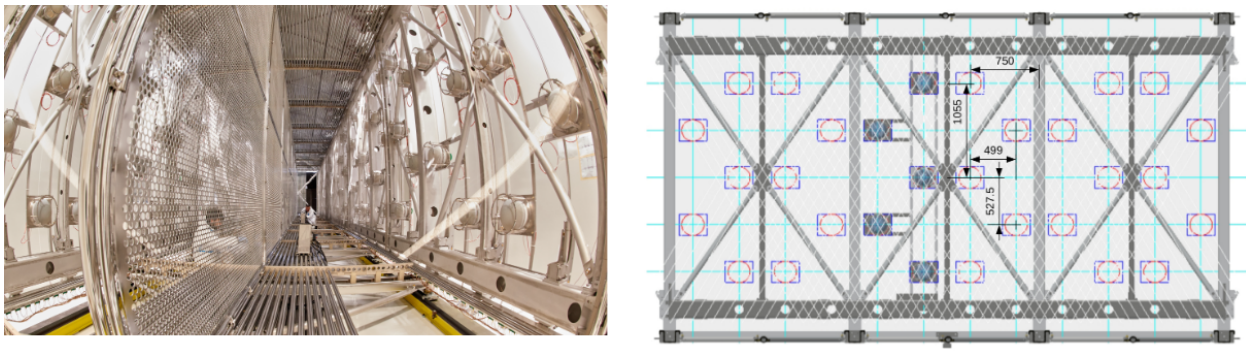

Figure 2.6: (left) Internal view of an ICARUS T300 module, during the refurbishing activities at CERN. The pierced cathode in the middle separates the two liquid Argon TPCs and the structures holding the 90 PMTs per TPC are visible. (right) Technical drawing of the mechanical structure holding the PMTs behind the wire planes in three frame sectors, corresponding to a 6 m longitudinal section of an ICARUS T300 module, namely a third of the 18 m whole module length (units of measurement in the figure are millimeters).

- a $1.3 \cdot 10^7$ gain at an 87 K cryogenic temperature, sufficient to detect single photons [90];
- an expected maximum dark count rate of $\sim$ 5 kHz (residual photons produced by the decay of ^{39}Ar and other radioactive contaminates);
- a $\mathcal{O}$(ns) time resolution to provide the absolute timing of each interaction in order to correctly identify the events in coincidence with the BNB or NuMI beam spill, and possibly the cosmic muons crossing the detector during the ms-long drift of the ionization electrons in the TPC.

The deployment was designed and optimized with dedicated Monte Carlo simulations during the refurbishing phase of the detector at CERN [87] and corresponds to a 5% photocathode coverage of the anode plane area. The high light detection granularity is needed to localize the track associated with each light flash with an accuracy of roughly 0.5 m, shorter than the expected average spacing between cosmic muons in each TPC snapshot.

Signal and power supply cables are driven in groups of 10 through the aforementioned stainless steel chimneys mounted on the roof of the cryostats. All the cables are 44 m in length, to guarantee uniformity among different channels. The electronics for the PMTs are designed to allow continuous read-out, digitization, and waveform recording from each one of the 360 PMTs [76, 87]. Groups of 15 PMTs are connected to a CAEN V1730B digitizer board: each V1730B module consists of a 16-channel 14-bit FLASH ADC, sampling PMT signals with a rate of 500 MS/s and writing them in a 10 μs wide circular buffer, to record both the fast and slow components of scintillation light. In each board, 15 channels are used for acquiring PMT signals, while a channel is exploited for collecting ancillary signals, e.g. beam gates. Furthermore, the V1730B boards combine with an OR logic two signals from pairs of nearby PMTs to generate Low-Voltage Differential Signaling (LVDS) 200 ns wide logic outputs, that are evaluated by the trigger electronics. When a V1730B board receives a trigger-request logic signal, the active buffers are frozen and stored data are available for download via CAEN proprietary CONET2 links, allowing up to 80 MB/s data transfer. For a detailed description of the ICARUS Trigger System, see upcoming chapters. Overall, the signals from the 360 PMTs

in the ICARUS T600 detector are digitized by 24 V1730B boards (12 boards per T300 module, 6 boards per TPC), from which 192 LVDS lines (96 LVDS lines per T300 module, 48 per TPC) are produced (see Figure 2.7).

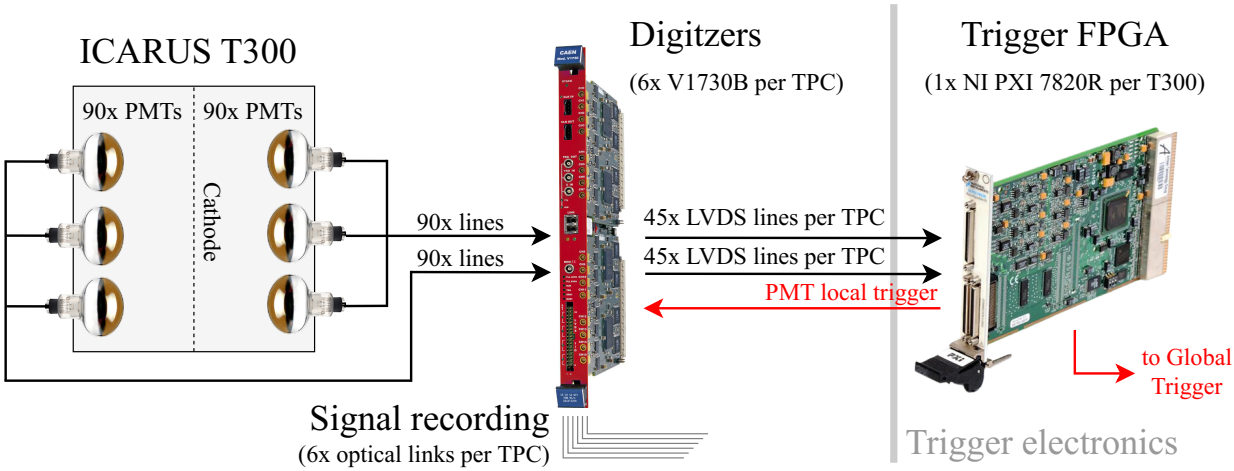

Figure 2.7: Deployment of the ICARUS Light Collection System electronics, interfacing with the trigger electronics. For each ICARUS T300 module, 180 PMTs lines are digitized by 12 CAEN V1730B boards, which produce 96 LVDS output lines, later processed by a NI PXI 7820R FPGA within the ICARUS Trigger System.

The 24 V1730B digitizer boards are deployed in 8 VME crates: for each crate, a master unit permits the daisy chain distribution of the trigger pulses and of the 62.5 MHz frequency, both generated by the trigger electronics. The master units allow the acquisition of trigger pulses together with the PMTs, crucial for timing purposes. To perform a synchronized reset of timestamps, a Pulse Per Second (PPS) signal is sent to each board by the trigger electronics. The primary -2000 V high voltage for the PMTs is produced by a BERTRAN 210-02R power supply system, one for each cryostat. The primary voltage is then fine-tuned and distributed to the PMTs by 8 48-channel CAEN A1932AN boards (4 boards for each T300 module), housed in a CAEN SY1527 crate. This system guarantees extremely low output ripple voltages, crucial to prevent the induction of PMT noise onto the wire planes.

2.1.3 Cosmic Ray Tagger

The ICARUS T600 detector at Fermilab is installed on the surface and is exposed to a huge cosmic ray activity. As a result, the primary component of the background for various physics analyses is given by cosmic rays, which could be misidentified as part of a neutrino interaction. The Cosmic Ray Tagger (CRT) system [76] was therefore developed to fully enclose the detector and tag cosmic muons to clearly identify neutrino interactions. The CRT system is organized into three sub-systems to cover top, sides and bottom of the detector and is based on plastic scintillator modules.

The Top-CRT is designed to cover the top side of the ICARUS T600 detector and intercepts approximately 80% of the overall cosmic muons flux at ICARUS. The Top-CRT system is composed of 123 detector modules, organized in 84 horizontal (horizontal Top-CRT) and 39 vertical modules placed along the perimeter of

the cryostat top surface (rim Top-CRT). Each module consists of a 1.86×1.86 m^2 Aluminum box containing two orthogonal layers made up of 8 plastic scintillator bars, in which the light is collected by wavelength-shifting optical fibers and read out on both sides by Hamamatsu S13360-1350C Silicon PhotoMultipliers (SiPMs). The 32 SiPM signals of each Top-CRT module are connected to a CAEN DT5702 Front End Board (FEB), to provide a bias voltage adjustable for each channel and to produce a trigger logic based on the coincidence between two SiPMs on the same bar and between two layers in a module.

The Side-CRT sub-system covers the four vertical sides of the ICARUS T600 detector and is made of modules from the MINOS experiment: each module consists of a metal sheath containing two layers of 20 Polystyrene scintillator strips with an embedded wavelength-shifting fiber. The light signals are read out on both sides by arrays of Hamamatsu S14160-3050HS SiPMs. The full Side-CRT system consists of 2710 readout channels across 93 FEBs.

The Bottom-CRT is made up of 14 modules placed under the cryostats and organized in two daisy chains of 7 modules each, for the two north and south sections. Each module is from the Double Chooz experiment and consists of two layers of 32 Polystyrene strips, whose light is collected by wavelength-shifting fibers read out on one end by Hamamatsu H7546B M64 multi-anode PMTs, while the other end is mirrored to maximize light collection. Note that as of this thesis, the Bottom-CRT was out of operation due to damage from severe weather conditions. The system is currently being recovered and the integration within the ICARUS DAQ is ongoing.

The Top and Side-CRT systems are fully installed and are taking data with the other sub-detectors since February 2022. Finally, a 2.85 m concrete overburden was introduced over the Top-CRT to partially shield the detector from cosmic radiation, absorbing the major part of cosmic photons and neutrons. Figure 2.8 shows the cosmic event rates before and after the installation of the overburden for some modules from the horizontal (Figure 2.8, left) and rim (Figure 2.8, right) Top-CRT systems.

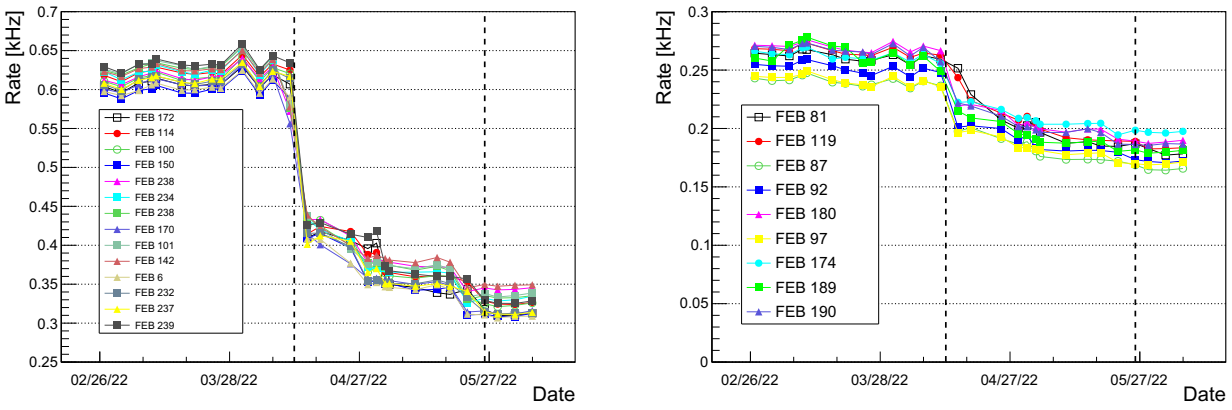

Figure 2.8: Cosmic ray rates as a function of time for some of the horizontal (left) and rim (right) Top-CRT modules. Dashed lines mark the beginning and the end of the overburden installation.

The installation of the overburden was completed on June 7, 2022, and led to a reduction of the mean cosmic ray rates per module in the horizontal Top-CRT roughly from 0.6 kHz to 0.3 kHz and in the rim Top-CRT from 0.3 kHz to 0.2 kHz. Note that some modules experience a slightly higher event rate due to the proximity to the cryogenics, leading to higher electrical noise rates.

2.2 The Short Baseline Neutrino Program

The Short Baseline Neutrino (SBN) program at Fermilab [75] was designed with the primary goal of studying short-baseline neutrino oscillations, to address the light sterile neutrino interpretation of anomalous results in past neutrino data, mostly from LSND and MiniBooNE (for reference, see section 1.2). The program includes three LArTPC detectors located on-axis along the Booster Neutrino Beam (BNB) at Fermilab, at different distances from the BNB target. The basic features of the detectors are summarized in Table 2.1.

	Baseline	Total / Active mass
SBND	110 m	220 ton / 112 ton
MicroBooNE	470 m	170 ton / 89 ton
ICARUS	600 m	760 ton / 476 ton

Table 2.1: Summary of the SBN detectors' locations with respect to the Booster Neutrino Beam target (baseline), Liquid Argon total mass, and active mass.

The ICARUS detector is located at a baseline of 600 m from the BNB target, has completed its installation and commissioning in May 2022, and is presently collecting beam data with both the BNB and the Neutrinos at the Main Injector (NuMI) neutrino beams. The neutrino spectra detected at ICARUS, far detector within the SBN program, will be compared to those measured at a 110 m distance from the BNB target by the Short Baseline Near Detector (SBND), which is currently being installed. Finally, the MicroBooNE detector is located in the Liquid Argon Test Facility (LArTF) at a baseline of 470 m and has presently completed its data taking, producing the world's first high statistics results on neutrino-Argon interactions [91].
The layout of the SBN project is depicted in Figure 2.9, along with the scheme of the Fermilab accelerator complex: the locations of the detectors were chosen to maximize the sensitivity to neutrino oscillations on short baselines. The three SBN detectors are based on the same Liquid Argon Time Projection Chamber (LArTPC) technology, whose working principle and capabilities were outlined in subsection 2.1.1: the use of the same detection technology, hence the same medium for neutrino interactions, is critical to minimize systematic uncertainties when comparing event distributions at the different locations along the beam and searching for oscillation signals.

2.2.1 Neutrino Beams

The ICARUS physics program is based on the on-axis Booster Neutrino Beam [75, 92] and is enhanced by stand-alone studies on the off-axis neutrinos from the NuMI beam [93], relevant also for future long baseline experiments based on similar technology, e.g. the Deep Underground Neutrino Experiment (DUNE) [78, 79].

Booster Neutrino Beam The Booster Neutrino Beam [92] is generated by extracting protons from the Fermilab LINAC, injected in the Booster synchrotron and accelerated to 8 GeV (i.e., 8.89 GeV/c momentum). The maximum repetition rate for delivery of protons to the BNB is 5 Hz, with $5 \cdot 10^{12}$ Protons-On-Target (POT) per spill and a spill length of 1.6 μs grouped in 81 proton bunches, each with an FWHM of about 2 ns

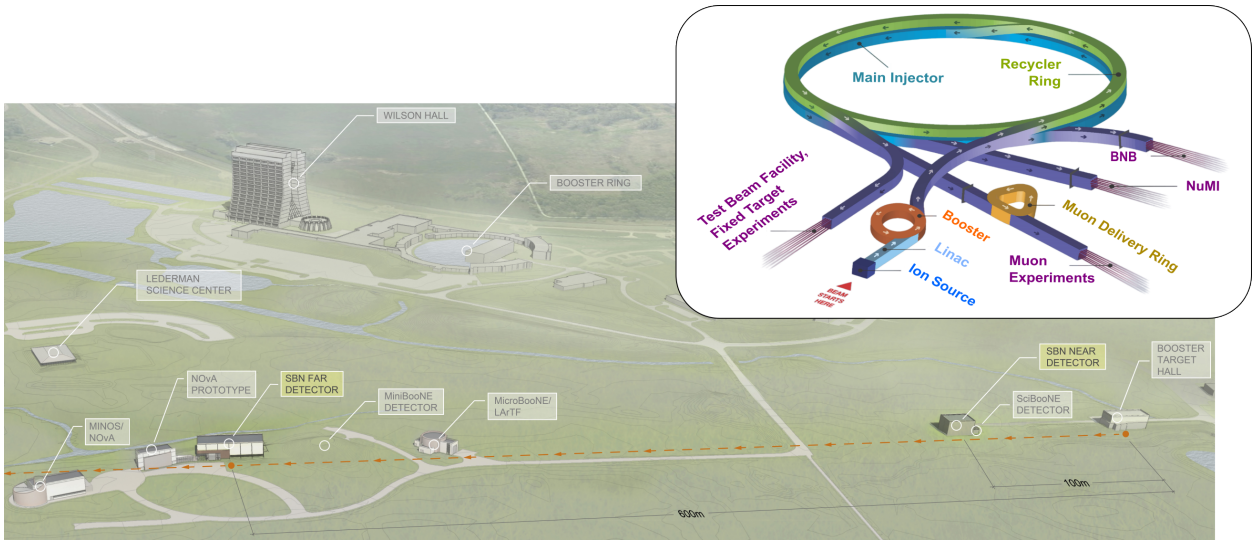

Figure 2.9: Short Baseline Neutrino project layout and Fermilab accelerator complex. The program includes three Liquid Argon (LAr) Time Projection Chamber (TPC) detectors, located on-axis along the Booster Neutrino Beam (BNB). From the right: SBND, at 110 m from the BNB target; MicroBooNE, at 470 m; ICARUS, at 600 m. Taken from [75].

and separated by a $\sim$ 19 ns gap. The time and intensity profiles of the proton pulses before impinging on the target is monitored with a Resistive Wall current Monitor (RWM) [94], which is placed upstream of the target and collects the currents induced by the protons traveling through the conductive metallic beam pipe. Figure 2.10 shows an example trace of the BNB bunched structure as measured with the RWM, along with the timing distributions of resulting ν_μ Charged-Current (CC) Quasi-Elastic (QE) events in the MiniBooNE detector [95].

After being transported through a series of magnets, the proton beam is focused onto the target, consisting of seven identical cylindrical rods of Beryllium ($\varnothing = 1$ cm). The p-Be interaction with the target produces a hadronic beam, mainly composed of pions with a smaller kaons contribution at the $\mathcal{O}(5\%)$ scale. Charged secondaries are then focused by a toroidal Aluminum-alloy focusing horn surrounding the target and pulsed with either polarity, focusing either positives in neutrino mode (positive current or Forward Horn Current, FHC) or negatives in anti-neutrino mode (negative current or Reverse Horn Current, RHC). The charged mesons [96] propagate down a 50 m air-filled pipe, and charged pions decay mainly from the dominant channel into muons and neutrinos,

$$\pi^{\pm} \longrightarrow \mu^{\pm} + \nu_\mu(\overline{\nu}_\mu) \,, \tag{2.1}$$

resulting in a neutrino beam primarily composed of muon neutrinos or anti-neutrinos, based on the focusing horn configuration. In particular, the 50 m decay pipe is designed to maximize the production of muon neutrinos from dominant pion decays, while minimizing the electron neutrino contamination from the decay of secondary muons [96] at the $\sim 0.5\%$ level,

$$\mu^{\pm} \longrightarrow e^{\pm} + \nu_e(\overline{\nu}_e) + \overline{\nu}_\mu(\nu_\mu) \,. \tag{2.2}$$

The remaining hadrons or leptons at the end of the decay pipe are absorbed by a beam stop made of steel

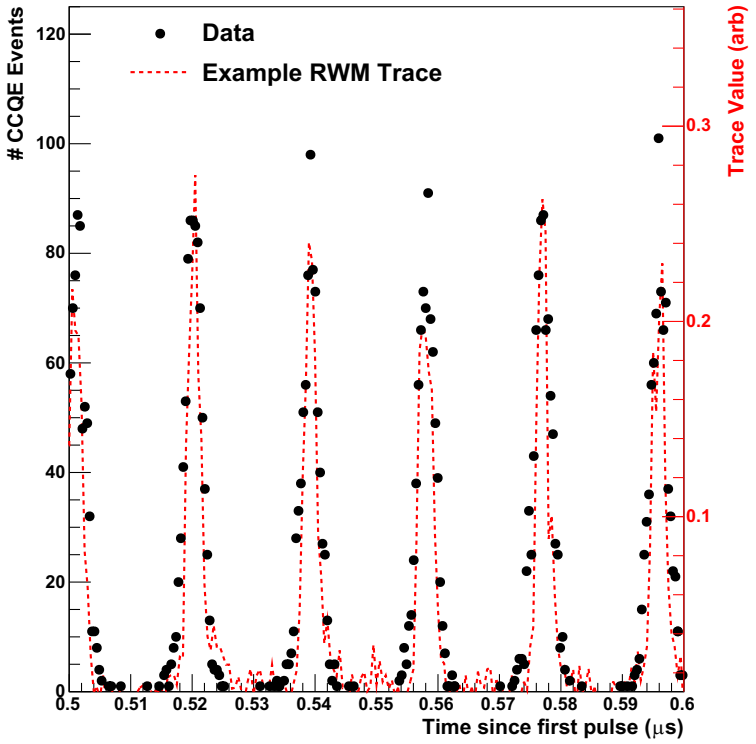

Figure 2.10: Overlay of the zoomed-in BNB bunched structure as measured with the Resistive Wall Monitor (RWM) and data points from ν_μ Charged-Current (CC) Quasi-Elastic (QE) interactions in MiniBooNE. Taken from [95].

and concrete, which contains an array of gas proportional counters to monitor the impinging muons. The Booster Neutrino Beam is schematized in Figure 2.11.

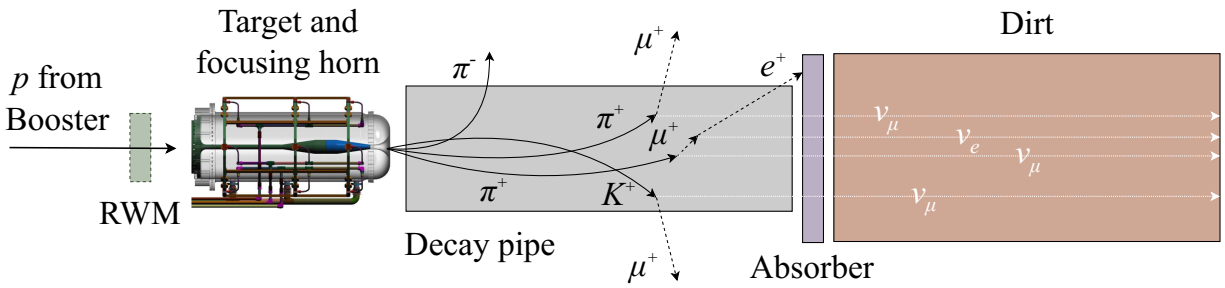

Figure 2.11: Schematic of the Booster Neutrino Beam line. From the left: the protons extracted from the Booster are monitored by the Resistive Wall Monitor (RWM) and interact with the Beryllium target, surrounded by the focusing horn. The mesons from the interaction are focused in the decay pipe, where they decay into neutrinos. The remaining hadrons and leptons are stopped by the absorber.

In-depth studies were carried out by the MiniBooNE collaboration [92] on the spectrum and composition of the Booster Neutrino Beam, which was first utilized to tackle the short-baseline LSND neutrino anomaly. A detailed simulation of the BNB was put in place, using external data whenever possible, e.g., deriving the π and K-production cross-sections from the Hadron Production Experiment (HARP) [97, 98] data collected

with a BNB target replica. The predicted BNB fluxes at the three SBN detectors are shown in Figure 2.12.

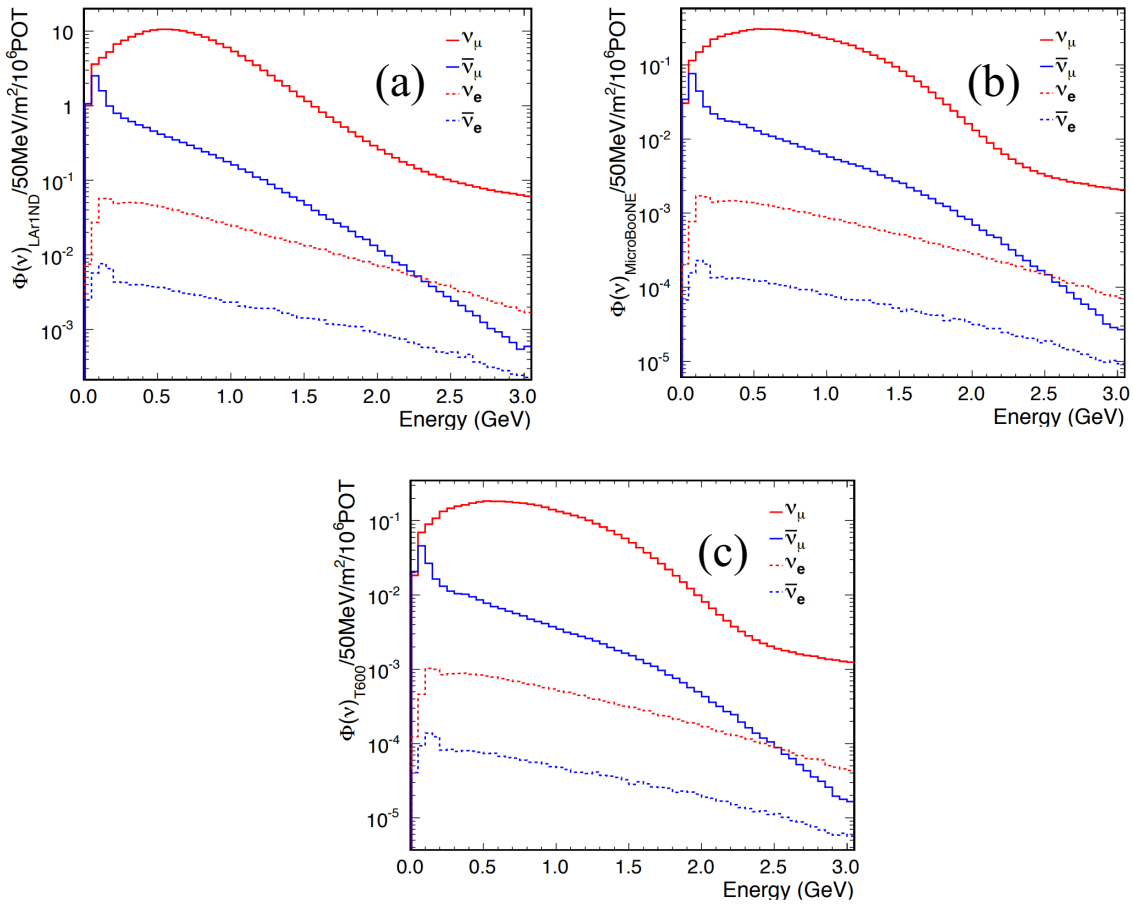

Figure 2.12: Booster Neutrino Beam neutrino fluxes at the three SBN detectors, namely SBND (a), MicroBooNE (b) and ICARUS (c). Solid lines represent the fluxes for $\nu_\mu/\overline{\nu}_\mu$, dashed ones for $\nu_e/\overline{\nu}_e$. Taken from [75].

The BNB flux [92] is characterized by a ~ 0.8 GeV average energy, extending up to 2.5 GeV. The flux composition depends on the energy; in neutrino mode, on average:

- the spectrum is dominated at the $\sim 93.6\%$ level by ν_μ, that given the 50 m decay channel length are produced mainly by pion decays (Equation 2.1) for energies up to roughly 2 GeV. For energies higher than 2 GeV, the dominant ν_μ-flux arises from kaon decays, $K^+ \to \mu^+ + \nu_\mu$ (BR $\sim 63.56\%$);
- the second major component of the spectrum is given by $\overline{\nu}_\mu$ ($\sim 5.9\%$). In neutrino mode, the contamination of muon anti-neutrinos comes from the decay of de-focused π^- (Equation 2.1) and decays of μ^+ (Equation 2.2);
- there is an intrinsic $\nu_e + \overline{\nu}_e$ contamination to the ν_μ flux at the level of $\sim 0.5\%$. For energies of the order of 1 GeV, the muon decay (Equation 2.2) is the primary source of electron neutrinos and anti-neutrinos. For energies exceeding roughly 1.2 GeV, the dominant contribution comes from kaon decays, like $K^\pm \to \pi^0 + e^\pm + \nu_e(\overline{\nu}_e)$ (BR $\sim 5.07\%$) and $K^0_L \to \pi^\mp + e^\pm + \nu_e(\overline{\nu}_e)$ (BR $\sim 40.55\%$).

Neutrinos at the Main Injector Protons from the Booster are then accelerated by the Main Injector (recall Figure 2.9) up to 120 GeV. Since the Main Injector has a circumference that is 7 times the one of the Booster, it is possible to accommodate storage and acceleration of 6 Booster batches (note that one of the 7 slots is needed for the pulse kicker rise time), leading to a spill duration of 9.5 μs. The proton beam impinges on a Graphite target with a nominal $6 \cdot 10^{13}$ POT per spill at a repetition rate of 0.83 Hz. The produced hadrons, mostly pions and kaons, are focused with two magnetic horns and eventually enter a 675 m long Helium-filled decay pipe, and they mainly decay into muons and muon neutrinos. Again, a small portion of electron neutrinos arises from the subdominant electronic decay mode of K^+ hadrons, decays of K^0 particles, and decays of secondary muons.

The ICARUS detector receives off-axis the NuMI beam at a 795 m distance and an angle of 5.7° with respect to the target, resulting in an intense neutrino beam with energies of a few GeV [76]. Consider the kinematics of the in-flight 2-body decays of charged pions and kaons: in the laboratory frame,

$$E_\nu = \frac{m^2_{\pi(K)} - m^2_\mu}{m^2_{\pi(K)}} \cdot \frac{E_{\pi(K)}}{1 + \gamma^2 \theta^2_\nu} \,, \tag{2.3}$$

for neutrinos produced from a $(\pi, K)^\pm \to \mu^\pm + \nu_\mu(\overline{\nu}_\mu)$ decay at an angle θ_ν with respect to the meson direction and with $\gamma = E_{\pi(K)}/m_{\pi(K)}$. Figure 2.13(a) shows the neutrino energy as a function of the parent pion energy as reported in Eq. 2.3: while the off-axis angle increases, the energy of the neutrino has an increasingly looser dependence on the energy of the pion [99]. In practice, pions with different energies are producing neutrinos in the same low-energy range. This is visible also from Figure 2.13(b), which depicts the number of Charged-Current (CC) ν_μ interactions as a function of the neutrino energy with the NuMI beam as seen by the NOνA experiment [99]: while the off-axis angle increases, the neutrino spectrum becomes more narrow and peaked at lower energies.

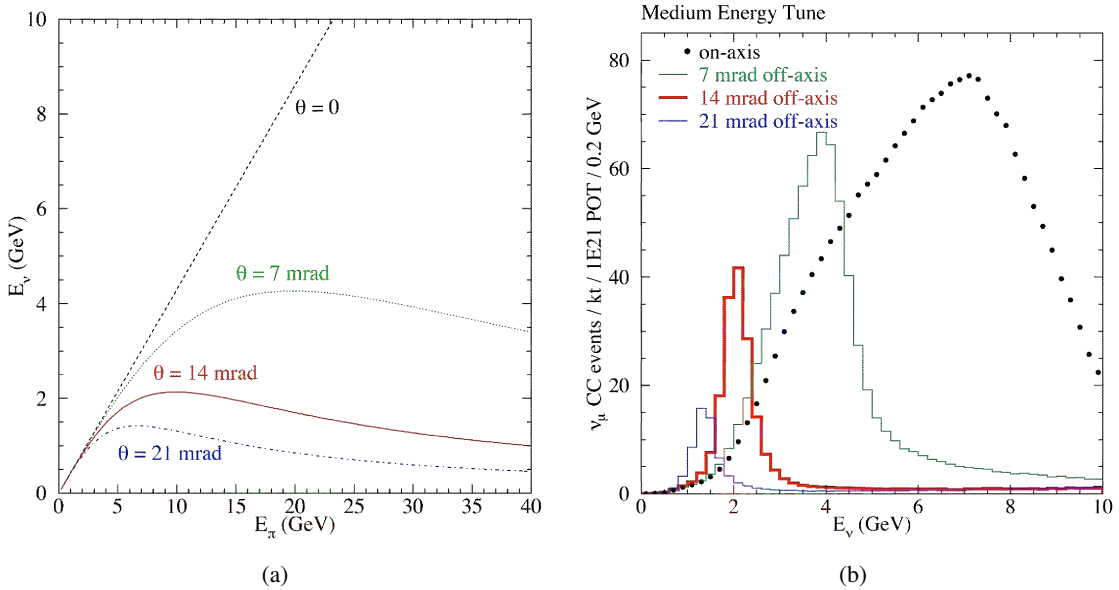

(a) (b)

Figure 2.13: (a) Energy of neutrinos produced at an off-axis angle θ with respect to the parent pion direction as a function of the pion energy. (b) Charged-Current (CC) ν_μ event rates for the NOνA experiment at various off-axis locations relative to the NuMI beam. Taken from [99].

The predicted NuMI flux at ICARUS is shown in Figure 2.14 and is produced by:

- a combination of muon decays for low energies, roughly around 0.5 GeV;
- pions either outside of the well-focused phase space (π^+ in positive current mode, π^- in negative current mode) or de-focused (π^- in positive current mode, π^+ in negative current mode) in the $0.5-2$ GeV energy range;
- high-angle kaon decays for high energies exceeding 2 GeV.

On average, the average energy is ~ 1.5 GeV, extending up to 4 GeV. Due to the large off-axis angle, the fluxes of neutrinos and anti-neutrinos are sensibly closer if compared to the on-axis case. In fact, a significant component of the NuMI neutrinos that reach ICARUS originate from kaon decays occurring close to the target and before the second NuMI horn magnet, hence reducing the horn acceptance and focusing. Furthermore, the difference of ν and $\overline{\nu}$ fluxes depends on the fact that at $\mathcal{O}(1\text{ GeV})$ energies the $\overline{\nu}$ cross-section is roughly half of the ν cross-section (recall subsection 1.1.1). Overall, a significant $\nu_e/\overline{\nu}_e$ contamination of the order of 5% is expected in the NuMI flux at ICARUS, allowing for high-statistics interaction cross-section measurements of both muon and electron-flavor neutrinos and anti-neutrinos, crucial for future Argon-based experiments, e.g. DUNE [78, 79].

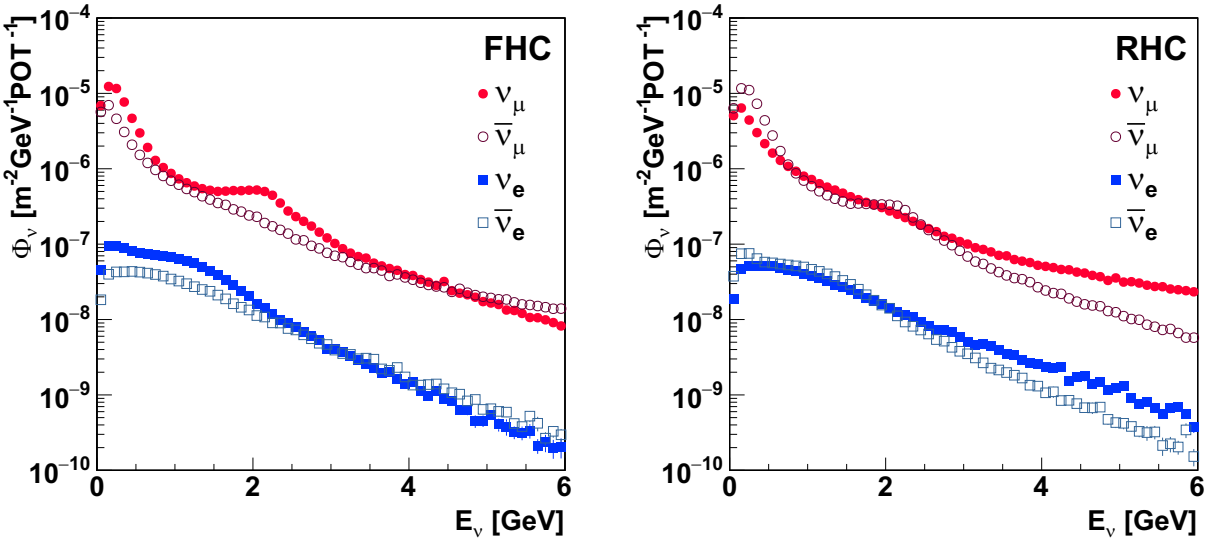

Figure 2.14: Neutrinos at the Main Injector beam neutrino fluxes at ICARUS in the neutrino mode or positive current (FHC, Forward Horn Current) and anti-neutrino mode or negative current (RHC, Reverse Horn Current) modes. Solid markers represent the fluxes for ν_μ/ν_e, empty ones for $\overline{\nu}_\mu/\overline{\nu}_e$.

2.2.2 Physics Program

The SBN program [75, 100] was designed with the primary goal of studying short-baseline neutrino oscillations to address the light sterile neutrino interpretation of recorded experimental anomalies, e.g. the LSND and MiniBooNE anomalies (for reference, recall section 1.2). Moreover, the SBN detectors are expected to detect millions of neutrinos per year: it will be possible to conduct high-precision studies on neutrinos

interacting with Argon, paving the way for future LArTPC-based experiments, e.g. DUNE. In addition, SBN is providing a development platform for the liquid Argon Time Projection Chamber neutrino detector technology. Finally, several Beyond the Standard Model (BSM) theories will be explored.

Search for Sterile Neutrinos The SBN program was designed with multiple LArTPC detectors at precise baselines to maximize the sensitivity to short-baseline sterile neutrino oscillations for the $\nu_\mu \to \nu_e$ appearance and $\nu_\mu \to \nu_\mu$ disappearance channels [75].

The exploitation of the SBND and ICARUS near-far detector combination will allow the direct far-to-near detector event comparison, minimizing the systematic uncertainties in the search for short-baseline oscillation signals. Since both SBND and ICARUS utilize the same interaction target medium and detection technique, the highly correlated event rates in the near and far detectors enable a significant cancellation of the Booster Neutrino Beam flux and neutrino-Argon cross-section uncertainties when comparing the two. Furthermore, the liquid Argon TPC technology is a strong advantage for SBN in the sensitive search for anomalous neutrino signals. As already mentioned in subsection 2.1.1, the high radiation length of liquid Argon coupled to the mm-scale event imaging and reconstruction enables for clearly distinguishing photon and electron-induced electromagnetic showers, unlike Cherenkov detectors like MiniBooNE. In particular, the global $\nu_\mu \to \nu_e$ appearance data point to a mass splitting Δm^2_{41} with values between 0.3 eV^2 and 1.5 eV^2, with a mixing strength $\sin^2 2\theta_{\mu e}$ between 0.002 and 0.015 (for reference, recall section 1.2). Figure 2.15 shows the $\nu_\mu \to \nu_e$ oscillation probability for SBND at a baseline of 110 m and ICARUS at a baseline of 600 m, for two sets of parameters: $\Delta m^2_{41} = 0.3$ eV^2, $\sin^2 2\theta_{\mu e} = 0.015$ (Figure 2.15, left) and $\Delta m^2_{41} = 1.5$ eV^2, $\sin^2 2\theta_{\mu e} = 0.002$ (Figure 2.15, right).

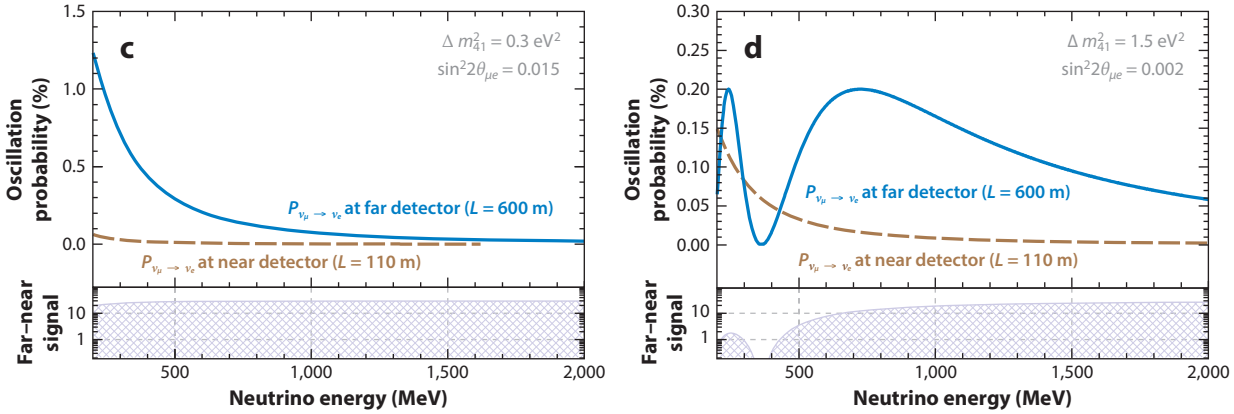

Figure 2.15: $\nu_\mu \to \nu_e$ oscillation probability as a function of the energy in the $(3+1)$ oscillation scenario at 110 m and 600 m, for two sets of parameters: $\Delta m^2_{41} = 0.3$ eV^2, $\sin^2 2\theta_{\mu e} = 0.015$ (left) and $\Delta m^2_{41} = 1.5$ eV^2, $\sin^2 2\theta_{\mu e} = 0.002$ (right). The lower panels in each plot show the far detector over near detector appearance probability ratio. Taken from [100].

Oscillations are visible in the far detector for all oscillation parameters in the range indicated by global analyses. At larger Δm^2_{41} values, a small oscillation signal appears at low neutrino energies also in the near detector, but the very different shape and a higher level of oscillations at most energies at the far detector preserve the strong sensitivity of SBN when using the near-far combination.

Overall, the SBN program is expected to take data at least for three years in order to cover the allowed region related to the LSND anomaly with a sensitivity of 5σ: the status of the projected SBN oscillation sensitivities respectively for the $\nu_\mu \to \nu_e$ appearance and the $\nu_\mu \to \nu_\mu$ disappearance channels is depicted in Figure 2.16. Statistical uncertainties are computed by assuming a $6.6 \cdot 10^{20}$ POT from BNB exposure for both SBND and ICARUS, corresponding to roughly 3 years of operation. Systematic uncertainties linked to event rates and fluxes are determined through dedicated BNB simulations [92], while an uncorrelated detector systematic uncertainty amounting to 3% was assumed. Note that studying the ν_e-appearance and ν_μ-disappearance channels at the same time, allowed by having an intense muon neutrino beam and multiple detectors, is key to tackling the existing tension between the two channels' data (for reference, see section 1.2).

Initially, the ICARUS detector will seek evidence for the Neutrino-4 experiment sterile neutrino claims [64] in its early runs, before the activation of the SBND detector. In particular, the oscillations in the ν_μ disappearance channel with BNB and in the ν_e disappearance channel with NuMI produce patterns in the same $L/E \sim 1 - 3$ m/MeV, but with event energies larger by a factor 100 with respect to the Neutrino-4 case. Note that the L/E effect is mostly related to the energy variation, considering that the baseline can be considered to be constant and large for both BNB and NuMI.

Cross-section Measurements As previously mentioned, precise neutrino-Argon cross-section measurements are crucial for any experiment based on the LArTPC approach, and this will include the DUNE experiment [78, 79]. In particular, neutrino interactions with Argon in the energy range of $\mathcal{O}(1\ \text{GeV})$ include a huge variety of final states: other than leptons in the leading charged-current channels, other charged-current or neutral-current more complex states are possible, e.g. including the emission of nucleons, pions or other hadrons. The SBN program is well-suited for a study of this type since the LArTPC technology has excellent particle identification capabilities, and the BNB provides neutrinos in the few hundred MeV up to a few GeV range and its flux is well characterized by past in-depth studies with MiniBooNE [92]. Furthermore, the three detectors are expected to collect millions of neutrinos per year, being able to yield world-leading measurements of ν_μ-Ar and ν_e-Ar cross-sections. As already anticipated, ICARUS is also collecting neutrinos from the off-axis NuMI beam, characterized by an increased electron neutrino content and a different energy spectrum with respect to BNB. Finally, note that a first measurement of the neutrino-Argon interaction cross-section was recently made available by the MicroBooNE collaboration [91].

Beyond the Standard Model New physics scenarios may be probed at SBN, thanks to the unprecedented event reconstruction and particle identification capabilities of the LArTPC technology, coupled to high-intensity neutrino beams [75, 100]. Beyond the Standard Model (BSM) theories mainly consist of modifications to standard neutrino oscillations or new experimental signatures and include: heavy sterile neutrinos, dark neutrino sectors, light dark matter, light sterile neutrino decays [100].

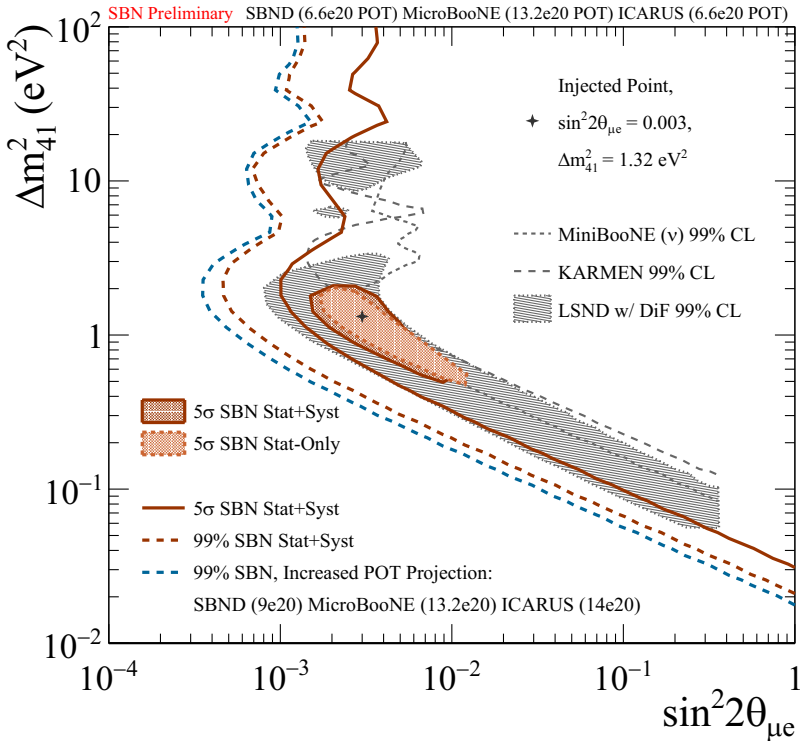

(a)

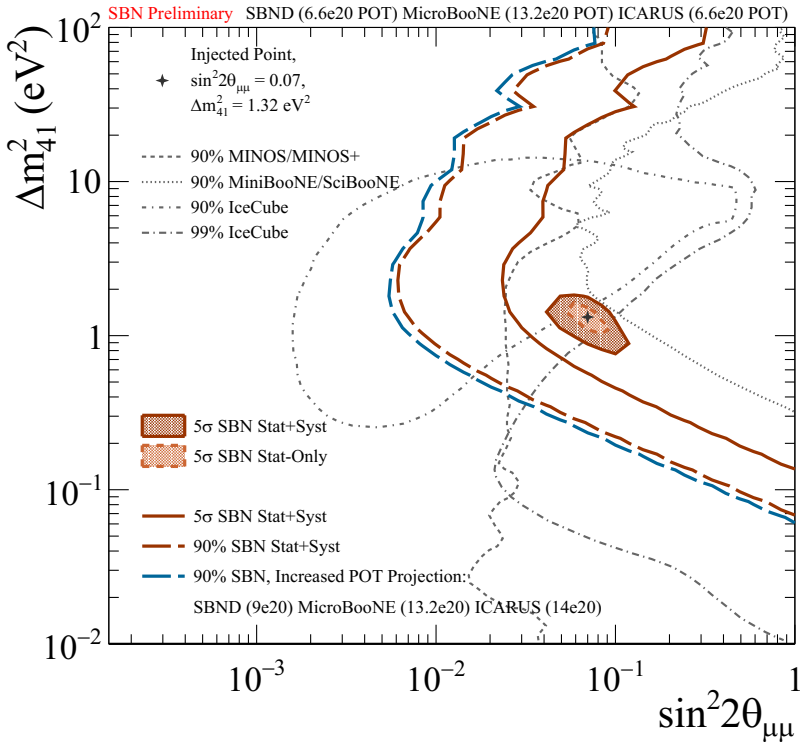

(b)

Figure 2.16: Status of the expected SBN sterile neutrino oscillation sensitivities in the context of existing data, for the $\nu_\mu \rightarrow \nu_e$ appearance channel (a) and for the ν_μ disappearance channel (b).

3

Design of the ICARUS Trigger System

This Chapter contains:

The Booster Neutrino Beam has a nominal intensity of $5 \cdot 10^{12}$ POT per spill (PPP, POT Per Pulse) in a 1.6 μs spill window at a 4 Hz repetition rate. Detailed Monte Carlo calculations indicate one expected neutrino interaction inside the active volume every 180 spills for deposited energies higher than 100 MeV. A similar rate is expected from other events associated with the BNB, like muons from the beam halo and neutrinos interacting with the material surrounding the ICARUS T600 detector. The dominant contribution comes from one cosmic ray event out of 55 beam spills ("in-time" cosmics). One event is expected every 35 BNB spills or 7 seconds in the ICARUS T600 detector. The Neutrinos at the Main Injector beam has an intensity of $6 \cdot 10^{13}$ PPP with a 9.5 μs spill window at a 0.83 Hz repetition rate. The NuMI-related expected rate consists of one neutrino event in LAr every 53 spills and one background event mainly from cosmic rays every 7 spills. The NuMI-related activity translates into roughly 1 event out of 6 spills or 9 seconds in the T600 detector. The global expected physical event rate is approximately $\mathcal{O}(0.3$ Hz), including beam neutrinos interacting with the LAr, beam halo events, and cosmic interactions during the spills. Roughly 40,000 events per day are expected in ICARUS T600: an online trigger system is needed to select the physi-

cal event rate and to manage the huge amount of data, and a further offline step will be associating the events with the true neutrino interactions.

In the initial phase of the experiment, the trigger system is based on the recognition of the PMT scintillation light signals inside the gate of the BNB and NuMI proton beams extraction, with the detector well synchronized to the accelerators' clocks. Information from the CRT system and possibly on the bunched beam structure will be exploited at a later stage to improve the capability to reject the contamination of cosmic rays. The adopted trigger architecture based on programmable logic boards gives the required flexibility for a staged trigger logic, where the algorithms are initially introduced according to Monte Carlo calculations and then tuned on real events to match the actual experimental conditions. Due to the softer neutrino energy spectrum of BNB compared to the NuMI, the study of the trigger system has been focused on the BNB, whose neutrinos would require a more challenging event recognition process.

Trigger Electronics In the ICARUS light collection system (subsection 2.1.2) groups of 90 PMTs are connected to 6 CAEN V1730B digitizer boards in each TPC, and each board samples 15 signals from nearby PMTs, corresponding to 3 m longitudinal portions of a TPC. The V1730B boards generate a set of discriminated output Low Voltage Differential Signaling (LVDS) logic signals in terms of an OR logic between pairs of adjacent PMT signals. The 48 LVDS output signals from each TPC are then processed by a NI-PXIe 7820R FPGA (one per each T300 module) with programmable logic. Figure 3.1 shows the deployment of the ICARUS PMT electronics and its link to the trigger system.

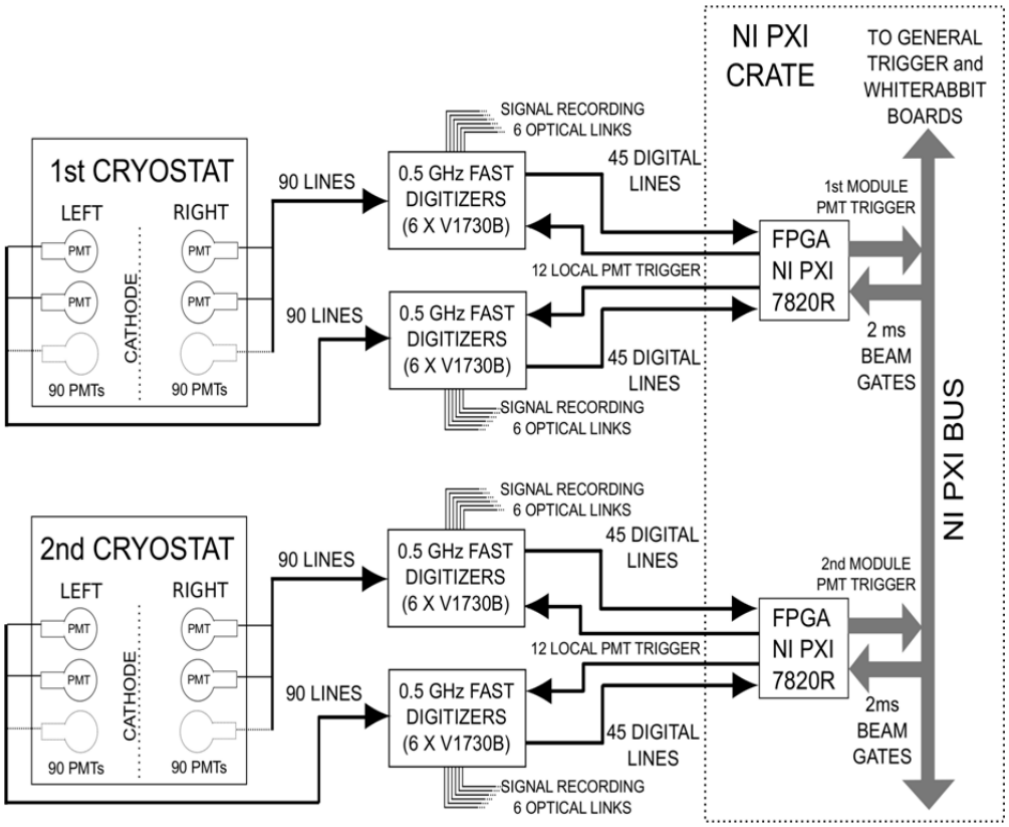

Figure 3.1: Scheme of the PMT-based Trigger System, interfacing the Light Collection System electronics with the trigger setup.

The ICARUS trigger system electronics are based on National Instrument (NI) PXIe instrumentation, installed in one NI-1082 PXIe crate:

- a NI PXIe-8135 Real-Time Controller (RTC), that implements the communication with Data AcQuisition (DAQ) processes;
- a SPEXI board by INCAA Computers, which synchronizes the timing of the detector, handles the beam extraction messages, and also handles the communication with the other boards in the crate;
- three NI PXIe-7820R FPGAs. Two of the three boards are used to generate the trigger signal and to activate the PMT activity recording when needed. The third FPGA is used for the general trigger, which combines the inputs from the two PMT trigger boards with the SPEXI, in order to generate a global trigger.

The hardware implementation of the ICARUS trigger setup is represented schematically in Figure 3.2.

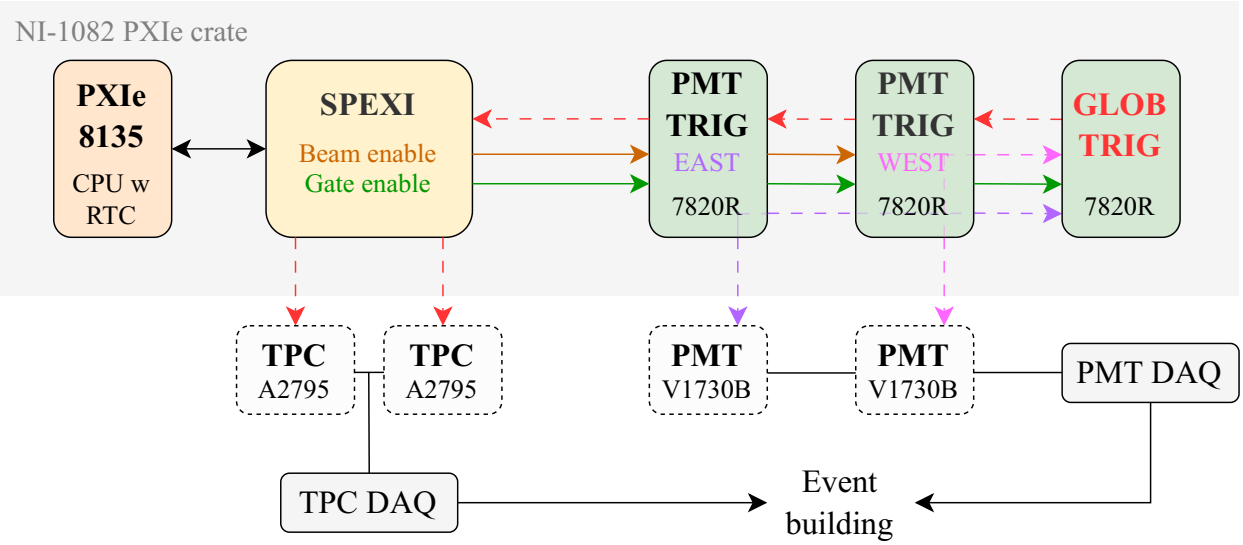

Figure 3.2: Representation of the ICARUS trigger hardware deployment. The NI-1082 PXIe crate includes the PXIe Real-Time Controller, the SPEXI board, and the three FPGAs exploited for the trigger handling.

The generation of the beam spill gates starts by receiving dedicated "early warning" signals 35 ms and 730 ms before the protons hit the target respectively for BNB and NuMI. All the detector subsystems are synchronized with the proton beam spill extraction with a White Rabbit (WR) network, an Ethernet-based network for the synchronization of distributed systems with sub-ns accuracy [101]. The SPEXI generates the 62.5 MHz and 2.5 MHz digitization clocks for the PMT and TPC digitizers respectively based on a reference PPS GPS absolute timing signal. The latter is used also for time-stamping the beam gates and trigger signals. Moreover, the signals from the Resistive Wall-current Monitors (RWMs) of BNB and NuMI are sampled at 2 GHz to measure the timing and bunched structure of the protons on targets.
When a trigger is present, the DAQ activates the readout of the whole detector, with 1.5 ms and 28 μs acquisition windows respectively for the TPC and PMT signal recording. The SPEXI also enables a 2 ms time window around the global trigger for acquiring PMT waveforms, recording all the cosmic muon activity

during the electron drift time in the TPCs. The RTC retrieves the beam gate's timestamp from the SPEXI and the global trigger's timestamp and transfers the data to the DAQ via TCP/IP transfer protocol.

3.1 Monte Carlo Simulation

The logic of the ICARUS trigger was developed with data-driven Monte Carlo simulations, combining information on detector geometry, event type and topology, and scintillation light in liquid Argon.
The ICARUS LARSOFT [102] MC simulation chain consists of various steps: the BNB and NuMI fluxes are used as input to generate the neutrino interactions; the involved particles are propagated through the components of the detector and the expected detector response is extracted, in terms of PMT, TPC, and CRT signals.

Beam Fluxes and Generators The first step in the MC chain is to calculate the BNB and NuMI neutrino beam fluxes. The hadronic cross-sections on the Beryllium and Graphite targets and Aluminum-alloy horns govern the rate of primary proton interactions in the target and hence are crucial for determining the properties of the beam neutrinos. All possible elastic coherent scattering processes, inelastic scatterings, and quasi-elastic scatterings are considered with a data-driven approach, by including constraints from external data, e.g., from the HARP [97] experiment for pion production cross-sections [98]. The primary sources of BNB and NuMI neutrinos are the decay of secondary particles from p-Beryllium and p-Graphite interactions respectively, consisting mostly of pions and kaons.
The flux estimation has to take into account the particle transport before and after the interaction between protons and the target: this is based on a GEANT4 [103] simulation, which includes a detailed description of the beamline geometry and materials traversed by the particles. The base parameters of the two beams considered in the fluxes simulations are listed in Table 3.1.

	PPP	Spill	Bunches / Batches	Bunch Spacing	Bunch FWHM
BNB	$5 \cdot 10^{12}$	1.6 μs	81 / 1	18.8 ns	2 ns
NuMI	$6 \cdot 10^{13}$	9.5 μs	81 / 6	18.8 ns	0.75 ns

Table 3.1: Basic parameters of the BNB and NuMI neutrino beams in the fluxes simulation, including Protons On Target (POT) per spill or PPP, spill windows, bunches per spill over the number of batches, spacing, and width of single bunches.

The GENIE [104, 105] neutrino event-generator is used to simulate the interaction of BNB and NuMI neutrinos with the materials of the detector and its immediate surroundings. The interactions are simulated by combining nuclear physics, cross-sections, hadronization, and hadron transport models, using external neutrino scattering data. Once the type of interaction with the medium is generated, the simulator creates a `MCNeutrino` object, which contains basic information characterizing a neutrino event, e.g.: type of interaction, vertex location, the energy associated with the vertex, secondary particles, and their kinematics. Several types of interactions may take place in the SBN energy range, for neutrino energies around $\mathcal{O}(1\ \text{GeV})$: the dominant channel is the quasi-elastic one, followed by resonant pion-production processes, 2p2h, and deep inelastic scattering at higher energies (for reference, see subsection 1.1.1).

Cosmic muons are generated with the COsmic Ray Simulation for KAscade (CORSIKA) [106] toolkit. The software exploits Monte Carlo calculations to model the extensive air shower originating from the interaction between a high-energy cosmic particle (e.g., a proton, photon, nucleus, or any other particle) and nuclei in the Earth's atmosphere. The particle showers are propagated to the detector's surroundings with respect to a bounding box that includes the detector and the overburden. All the particles in this box are considered, as they may induce some light activity in the PMTs even if they are not traversing the detector's active volume.

Particle Propagation The third step in the MC chain is the propagation inside the ICARUS geometry of secondary particles, arising from the interactions of muons or neutrinos with the active Argon volume or its immediate surroundings. This is achieved with a GEANT4-based [103] simulation in the LARSOFT software. As the secondary charged ionizing particles propagate through the liquid Argon, roughly 20,000 ionization electrons are produced per MeV, considering an ionization potential of 23.6 eV per ion-electron pair in liquid Argon. The electron clouds drift in the electric field toward the anode plane of the TPCs, where the absorption of the ionized electrons from electronegative impurities are simulated, according to a certain electron lifetime in the liquid Argon, and assuming a Gaussian diffusion model in the longitudinal and transverse directions.
Roughly 20,000 scintillation photons per MeV of track are generated isotropically in the liquid Argon with the nominal 500 V/cm drift field, according to two fast and slow components, respectively characterized by the 6 ns and 1.6 μs time constants. Table 3.2 shows the number of scintillation photons with respect to the deposited energy and fast component fraction, for various types of ionizing particles.

	γ / MeV	Fast/Total
p, $\pi^{\pm}$, $\mu^{\pm}$	19,200	0.29
$K^{\pm}$	24,000	0.23
α	16,800	0.56

Table 3.2: Amount of scintillation photons emitted in liquid Argon with respect to the deposited energy and fast component fraction per ionizing particle type.

To propagate the scintillation photons to the PMTs, LARSOFT uses a pre-calculated look-up table (here called "photon library") approach to reduce the computational needs of the event simulation. The volume of an ICARUS T300 module is voxelized into $70 \times 78 \times 392 \sim 2 \cdot 10^6$ cubes with a size of $(5\text{ cm})^3$, and the two modules share the same photon-library, built using a full optical simulation of scintillation light, including emission spectra, Rayleigh scattering, and refraction indices, together with the detector geometry. Roughly $\sim 10^6$ scintillation photons are generated at the center of each voxel to compute the PMT "visibility", namely the fraction of scintillation light each PMT collects on average with respect to the amount of produced light, mostly driven by the distance between the light source and the PMTs, with large fluctuations due to the detector geometry, e.g., the pierced cathode (58% transparency). The quantum efficiency of the PMTs, set to 12.1% as measured on PMTs with the TPB evaporated on them [88], is included in the photon library. The time distribution of the photoelectrons at each PMT is parametrized as a function of the distance between the source and PMT location. This parametrization relies on a full optical simulation and takes into account

Rayleigh scatterings and the fast and slow components of scintillation light in liquid Argon. At the end of the MC particle propagation step, a `SimPhotons` object is generated, containing information on the number of photons collected by the PMTs and their arrival times.

Detector Response The last step in the LArSoft MC chain is the simulation of the detector response, converting the information on the charge, energy, and timing of the event into physical objects.
The simulated ionization electrons are propagated to the TPC wire planes according to the electric drift field, the longitudinal and transverse diffusion, and the liquid Argon purity. The 2-dimensional wire field response is simulated within one wire pitch. Electrical noise is described channel-by-channel with a data-driven approach, specific to the ICARUS detector and modeled from the measured noise spectra of different wires, depending on their length. The waveforms from the wires are finally obtained by simulating the amplification and shaping of the electronics.
For the light collection system, the information on the number and timing of photons is used to build the waveform at each PMT, by summing the fixed response of the photons converted into PhotoElectrons (PEs). Originally, an analytical Single Photoelectron Response (SPR) function was exploited in the MC chain. As will be discussed, this work exploits a digitized SPR as measured in the ICARUS LArTPC, hence driving the Monte Carlo simulation from data. For reference, the analytical SPR function is defined with respect to the time t_0 the photon arrives at the PMT:

$$A(t) = \begin{cases} 0 & \text{if } t < t_0 \\ 10^9 \frac{ge\rho}{\tau_d - \tau_r} \cdot \left[\exp(-\frac{t-t_0}{\tau_r}) - \exp(-\frac{t-t_0}{\tau_d})\right] & \text{if } t \geq t_0 \end{cases}, \tag{3.1}$$

in which $g = 5 \cdot 10^6$ is the PMT gain, e is the electron charge, $\rho = 51\ \Omega$ is the cable impedance, $\tau_d = 4.142$ ns is the decay time constant and $\tau_r = 1.775$ ns is the rise time constant. Figure 3.3 shows a comparison between the analytical SPR and the digitized SPR: the two response functions are quite different in amplitude and in the fact that the digitized SPR presents a tail, interpreted as due to cable effects (not perfect impedance match, frequency response).

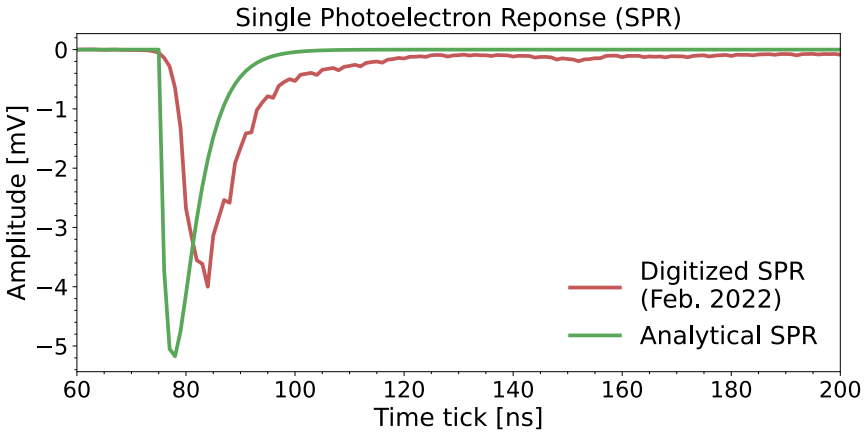

Figure 3.3: Single Photo-electron Response (SPR) trends as a function of time, computed analytically and digitized as of 2022.

The PMT simulation includes the digitization of the light signals, which takes as input the set of PEs arriving at each PMT within an "enable" time window of 2 ms, to match the drift time of electrons in the TPCs. The digitization itself is simulated independently on each PMT channel: the arrival times of PEs are processed in 2 ns bins, and in each bin, the SPR is computed and summed into the total response, which is then subjected to PMT gain fluctuations. The response is then superimposed to a baseline of 15,000 ADCs, dark noise is considered and the waveform is clipped and rounded to 14 bits, before being discriminated.

3.1.1 Data-driven Light Simulation

A more realistic Monte Carlo description of scintillation light is obtained by associating each generated PhotoElectron (PE) with the digitized SPR (Figure 3.3), shifted in time according to the corresponding arrival time, hence driving the simulation from data. Figure 3.4(a) shows the distribution of arrival times of the PEs at a PMT of the West TPC of the West cryostat (WW), for a simulated Quasi-Elastic (QE) Charged-Current (CC) BNB ν_μ interaction. The PMT waveform is progressively built by summing incoming PEs and their SPRs, as shown in Figure 3.4(b). The final waveform shows the typical fast scintillation light component, leading to the early peak, and the slow scintillation component for the tail. A PMT discrimination threshold of 13 PEs (namely, ~ 49 mV or 390 ADC) was applied, to reject the activity linked to the ^{39}Ar contaminant in the liquid argon, for which a ~ 1 Bq/kg activity is foreseen. Recall that 1 PE corresponds to approximately 30 ADC counts or 3.75 mV.

The data-driven simulation can be exploited to analyze the scintillation light yield of different neutrino flavors and interactions from the BNB and NuMI beams, in terms of energy, event topology, and containment. The simulated light signals on PMTs are studied to define an optimal trigger logic for the ICARUS detector, to be based on the detection of scintillation light as a prompt signal in coincidence with a beam gate.

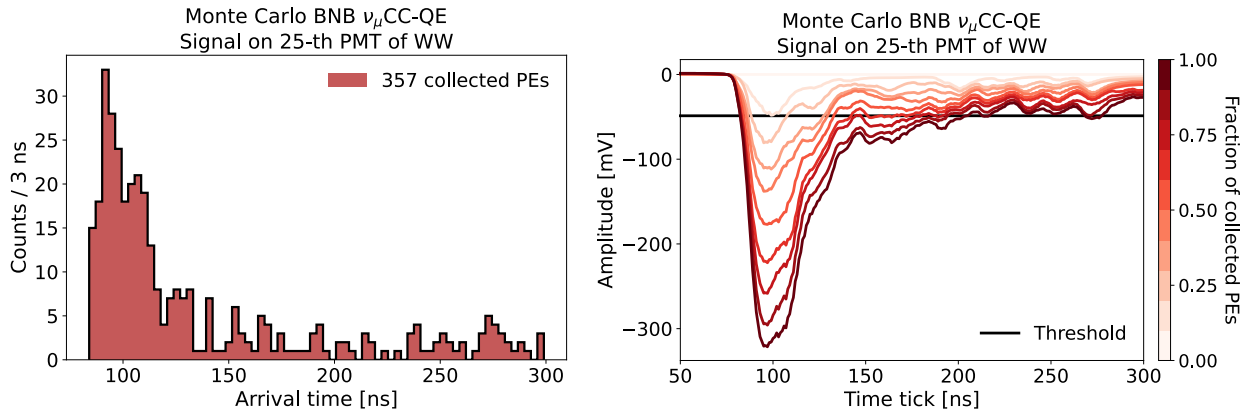

(a) (b)

Figure 3.4: (a) Distribution of PE arrival times at the 25-th PMT in the West TPC of the West cryostat (WW), for a BNB ν_μ Charged-Current (CC) Quasi-Elastic (QE) event. (b) Waveform at the 25-th PMT for the same event, progressively built as more photoelectrons are considered.

3.1.2 Produced Samples

The evaluation of an optimal trigger configuration in ICARUS is based on the analysis of Monte Carlo BNB muon and electron neutrino samples, as well as of cosmic muons. ICARUS foresees analyses with both flavors and neutrino beams, as a stand-alone experiment and also within the SBN program. Moreover, triggering on muons out of the beam gates as efficiently as possible is crucial for acquiring "off-beam" statistics, to be compared with beam-related spectra. The analysis focuses on one ICARUS T300 module, and conclusions apply to both modules.

BNB Neutrinos Figure 3.5 shows the energy spectra of Monte Carlo BNB ν_μ (a) and BNB ν_e (b), stacked with respect to CC and NC interactions. The available statistics in the West T300 active volume consist of 79,924 ν_μ, of which 59,668 CC (75%) and 20,256 NC (25%), and 31,936 ν_e, of which 24,475 CC (77%) and 7,661 NC (23%). The coordinates of the active detector volume are described in Table 3.3:

	East T300	West T300
Drift [cm]	$(-358.49, -61.94)$	$(61.94, 358.49)$
Vertical [cm]	$(-181.86, 134.96)$	
Longitudinal [cm]	$(-894.95, 894.95)$	

Table 3.3: Coordinates defining the two ICARUS T300 West and East modules in the LARSOFT Monte Carlo framework. The longitudinal coordinate refers to the direction of the Booster Neutrino Beam.

The spectra also show the Fiducial Volume (FV) selection, namely a request on the position of event vertices to be contained in a portion of the active detector volume, to ensure the optimal reconstruction of neutrino events in the data analysis. The fiducial volume is defined as follows:

- the drift and vertical directions are cut by 25 cm on both sides to address the "beam halo" background, namely secondary particles entering the active volume and originating from neutrino interactions with the passive Argon or the surroundings of the detector. Some buffer volume is also needed to deal with neutrons from cosmic ray interactions, characterized by interaction lengths of $\mathcal{O}(10$ cm$)$ [107]. Moreover, events that are too close to the anode wire planes may not be reconstructed fully, and are hence discarded;

- the longitudinal direction is reduced by 30 cm upstream and 50 cm downstream with respect to the direction of BNB neutrinos, being secondaries from neutrino interactions forward-oriented. The upstream cut is mainly needed to deal with "dirt events", namely secondary particles entering the active volume and produced by interactions with the passive Argon or external material upstream of the detector.

Considering the Fiducial Volume, the ν_μ and ν_e spectra are reduced by $\sim 33\%$, as expected from the ratio of the fiducial volume with respect to the active ICARUS T300 volume.

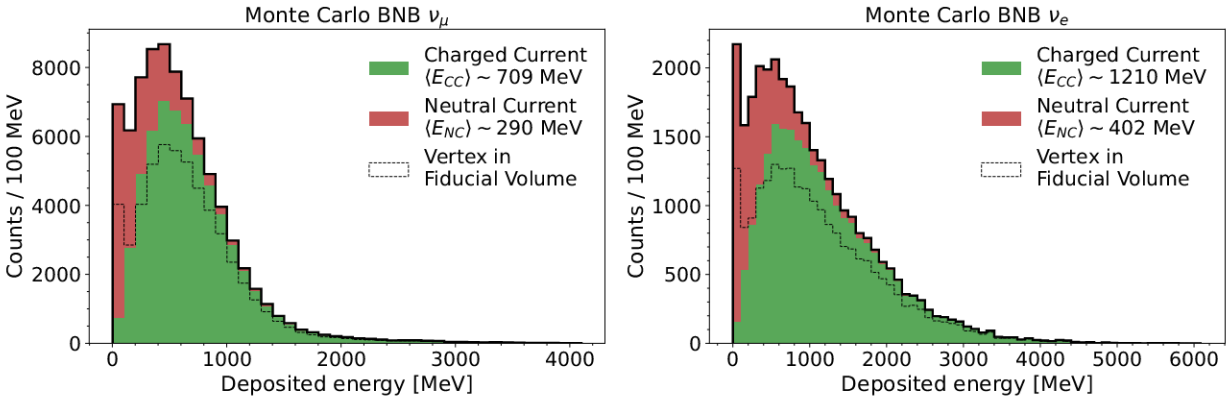

Figure 3.5: Energy spectrum of Monte Carlo BNB ν_μ (left) and BNB ν_e (right) in the West ICARUS T300 module, stacked with respect to CC and NC interactions. The spectra after the Fiducial Volume cut are highlighted.

Cosmic Muons Figure 3.6(left) shows the distribution of the charge barycenters in the longitudinal-drift plane for the 65,694 cosmic muons simulated in ICARUS T600. The charge barycenter is calculated for each track as the mean of the true MC charge deposition positions in ICARUS T600 weighted by the amount of charge and can be used for localizing cosmic muons in the detector.

The spectrum of the Monte Carlo muons with non-zero energy deposition in the ICARUS T600 detector is reported in Figure 3.6(right). The lower-energy peak in the spectrum is linked to cosmic muons slightly outside the detector, crossing the passive argon or crossing the detector only for small lengths, but still inducing some light activity in the modules. At higher energies, a flat component of the spectrum follows, mainly given by muons crossing the detector for small lengths (e.g., in the corners) with various orientations. The peak at intermediate energies is then related to particles crossing the detector in a vertical direction. Finally, the high-energy tail comes from longer muon tracks, leading to higher energy depositions.

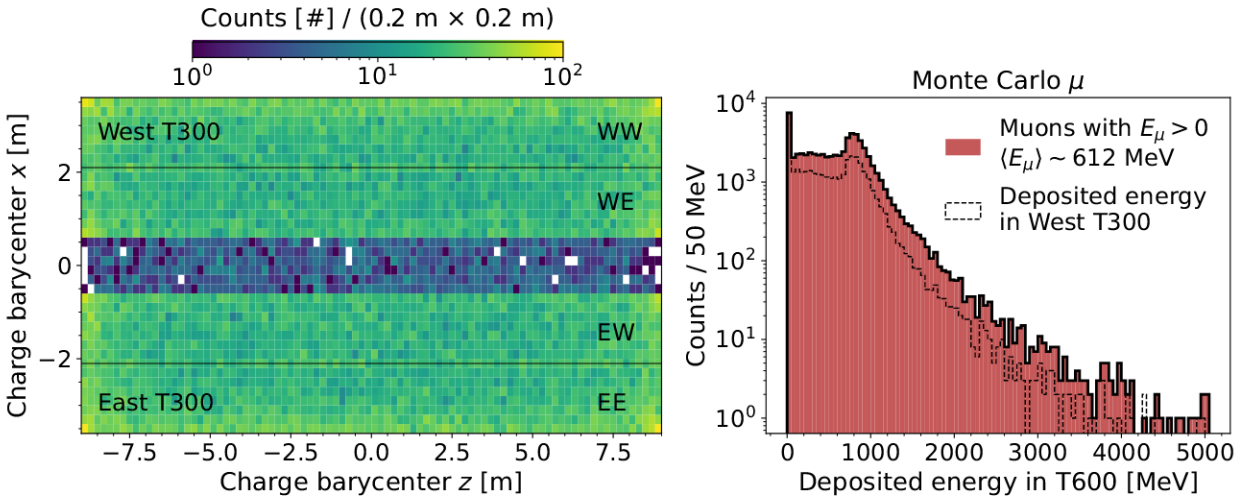

Figure 3.6: (left) Distribution of charge barycenters of Monte Carlo cosmic muons generated in ICARUS T600. Charge barycenters are computed with charge depositions in both the T300 modules. (right) Energy spectrum of the same sample, selected with non-zero energy depositions. The spectrum of muons for energy depositions in the West ICARUS T300 module is highlighted.

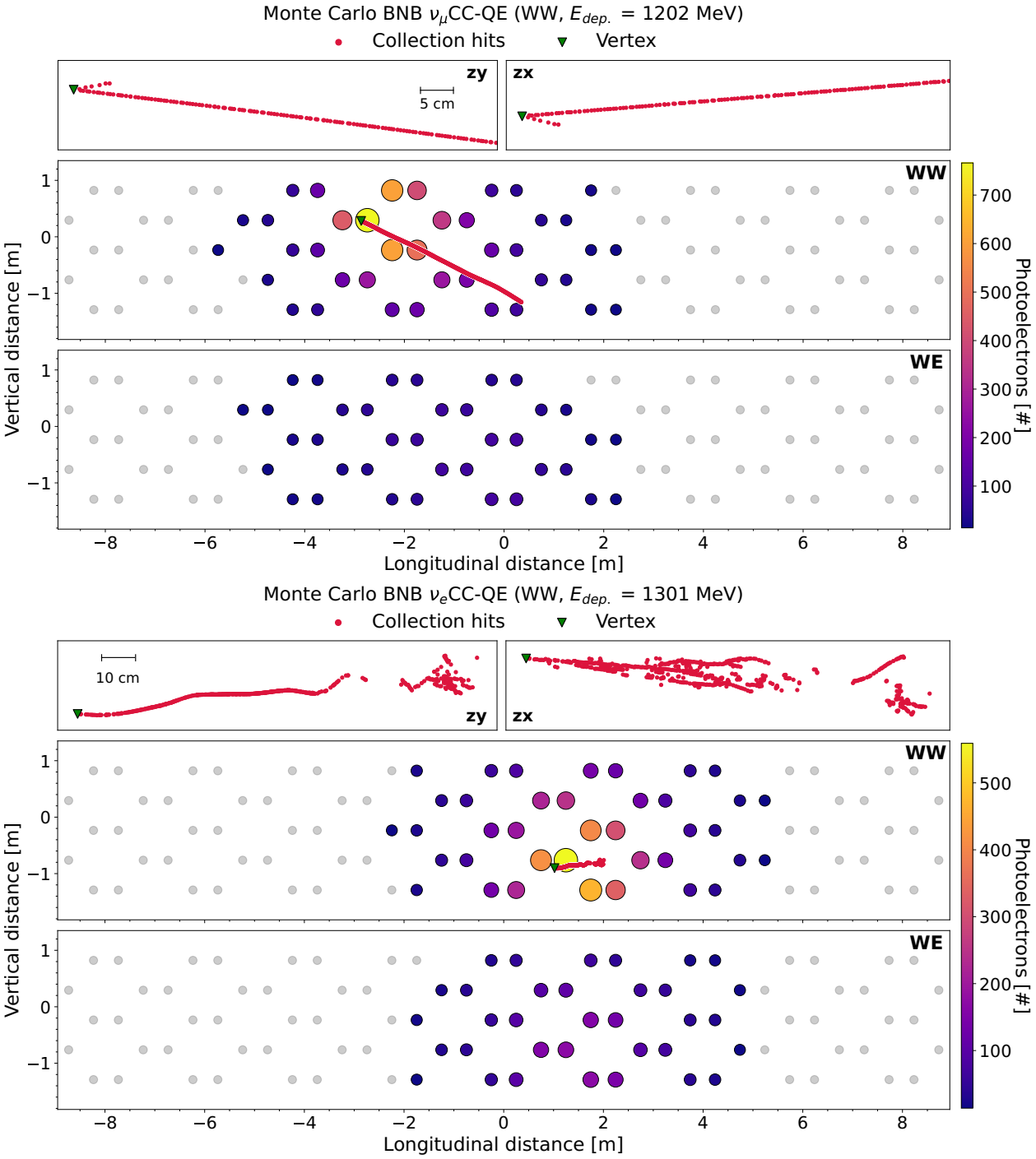

Figure 3.7: Event display of a Monte Carlo BNB ν_μ Charged-Current (CC) Quasi-Elastic (QE) event with a 1202 MeV deposited energy (top) and a BNB ν_eCC-QE event with a 1301 MeV deposited energy (bottom), in the West ICARUS T300 module. The events are shown in terms of TPC and PMT signals in the WW and WE adjacent TPCs, separated by a common semi-transparent cathode. PMTs are colored according to the number of photoelectrons collected and exceeding a 13 PEs threshold. The upper panels show the TPC Collection hits projected onto the *zy* (side view) and *zx* (top view) planes.

3.2 Development of the PMT-Majority Logic

Considering that $\sim 20,000$ photons per MeV are produced in liquid Argon at the nominal 500 V/cm drift field, coupled with the GeV-energies of BNB and NuMI neutrinos and the 3 m drift length of each ICARUS T300 module, interactions are expected to develop in ~ 3 m longitudinally. It is reasonable to evaluate trigger signals in limited longitudinal TPC windows, still recording single PMT waveforms to maintain the granularity of the time information.

Produced Monte Carlo data have been first analyzed to identify the number of fired PMTs above the threshold produced by neutrino events and their localization in the TPCs. Figure 3.7 (top) shows the light distribution in the West T300 module for a Quasi-Elastic (QE) CC interaction of a simulated BNB ν_μ, while Figure 3.7 (bottom) for a CC-QE interaction of a BNB ν_e. The vertices of the selected events are contained in the WW TPC, and PMTs of both the TPCs in the West T300 module are considered. Note that only PMTs with a signal exceeding a 13 PEs threshold are highlighted, and ionization tracks are represented by the hits simulated on the TPC Collection wire plane. The ν_μCC-QE interaction yields a short highly-ionizing proton track and a longer muon track, leading to a focused light deposition in terms of PMTs receiving a large amount of photons. On the other hand, the ν_eCC-QE interaction leads to the production of a proton and an electron, which translates into a short shower in the liquid argon, resulting in high light depositions spread out among several PMTs.

Figure 3.8 shows the distribution of the number of PMTs over the 13 PEs threshold for BNB ν_μCC and ν_μNC interactions, focusing on the 90 PMTs of the West TPC in the West T300 module (WW). Approximately 24 PMTs are on average over the discrimination threshold in ν_μCC events from the BNB with the vertex in the West T300 module, while for ν_μNC interactions 14 PMTs are on average flashed due to smaller energy depositions (see Figure 3.5).

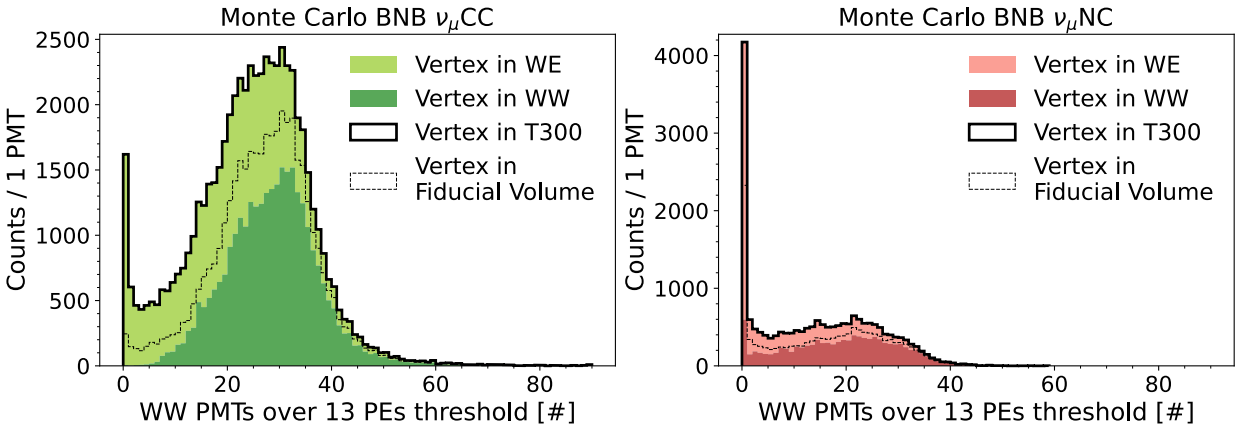

Figure 3.8: Distribution of the number of PMTs over a 13 PEs threshold for CC (left) and NC (right) interactions of MC BNB ν_μ in the West TPC of the West cryostat (WW), stacked with respect to the vertex position in the WW TPC or the adjacent WE TPC in the same ICARUS T300 module.

The average amount of fired PMTs increases to 27 and 16 respectively for ν_μCC and ν_μNC events when applying the fiducial volume cut, which is discarding events with a small light yield originating close to the anode planes and to the downstream TPC wall, leading to secondaries scarcely contained in the liquid argon.

Moreover, the distributions in Figure 3.8 discriminate between event vertices in the WW TPC, the same as the PMTs that are being considered, and the adjacent WE TPC. When the vertex is in the same TPC as the PMTs, on average more PMTs are flashed: for CC interactions, all the cases with less than 5 flashed PMTs are linked to ν_μCC event vertices in the opposite WE TPC.
In fact, when the event vertex is farther from the PMTs, the light yield decreases, due to the limited cathode transparency between the two WW and WE TPCs (Figure 3.9). This is evident also from the previously shown Monte Carlo event displays (Figure 3.7). Furthermore, the number of fired PMTs decreases when the vertices are close to the upstream and downstream TPC sides, which are not instrumented with PMTs, due to the BNB neutrino interactions being forward-oriented.

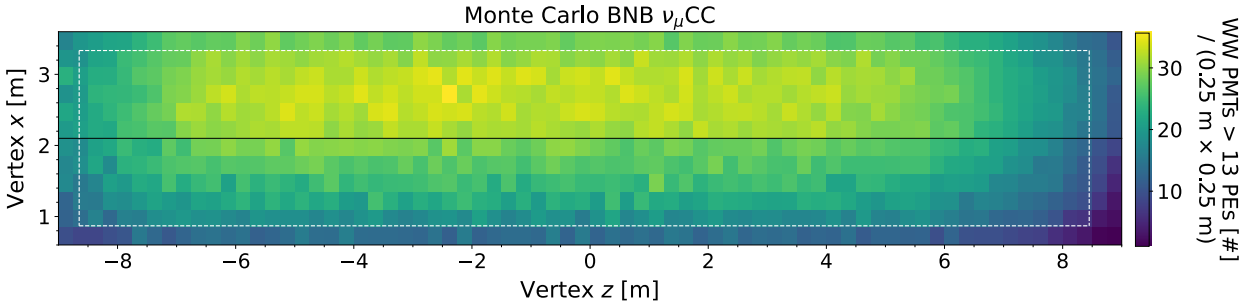

Figure 3.9: View of the West ICARUS T300 module from the top. Distribution of the event vertices, colored by the average amount of PMTs in the bottom West TPC (WW) exceeding the 13 PEs threshold. The two WW and WE TPCs share a common semi-transparent cathode. The fiducial volume cut is highlighted with dashed white lines.

The scintillation light collection also depends on the energy of the events: the higher the energy, the broader the light deposition on PMTs. Figure 3.10 reports the distribution of PMTs over the threshold in the WW TPC as a function of the deposited energy for BNB ν_μCC and ν_μNC interactions.

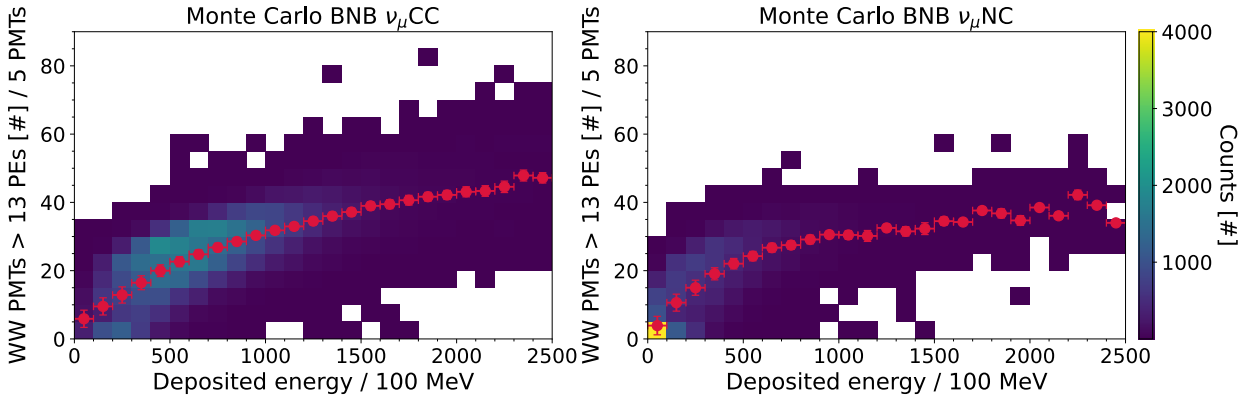

Figure 3.10: Distribution of the number of PMTs over a 13 PEs threshold for CC (left) and NC (right) interactions of MC BNB ν_μ in the West TPC of the West cryostat (WW), with respect to the energy deposited in the liquid Argon. The average values over energy bins are reported on top of the distributions.

On average, $\sim$ 10 PMTs are fired for ν_μCC and NC interactions with $E_{\text{dep.}} > 100$ MeV in a single TPC. Indeed, since CC interactions are generally more energetic than NC interactions, the latest will generally

lead to fewer PMTs being fired.

The distribution of PMT flashes in the TPCs suggests that prompt scintillation light signals can be used to build an efficient trigger based on a PMT-multiplicity logic condition. Moreover, the two adjacent TPCs should not be considered in coincidence with each other, given the semi-transparency of the common cathode, but rather the PMT counts in the two should be summed.

3.2.1 Spatial Containment of PMT Signals

The longitudinal extension of the PMT light signals associated with a neutrino interaction can be determined by the fraction of light collected by PMTs inside a window centered around the light barycenter, namely the average of the coordinates of PMTs over a 13 PEs threshold weighted by the corresponding collected PEs. In Figure 3.11, the event "containment" is reported in terms of collected PEs for PMTs with signals exceeding the 13 PEs discrimination threshold in the West TPC of the West cryostat (WW).

Note that NC interactions show a slightly higher containment with respect to CC interactions, due to lower average deposited energies translating in more compact events (see Figure 3.5). In general, more than 90% of the light signals are detected inside a ~ 4 m longitudinal window. Indeed, the highest light depositions occur in a small number of adjacent PMTs (for reference, see Figure 3.7): this can be inferred by the lower containment fraction of fired PMTs counts for a selected window, with respect to the number of PEs. As a result, the trigger logic needs to recognize the beam-related light activity only in a limited portion of the TPCs.

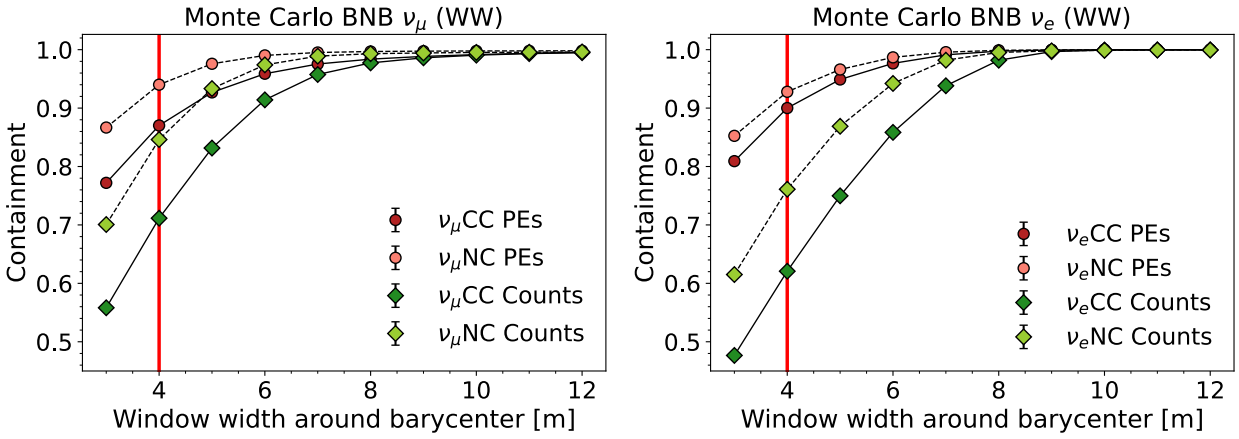

Figure 3.11: Event containment in a window along the longitudinal direction centered around the light barycenter of the event, for BNB ν_μ (left) and BNB ν_e (right). Solid dark-shaded lines indicate CC interactions, while dashed light-shaded lines NC interactions. The containment is defined as the fraction of the amount of PEs or flashed PMTs inside the window over the total amount of signal or counts.

3.2.2 PMT Pairing

In the ICARUS light collection system, CAEN V1730B boards digitize groups of 15 PMT signals, corresponding to 3 m longitudinal TPC sections. In particular, each digitizer board combines the signals from two adjacent PMTs with programmable logic and provides 8 Low Voltage Differential Signaling (LVDS)

outputs. Each of the four ICARUS TPCs hosts 90 PMTs, digitized by 6 V1730B boards, providing 45 LVDS outputs. Figure 3.12 shows how nearby PMTs are coupled by the digitizers.

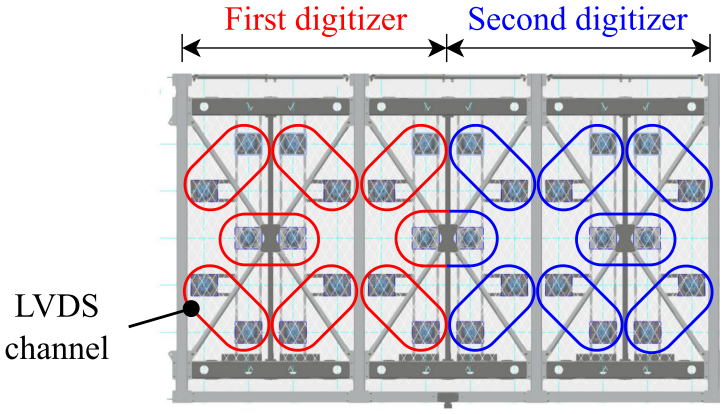

Figure 3.12: View from the side of a 6 m longitudinal portion of an ICARUS TPC. Adjacent PMTs are combined to provide LVDS outputs.

Figure 3.13 shows the distribution of fired simulated LVDS channels in the West TPC of the West cryostat (WW) when combining the adjacent PMTs discriminated with a 13 PEs threshold and combined with logical AND/OR conditions, for BNB ν_μCC and NC interactions in the WW TPCs.
On average 16 (14) LVDS channels in the WW TPC are fired for BNB ν_μCC interactions when combining adjacent PMTs in OR (AND): clearly, an AND logic would be more stringent, leading to a lower multiplicity yield (Figure 3.13). This result is consistent with the average number of fired PMTs in the same TPC, as observed in Figure 3.8. The impact of the AND condition is even more effective for ν_μNC interactions, where 886 events are not able to fire any LVDS channel, a number that decreases to 587 with the OR logic condition. Considering the geometric deployment of PMTs in the TPCs where the distance between the PMT pairs is generally less than 1 m and the higher multiplicity yield in neutrino events, the OR logic was chosen to combine pairs of PMTs in LVDS channels.

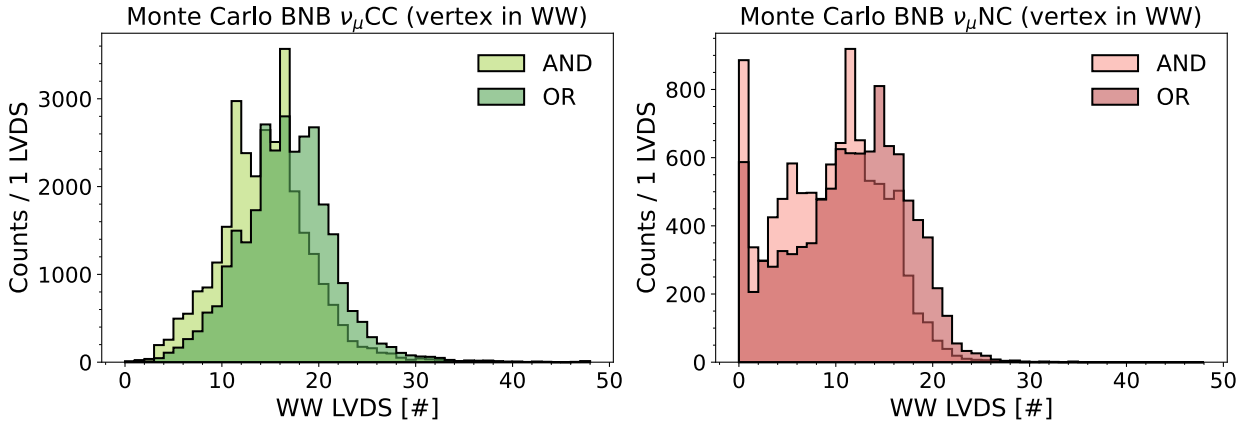

Figure 3.13: Distribution of fired LVDS channels in the West TPC of the West cryostat (WW) for CC (left) and NC (right) interactions of MC BNB ν_μ, combining two adjacent PMTs with AND/OR conditions. Event vertices in the WW TPC are selected.

According to the PMT electronics deployment, each 18 m long ICARUS TPC can be sliced in three 6 m long fixed windows along the longitudinal direction, containing 30 PMTs digitized by two V1730B boards and 16 LVDS output lines each (Figure 3.14). Front-facing slices in two adjacent TPCs are combined by taking the sum of the fired LVDS channels in the two windows, instead of asking for any coincidence between the two, in order to mitigate the impact of the cathode semi-transparency.

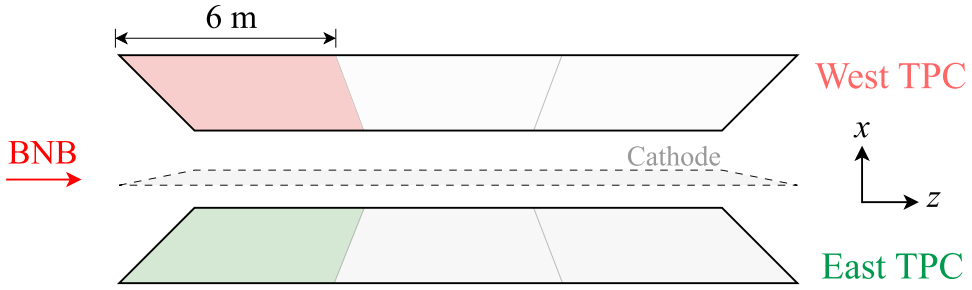

Figure 3.14: View of the West ICARUS T300 module from the top, with the cathode highlighted in the middle. The module is divided into three 6 m longitudinal windows, defined as the sum of front-facing TCP slices, each containing 30 PMTs read out by two digitizers.

Figure 3.15 shows the distribution of BNB ν_μCC vertices, with respect to the multiplicity of fired LVDS channels in the central 6 m slice of the detector defined in the -3 m $< z < 3$ m range, consisting of the sum of two front-facing TPC windows with 30 PMTs or 16 LVDS lines each. The LVDS channels are defined as the OR of adjacent PMTs, discriminated at a 13 PEs threshold.

It can be observed that the distribution of the interaction vertices is not symmetric with respect to the center of the window, but it is rather shifted upstream, due to the BNB neutrinos' direction and the fact that secondaries are forward-oriented (for reference, recall Figure 3.7). Furthermore, considering the sum of the two adjacent TPCs removes any asymmetry in the PMT scintillation light yield due to the semi-transparency of the cathode.

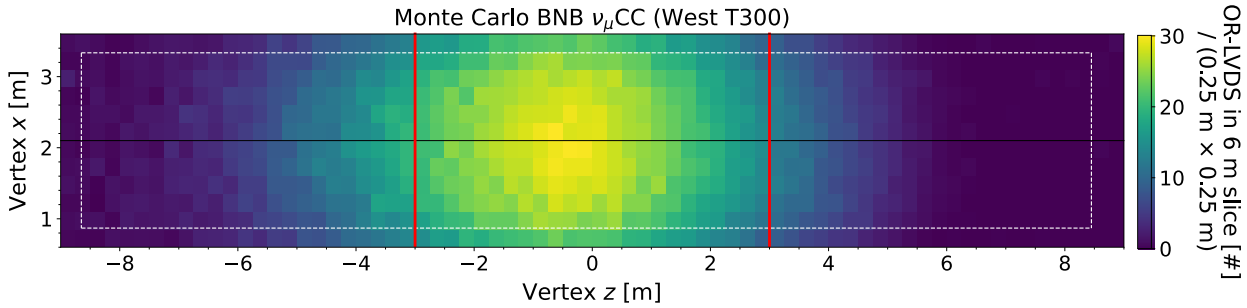

Figure 3.15: View of the West ICARUS T300 module from the top, with the cathode highlighted in the middle. Distribution of the event vertices, colored by the average amount of fired LVDS channels in the two front-facing 6 m windows, defined in the -3 m $< z < 3$ m range. The fiducial volume cut is highlighted with the dashed white lines.

On average, 10 LVDS channels are fired in the central slice, considering all the available BNB ν_μCC events. When the event vertices are within the slice, the average multiplicity increases to 22 LVDS channels. Figure 3.16 shows the distribution of LVDS channels in the central West ICARUS T300 slice for BNB ν_μCC

and NC interactions. A low multiplicity threshold of 5 LVDS channels guarantees that 99.5% of the ν_μCC events are preserved, cutting only 100 out of the 19,827 selected vertices. The majority-5 threshold keeps roughly 60% of the ν_μNC vertices contained in the central slice. The remaining events should be recovered by the signals from the adjacent 6 m detector slices.

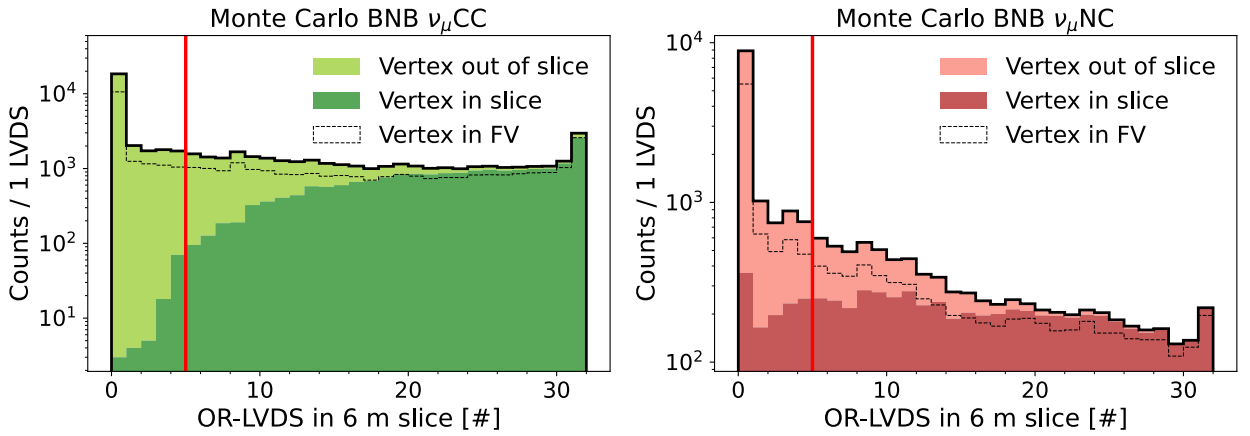

Figure 3.16: Distribution of fired LVDS channels in one -3 m $< z <$ 3 m slice of the ICARUS T300 West module, consisting of two front-facing TPC windows with 30 PMTs and 16 LVDS lines each, stacked with respect to the location of event vertices. A multiplicity threshold of 5 is highlighted ("majority-5").

3.2.3 Monte Carlo Trigger Efficiency

A trigger logic configuration has been built according to previous considerations, and tested in terms of the detection efficiency, starting from building the PMT waveforms for each event, with a data-driven approach that exploits a digitized SPR to mitigate data/MC discrepancies. The waveforms are discriminated at a 13 PEs threshold, and adjacent PMTs pairs are combined with an OR logic to form LVDS channels. Each ICARUS T300 module is then sliced into three 6 m windows, containing 30 PMTs (or 15 LVDS lines) on one TPC and 30 PMTs on the other, front-facing. The multiplicity of lightened PMTs in each slice is evaluated by the sum of the fired pairs on the two TPC windows, in order to define a trigger PMT-majority condition in one of the three windows. Various conditions were tested: those will be referred to as "majority-N" or "mj-N", with N being the chosen threshold for the LVDS multiplicity in the longitudinal slices.
Monte Carlo truth information is fetched for each event, including interaction type, vertex location, deposited charge barycenter, deposited energy, and PMT information, and the data-driven trigger simulation determines whether an event meets the PMT-majority requirement in at least one of the three 6 m T300 module windows. The trigger event recognition efficiency is evaluated as the number of triggering events over the total number of events. The related asymmetric errors are estimated as a 68% binomial proportion confidence interval with the Clopper-Pearson method, which guarantees coverage [108].

BNB Neutrinos Figure 3.17 shows the detection efficiency for BNB ν_μCC interactions in the fiducial volume of the West ICARUS T300 module, with respect to the longitudinal z coordinate of the vertices, for three majorities, mj $= 5, 10, 15$.

The majority-5 condition yields a $> 99.5\%$ efficiency for BNB ν_μCC events, while minor inefficiencies at the 0.5% scale arise near the borders of the 6 m slices used to evaluate the multiplicity of LVDS channels. Using stricter majority-10 and 15 conditions leads to more pronounced inefficiencies, with dips up to 20% from the unity in the same regions. The efficiency strongly drops near the upstream and especially downstream detector walls, which are not instrumented with PMTs, because the secondary particles are emitted in the forward direction with respect to the interaction vertex position and the BNB beam direction. Furthermore, some inefficiencies originate at the edges of the three side-by-side windows, where the light signal could be split into two nearby slices and the LVDS multiplicity in a single slice decreases.

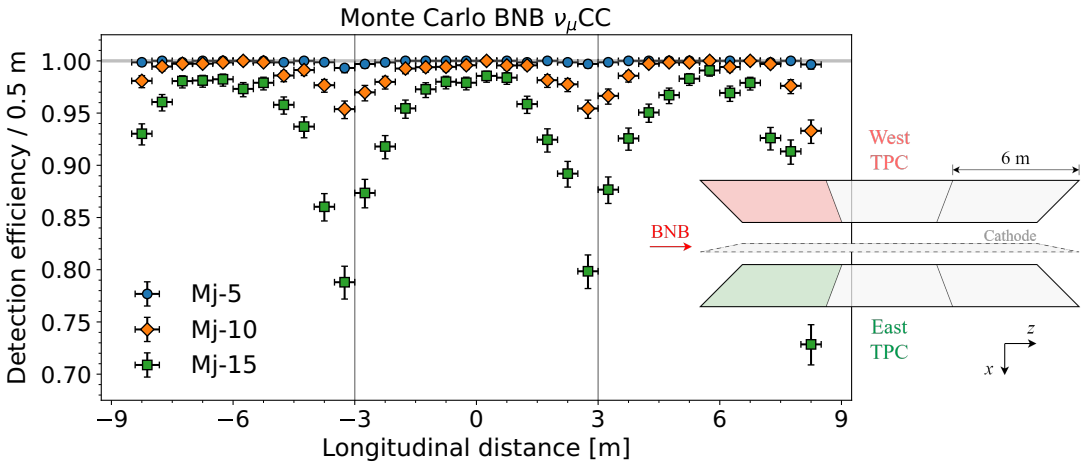

Figure 3.17: Detection efficiency as a function of the vertex longitudinal z coordinate for BNB ν_μCC interactions. The inset image shows the trigger configuration, with a scheme of the West ICARUS T300 module viewed from the top.

To recover missed events in the bulk of the detector, in addition to the previous configuration, two 6 m windows can be superimposed to the existing ones and placed around the center of the cryostat along the longitudinal direction ("sliding windows configuration", Figure 3.18).

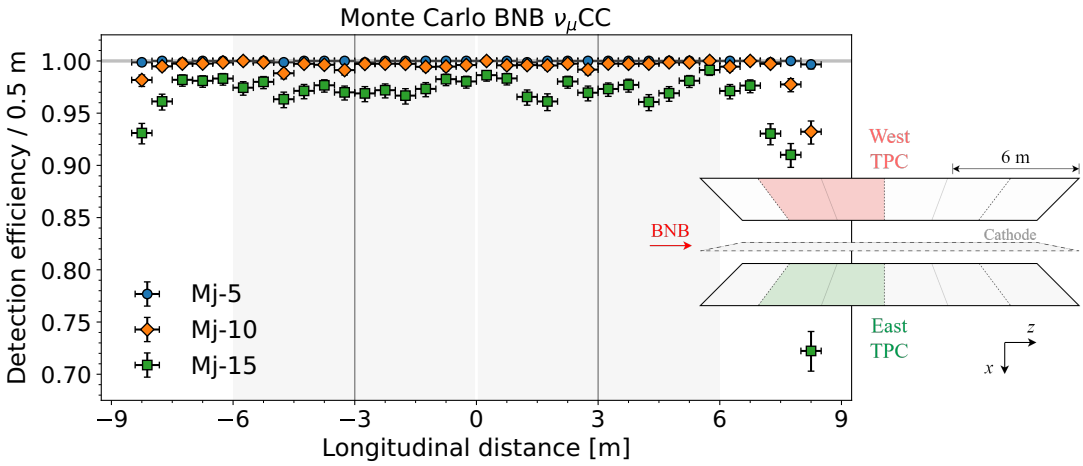

Figure 3.18: Detection efficiency as a function of the vertex longitudinal z coordinate for BNB ν_μCC interactions, using the improved "sliding windows configuration" and including the FV cut. The inset image shows the trigger configuration, with a scheme of the West ICARUS T300 module viewed from the top.

The majority-5 condition yields an improved $> 99.9\%$ efficiency for BNB ν_μCC events, while the average efficiency for the majority-10 and 15 logics are 99% and 96% respectively. The sliding windows configuration proves to be highly efficient, resolving most of the inefficiencies in the bulk of the detector and making the detection efficiency uniform along the longitudinal distance of the detector. It was hence set down to use the sliding-windows mj-5 condition for neutrinos. Note that lowering even further the request on the majority would imply increasing the trigger rate to be sustained by the DAQ, resulting in a trade-off between rate and efficiency.

The predicted trigger efficiencies for ν_μ and ν_e from the BNB with respect to the energy deposited in the liquid argon are shown Figure 3.19, with respect to CC and NC interactions and using the mj-5 logic. An almost full detection efficiency is found for ν_μCC and ν_eCC interactions for $E_{\text{dep.}} > 100$ MeV. Few inefficiencies arise for the detection of CC interactions below 100 MeV, where 8 (3) events out of 78 (16) did not meet the majority-5 requirement for ν_μCC (ν_eCC) interactions. The efficiency with neutral currents slightly worsens: above 100 MeV of deposited energy, a global efficiency of 99.9% ($> 99.9\%$) is predicted for ν_μNC (ν_eNC) interactions, decreasing below to roughly 58% for both ν_μ and ν_e.

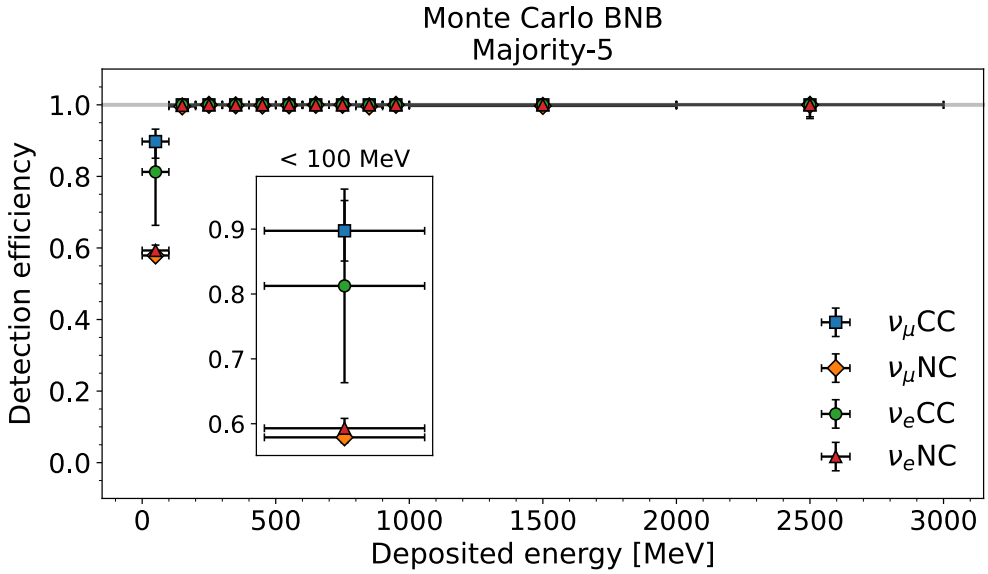

Figure 3.19: Trigger efficiency predicted with Monte Carlo for BNB ν_μ and ν_e, with respect to the deposited energy and to CC and NC interactions and including the FV cut. The chosen logic configuration is the majority-5. Energy bins are 100 MeV and 1 GeV wide.

As already anticipated, the sliding windows configuration guarantees uniformity of detection efficiency along the direction of the BNB neutrinos (see Figure 3.20). The mj-5 efficiency for CC interactions exceeds the 99.9%, and slight inefficiencies are localized mainly in the downstream wall of the TPCs. In the case of NC interactions, the efficiency is again fairly uniform but averages at lower values, around 87% (90%) for ν_μNC (ν_eNC) interactions, with a dip close to the downstream detector wall.

Finally, the efficiency was evaluated along the drift direction, as shown in Figure 3.21: no clear dependence of the detection efficiency with respect to the x vertex position was found with the mj-5. Recall that the fiducial volume cut prevents considering events that are very close to the anode planes, for which the detection

efficiency would not be optimal.

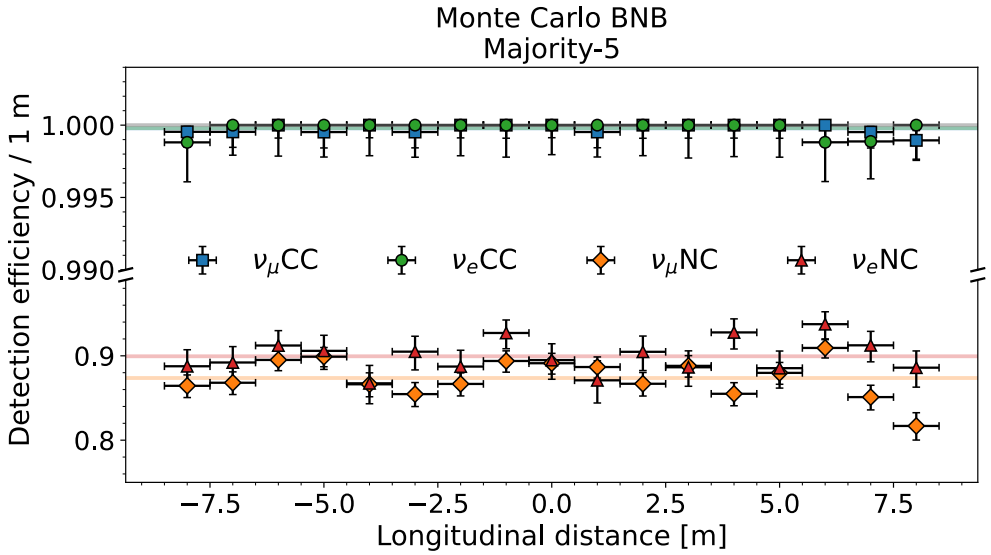

Figure 3.20: Trigger efficiency predicted with Monte Carlo for BNB ν_μ and ν_e, with respect to the longitudinal z vertex coordinate and to CC and NC interactions and including the FV cut. The chosen logic configuration is the majority-5. The average efficiency for each flavor and interaction type is highlighted.

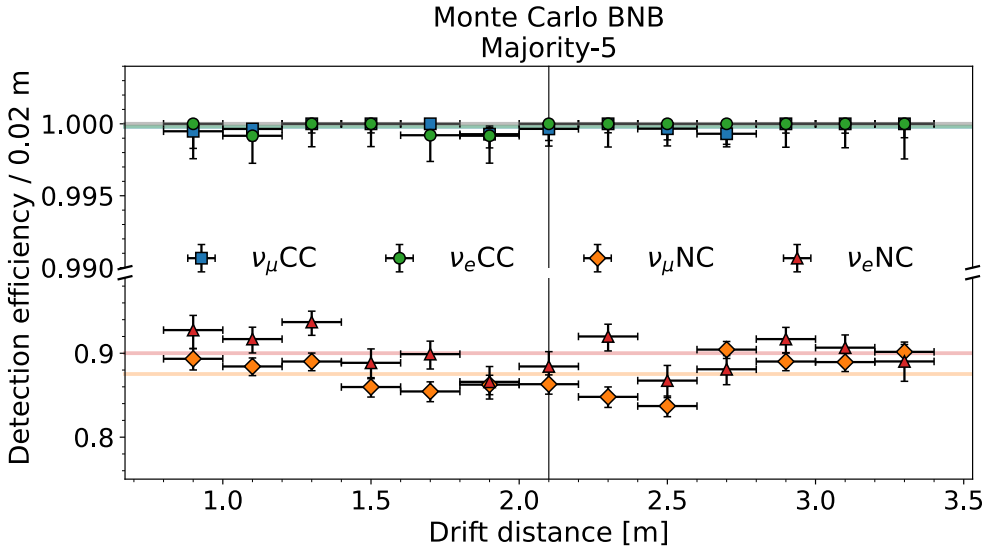

Figure 3.21: Trigger efficiency predicted with Monte Carlo for BNB ν_μ and ν_e, with respect to the longitudinal x vertex coordinate and to CC and NC interactions and including the FV cut. The chosen logic configuration is the majority-5. The average efficiency for each flavor and interaction type is highlighted. The cathode is drawn in the middle of the module.

As a conclusion, focusing on charged-current neutrino interactions with BNB, the proposed trigger configuration would provide an almost maximal and spatially uniform efficiency for deposited energies $E_{\text{dep.}} > 100$ MeV. The few very-low-energy events that were not able to fire a majority-5 trigger are located mainly near the upstream and mostly downstream non-instrumented detector walls, as shown in Figure 3.22 for ν_μCC interactions: only 8 events out of the 40,263 ν_μCC vertices in the fiducial volume did not meet the

trigger requirements, and all of them have energies $E_{\text{dep.}} < 100$ MeV. Moreover, 6 out of the 8 missed events are located near the borders of the TPCs, especially near the downstream non-instrumented wall.

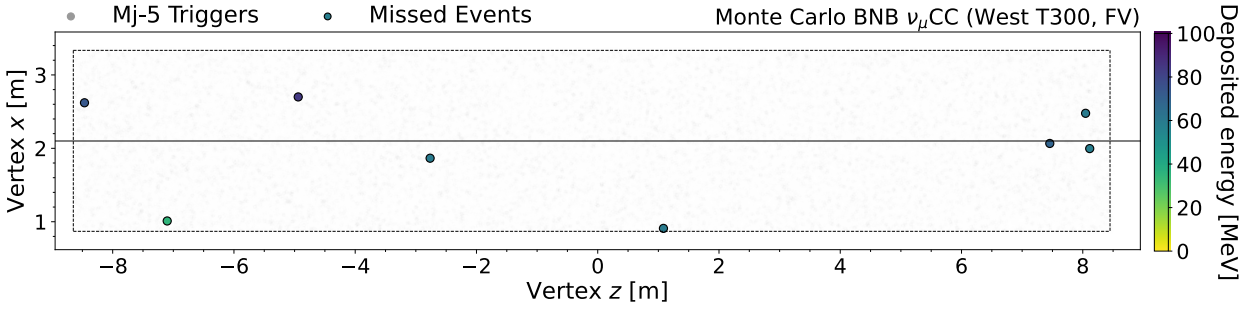

Figure 3.22: View of the West ICARUS T300 module from the top, with the cathode in the middle. Distribution of Monte Carlo BNB ν_μCC events vertices in the fiducial volume. The events that did not trigger the majority-5 are highlighted and colored with respect to their deposited energies.

Cosmic Muon Detection The aim of the trigger is primarily to ensure high efficiency for the detection of BNB and NuMI neutrinos. Indeed, it is also key to recognize the cosmic muons inside and outside of the beam gates and during the drift of ionization electrons in the TPC, to enhance cosmic background rejection in the data analysis. The predicted trigger efficiencies for Monte Carlo cosmic muons are reported in Figure 3.23, evaluated with respect to the deposited energy, the drift, and the longitudinal coordinates of the deposited charge barycenter in the TPC. The latter is used to quantify the average positioning of a cosmic muon track, and the tracks are selected to have the charge barycenter inside the West ICARUS T300 module[i].

The trigger configuration is set to the mj-5 and mj-10 conditions, the former guaranteeing an almost maximal detection efficiency for charged-current interactions in the fiducial volume with $E_{\text{dep.}} > 100$ MeV. As will be pointed out, the chosen configuration will have to yield manageable trigger rates from the point of view of the data acquisition. To avoid overcrowding the DAQ, a stricter majority-10 requirement is chosen for triggering on cosmic muons outside of the beam gates, within 2 ms wide window around the trigger.

Figure 3.23(a) shows the efficiency over the deposited energy for MC μ: the efficiency saturates at the $> 99\%$ level for energies higher than 400 MeV (200 MeV) for the mj-10 (mj-5) condition. Assuming cosmic muons to be Minimum Ionizing Particles (MIPs) and considering a stopping power of roughly $\mathrm{d}E/\mathrm{d}x \sim 2$ MeV/cm, the prediction translates into an almost maximal detection efficiency for muon tracks longer than $1.5 - 2$ m inside the TPCs.

Low energy non-triggering tracks are in fact muons crossing the active LAr for small lengths, e.g., across the detector's corners, as recognized in the trend of the efficiency with respect to the charge barycenter's drift coordinate, in Figure 3.23(b). The efficiency for the mj-5 is uniform at the 90% level, while with the mj-10 the mean trigger efficiency is roughly 77% and presents dips when the charge barycenter is close to the anode plane of the TPCs. The drop in efficiency is linked to tracks crossing the corners of the detector, and possibly to tracks being too close to the PMTs. The latter explanation implies that few PMTs collect most

[i] To localize the tracks in the West cryostat, the charge barycenter was computed considering only the portion of ionizing tracks contained in the same module, instead of the whole T600 detector.

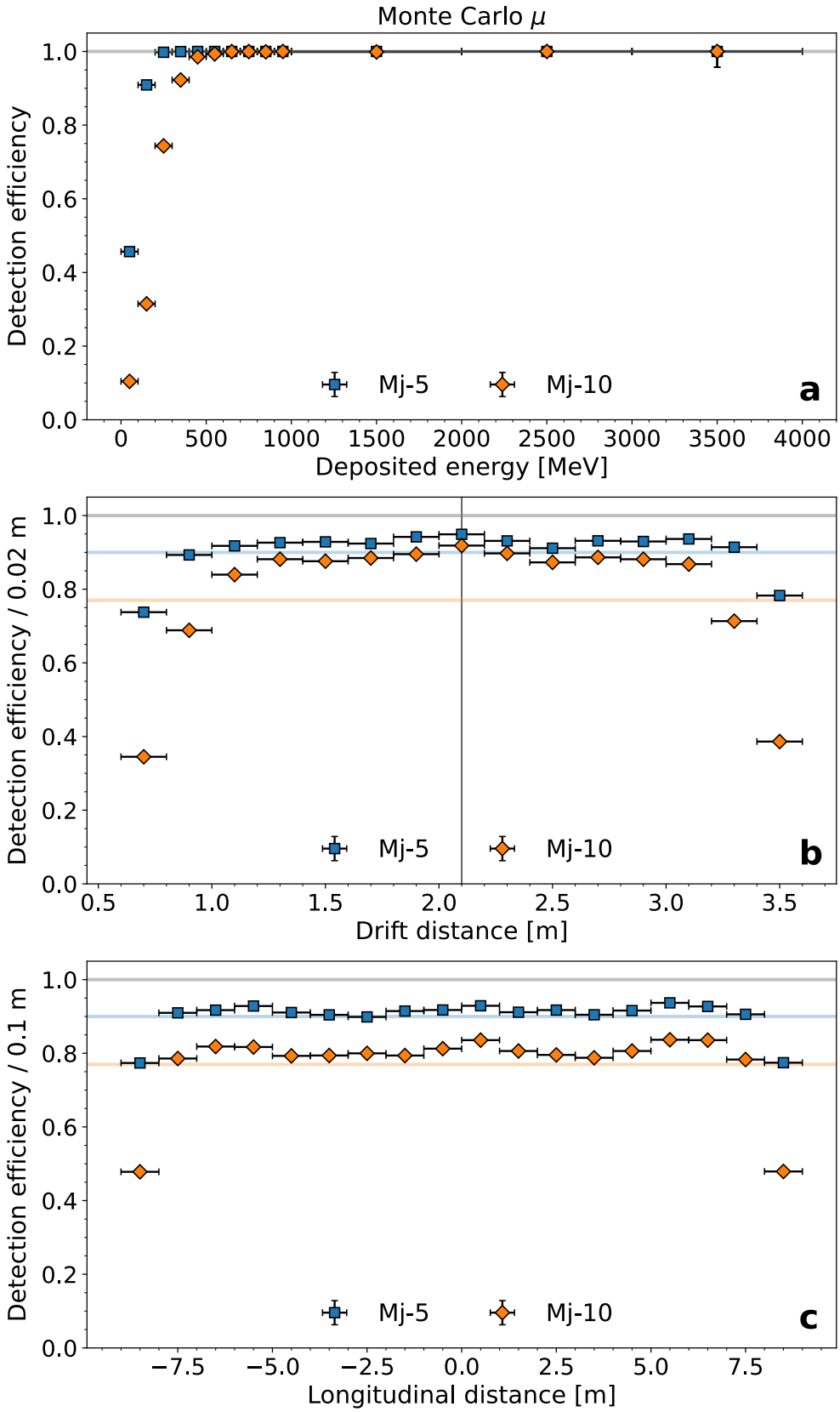

Figure 3.23: Trigger efficiency predicted with Monte Carlo cosmic muons, with respect to the deposited energy (a), drift (b), and longitudinal (c) coordinate of the tracks' charge barycenters. Energy bins are 100 MeV and 1 GeV wide. The vertical line in (b) represents the cathode. The average efficiencies for the two majority-5 and majority-10 settings are highlighted.

of the light, not meeting the mj-10 requirement. Similarly, along the longitudinal direction, the majority-10 efficiency presents dips near the upstream and downstream detector sides, not instrumented with PMT (Figure 3.23, c).

The localization of non-triggering μ events can be visualized from Figure 3.24, showing the distribution of tracks' charge barycenters in the West ICARUS T300 module with respect to their energies and confirming the previous considerations on the origin of missed events.

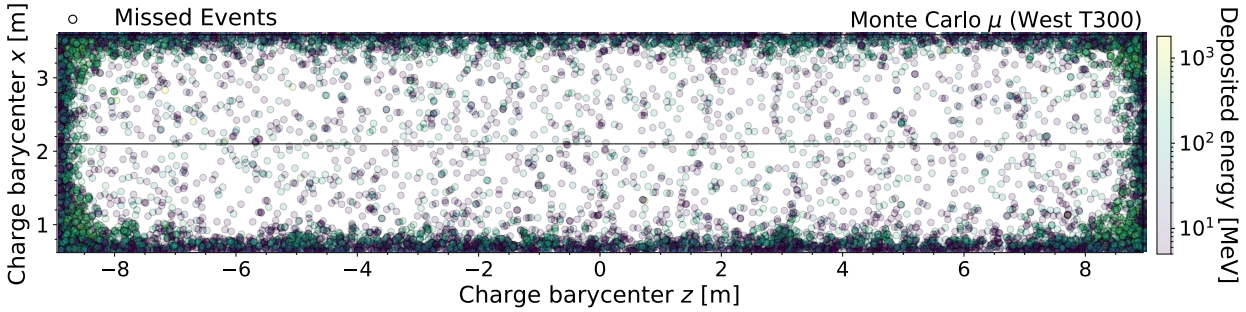

Figure 3.24: View of the West ICARUS T300 module from the top, with the cathode in the middle. Distribution of Monte Carlo μ charge barycenters. The events that did not trigger the majority-5 are highlighted and colored with respect to their deposited energies.

A visual representation of the relationship between track orientation and position of the charge barycenter is shown in Figure 3.25.

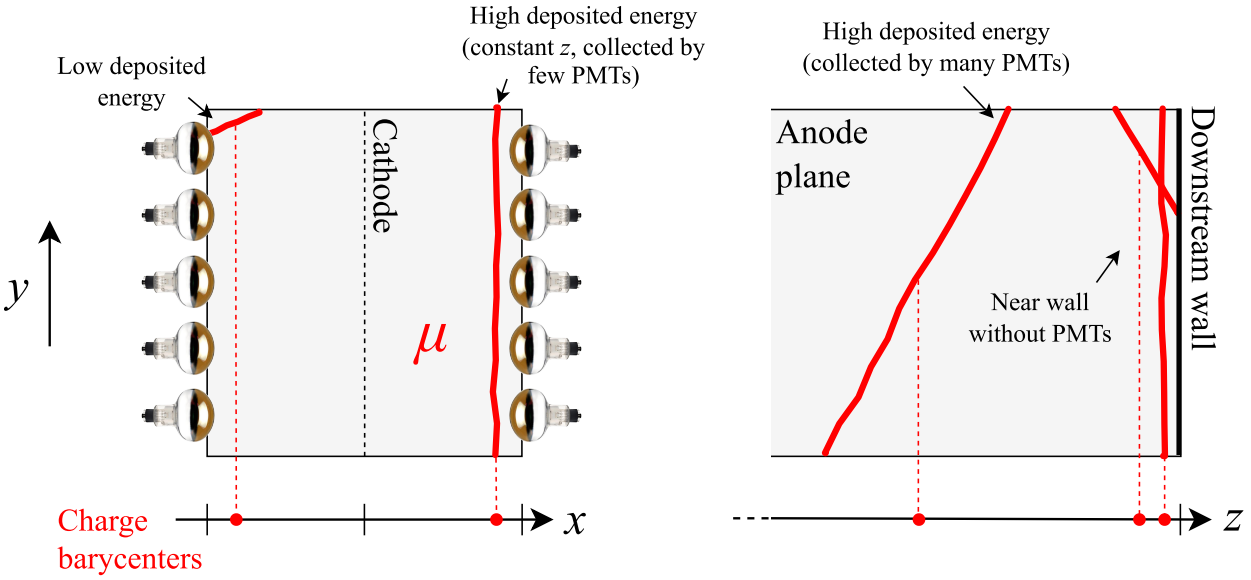

Figure 3.25: Visual representation of reconstructed muon tracks in the TPCs, with respect to their orientation and the position of the charge barycenters along the drift (x) and longitudinal (z) directions.

4

Performance of the Trigger System

This Chapter contains:

The ICARUS trigger was implemented according to the previous Monte Carlo calculations, which allowed to define a logic for the trigger FPGA boards, programmed within the LabVIEW environment to process the PMT LVDS signals in terms of a majority logic. During Run0 and Run1 the trigger exploited scintillation light detected in one of three 6 m longitudinal windows in coincidence with the beam gate. The trigger was then upgraded to use the sliding windows configuration with five overlapping 6 m longitudinal windows in Run2. Finally, a sample of cosmic muons was collected to measure the trigger performance.

4.1 The ICARUS Trigger Implementation

The neutrino event recognition is performed by looking for the required PMT majority in one of the two ICARUS T300 modules independently. As already discussed, each cryostat is divided into 6 m long slices containing 60 PMTs (or 30 LVDS lines) each: 30 PMTs are on the west TPC and 30 on the east TPC, front-

facing. On top of three windows slicing an 18 m long ICARUS T300 module longitudinally, there are two additional overlapped 6 m long windows positioned around the longitudinal center of a cryostat. PMTs are discriminated at a 13 PEs threshold and combined into 200 ns wide LVDS outputs: when at least 5 LVDS signals are present in one of the five sliding windows (majority-5), a "PMT-majority trigger" primitive is produced (Figure 4.1).

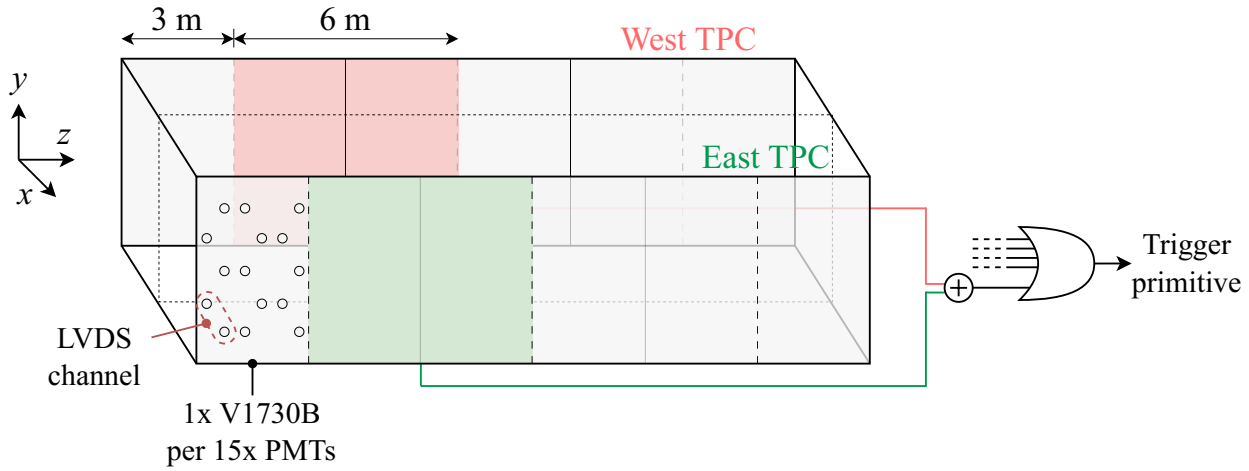

Figure 4.1: Schematic of one ICARUS T300 module and the 5 overlapping 6 m long windows. Each V1730B digitizer board covers 3 m) sections of each TPC, namely 15 PMTs. If the majority condition is met in at least one of the 5 front-facing windows, a PMT-majority trigger primitive is produced.

If the primitive is temporally coincident with the beam gate windows (2.2 μs for BNB and 10.1 μs for NuMI time windows, slightly enlarged to contain the beam spills), a global trigger is fired, activating the readout of each detector sub-system. The TPC is readout for $\sim$ 1.6 ms, covering the $\sim$ 1 ms drift time of ionization electrons in the drift field; PMT signals are recorded for 2 ms around the trigger time; CRT signals are recorded for 6 ms around the trigger time, to recognize and tag cosmic rays crossing the detector during the electrons' drift time.

There are different types of data streams (Figure 4.2):

- the "on-beam" trigger is the main physics trigger for ICARUS. The gate signal is synchronized with the beam spill and PMT waveforms are recorded in the 28 μs around the trigger time to fully cover the BNB and NuMI spill regions. In this case, data are recorded in both cryostats, even if the triggering signal refers to only one T300 module. Additionally, a majority-10[i] condition is used to acquire PMT waveforms with shorter 10 μs acquisition windows outside of the beam gate and in a 2 ms window around the global trigger ("out-of-time primitives"). Since there is no coincidence with any beam-related activity, primitives are used to record the scintillation light linked to cosmic ray activity during the electron drift time in the TPC;

- "off-beam" triggers work in a similar way, using an mj-5 condition to fire a global trigger, and registering 10 μs out-of-time primitives with a mj-10. In off-beam triggers, the gate signal is not synchro-

[i] The requirement may be lowered if the DAQ allows for an increased trigger rate.

nized with the neutrino beams' activity but is rather opened in between consecutive beam spills. One off-beam gate is opened for each on-beam gate, with no prescale.

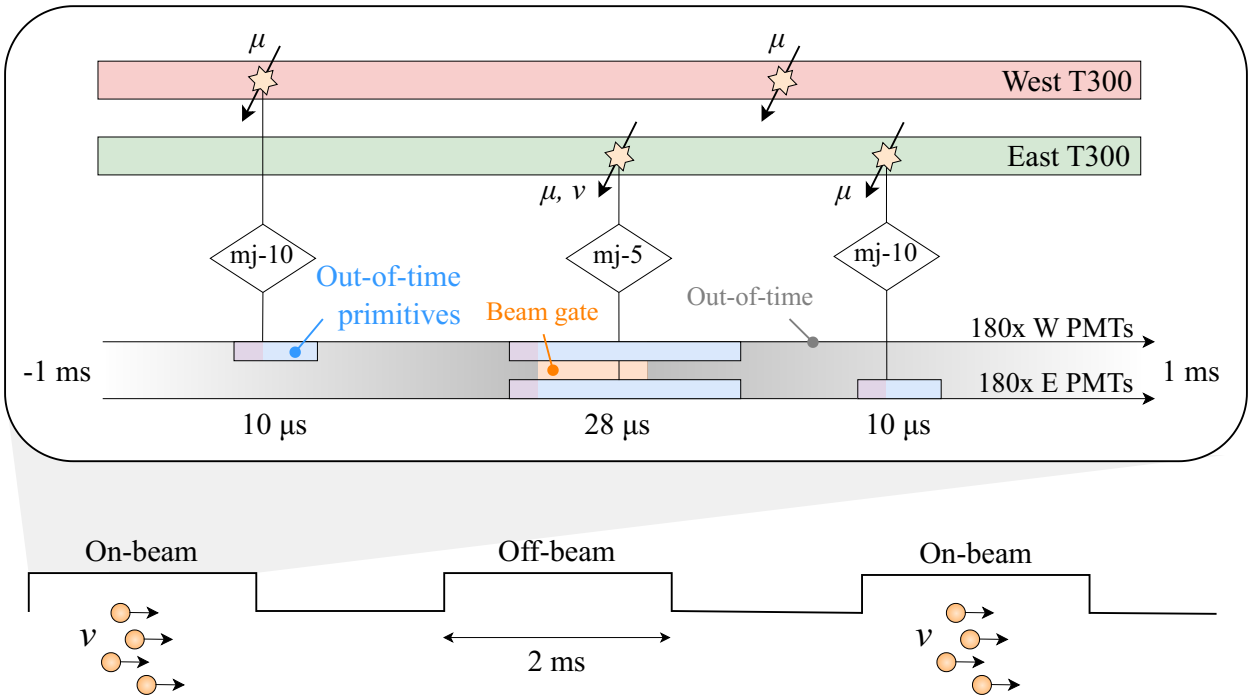

Figure 4.2: Summary of the ICARUS PMT-majority trigger menu. A global trigger is fired with the coincidence between a majority-5 logic and the beam gate, enabling waveform recording from both cryostats for 28 μs around the trigger time. Out-of-time triggers are generated with a majority-10 condition outside of the beam gate within 2 ms around the trigger time and are characterized by shorter 10 μs PMT waveform acquisition windows. In on-beam triggers, the beam gate is synchronized to the BNB and NuMI spills.

Minimum Bias Trigger Alternatively to the PMT-majority trigger, the Minimum Bias (MinBias) trigger allows the data acquisition without imposing any requirement on the coincidence of light. The MinBias trigger can be fired both synchronously with the beam and off-beam, as for the standard majority trigger. The events collected with a MinBias trigger can be used for timing purposes at detector activation, for simulation studies and to have an unbiased data sample for trigger efficiency studies.

The distribution of the trigger times with respect to the beam gate opening times for the on-beam and off-beam triggers in the ICARUS Run2 data are shown in Figure 4.3. The excess of beam-related events during the beam spills is visible on top of the off-beam baseline. The NuMI distribution also shows the underlying structure of the beam: the excess is split into 6 groups, linked to the 6 proton batches first accelerated by the Booster and later by the Main Injector, before being sent to the NuMI target.
The peak at the opening of the beam gates is referred to as "early light" peak, generated by the μs-long slow light component tail of cosmic rays traversing the detector before the beam gate. When a trigger gate is opened at a t_G time, if the signals of the late light from a muon that just traversed the detector are strong enough and meet the trigger requirements, a global trigger is fired at a time $t = t_G$. By using beam gates larger than the actual beam spill windows, the spill is fully preserved when subtracting off-beam from on-beam data.

The same mechanism occurs along the beam gates and is visible especially for NuMI (Figure 4.3, right). Inside the gate, the trigger may be fired from the accumulation of late light from previous cosmic rays, vetoing out any successive event within the same gate that may have met the trigger requirements. This effect gets stronger while considering times closer to the end of the gate, due to the bigger time window in which late light accumulates. The number of triggers hence slowly decreases due to the first triggers from late light in the gate vetoing out any successive ones.

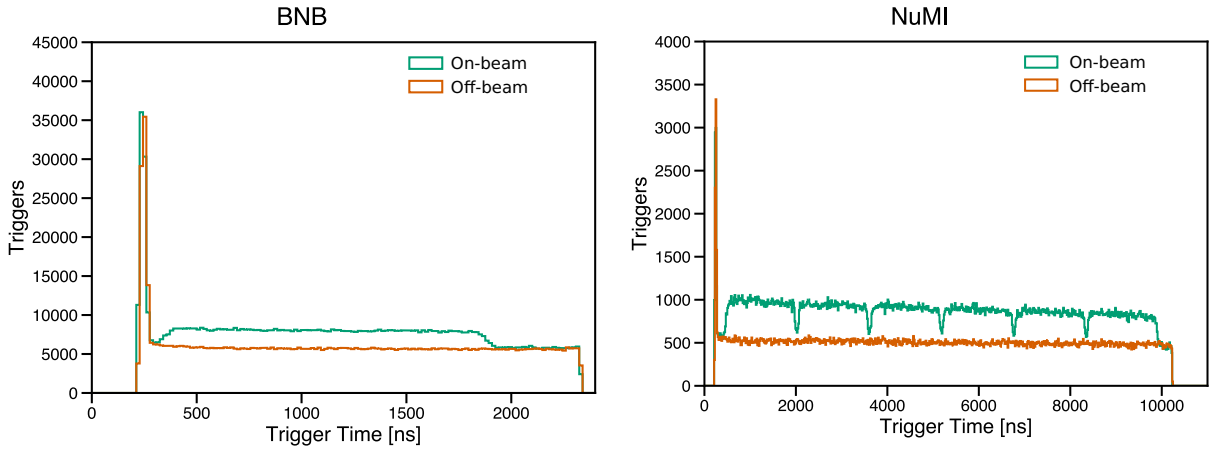

Figure 4.3: Distribution of the trigger times with respect to the BNB (left) and NuMI (right) gates opening times, for the PMT-majority beam and off-beam data streams in the ICARUS Run2 data (December 20th, 2022 - July 14th, 2023). The BNB and NuMI gates are respectively 2.2 μs and 10 μs, larger than the actual 1.6 μs and 9.5 μs beam spill windows.

The trigger rates for each data stream and neutrino beam, as calculated on the 39 hours-long run 8552 and scaled on the nominal BNB (4 Hz repetition rate, $5 \cdot 10^{12}$ POT per spill) and NuMI (0.83 Hz repetition rate, $6 \cdot 10^{13}$ POT per spill) specifications are reported in Table 4.1.

	Trigger	Gate Type	Prescale	Rate [mHz]
BNB	PMT-majority	On-beam	-	97
		Off-beam	-	64
	MinBias	On-beam	200	20
		Off-beam	20	200
NuMI	PMT-majority	On-beam	-	146
		Off-beam	-	75
	MinBias	On-beam	60	14
		Off-beam	20	42

Table 4.1: Trigger rates with the BNB and NuMI beam for the PMT-majority and MinBias triggers, computed on the 39 hours-long run 8552. The "prescale" factor indicates the number of PMT-majority triggers between consecutive MinBias triggers.

The "prescale" factor indicates the number of PMT-majority gates between consecutive MinBias gates. A total rate of approximately 0.7 Hz is estimated. The predicted cosmic ray rates with the out-of-time majority-10 condition are roughly 2.96 kHz and 2.67 kHz respectively for the west and east ICARUS T300 modules.

It is estimated by analyzing the data collected in spill with the mj-5, that about 3% of the beam proton extraction spills contain physical events, i.e. neutrino interactions and in-time cosmic muons. This means that the trigger system is rejecting non-physical events with a factor ~ 30, as roughly expected from Monte Carlo simulations.
This is a manageable data read-out bandwidth, and good operational stability was reported, with uninterrupted physics runs lasting from 1 day up to 5 consecutive days.

4.2 Event Reconstruction

The ICARUS reconstruction has to handle data coming from the three PMT, CRT, and TPC sub-systems. The ultimate goal is identifying and creating track or shower objects in the TPC from individual wire hits, matching them with scintillation light activity collected by the PMTs, and with hits on the CRT systems.

Optical Reconstruction The "optical reconstruction" aims at identifying the scintillation light activity in simulated or recorded PMT waveforms and building clusters of fired PMTs to be matched in time and spatially with events in the TPC and hits on the CRT.
The first step consists of a threshold-based signal-finding algorithm applied to single PMT channels: the baseline is estimated and subtracted from the waveforms, a signal region significantly above a low 0.5 PEs threshold is found, and the signal amplitude and integral are computed. The information on the reconstructed signals or "optical hits" for each PMT is stored in `OpHit` objects, where the time is defined as the point at which the signal crosses the threshold. The optical reconstruction then looks for spatial and time coincidences within a 40 ns window between the event `OpHits` and clusters them into "optical flashes", whose information stored in the `OpFlash` objects consists of light from a few to tens of involved PMT signals and the corresponding light barycenter (see subsection 3.2.1). The t_0 time of the optical flash is extrapolated from the distribution of `OpHits` times referring to the bin with the largest number of integrated PEs. After an optical flash is produced, there is a 1 μs dead time before the flash from another interaction can be detected. Ideally, all the light gathered by an optical flash should be produced by the same neutrino or cosmic ray interaction inside the TPC, localized in the longitudinal-vertical plane with the light barycenter and with time t_0 given by the reconstructed flash, from which the drift coordinate of wire hits can be reconstructed.

CRT Reconstruction The CRT reconstruction chain starts from CRT data fragments, formatting the raw data from each Front End Board (FEB) in terms of "hits". The CRT hits are reconstructed inside a single CRT module and later shifted to the coordinate system of the detector, by selecting channels with the highest PEs yield and using a coincidence logic specific to each CRT sub-system. For instance, in the Top-CRT each model consists of two orthogonally-oriented layers of scintillator strips, each one read by two SiPMs, and the coincidence between two scintillator bars from the two layers uniquely identifies a Top-CRT hit.
The spatial resolution for the CRT hits depends on the sub-system and on the region of the CRT. In general, considering a geometrical survey of the detector coordinates more accurate than 1 cm, the resolution mostly depends on the width of the scintillator strips and is around $\mathcal{O}(10\text{ cm})$.
Each CRT hit is associated with a timestamp, and timing calibrations and delay corrections are performed,

e.g., to account for the light propagation inside the plastic scintillator slabs from the hit position to the SiPM readout. Moreover, each CRT readout channel is individually calibrated in gain, and a number of PEs is associated with the CRT hit.

TPC Reconstruction The aim of the TPC reconstruction workflow is to build and identify particle objects in the detector and define the type of interaction in each event.
The anode plane in each one of the four ICARUS LArTPCs consists of three consecutive planes of wires, and each wire is read out as a single channel. The waveforms recorded from each wire are a convolution of the real charge-over-time signal with detector effects, e.g., the electric field and the electronics response. Therefore, a two-dimensional deconvolution over time and wire coordinate is performed, after the removal of coherent noise. The energy of the event is measured by the total charge from the last Collection wire plane. The deconvolved Induction-1 and 2 signals become unipolar for each wire plane and ideally reproduce the current of the ionization electrons cloud drifting to the anodic plane. This opens the possibility to extract some calorimetric information even from the Induction wires.
A dedicated algorithm identifies the Regions Of Interest (ROIs) for each wire waveform significantly above a threshold. By fitting the peaks in each ROI with Gaussian functions, it is possible to define "wire hits", namely objects containing the charge information through the hit area, and the hit time, defined as the time of the signal peak.
The substantial event rates expected at ICARUS highlight the need for an automated algorithm to match the hits in three wire planes and build track objects in the TPCs. ICARUS and the Short Baseline Neutrino program exploit the PANDORA pattern-recognition software, which applies a multi-algorithm approach with a combination of traditional and machine learning techniques [109]. The inputs to the PANDORA workflow are the reconstructed wire hits from the Induction-1, Induction-2, and Collection planes. The hits in each plane are organized as two-dimensional images or "views", representing an event in the active volume with the wire number on one axis and the time on the other (Figure 4.4).
Note that the x drift coordinate of the hits is common to the three views: the reconstruction exploits this redundancy to correlate and match topological features in different images into three-dimensional hits called "space points". The next step in the reconstruction is the identification of particle clusters among the reconstructed hits first in the 2-d. views and then on the matched space points, under the cosmic ray hypothesis, storing information in `Track` objects. The cosmic reconstruction is first used to process all the hits, and unambiguous cosmic ray candidates, based on their start and end positions, are flagged and removed from the event, and data is re-processed by beam-particle specific algorithms to look for both electromagnetic showers (stored in `Shower` objects) and `Tracks` to reconstruct the hierarchy of particle interactions, grouped in so-called "slices". The slices, containing a certain type of interaction, are identified with the help of dedicated algorithms based on topological event information.
Figure 4.5 shows the projected space points of an example ν_μCC event with resonant charged pion production, before and after the pattern recognition and particle identification steps. The output of the reconstruction contains information on the location of the three-dimensional neutrino vertex and then classifies "daughter" particles as `Track`-like or `Shower`-like. In charged-current interactions, the flavor of the neutrino is determined by the primary lepton, being a ν_μ for a daughter muon and ν_e for a daughter electron.

Particle identification is based on the reconstructed dE/dx (stopping power) of the particles, obtained from the collected charge from the wires with a mm-scale sampling defined by the pitch between reconstructed trajectory points.

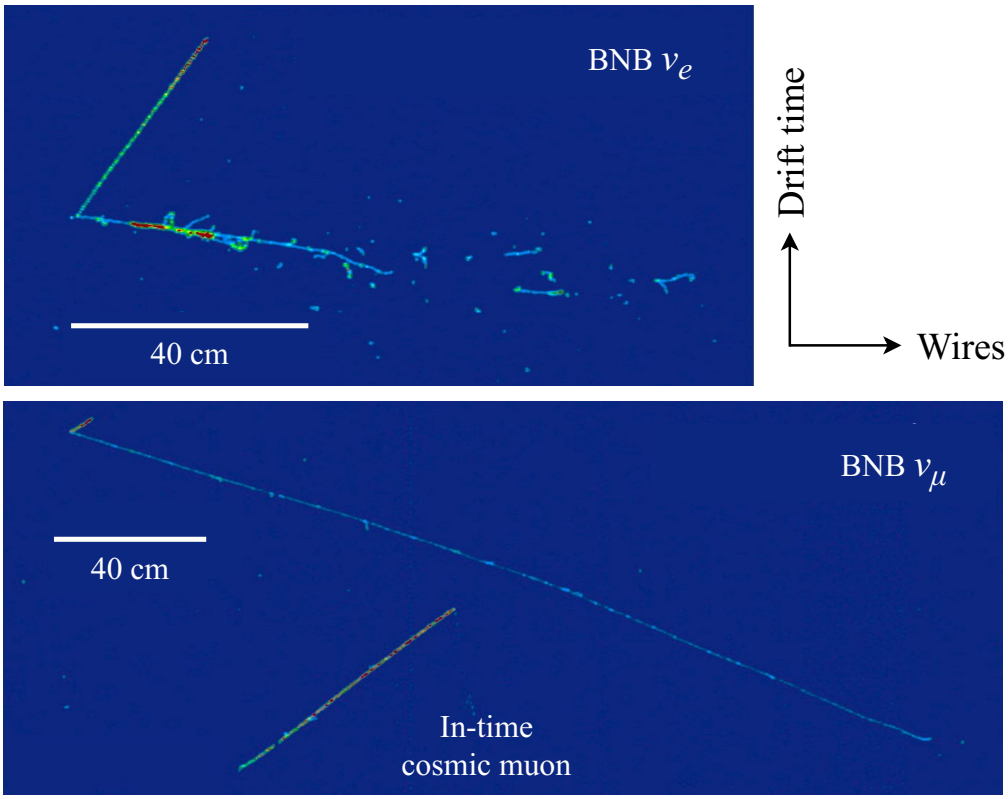

Figure 4.4: Examples of Collection views for two BNB ν_e and ν_μ charged-current quasi-elastic events.

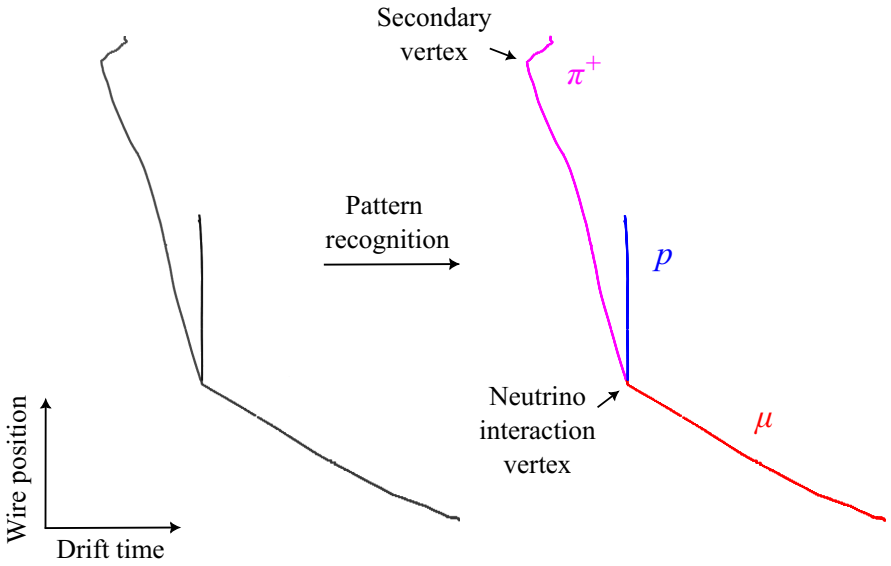

Figure 4.5: PANDORA reconstruction of a 1.1 GeV ν_μCC interaction with resonant charged pion production, before (left) and after (right) the pattern recognition step. The reconstructed particles are the muon, proton, and charged pion. Taken from [109].

4.2.1 Track Timing

The t_0 is defined as the time at which an ionizing track occurs in the TPC active volume, measured with respect to the global trigger. Assigning the t_0 time to each reconstructed cosmic track or interaction in the TPC is a crucial step to reconstruct the actual position along the drift coordinate in the event reconstruction, and in particular for the study of the trigger performance to account for the distance of tracks from the PMTs. The measured time of the i-th hit with respect to the trigger is a function of the track time and of the x drift coordinate, $t_i = t_0 + x/v_D$: by knowing t_0, the drift coordinate associated with each hit is determined. The track time can be accurately measured with the PMTs if the optical flash produced by the track can be matched to the object reconstructed by PANDORA in the TPC by the so-called "PMT-TPC matching" algorithm. Nevertheless, it could be challenging to unambiguously assign a unique t_0 time to each of the ~ 5 cosmic muons in each TPC snapshot. As an alternative, the TPC can measure with a precision of $\mathcal{O}(1\ \mu s)$ the t_0 of cathode-crossing tracks. This method is based on the fact that the PANDORA reconstruction assumes by default a $t_0 = 0$ time for a reconstructed track, presumed to be on time with the global trigger. In the case of a physical track not in time with the trigger and crossing the cathode plane, the drift coordinate reconstruction will produce two separate tracks in the two adjacent TPCs, shifted from the cathode by the same Δx, proportional to the proper t_0 track time and inversely proportional to the drift velocity v_D. The direction of the shift, which is an artifact of the reconstruction, is based on whether the physical track occurred before ("early track") or after ("late track") the global trigger time (Figure 4.6).

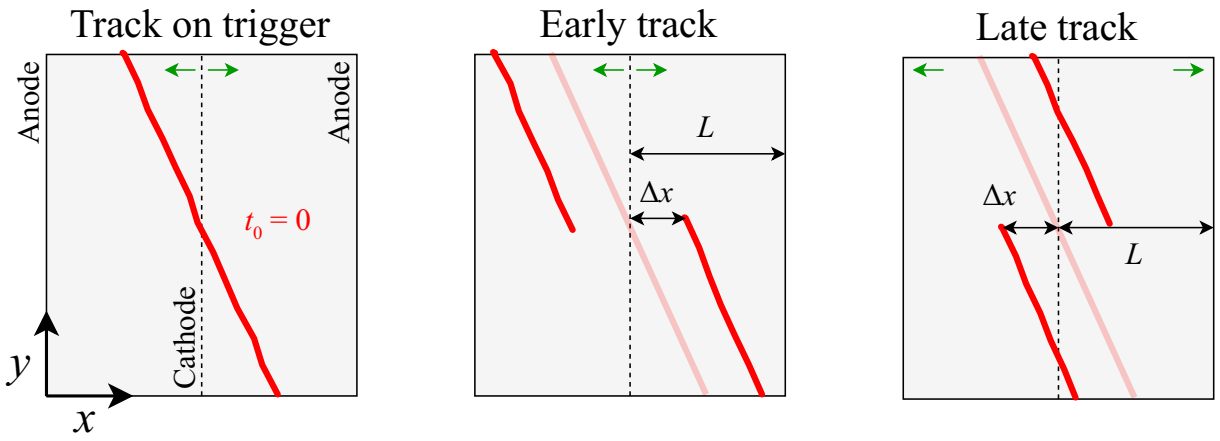

Figure 4.6: Representation of how the TPC is used to assign the t_0 time tag to cathode-crossing tracks. The TPCs are represented with respect to the drift x and vertical y directions. Tracks that are early or late with respect to the global trigger are split in the reconstruction and shifted by a Δx quantity from the cathode. View of an ICARUS T300 module from the drift-vertical plane. Green arrows indicate the drift field direction in each TPC.

To recover the physical track, PANDORA looks for collinear tracks that are shifted by roughly the same amount from the cathode, and stitches them back. With this procedure, the track time is also estimated through

$$t_0 = t^* - (L - \Delta x)/v_D \ , \tag{4.1}$$

with t^* being the largest hit time of the split track in a TPC (i.e., the time of the closest hit to the cathode),

$L \sim 1.5$ m the distance between the anode and cathode, Δx the distance between the cathode and the last hit, and $v_D \sim 1.6$ m/ms the drift velocity of electrons in the nominal 500 V/cm drift field. Note that 846 time-samples in the TPC readout are reserved for the "pre-sampling", namely the wires are readout ~ 0.34 ms before the trigger (recall the 400 ns sampling time for the TPC). To obtain the t_0 track time with respect to the trigger, the pre-sampling time has to be subtracted.
Indeed, limiting the cosmic muon data sample only to cathode-crossing tracks hinders the phase space of the exploitable cosmic muons and biases the evaluation of the trigger efficiency. In this work, the CRT is exploited to assign the time to cosmic tracks.

4.2.2 CRT-TPC Matching

As previously mentioned, the TPC reconstruction software assumes the reconstructed tracks to be on time with the trigger, leading to tracks with a shifted drift position when early or late with respect to the trigger. In the "CRT-TPC matching" algorithm, the time of the tracks is found by matching them with hits in the CRT, which have a well-defined timestamp corresponding to when the particle crossed the CRT module. Initially, the algorithm defines the window of "allowed" track times, namely the minimum and maximum t_0 times so that the shifted track remains within the TPC. For instance, consider a track that does not cross the cathode as in Figure 4.7. If x_C and x_A are the distance between the track with respect to the cathode and anode planes respectively, it holds that

$$t_0^{\min} = \min(x_C,\, x_A)/v_D\ , \quad t_0^{\max} = \max(x_C,\, x_A)/v_D\ , \tag{4.2}$$

where $v_D \sim 1.6$ m/ms is the electron drift velocity.
All the CRT hits in the $(t_0^{\min},\, t_0^{\max})$ time range are considered. For each CRT hit with a t time, the track is shifted along the drift direction by $\Delta x = -v_D \cdot t$. The algorithm considers for each track two vectors defined by the local direction from the start and the end points of the track, by linearly fitting its first and last hits. The Distance of Closest Approach (DCA) is then calculated as the distance between the CRT hit and the lines projected from the local start and end directions, and the smaller DCA between the two is considered, since it may happen that PANDORA inverts the direction of the reconstructed track.
Once a match between the track and a CRT hit with time t is found, the track gets assigned the time $t_0 = t$.
Note that some basic selections are applied before carrying out the DCA calculation, considering only tracks with a length higher than 20 cm in the TPC, and CRT hits with more than 60 PEs, with a maximum spatial uncertainty of 20 cm.

4.3 Trigger Efficiency Measurement with Cosmic Muons

The trigger efficiency has been evaluated on data by using MinBias runs, for which there is no request on the scintillation light, and data is collected at every beam gate opening. In this way, an unbiased sample of cosmic muons selected with the CRT-TPC matching is obtained and the trigger logic software emulated considering the recorded PMT waveforms, reproducing the hardware PMT-majority trigger chain. Specifically, special MinBias runs were collected by using the BNB off-beam data stream and a PMT readout window at

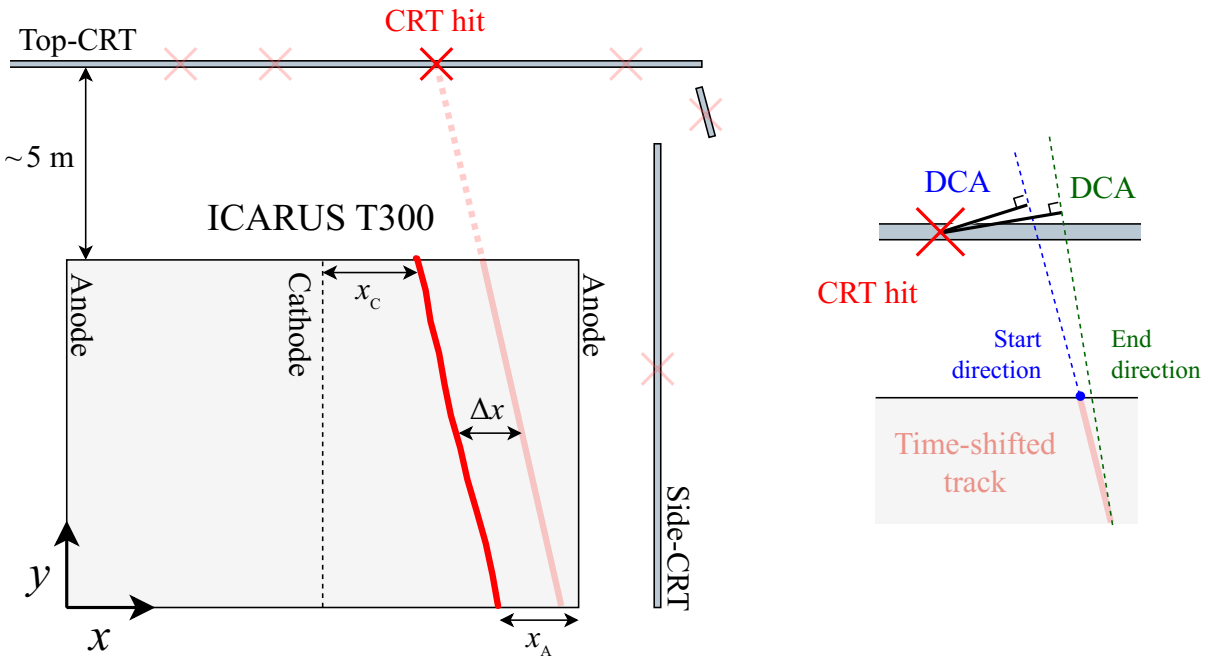

Figure 4.7: Representation of the CRT-TPC matching algorithm. The reconstructed track is matched with a CRT hit with a certain time, which is used to define the track t_0. The matching is based on a Distance of Closest Approach (DCA) calculation. The TPCs are represented with respect to the drift x and vertical y directions. Not to scale.

the time of the trigger enlarged from 28 μs to 166 μs, in order to enrich the event sample.

Approximately 50 hours worth of data were processed, and 526,440 (513,724) cosmic tracks were recorded in terms of CRT, TPC, and PMT signals in the west (east) T300 module. The number is roughly compatible with the expectation for a 166 μs PMT readout window, a $\sim$ 10 kHz cosmic ray rate in the ICARUS T600 detector, and a 4 Hz gate rate.

Figure 4.8 (left) shows the distribution of the CRT-matched tracks with respect to the CRT region the hit belongs to, without any selection. The Top-CRT is crossed by 76% of the tracks (in agreement with expectations), subdivided on the horizontal Top-CRT (64% of the tracks) and in the west, east, south, and north rim Top-CRT (12% of the tracks); 23% cross the eight Side-CRT regions (respectively, the three sections of the west and east walls, south, and north). Note that the west wall of the Side-CRT is close to the West T300 module, resulting in more tracks matched with its CRT hits with respect to the more distant east Side-CRT wall. The north Side-CRT wall has fewer matched tracks due to the higher CRT-hit threshold used to mitigate the larger electronic noise induced from the close cryogenics (recall Figure 2.8).

The distribution of the Distance of Closest Approach (DCA) between the reconstructed track and the matched CRT hit is reported in Figure 4.8 (right), where the matching algorithm is designed to accept DCA values < 2 m. Considering the actual spatial resolution of the CRT hits reconstruction and the ~ 5 m distance between CRT and the active LAr volume, a match between a track and a CRT hit can be considered reliable when DCA < 30 cm, i.e., selecting the peak of the DCA distribution. While the Top-CRT is primarily linked to well-matched tracks with 44% of the tracks below the DCA threshold, the Side-CRT distribution is flatter, and only 20% of the corresponding tracks are selected, due to the lower average spatial

resolution associated with Side-CRT hits.

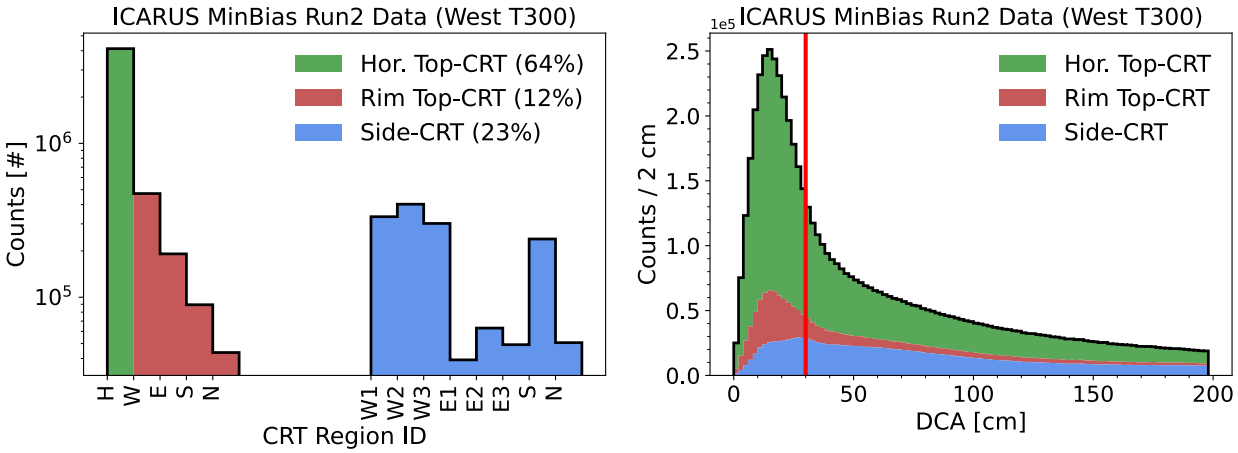

Figure 4.8: (left) Distribution of tracks with respect to the CRT region ID, respectively for the Horizontal and rim Top-CRT (West, East, South, and North portions), and for the Side-CRT (three West and East sections, South and North walls). (right) Distribution of the Distance of Closest Approach (DCA) as computed from the CRT-TPC matching, with no selection on the tracks and stacked with respect to the CRT region. A selection cut for DCA < 30 cm is shown.

Track Timing The distribution of the t_0 track times from the CRT-TPC matching with DCA < 30 cm is shown in Figure 4.9. As previously mentioned, the CRT is read out for 6 ms around the global trigger, set for reference at zero. The CRT-TPC matching algorithm loops over the collected CRT hits inside this time window and matches them to reconstructed TPC tracks, assigning them a t_0. The time distribution of CRT-TPC matched tracks that cross the cathode matches as expected the distribution related to the "TPC-only" timing technique (recall that PANDORA can assign a t_0 to tracks crossing the cathode between adjacent TPCs, see subsection 4.2.1). With the TPC-only method, $\sim 20\%$ of all the tracks were assigned a definite time, but their phase space is limited because they have to cross the cathode. Recall that the TPC is read out for 1.64 ms to cover the ~ 1 ms drift of ionization electrons after the global trigger, with a pre-sampling time of 0.34 ms. The time interval of cathode-crossing tracks is defined by the fact that the crossing point is observed if the corresponding hit time $t_C = t_0 + L/v_D$ is within the TPC readout window $[-0.34,\ 1.3]$ ms, with $L \sim 1.5$ m drift length. This translates into a constraint on the cathode-crossing track times, $t_0 \in [-1.28,\ 0.36]$ ms.
Indeed, the CRT-TPC matching may miss some of the tracks that were available through the TPC reconstruction, but does not introduce a significant bias on their orientation and yields a larger sample overall. Note that the difference in the number of TPC-tagged and cathode-crossing CRT-matched tracks arises from the fact that not all the cathode-crossing tracks are necessarily matched to a CRT hit, especially when selecting a strict DCA < 30 cm condition.
The dip in the cathode-crossing and TPC-only distributions is an artifact of the TPC reconstruction software, which tries to match collinear tracks split at the cathode to shift them from the trigger time. If the algorithm is too aggressive, more tracks than expected get shifted from zero. Moreover, PANDORA assigns a t_0 by default only to unambiguous cosmic `Tracks`: if a `Track` is tagged as possibly belonging to a neutrino event, it does not have a t_0.

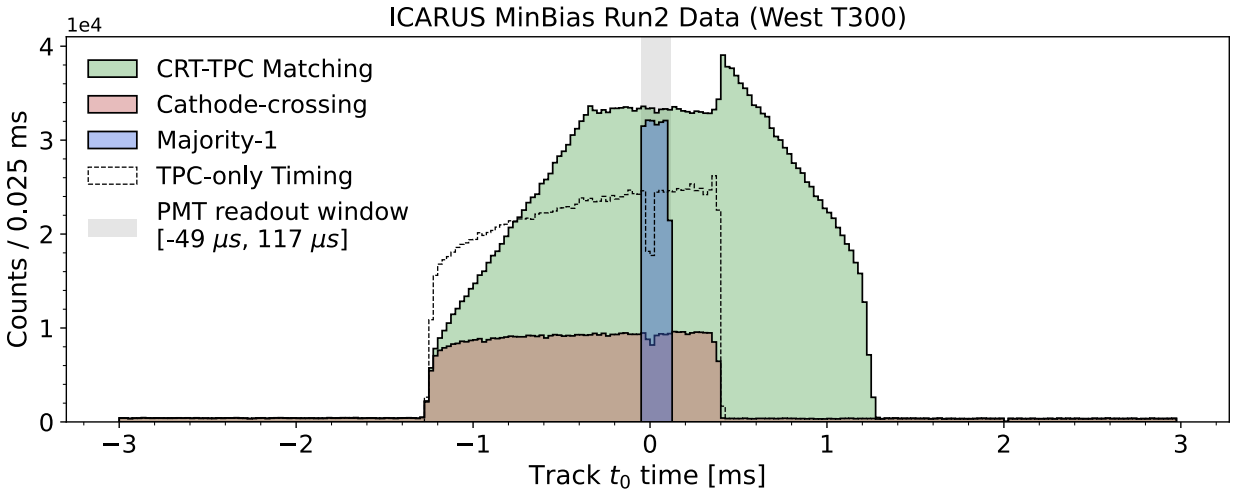

Figure 4.9: Time distribution of cosmic tracks from MinBias Run2 data. The CRT-TPC matching algorithm includes tracks with a DCA lower than 30 cm. Cathode-crossing tracks and majority-1 triggering tracks are selected from the CRT-TPC matched sample. The dashed histogram shows the distribution of times assigned by PANDORA to cathode-crossing tracks ("TPC-only timing").

To explain the time distribution of CRT-TPC matched tracks in Figure 4.9, consider that an ionization electron at the cathode is readout if the corresponding wire hit time $t_C = t_0 + L/v_D$ is within the TPC $[-0.34,\ 1.3]$ ms readout window, with $L \sim 1.5$ m drift length, while an ionization electron at the anode is readout if its hit time $t_A = t_0$ is within the TPC window. The two conditions have to be combined to read out a track that crosses both the anode and the cathode, yielding a constraint on the track time, $t_0 \in [-0.34,\ 0.36]$ ms, where the time distribution is flat. Outside of this window, the readout of anode-to-cathode tracks gets problematic:

- for tracks occurring before the TPC pre-sampling, $t_0 < -0.34$ ms, the TPC readout misses the first ionization electrons, hence the reconstructed track points closer to the anode planes (Figure 4.10, left). While the t_0 decreases, the reconstructed track gets shorter, and the CRT-TPC matching more challenging, hence the decrease in the statistics of the time distribution in Figure 4.9;

- for tracks occurring after ~ 0.36 ms, the TPC readout window is closed before the last ionization electrons (closer to the cathode) are able to arrive at the anode plane, and the physical tracks are split in the readout (Figure 4.10, right). The consequences are that tracks that are not stitched back by PANDORA are double-counted, hence the spike in the time distribution (Figure 4.9), and that the higher is the t_0, the wider the gap between the split tracks, hence fewer tracks are matched with the CRT.

A visual representation of the link between track t_0 time and the average TPC readout buffer is provided in Figure 4.10.

Finally, a selection on the tracks triggering at least one LVDS channel ("majority-1") is made to highlight the time window compatible with the PMT readout, going from -49 μs through 117 μs, which is the region of interest for studying the trigger response from collected PMT waveforms.

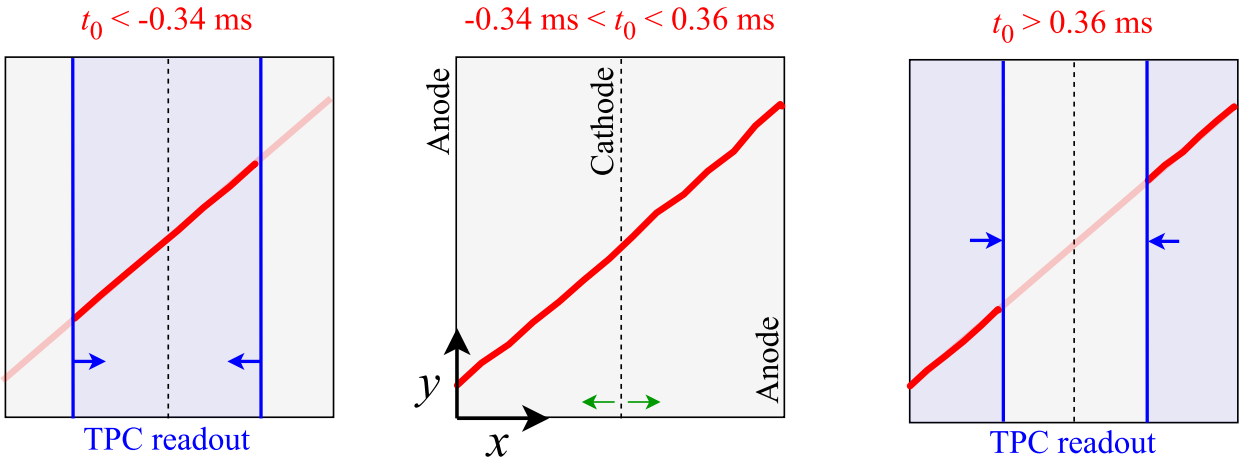

Figure 4.10: Representation of the link between the TPC readout window and the track t_0 time for anode-to-anode track. The track on the left occurs before the TPC pre-sampling, and the first ionization electrons close to the anodes are missed. For the track on the right, the TPC readout window closes before the last ionization electron (close to the cathode) are able to reach the anode plane. View of an ICARUS T300 module from the drift-vertical plane. Green arrows indicate the drift field direction in each TPC.

The CRT-TPC matching can be validated by comparing track-by-track the times of CRT-matched cathode-crossing tracks to the times assigned by the TPC reconstruction (Figure 4.11).

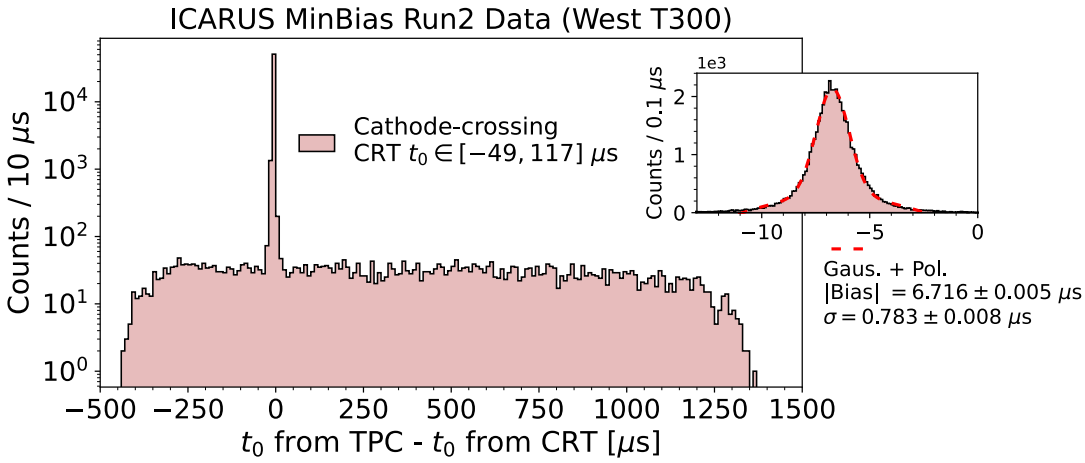

Figure 4.11: Difference between the time from the CRT-TPC matching and the time from the TPC reconstruction for tracks having the CRT time between the PMT readout window. The peak in the inset was fitted with a Gaussian plus polynomial function, and a 6.7 μs bias between the CRT and TPC track timings was found. The peak contains $\sim$ 90% of all the cathode-crossing tracks.

Note that $\sim$ 90% of all the cathode-crossing tracks are contained within $\pm 3\sigma$, as derived from the Gaussian fit of the peak (Figure 4.11, inset). A bias value of $\sim$ 6.7 μs is observed, which requires further investigation, even if it does not impact the present analysis. In fact, considering the nominal drift velocity $v_D \sim 1.6$ mm/μs, a $6-7$ μs time bias of the CRT with respect to the TPC corresponds to a $\Delta x \sim 1$ cm shift for the track along the drift direction, having an overall sub-percent effect in the 1.5 m long TPC drift. Tracks that are farther from the peak are either wrong matches of tracks in the TPC or wrong associations

of reconstructed tracks to CRT hits.

Trigger Emulation The trigger emulation is based on the CRT-assigned time of the reconstructed tracks within the PMT readout window, to reproduce from the measured PMT waveforms the PMT-majority trigger chain and determine whether the track met the trigger requirements or not. The trigger is emulated inside a gate ("trigger gate") opened around the t_0 time of a track.

This gate width is tuned around the track times as extracted from the CRT-TPC matching: the longer the trigger gate, the higher the probability that accidental triggers are fired. For instance, if there are two tracks within the same gate, the emulation may assign the trigger time to both, even if only one of them would have fired the trigger by itself. Initially, a large 20 μs trigger gate was being considered around each track time. The introduction of the CRT-TPC matching algorithm allowed to evaluate the timing of tracks more reliably, not depending exclusively on the TPC reconstruction algorithm of cathode-crossing tracks. As a result, the trigger gate was optimized by scanning possible time intervals on mj-5 triggering tracks around the track time from the CRT-TPC matching and looking for the smaller gate that preserves most of the tracks (Figure 4.12).

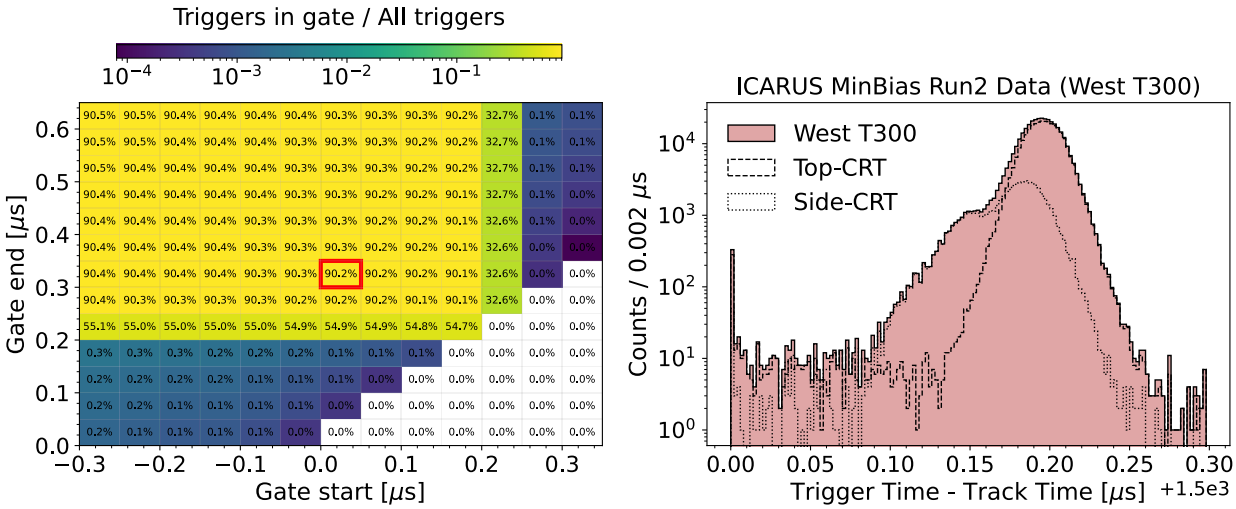

Figure 4.12: (left) Scan of the start and end limits for the trigger gates with 0.05 μs steps, evaluated on the distribution of trigger times with respect to track times. The optimal configuration is highlighted. (right) Distribution of mj-5 trigger times with respect to the track times with the tuned emulation trigger gate. Note that in the emulation the global trigger is associated to a fixed 1500 μs offset.

Figure 4.12(left) shows the result of the scanning procedure: a 300 ns emulation window was chosen to preserve the peak related to genuine triggering tracks and at the same time resolve the early light peak with no overlaps to the peak of interest. The resulting distribution of mj-5 trigger times with respect to the track times (Figure 4.12, right) shows that the trigger digitization occurs roughly $100-300$ ns after the t_0 of a triggering track in the TPC volume. The double peak structure indicates the presence of tracks entering or exiting the detector, matched to the different vertical walls of the Side-CRT, at different times with respect to the scintillation light flash that generated the trigger. In fact, the distribution of the previous events reported as a function of the difference Δt between the triggering PMT light flash time and the track t_0 (Figure 4.13)

shows the presence of three distinct event components:

- tracks entering from the Top-CRT, producing a triggering flash and leaving the detector volume, with $\Delta t > 0$ μs (major component);
- tracks entering through the Side-CRT, producing a flash and leaving the detector ($\Delta t > 0$ μs);
- tracks matched with Side-CRT while exiting the detector volume after having produced a PMT triggering flash ($\Delta t < 0$ μs).

The two peaks in the Side-CRT event distribution appear to be centered around the zero, with the $\Delta t > 0$ peak more populated than the other. This asymmetry is related to the detector position in the pit, and to the fact that only the west T300 module is being considered, to which the west Side-CRT is very close (see Figure 4.13, right). On the other hand, the east Side-CRT wall is much more distant, and tracks crossing it and reaching the west T300 module are suppressed, as already shown in Figure 4.8.
The Side-CRT covers almost all the $\sim$ 5 m space between the Top-CRT and the TPC. While tracks entering the detector volume can cross the whole Side-CRT, downward-going exiting cosmic muons producing an ionizing track in the TPCs may cross only a more limited portion. Finally, the overburden is by construction less thick near the rim Top-CRT, slightly increasing the number of entering muons.

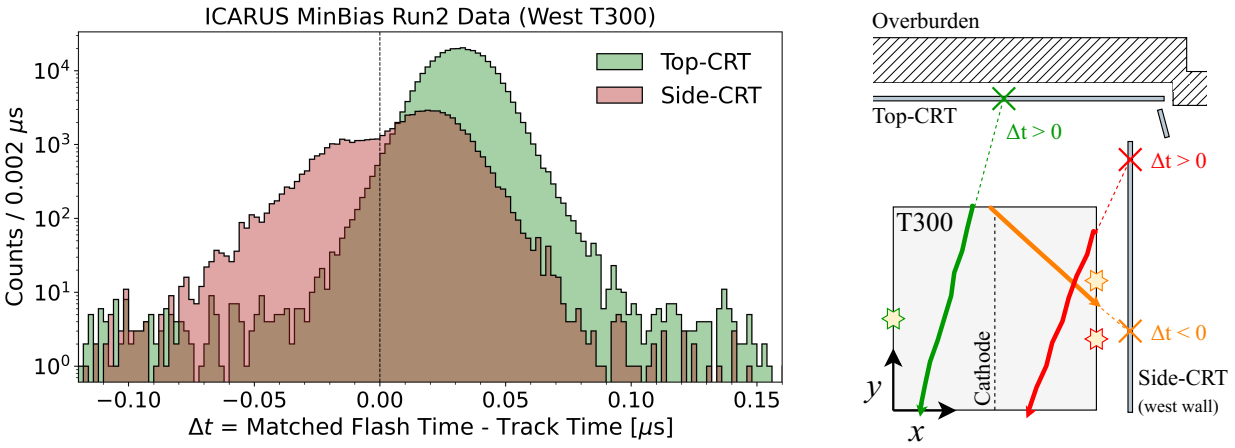

Figure 4.13: (left) Distribution of light flash times with respect to mj-5-triggering track times, for track crossing the Top and Side-CRT. Each flash is matched to each track by time. (right) Visual representation of tracks being tagged by the CRT while entering or exiting the detector. Matched PMT flashes produced by tracks are drawn. Not to scale.

4.3.1 Energy Calibration

The TPC reconstruction software provides for each track the matched three-dimensional hits, along with the deposited charge per unit length $\mathrm{d}Q/\mathrm{d}x$, in which $\mathrm{d}Q$ is the area of the Gaussian fit to the wire hits measured in ADC (1 ADC $\sim$ 82 e^-), and $\mathrm{d}x$ is the wire pitch. By calibrating the deposited charge, it is possible to obtain the stopping power $\mathrm{d}E/\mathrm{d}x$ for each track with a mm pitch. The fine-sampling calorimetry is one of the key advantages of the LArTPC technology, enabling the stopping power reconstruction for ionizing particles in the liquid argon, from which the particles can be identified. The particle energy can be

reconstructed with a $\mathcal{O}(3-5\%)$ resolution, depending on the particle type, event topology, and energy. The detection of charge in ICARUS is not perfectly uniform in space and time. Two key calibrations are applied to evaluate the track energy in this work.

Electron Lifetime Ionization electrons drifting toward the wire planes can be absorbed by electronegative impurities in the liquid argon (e.g., O_2, H_2O, CO_2) [110], reducing the signal collected at the TPC wires. The equalization along the drift direction is performed by considering the attenuation of the charge signal as a function of the electron drift distance, for cosmic muons crossing the whole TPC drift volume. Clean straight muon tracks with drift times longer than 600 μs are selected for the procedure. The $\mathrm{d}Q/\mathrm{d}x$ ionization charge is measured as the area of the signal on each Collection wire. A linear fit of the logarithm of the hit areas as a function of the drift time along the track provides an estimation of the attenuation associated with the selected track. The Gaussian distribution of the track attenuation for the whole muon sample provides a unique attenuation value, $\lambda = 1/\tau$, from which an effective electron "lifetime" τ in the LAr propagation is extracted. An in-depth description of the procedure can be found in [85]. The electron lifetime is computed for single DAQ runs, usually lasting a few hours to a few days, and the overall trend with respect to the ICARUS physics runs is shown in Figure 4.14.

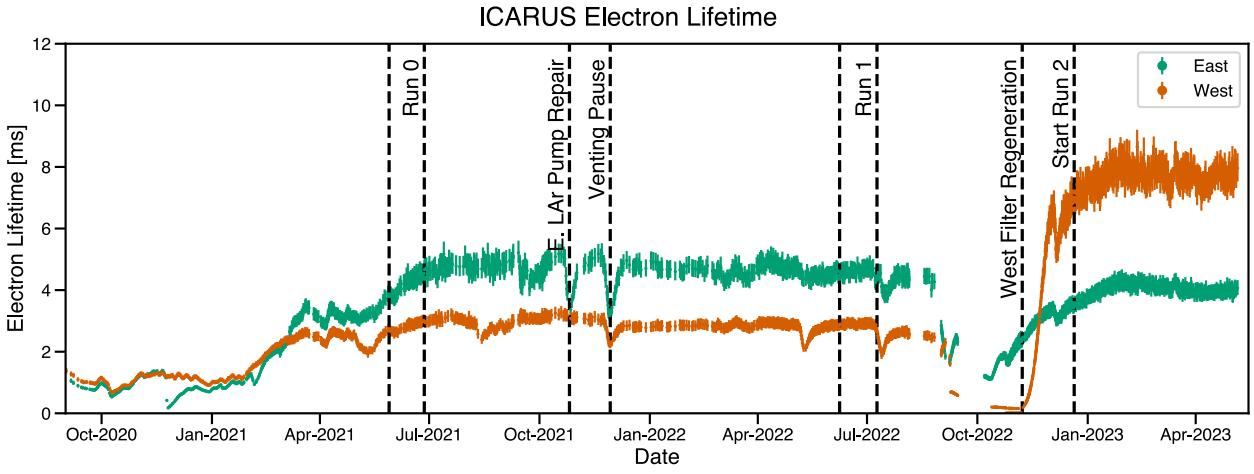

Figure 4.14: Effective electron lifetime as measured in the T300 modules across Run0, Run1, and Run2.

Space-charge Effect While ionization electrons produced by cosmic rays drift toward the anode with a $v_D \sim 1.6$ mm/μs velocity, more massive ions move slowly toward the cathode at $\sim 5 \cdot 10^{-6}$ mm/μs, leading to an accumulation of positive ions at the cathode ("space-charge") affecting the electric field at the percent level [111]. The space-charge effect has two main consequences: it affects the electron-ion recombination rate since the latter depends on the drift field intensity, and field distortions may deflect ionization tracks and bias the dx pitch reconstruction. In addition, small deviations of the TPC central cathode from planarity also induce small distortions in the drift field In practice, data-driven two-dimensional yz field distortion maps are provided to equalize the charge response.

In this work, the energy is calibrated track-by-track from the hits information. The $\mathrm{d}Q/\mathrm{d}x$ is obtained hit-by-hit as the integral of the wire hit measured in ADC over the pitch measured in cm. The space-charge

equalization is applied, and the stopping power is obtained for the i-th hit as

$$\frac{\mathrm{d}E_i}{\mathrm{d}x} = \frac{\mathrm{d}Q_i}{\mathrm{d}x} \cdot \exp\left(\frac{t_i - t_\mathrm{A}}{\tau}\right) \cdot \frac{W_\mathrm{ion} \cdot C}{Q} \,, \tag{4.3}$$

where t_i is the i-th wire-hit's peak time, the time at the anode t_A is extracted by adding the track time from the CRT-TPC matching to a constant 846 time-samples offset, τ is the electron lifetime (in the selected runs, $\tau \sim 7$ ms in west T300, see Figure 4.14). The C factor calibrates the charge in ADC to the number of ionization electrons (in the West T300 module, $C \sim 82$ e$^-$/ADC), $W_\mathrm{ion} \sim 23.6$ eV is the ionization potential in liquid argon, $Q \sim 0.7$ accounts for the recombination effect in LAr and holds for MIPs in TPCs at the nominal drift field [83]. Finally, the energy for a track can then be obtained as

$$E = \sum_i \mathrm{d}x_i \cdot \frac{\mathrm{d}E_i}{\mathrm{d}x} \,, \tag{4.4}$$

with i spanning through each reconstructed hit of the track.

The calibration procedure was validated by checking the $\mathrm{d}E_i/\mathrm{d}x$ distribution for single reconstructed tracks in the TPC. The distribution is then fit with a Landau function convoluted with a Gaussian to account for the detector effects. The compatibility between the fit MPV and the expected ~ 2 MeV/cm stopping power for a MIP muon in liquid argon is checked. An example is reported in Figure 4.15, showing the calibrated energy depositions for a 3.3 m long muon track in the west TPC of the west T300 module. Figure 4.15(right) shows an event display of the selected track.

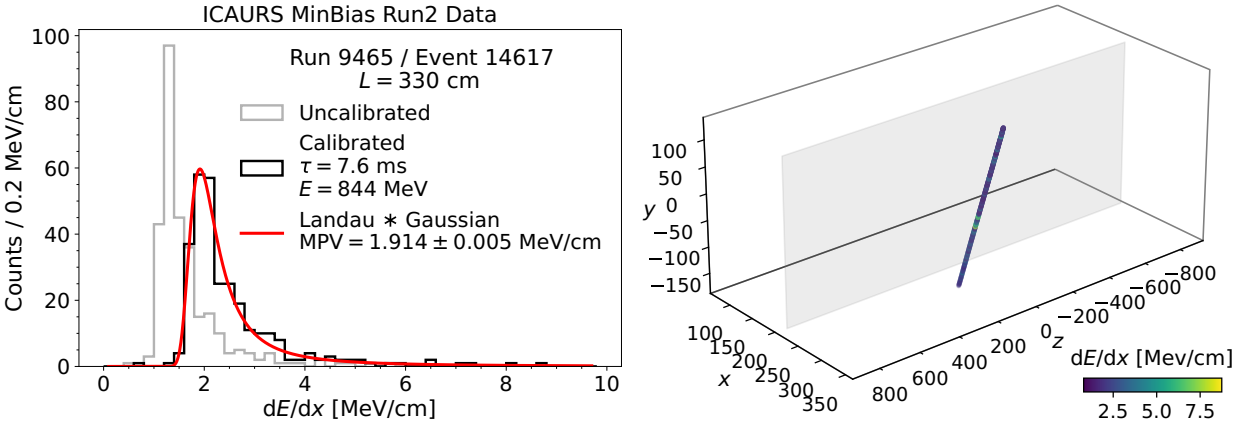

Figure 4.15: (left) Distribution of hit-by-hit energy depositions for a 3.3 m track calibrated according to Equation 4.3, accounting for recombination and for the electron lifetime against electronegative impurities. The MPV from the Landau-Gaussian fit is compatible with the expected stopping power of a MIP muon in liquid argon. (right) Event display of the same calibrated track, contained in the WW TPC. The cathode is drawn in the middle of the west T300 module. Units are in cm.

4.3.2 Event Selection

As already anticipated, the collected cosmic muon sample is processed with the CRT-TPC matching, requiring DCA < 30 cm to ensure the quality of the matching. This is crucial to obtain cosmic muon tracks with

a reliable t_0 time since the trigger software emulation is based exclusively on the track time to determine whether a track is able to trigger, starting from the collected PMT signals. Since the emulation is based on the measured PMT waveforms, the track time has to be compatible with the PMT readout window, hence $t_0 \in [-49, 117]$ μs is requested (recall Figure 4.9).

Track Splitting In the analysis of the collected data, some of the tracks are split by the TPC reconstruction algorithm, and particle showers are mislabeled as tracks, contaminating the sample. This can happen, for instance, in the presence of unresponsive channels in the wire readout, where the corresponding track will have missing hits in the reconstruction and it may be split. Track splitting may also be linked to a partial and localized failure in the wire hit reconstruction, having consequences on the 3-dimensional matched space points. As already mentioned, PANDORA tries to stitch split tracks back together by checking whether they are collinear; additionally, if the physical track crosses the cathode, the algorithm looks at whether the tracks split in the two adjacent TPCs have a similar distance with respect to it. Other potential contaminants are delta rays and Michel electrons from cosmic muons tagged as separate tracks or small particle showers containing a few aligned ionizing particles. PANDORA is generally conservative in the discrimination between `Track` and `Shower` objects, and small showers may be misrecognized as multiple almost collinear tracks in the TPC.

The CRT-TPC matching provides a handle to deal with this issue. Split tracks and mislabeled showers are matched to the same CRT hit due to being fairly collinear since they represent one physical particle, and they are recognized by the presence of multiple `Track` objects with the exact same t_0 within the same event. If a physical track is able to trigger a majority level and the reconstruction algorithm splits it, each segment with the same timing and smaller length (hence, energy) will be attributed to the same trigger. Therefore, only tracks with unique t_0 times in each event are selected for the analysis. Figure 4.16 shows two examples of pathological cases that are handled with the selection of unique track times.

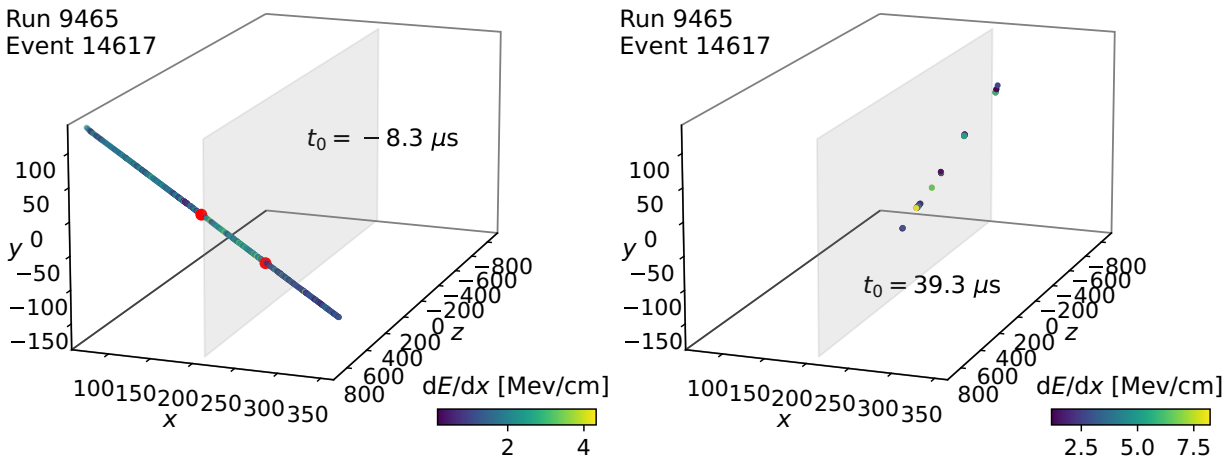

Figure 4.16: Examples of pathological TPC reconstruction cases include split tracks that can be handled with the unique t_0 times selection for each event. Gaps between separate tracks are highlighted with red markers. The cathode is highlighted in the middle of the west T300 module.

Isochronous Tracks Other pathologies in the TPC reconstruction that could impact the evaluation of the trigger system performance include "isochronous" tracks, which are characterized by a roughly constant drift coordinate, hence all the hits have very similar peak times. It may occur that the reconstruction algorithm wrongly associates hits from different planes, resulting in non-straight particle trajectories not linked to physical interactions (Figure 4.17).

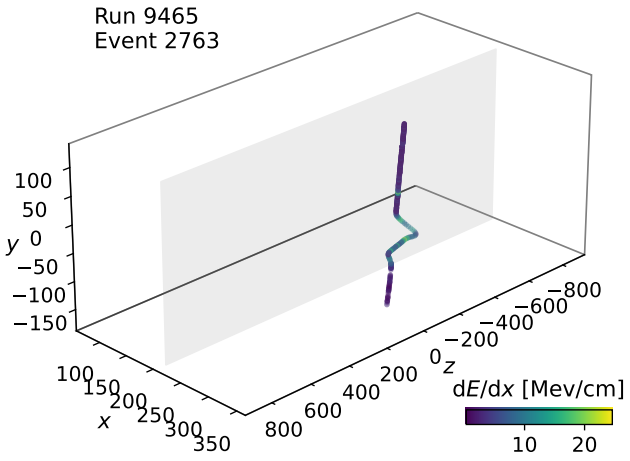

Figure 4.17: Example of a failure in the TPC reconstruction due to the track being isochronous. The drift coordinate along the track varies by less than a cm.

It is worth mentioning that the CRT-TPC matching is designed to be robust against abrupt changes in the particle trajectories by considering the local start and end directions to associate the tracks with CRT hits, and should yield a reliable time for emulating the trigger if the DCA selection is sufficiently tight.
The imaging capabilities of LArTPCs can be crucial in rejecting straight but badly reconstructed isochronous tracks. Deviations from a straight trajectory due to reconstruction issues are characterized through the ΔL variable, computed as the difference between the reconstructed length $L_{\text{reco.}}$ (i.e., the sum of the distances between successive space points along the track reconstructed in the TPCs) and the distance between the start and end points of the track, $L_{\text{s}\to\text{e}}$. The ΔL variable is then weighted over the $L_{\text{s}\to\text{e}}$ distance to account for diverse lengths and impacts of deviations. The $\Delta L/L_{\text{s}\to\text{e}} < 3\%$ selection was implemented, cutting out roughly 3% of the tracks (Figure 4.18).
The choice of the $\Delta L/L_{\text{s}\to\text{e}}$ variable is validated by the distribution with respect to the $\cos(\theta_x)$ variable, which describes the direction of the track projected onto the x drift axis (see Figure 4.19). A $\cos(\theta_x) \sim 0$ value would correspond to the direction perpendicular to the x axis, namely to tracks characterized by hits with a constant drift coordinate (isochronous tracks). Figure 4.18 (right) shows that $\Delta L/L_{\text{s}\to\text{e}}$ is systematically higher around $\cos(\theta_x) \sim 0$, i.e., isochronous tracks present systematic deviations in the trajectory due to a "fake" TPC reconstruction.

Vertical Tracks Further selection rules were developed on top of the "basic selection", where events are characterized by a unique time, and isochronous tracks with large deviations from straight trajectories are discarded. By selecting almost vertical tracks, most of the deposited charge is contained in small bins in the zx plane, enabling an absolute measurement of the trigger recognition efficiency, not strictly depending on

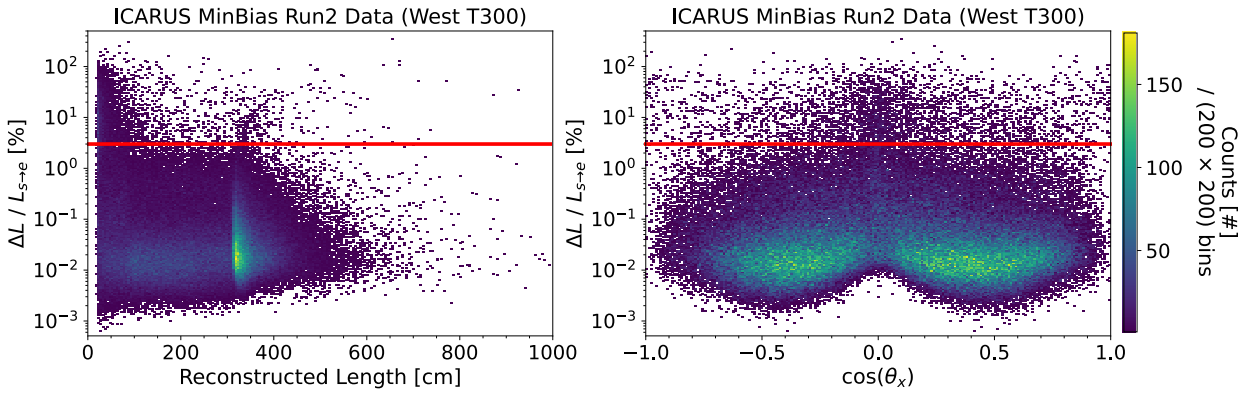

Figure 4.18: Distribution of the $\Delta L/L_{s\to e}$ variable, namely the difference between the reconstructed length $L_{reco.}$ and the distance between the start and end points of tracks $L_{s\to e}$ weighted by $L_{s\to e}$, with respect to the reconstructed length (left) and direction of the track with respect to the drift axis (right). The $\Delta L/L_{s\to e} < 3\%$ cut is highlighted. A pre-selection on muons with DCA < 30 cm and unique t_0 times within the PMT readout is made.

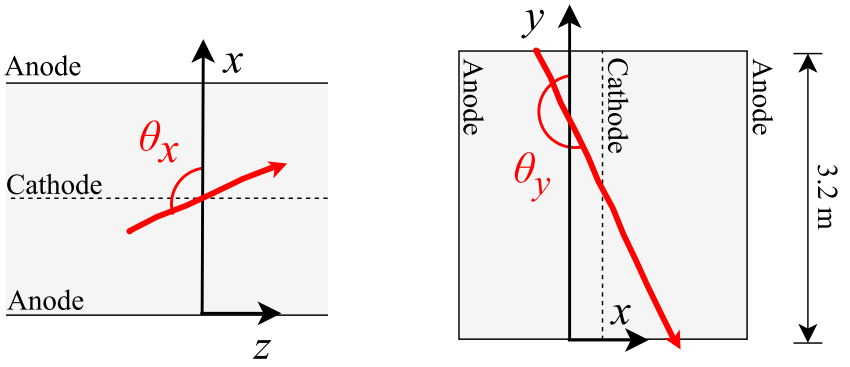

Figure 4.19: Visual representation of how the TPC reconstruction handles the angles with respect to the drift (left) and vertical (right) axes, considering a reconstructed muon track in the TPC. The figure on the left represents a T300 module from the top, the one on the right from the front.

the orientation of cosmic muons and with high granularity along the longitudinal direction and at different distances from the PMTs along the TPC drift coordinate.

The first step identifies "through-going" tracks, having the initial coordinate near the top and side walls of the TPCs, and the end one near the bottom and side walls of the TPCs. A 10 cm tolerance between walls and starting or ending points is set to have some buffer for mitigating reconstruction issues and biases in the time reconstruction (recall Figure 4.11), which could imply slight shifts in the reconstructed space points with respect to the real track. Note that $\sim 10\%$ of the cosmic muons are expected to stop inside the TPCs, and this could bias the evaluation of the trigger performance. Moreover, in rarer cases, a physical track is split in the TPC reconstruction and one of its segments could be not correctly tagged by the CRT, resulting in fake stopping muons not discarded by the "basic selection". Therefore, only through-going tracks have been considered.

"Vertical" muons are selected by the $\theta_y < 20°$ angle with respect to the vertical for downward going muons, namely $\cos(\theta_y) < -0.94$ (for reference, see Figure 4.19 and Figure 4.20, left). Through-going muons from the top to the bottom TPC wall with $\theta_y < 20°$ span less than 1 m along the longitudinal z and drift x axes,

implying that the deposited charge is contained in 1×1 m^2 or less in the longitudinal-drift plane.
Finally, tracks crossing the Top-CRT (horizontal and rim) exclusively are selected. This last step does not impact the event statistic much: Figure 4.20(left) shows that the vertical tracks selected with $\theta_y < 20°$ are almost entirely matched to Top-CRT hits. Indeed, it was observed that the Top-CRT is crossed by 70% of all the cosmic muons, most notably by the vertical ones. Moreover, the spatial uncertainties related to CRT hits and the DCA are generally smaller for the Top-CRT (recall Figure 4.8). An example of cosmic muon track passing all the selection rules is visualized in Figure 4.20(right).

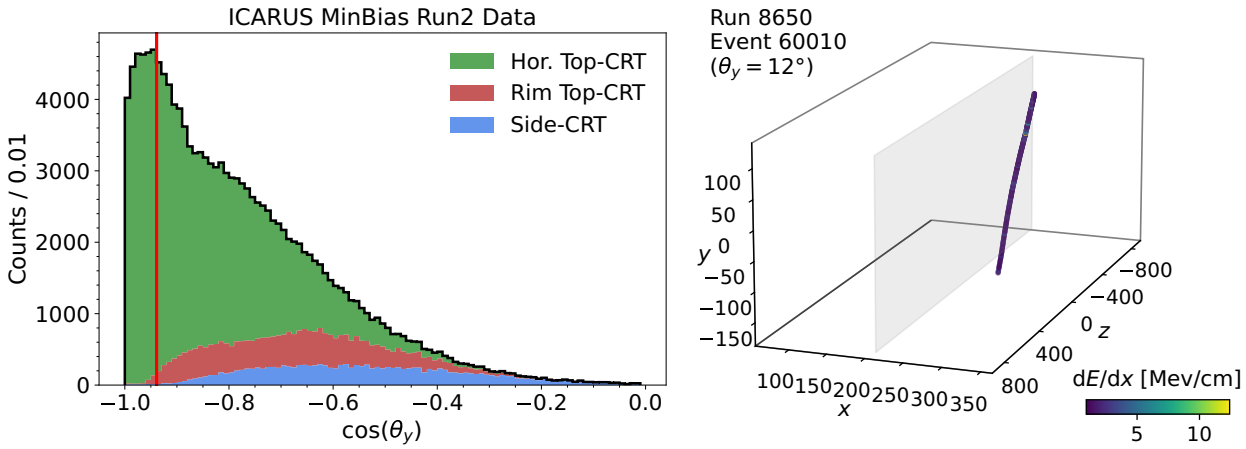

Figure 4.20: (left) Distribution of $\cos(\theta_y)$, namely the track direction with respect to the vertical y axis, stacked with respect to the horizontal and rim Top-CRT and Side-CRT matched hits. Tracks recorded from the west ICARUS T300 module are considered. The $\cos(\theta_y) < -0.94$ cut for vertical tracks is highlighted. (right) Event display of a vertical through-going track.

The developed selection procedures on the cosmic muon samples are summarized in Table 4.2.

	Selection	West T300	East T300	Ref.
"Basic selection"	1. t_0 in PMT readout	526,440 (100%)	513,724 (100%)	Figure 4.9
	2. DCA < 30 cm	221,137 (42.0%)	202,031 (39.3%)	Figure 4.8
	3. Unique t_0 times	144,372 (27.4%)	133,042 (25.9%)	Figure 4.16
	4. $\Delta L/L_{s\to e} < 3\%$	140,131 (26.6%)	128,651 (25.0%)	Figure 4.18
"Vertical selection"	5. Through-going	83,177 (15.8%)	78,747 (15.3%)	
	6. $\cos(\theta_y) < -0.94$	19,599 (3.7%)	20,115 (3.9%)	Figure 4.20
	7. Top-CRT	19,595 (3.7%)	20,114 (3.9%)	

Table 4.2: Description and impact of the developed event selection procedures applied on the west and east T300 data, grouped with respect to the "basic" and "vertical" selections.

The results of the selections with respect to the reconstructed muon length are visualized in Figure 4.21, showing the distribution of track lengths and the selection efficiency for different selections with respect to the base sample defined by selecting DCA < 30 cm and t_0 in the PMT readout.
The "basic selection" selects tracks with unique times to reject badly reconstructed isochronous tracks, resulting in 140,131 (128,651) tracks in the west (east) ICARUS T300 module, namely 27% (25%) of the initial dataset. In the "vertical selection" through-going vertical tracks crossing the Top-CRT are consid-

ered, yielding 19,595 (20,114) tracks, namely 4% of the initial sample. In the end, with the vertical selection roughly 40% of all the tracks with a ~ 3 m length are selected, namely the ones needed to generally characterize the trigger efficiency, while discarding $> 99\%$ of the others (Figure 4.21).

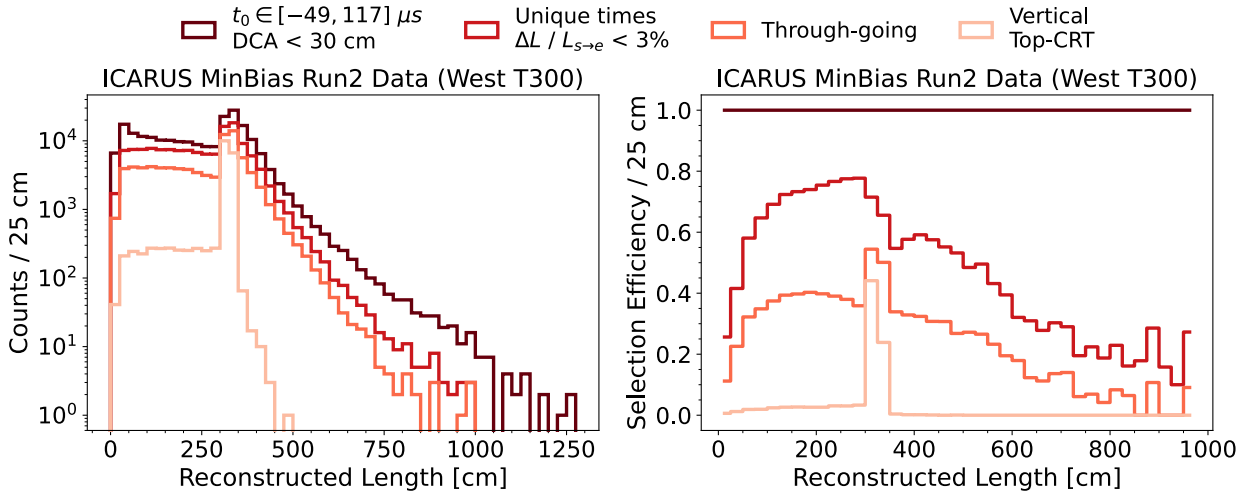

Figure 4.21: (left) Distribution of reconstructed lengths for muon tracks in the West T300 module. The selection procedure described in the text are applied progressively to the sample. (right) Ratio of progressively selected samples with respect to the base one (muons matched with CRT with t_0 in PMT readout and DCA < 30 cm) as a function of the reconstructed length.

4.3.3 Mapping the Trigger Efficiency

This study is performed by measuring the cosmic event recognition efficiency as a function of the position of the collected charge-barycenter in the event both along the drift and the beam directions, as well of the deposited energy in the TPCs. In practice, the trigger efficiency is evaluated on data as the number of events firing the emulated majority over the total number of events, and relative errors are estimated with the Clopper-Pearson method. The produced "map" will enable to estimate the detection efficiency for the mj-5 used for the BNB and NuMI neutrino recognition as well as of the mj-10 for the detection of out-of-time cosmics during the ~ 1 ms drift of ionization electrons in the TPCs.

Detection Efficiency of In-time Beam Events The efficiency for the recognition of cosmic muons with the majority-5 is shown in Figure 4.22, using the vertical selection to focus on clean straight tracks crossing the Top-CRT with $\theta_y < 20°$, and rejecting most of the tracks crossing the detector's corners (recall Figure 4.21). As a result, the detection efficiency works out to be uniform along the drift and longitudinal directions, averaging roughly 98%.

The applied event selection considers tracks well contained in terms of deposited charge in < 1 m along the longitudinal and drift directions. The evaluation of the trigger event recognition efficiency on the vertical sample can hence be compared to the efficiency for the detection of neutrinos as predicted with the data-driven Monte Carlo (for reference, see subsection 3.2.3). Figure 4.23 shows the measured mj-5 trigger efficiency evaluated on Run2 MinBias data, and the Monte Carlo truth-level prediction for BNB ν_μCC and

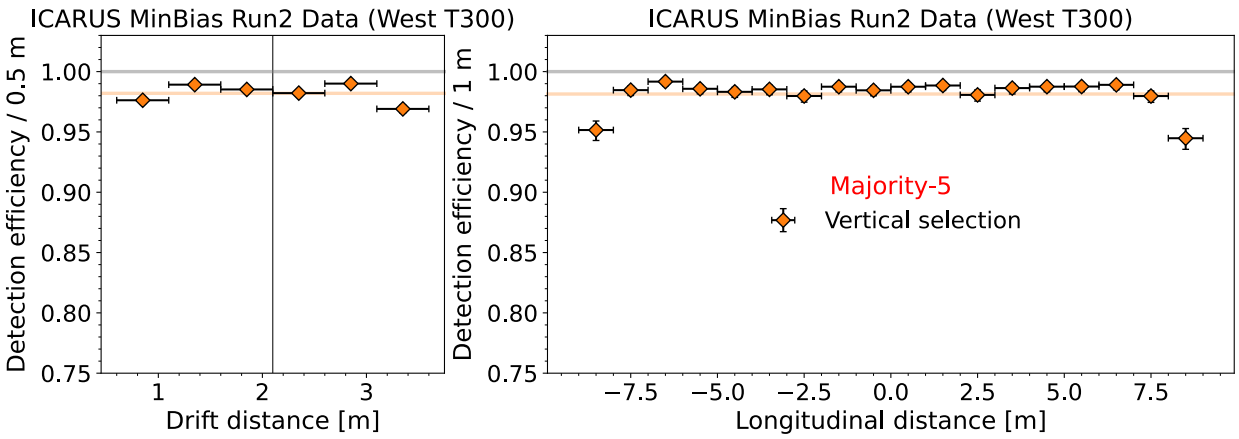

Figure 4.22: Mj-5 trigger efficiency evaluated on MinBias Run2 data, with respect to the drift (left) and the longitudinal (right) coordinate of the tracks' charge barycenter, in the west T300 module. The vertical selection (basic selection, through-going, Top-CRT, $\theta_y < 20°$) is applied. The vertical line represents the cathode.

ν_eCC interactions, without selecting any fiducial volume. Both the Monte Carlo prediction and data show an almost full detection efficiency for $E_{\text{dep.}} > 200$ MeV, with a 90% efficiency in the $100-200$ MeV range.

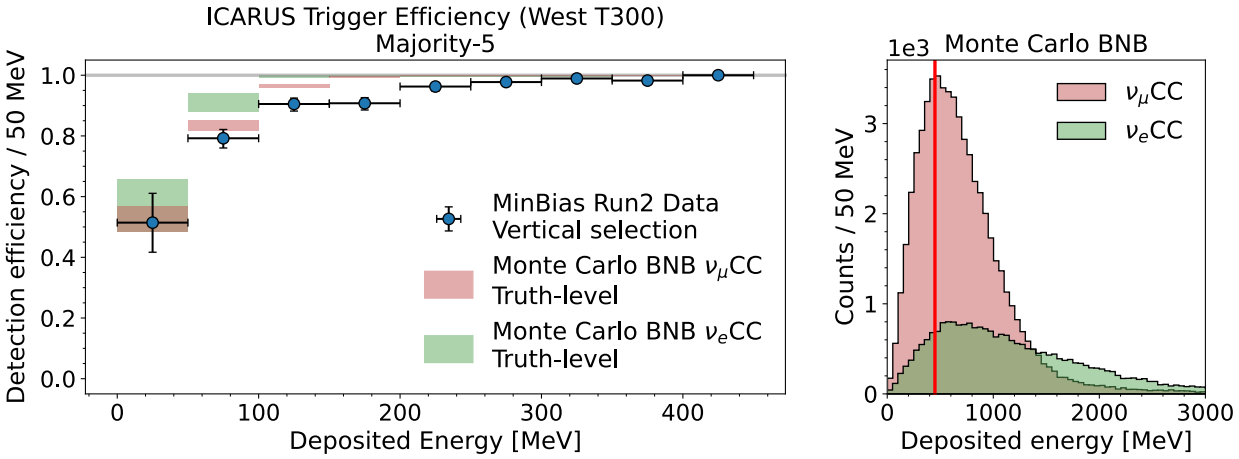

Figure 4.23: (left) Trigger efficiency evaluated on MinBias Run2 data with the vertical selection (basic selection, through-going, Top-CRT, $\theta_y < 20°$), compared with the truth-level data-driven Monte Carlo prediction for BNB ν_μCC and ν_eCC. (right) Energy spectrum of Monte Carlo BNB ν_μCC and ν_eCC, normalized to the number of MC events produced, and not accounting for the relative 0.5% contamination in the BNB. The red line indicates the $[0,\ 450]$ MeV interval the efficiency was evaluated on.

Note that only negligible inefficiencies arise in the data above 200 MeV. Indeed, missed events did not fire a trigger due to a time mismatch with potential triggering PMT light flashes reconstructed in the same event. The causes of such inefficiencies were assessed to be related to reconstruction issues rather than having a physical nature, like multiple tracks in the same trigger emulation window wrongly assigned the same trigger time, or inefficiencies of the CRT-TPC matching algorithm leading to a shifted track time.

Data confirmed the hints from the data-driven Monte Carlo regarding the excellent performance of the

majority-5 trigger. In particular, the result matched the prediction for BNB neutrinos and can be extended to the NuMI neutrinos as well, being characterized by higher energies overall (recall subsection 2.2.1).

Detection Efficiency of Out-of-time Cosmic Rays The trigger event recognition efficiency was tested on MinBias Run2 data with the majority-10 condition (Figure 4.24), which was initially used for recording cosmic tracks within the out-of-time primitives windows. Being interested in recognizing all possible tracks independently of their orientation, length, and energy deposition, the event sample corresponding to the "basic selection" was used. As a result, an average 70% detection efficiency for the mj-10 was found, and inefficiencies are mostly located near the anode, upstream and downstream walls of the TPCs, in rough agreement with the Monte Carlo μ truth prediction (for reference, see subsection 3.2.3). These efficiency dips are less pronounced with looser majority requirements, being related to tracks too close to the PMTs, leading to few LVDS channels being fired, not reaching a tighter majority requirement.
Indeed, it was tested that it is possible for the DAQ to withstand even higher out-of-time trigger rates with respect to the mj-10. It was hence decided to lower the out-of-time majority requirement to 8, increasing the event recognition of the muon background during the TPC readout (Figure 4.24) by 13% and averaging to 79%.
The localization of non-triggering vertical muon tracks is reported in Figure 4.25: most of the tracks not meeting an mj-8 requirement have the corresponding charge barycenters near the PMTs or in the corners of the T300 module, and are mostly characterized by < 100 cm reconstructed lengths (roughly < 200 MeV, considering the $\mathrm{d}E/\mathrm{d}x \sim 2$ MeV/cm muon MIP-deposit in liquid argon). The distribution confirms the indications from the data-driven Monte Carlo μ study (Figure 3.24). This study suggests the need for a complementary trigger system based on the PMT signals and the corresponding collected charge, rather than only considering a multiplicity logic. This would help in recovering some of the events that are lost when too close to the anode planes, where few PMTs collect most of the light. This is especially important for the stricter mj-8 or mj-10 conditions used for collecting out-of-time primitives, where cosmic muons need to be recognized in the whole active volume to guarantee the cosmic background rejection during the ionization electron drift in the data analysis.

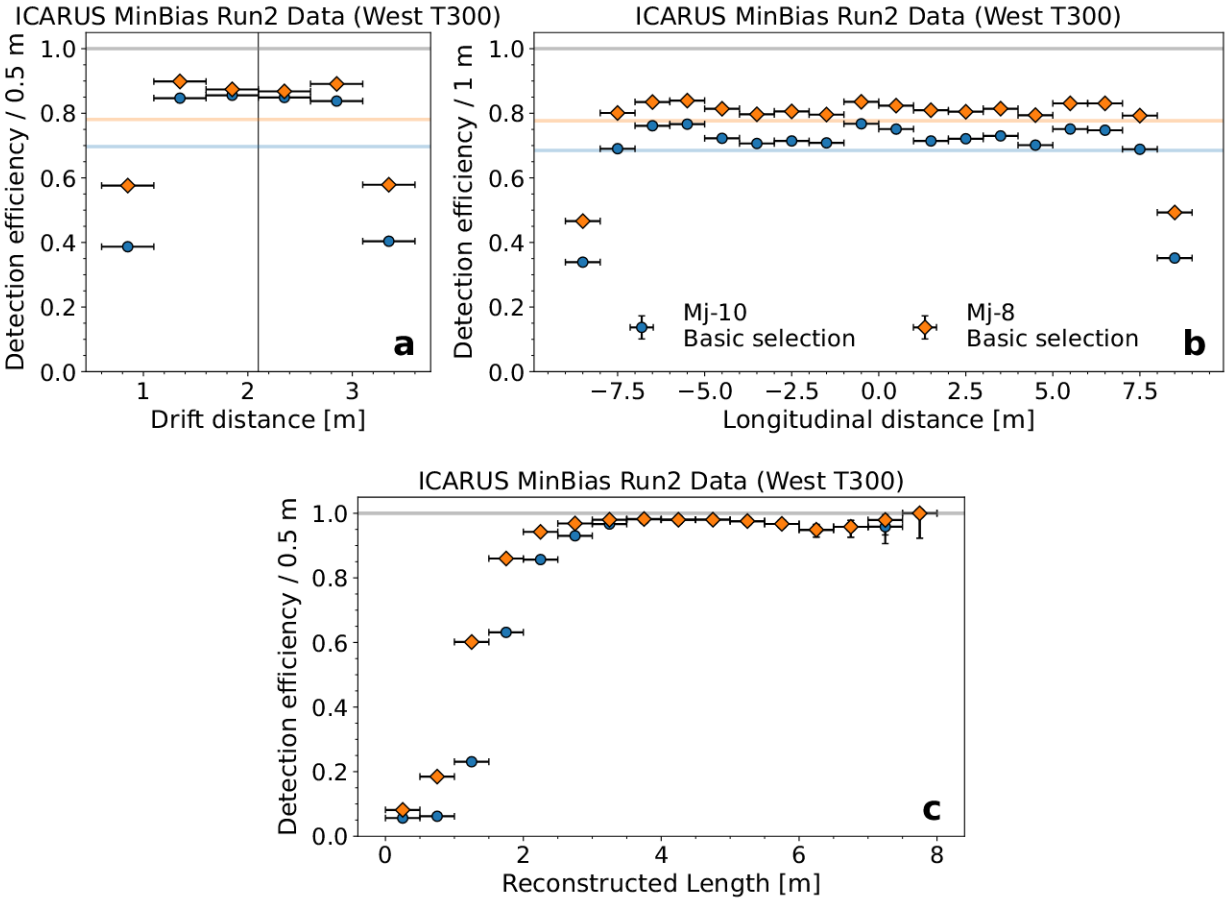

Figure 4.24: Mj-10 and mj-8 trigger efficiencies evaluated on MinBias Run2 data, with respect to the drift (a) and longitudinal (b) coordinate of the tracks' charge barycenter and to the reconstructed length (c), in the west T300 module. The basic selection is applied. The vertical line in (a) represents the cathode.

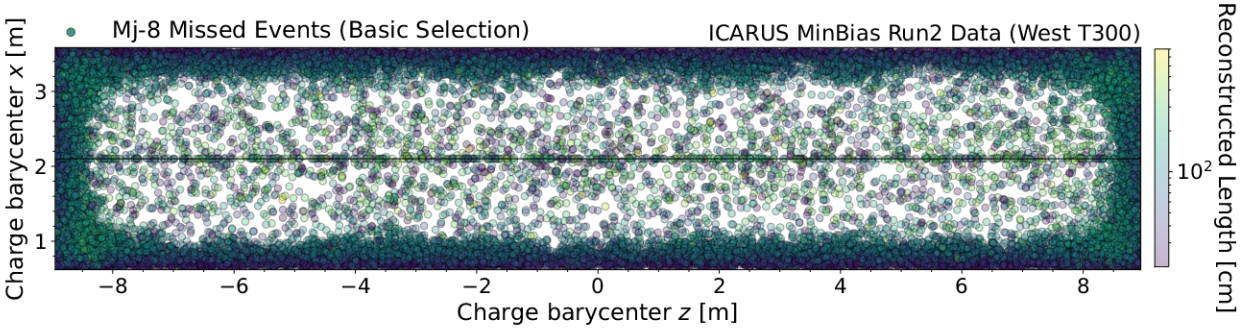

Figure 4.25: View of the West ICARUS T300 module from the top, with the cathode in the middle. Distribution of tracks' charge barycenters from MinBias Run2 data. Events not triggering the majority-8 are highlighted and colored with respect to the reconstructed track length.

5

Adder-based Trigger System

This Chapter contains:

The PMT-majority trigger is based on the multiplicity of the fired LVDS channels over a threshold for each interaction, a choice that also assures the single-PMT time granularity required in the event reconstruction. The analysis of the collected data (chapter 4) suggests a full efficiency for $E_{\text{dep.}} > 200$ MeV, identifying non-triggering lower-energy events mostly for short cosmic tracks near the corners of the detectors and close to the PMTs.

In parallel, an ancillary trigger system based on the detection of the total scintillation light in the event determined by the sum of adjacent PMT signals performed by so-called "adder boards" is being developed to provide a piece of complementary information on the total light signal of the event, independently from any multiplicity of fired PMTs. For instance, for a cosmic track close to the corners of the detector or to the wire planes, there may be a huge amount of light collected only by a small number of PMTs (Figure 5.1), possibly failing the requested PMT-majority logic. By triggering on the sum of adjacent PMT signals, it may be possible to recover non-triggering events associated with highly localized energy depositions both

in the beam gate and out-of-time.
Eventually, an adder-based trigger system would be used in combination with the PMT-majority trigger, in order to improve the event recognition below 100 MeV energy depositions with out-of-time cosmic muons, crucial for background rejection in the neutrino data analysis, and potentially also with low-energy neutrino charged-current and neutral-current interactions. Furthermore, this complementary system may be useful to study the relative trigger efficiency of the majority logic, monitoring its performance online.

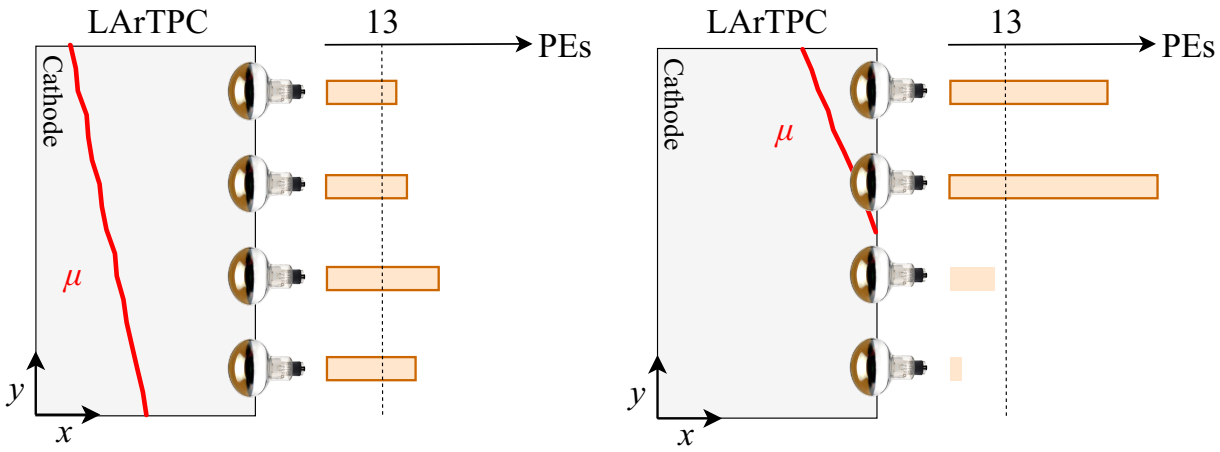

Figure 5.1: Visual representation of how light is collected by PMTs for two cosmic muons, far (left) and close (right) to the anode plane in a TPC. In the latter case, most of the light is collected by few PMTs, and adders may be able to recover events missed by the majority logic. Not to scale.

Adder Boards Adder boards are custom-made and can be added into the trigger system as schematically represented in Figure 5.2. Each board is composed of two main stages:

1. signal splitter: each board receives signals for 15 adjacent PMTs, corresponding to 3 m longitudinal sections of the TPCs, the same as in the case of the V1730B PMT digitizer boards (see Figure 3.12). The signal from each PMT is split into two 50 Ω lines, the first corresponding to 95% of the amplitude is sent as input to the corresponding V1730B digitizer board, and the second one, scaled by a 5% factor, is processed by the second stage;

2. adder stage: it performs the analog sum of the 15 nearby PMT signals scaled with a 5% factor coming from the splitter stage.

The analog sum signal is then fed to a CAEN DT1081B Programmable Logic Unit (one for each T300 module). The module performs all the requested processing of the output lines: discrimination, Transistor-Transistor Logic (TTL) signal conversion, and counting. The final output in TTL format can be directly sent to the trigger FPGA for further handling, to be eventually exploited for the global trigger production.
The signals for 90 PMTs in each TPC (180 PMTs in ICARUS T300) are grouped in 6 adder boards (15 PMTs per board). Globally, 24 adder boards were installed within the ICARUS T600 light collection system and were preliminarily tested.

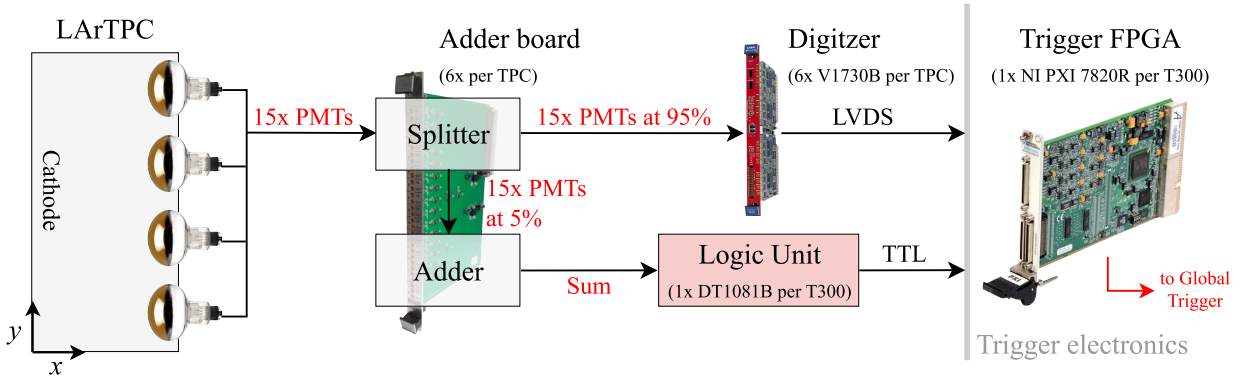

Figure 5.2: Scheme of the adder trigger system setup. From the left: the 15 PMT signals are split into two 95% and 5% components. The first one continues to the digitizer, and the adder stage sums up the 15 signals scaled by 5%. Finally, an external logic unit is used for discrimination.

5.1 Characterization of Adder Boards

The functionality of all the channels was verified by injecting a negative square pulse (1 V amplitude, 1 MHz frequency, 99% duty cycle), directed to an input channel of an adder board. The input signal was compared to the channel output (95% of the input signal) and the board output (5% of the signal) on the oscilloscope, and the splitting fractions were preliminarily verified.

The impact on the standard PMT trigger system was investigated by measuring the rates of discriminated LVDS signals. A dedicated LabVIEW software running on the trigger FPGAs was used to determine the number of LVDS signals recorded in each channel every 10 s, with runs lasting up to $\sim$ 10 minutes. Figure 5.3(left) shows the distribution of LVDS rates for each one of the 90 LVDS channels in the West ICARUS T300 module, using a PMT discrimination threshold of 13.3 PEs (i.e., 400 ADC). The low-frequency tail is due to PMTs being off in some of the LVDS channels.

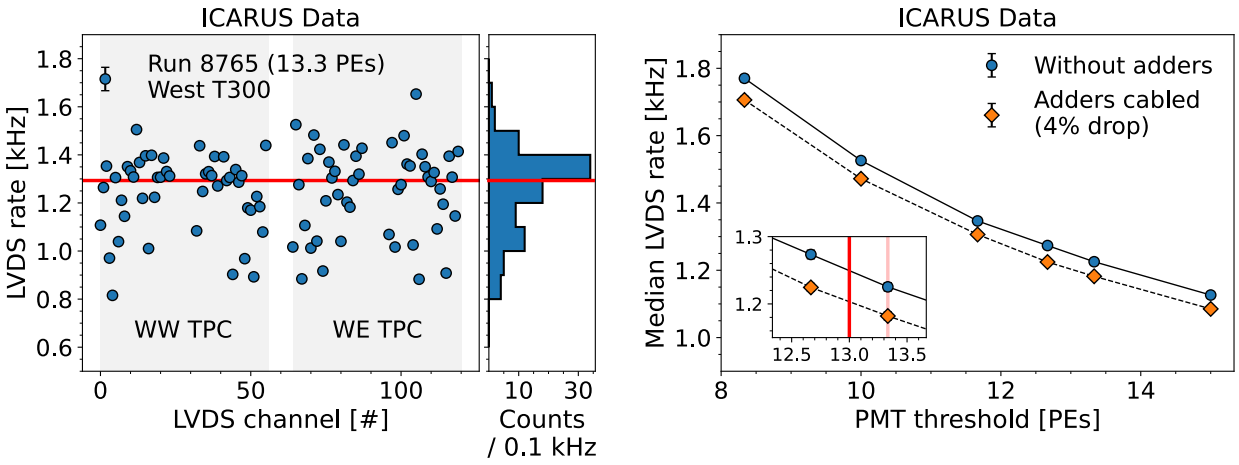

Figure 5.3: (left) LVDS rate as a function of the channel number, for a PMT discrimination threshold of 13.3 PEs and without adders. The rates are obtained as the channel-by-channel average. The median of the rates is highlighted. (right) Median LVDS rate as a function of the PMT discrimination threshold, before and after cabling the adder boards within the light collection system. To account for the 4% rate drop, the PMT discrimination threshold was lowered to 13 PEs.

The rate for each configuration is estimated as the median of the LVDS rate distribution and compared to the original PMT system configuration without adders Figure 5.3(right).
The introduction of the adders resulted in an average 4% drop in the LVDS rate. Originally, a 13.3 PEs PMT threshold was being used, later slightly lowered to 13 PEs to mitigate the impact on the established PMT-majority trigger.
The rates of single adder boards were then measured with cosmic rays as a function of the adder discrimination threshold as set on the CAEN DT1081B module. The counting is performed with a dedicated LabVIEW software running on the trigger FPGAs (Figure 5.4). The naming convention of adder boards is based on their positioning in the electronics racks within the ICARUS light collection system. Considering a TPC, the six adder boards collecting 15 PMT signals each in 3 m longitudinal sections are ordered from south to north with respect to the BNB direction. It can be noted that groups of adders that are adjacent in their localization within a TPC have generally similar rates, compatible within a 100 Hz maximal dispersion range.

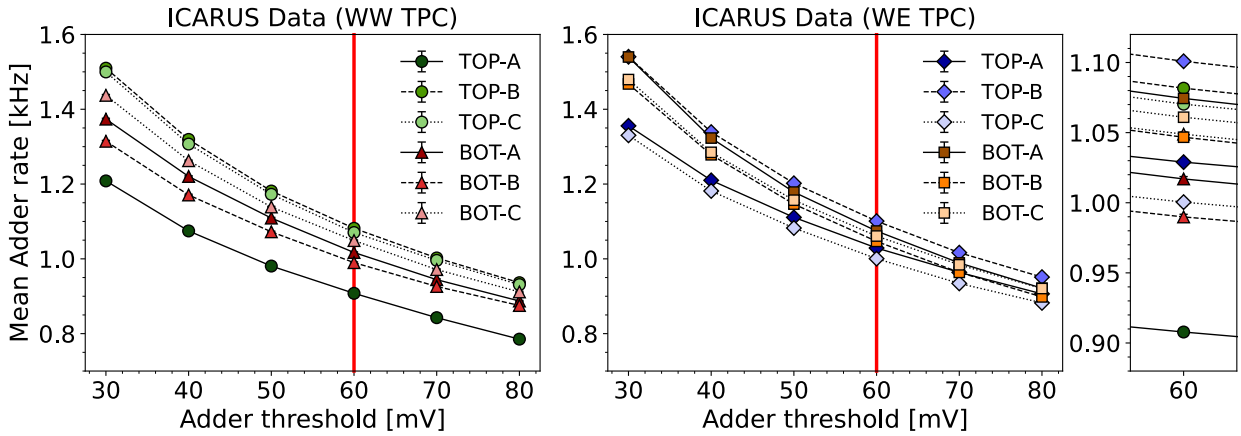

Figure 5.4: Mean adder board rate as a function of the adders discrimination threshold, for the west ICARUS T300 module, split for the west (left) and east (center) TPCs. The six adder boards per TPC are ordered from south to north with respect to the BNB direction. The rates at 60 mv are compared in the right panel.

5.1.1 Features of Adder Waveforms

The 3-hour `8888` MinBias run was collected with cosmic rays, also digitizing the adder signals with one channel of the V1730B PMT digitizer boards (see subsection 2.1.2), without discriminating them.
Figure 5.5 shows the number of events from the `WW-TOP-C` adder board as a function of a software discrimination threshold. The initial drop is related to the electronic noise removal, ensured by requesting signals above $\sim$ 100 ADC. No other drop linked to potential background sources is reported. Eventually, it will be crucial to fine-tune the discrimination threshold for adder signals, depending on the trade-off between adder-trigger rate, DAQ requirements, and event recognition efficiency, and also depending on their implementation with respect to the PMT-majority trigger.

The signal properties of the same board in the WW TPC are compared with those of one of the PMTs it collects the signal from (Figure 5.6), using data from a 10-hour `8889` mj-5 run with cosmic rays, in which the

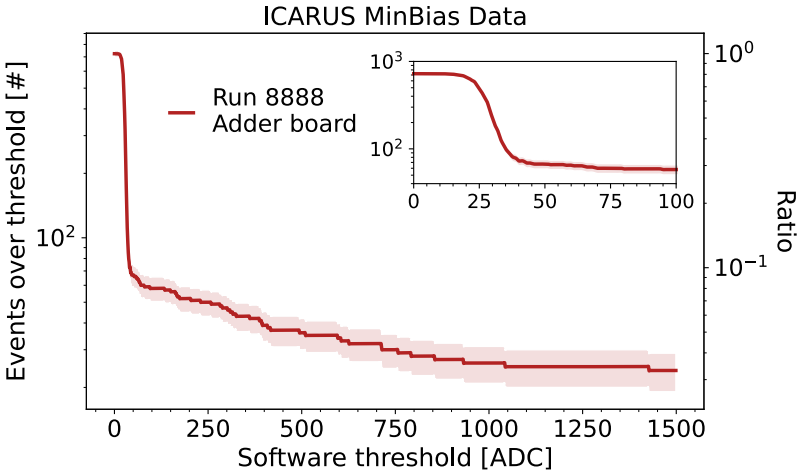

Figure 5.5: Number and ratio of events over the software discrimination threshold as a function of the threshold in the MinBias run 8888, for the WW-TOP-c board. The uncertainty on data points is assumed to be Poissonian.

adder waveforms were again digitized. A hit-finding algorithm was developed to calculate the waveforms' baseline and find events with light activity, identifying light signals. The signal amplitude (height of the waveform at the peak over the average baseline), noise-RMS (standard deviation of the baseline, represented by non-hit samples), and rise time (i.e., the interval between the start and the peak of the signal) were computed. The latter was evaluated by selecting events with a > 100 ADC amplitude, cutting over the electronics noise (recall Figure 5.5).

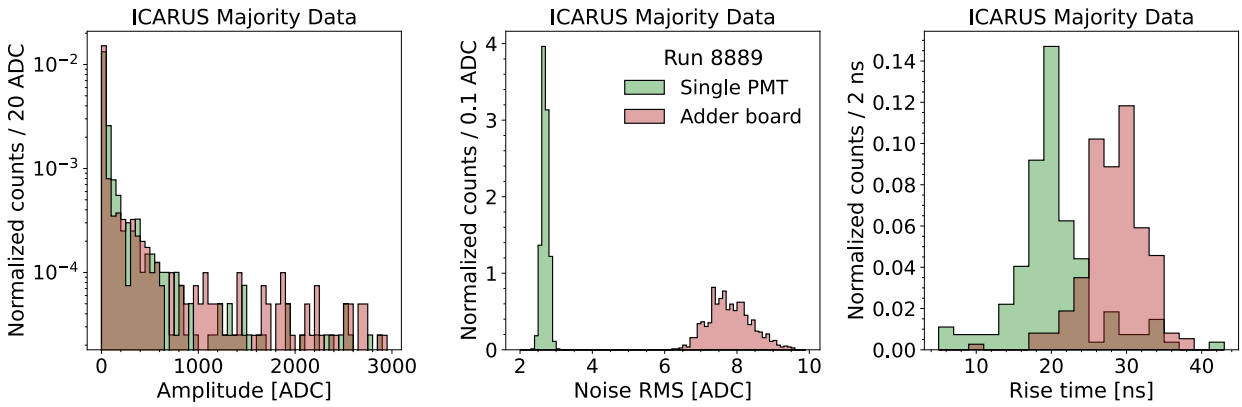

Figure 5.6: Comparison of signal properties from the WW-TOP-C adder board and its first PMT: distribution of signal amplitudes (left); noise RMS distribution (center); rise time distribution (right).

The signal amplitude varies over a large scale since the sample is dominated by cosmic rays, with a large variability in the amount of light collected in each cryostat. Moreover, light signals are recorded even if the triggering signal is far away in the same cryostat, leading to an accumulation of baseline-only events.

Figure 5.6 (center) shows that signals from adder boards are affected by a higher noise-RMS than PMTs by a factor ~ 3 ($\text{RMS}_{\text{add.}} \sim 7.8$ ADC and $\text{RMS}_{\text{PMT}} \sim 2.7$ ADC), with a spread wider by a factor ~ 6 ($\sigma_{\text{add.}} \sim 0.6$ ADC and $\sigma_{\text{PMT}} \sim 0.1$ ADC). Indeed, a discrimination threshold higher than 100 ADC will be used to reject the electronics noise, with a signal-to-noise ratio $S/N > 10$.

Finally, the PMT rise time is roughly $\sim$ 20 ns, shaped from the initial nominal value of 8 ns. The adder boards shape the PMT rise times to $\sim$ 30 ns (Figure 5.6, right), likely due to the following factors:

- the adder sums up 15 non-synchronized PMT pulses since photons from events in the TPC arrive at different PMTs at different times, with some spread due to the signal cable length;
- the triggering event might be far from the PMTs of the considered adder board.

In practice, an appropriate shaping of adder output signals may be introduced before any further logic processing, to account for the increased rise time of the waveforms.

5.1.2 Reproducing the Adders Signals

The signal processing of adder boards was emulated starting from the measured PMT waveforms collected with a standard PMT-majority (run 8889, on-time mj-5, out-of-time mj-10), to check whether it matches the expectations. Only the 28 μs waveforms coincident with the beam gate are analyzed (recall Figure 4.2). Note that the signals are digitized from the CAEN V1730B board at 500 MHz, hence each waveform is defined with 2 ns steps (Figure 5.7, left). The simple emulation of the adder function where the PMT waveforms are scaled sample-by-sample by 5.3%[i] shows a timing and amplitude mismatch when compared to the corresponding digitized waveform (Figure 5.7, center). Each adder circuit contains a Sallen-Key filter at each input stage, responsible for a $\sim$ 20 ns shaping. Signals from different PMTs are asynchronous, due to photons from cosmic tracks arriving at PMTs spread in time. In practice, the adder integrates the asynchronous input signals, leading to a bigger pulse height than the simple sum of PMT signals.

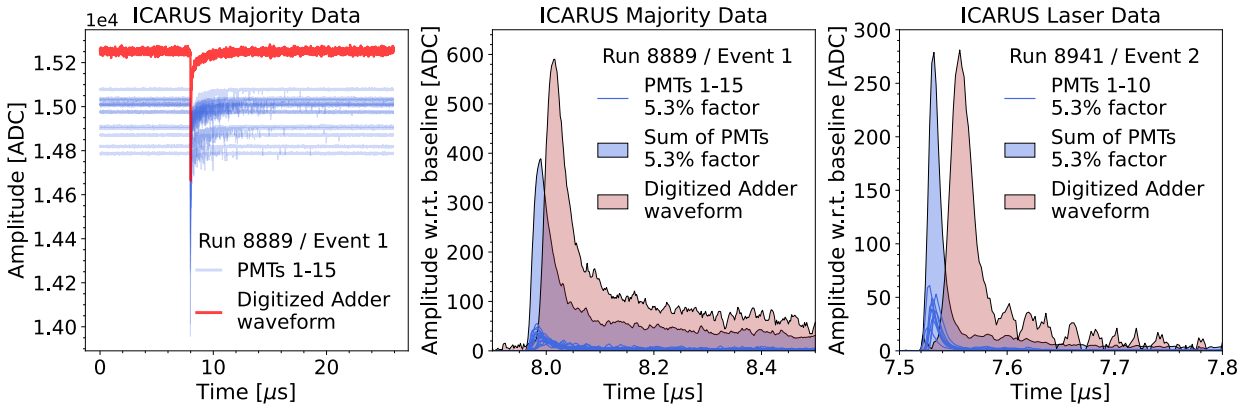

Figure 5.7: (left) Acquired on-beam 28 μs waveforms from 15 PMTs, and from the corresponding adder board. (center) Comparison between the digitized adder signal and the sum of the corresponding 15 PMT signals, scaled by the nominal 5.3% factor. Waveforms are inverted and baseline-subtracted. (right) The same analysis for PMT waveforms with the laser calibration system.

This issue was investigated with the laser calibration system (see subsection 2.1.2), where fast, well-defined, and synchronized pulses ($\sim$ 60 ps FWHM, 30 ps rise time, $\sim$ 400 ADC height) are delivered to groups of 10 PMTs at a time. As a result, the integration effect is negligible, and the sum of PMT waveforms with the

[i] The 5.3% scaling factor corresponds to the nominal board 5% factor, applied on waveforms that are digitized with 95% of the original signal amplitude.

nominal 5.3% scale factor matches the digitized adder waveform well in height (Figure 5.7, right), even if a mismatch in timing and pulse area still remains.

At the time of writing, the full adder electronics emulation was not implemented yet, and it was chosen to empirically tune the scale factor and the delay to match the PMT sum with the digitized adder waveform in the PMT-majority data, to be used for the Monte Carlo data-driven simulation of an adder-based trigger. In particular, a scale factor of 8% and a delay of 26 ns are able to minimize a variable defined as the sum of the squared sample-by-sample difference between the PMT-sum signal and the digitized waveform, over the PMT-sum, as shown for a single board and event (Figure 5.8, left). Figure 5.8(right) shows the match between the tuned emulation and the digitized adder waveform. It was checked that the same factors fit well with other boards and events.

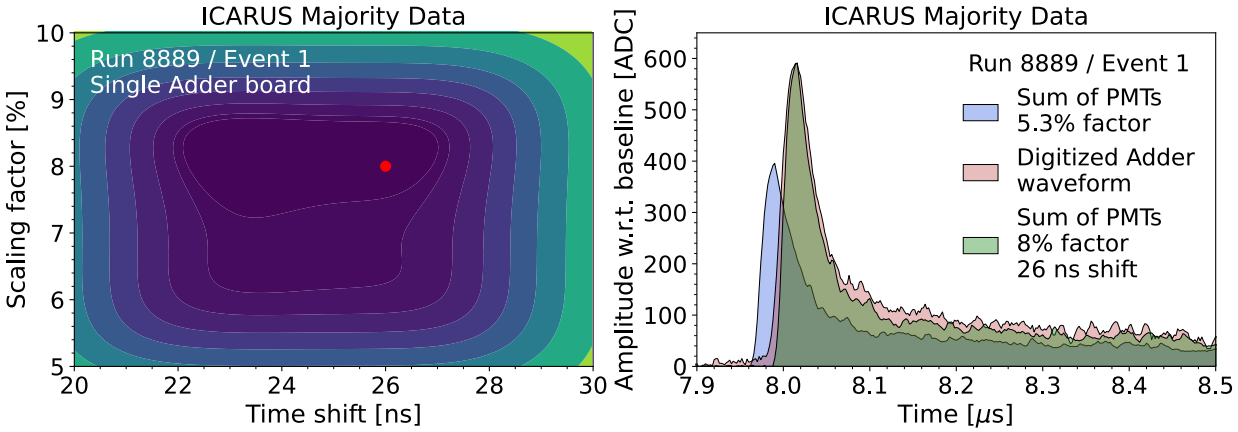

Figure 5.8: (left) Distribution of a chi-squared-like variable, where the observation is the sum of scaled PMT signals and the expectation is the digitized adder waveform. The scaling factor and the delays are optimized to 8% and 26 ns. (right) Comparison between the sum of PMT signals scaled with the nominal 5.3% factor, and with the delayed and tuned 8% PMT sum, with respect to the digitized adder waveform.

5.2 Design of an Adder Trigger

The most straightforward implementation of an adder-based trigger would be defining three longitudinal 6 m windows, and then checking the combination of the windows.

Figure 5.9 shows the rate measured with cosmic rays for each non-overlapping window, defined from south to north with respect to the BNB direction, as a function of the adder discrimination threshold set on the DT1081B logic unit. Each window consists of four adder boards (two per TPC, front-facing) and different window rates are compatible within $100 - 200$ Hz. In practice, considering a trigger in at least one of the adder windows is equivalent to requesting an OR condition among the 12 adder boards of the ICARUS T300 module (Figure 5.9, upper panel). Considering a tentative 60 mV adder discrimination threshold, the global-OR condition yields a ~ 6.5 kHz average rate in ICARUS T300.

Rate of In-time Beam Events The measured 6.5 kHz rate of the global-OR signal generated by the 12 adders in one T300 module with cosmic rays can be exploited to infer the on and off-beam trigger rates with

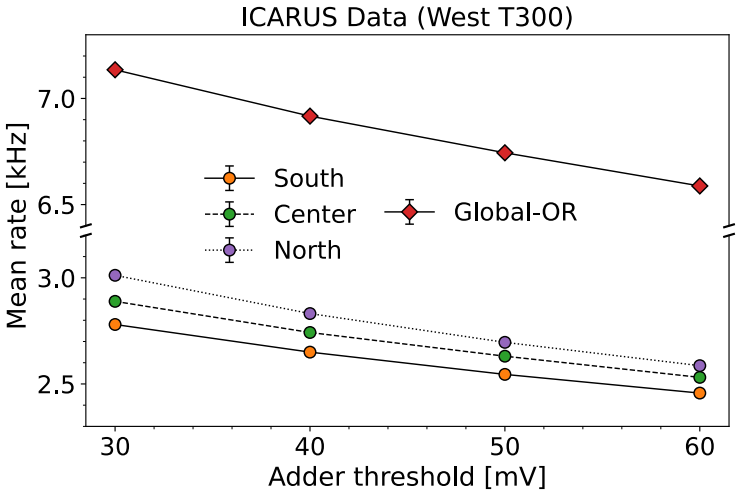

Figure 5.9: Mean rate of majority-like windows defined with four adder boards each, from south to north with respect to the BNB direction, in the west ICARUS T300 module. The rate of the global-OR of 12 adder boards in the west module is shown.

BNB and NuMI:

- BNB. Given the 2.2 μs BNB gate width, ~ 0.014 (~ 0.028) off-beam triggers should be produced per gate in ICARUS T300 (T600)[ii]. With the nominal 4 Hz gate rate, this translates into a ~ 0.11 Hz BNB off-beam trigger rate in T600. According to the expected cosmics-to-beam ratio of roughly 3 : 2 (see Table 4.1, Figure 4.3), a ~ 0.16 Hz BNB on-beam trigger rate is foreseen with the global-OR adder configuration;
- NuMI. Considering the 10.1 μs wide NuMI gate and the 0.83 Hz repetition rate, a ~ 0.11 Hz NuMI off-beam trigger gate is expected. With the predicted cosmics-to-beam ratio of about 2 : 1 (see Table 4.1, Figure 4.3), a ~ 0.2 Hz NuMI on-beam trigger rate is predicted.

The overall predicted trigger rates (Table 5.1) with the global-OR configuration do not differ greatly with respect to the standard PMT-majority rates reported in Table 4.1 and amounting to ~ 0.16 Hz and ~ 0.22 Hz for on and off-beam majority-5 triggers with BNB and NuMI respectively. This suggests that it is feasible to combine the global-OR adder configuration with the PMT-majority logic for in-time triggers by using, for example, a simple logic OR between the two: considering the impact of the common triggers, the overall in-time trigger rate is predicted to be manageable by the DAQ.

	On-beam	Off-beam	Out-of-time triggers / 2 ms
BNB	~ 0.16 Hz	~ 0.11 Hz	~ 26
NuMI	~ 0.2 Hz	~ 0.11 Hz	

Table 5.1: Predicted trigger rates in ICARUS T600 with BNB and NuMI for the global-OR adder configuration, starting from the measured 6.5 kHz cosmic ray rate with the global-OR of 12 adders per T300 module, at a 60 mV adder discrimination threshold.

[ii] The impact of common triggers between the two T300 modules is neglected, and the trigger is assumed to be at almost full efficiency for global triggers.

Rate of Out-of-time Cosmic Rays While a global-OR adder configuration is initially proposed in combination with the PMT-majority trigger for detecting beam neutrinos and cosmic rays in-time with the beam gate, the detection of out-of-time cosmic rays in the 2 ms window around the trigger to tag muons during the drift of ionization electrons is more challenging. The $\sim$ 6.5 kHz global-OR rate at a 60 mV threshold translates in $\sim$ 13 ($\sim$ 26) out-of-time primitives for T300 (T600) within the 2 ms window[iii] (Table 5.1). The global-OR out-of-time yield could exceed the present DAQ bandwidth (usually $\sim$ 15 primitives in T600 for each 2 ms window are collected).
Monte Carlo calculations (chapter 3) and studies on Run2 data (chapter 4) show that there is room for improvement for the detection of muons near the corners of the detector (e.g., see Figure 4.25). As an alternative to the global-OR, the logic OR among the four adder boards at the corners in each ICARUS T300 module ("corner-adders trigger") could be considered in addition to the standard PMT-majority trigger for out-of-time triggers, with an increase of out-of-time primitives that comply with the DAQ requirements.

Proposed Adder-based Trigger The PMT-majority trigger system can be integrated with adders in the following way (Figure 5.10):

- the global-OR configuration between the 12 adders in each ICARUS T300 module is combined in logic OR with the majority-5 logic for in-time on and off-beam triggers. The aim is to recover low-energy beam neutrino events in the fiducial volume for on-beam triggers, and cosmic events in off-beam triggers.
- the 4 adders at the corners of each module are combined in logic OR with the majority-8 logic for out-of-time cosmic ray detection in a 2 ms window around the global trigger, with the aim of recovering tracks at the corners of the detector or too close to the PMTs, possibly enhancing cosmic background rejection.

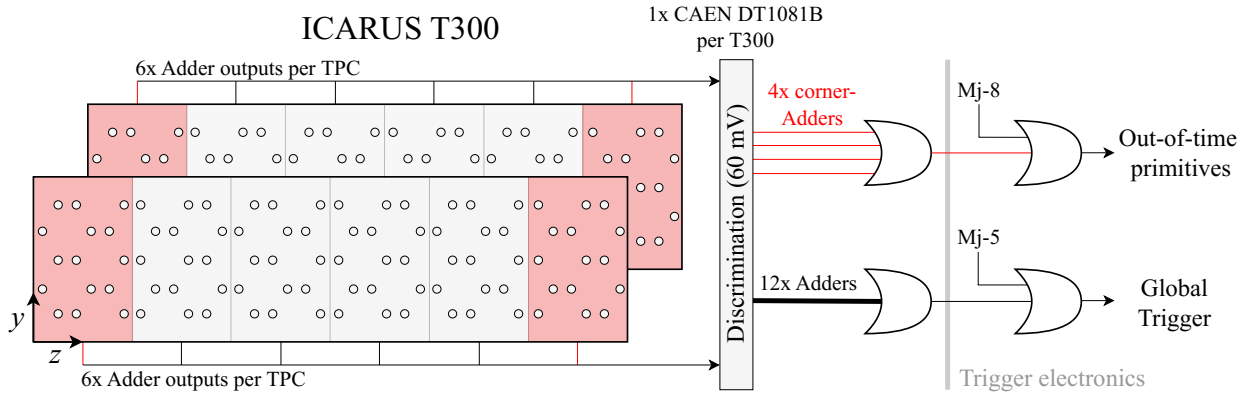

Figure 5.10: Side-view of the two TPCs in each ICARUS T300 module. From the left: 12 adder board signals are produced for each T300 module and discriminated by a CAEN DT1081B logic unit at a tentative 60 mV threshold. The global-OR between the 12 discriminated adders is used in combination with the mj-5 to produce on and off-beam global triggers. The 4 adders at the corners are combined with the mj-10 for the collection of out-of-time primitives around the global trigger.

[iii] The out-of-time trigger efficiency is assumed to be almost maximal with the global-OR among adders.

5.2.1 Monte Carlo Simulation of Adders

Monte Carlo simulations are performed to understand the potential of an adder trigger. The same neutrino and cosmic muon samples and methodology from chapter 3 are used here. The digitized SPR (Figure 3.3) is considered to build PMT waveforms for each event, and adder signals are calculated by adding PMT signals with the data-driven 8% scale factor, also introducing a 26 ns delay (see Figure 5.8). The discrimination threshold of the adder signals was tentatively fixed at 60 mV.

Figure 5.11 shows the distribution of BNB ν_μCC vertices in the west T300 module, with respect to the produced signal maximum on a single `WE-TOP-C` adder board, in the middle of the detector. The event distribution is not symmetrical with respect to the considered board, but rather shifted upstream, being mostly of secondary particles emitted in the beam direction. In practice, adders are complementary to the PMT-majority mechanism: the closer the vertex is to the corresponding PMTs, the higher is on average the maximum signal produced on the adders.

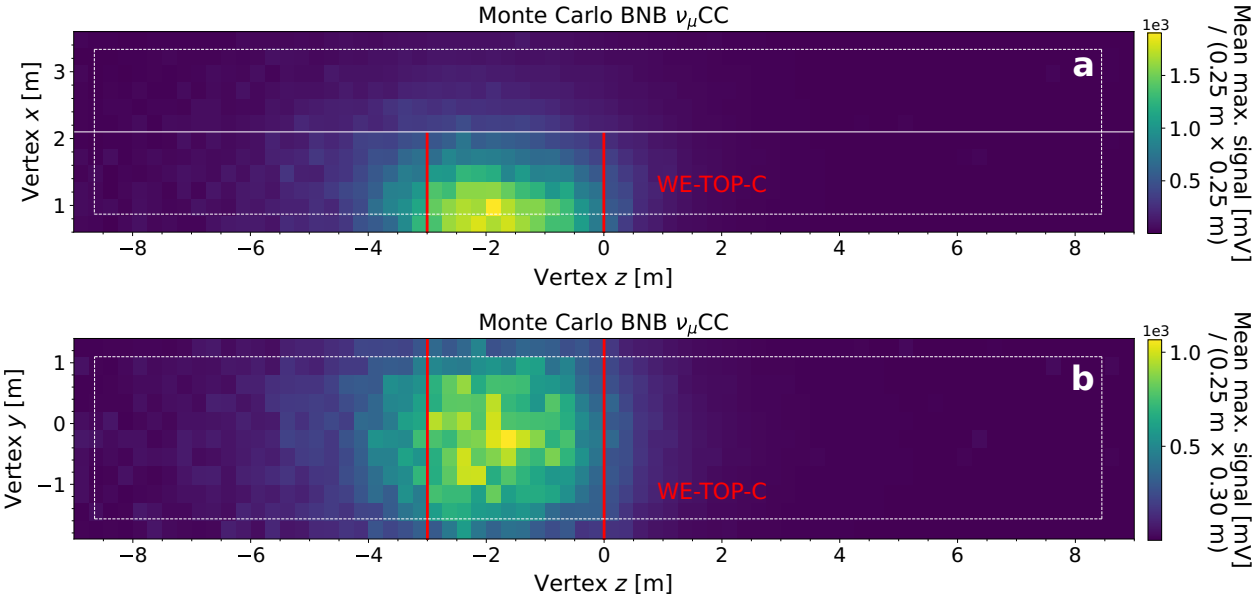

Figure 5.11: View of the West ICARUS T300 module from the top (a) and side (b). Distribution of the event vertices, colored by the average `WE-TOP-C` adder signal maximum. Adder boards are digitized at 60 mV discrimination threshold. The fiducial volume cut is highlighted with dashed white lines. The solid white line shows the cathode.

5.2.2 Monte Carlo Adder Trigger Efficiency

Monte Carlo truth information is retrieved for each event, and the trigger event recognition efficiency is evaluated as the number of events meeting the trigger condition over the total number of events (asymmetric errors are estimated with the Clopper-Pearson method; for reference, see chapter 3).

Detection of In-time Beam Events (MC) The detection efficiency for Monte Carlo BNB ν_μCC interactions in the fiducial volume with the PMT-majority trigger was already proved to be almost maximal at mj-5, with only 8 non-triggering events out of the 78 events with $E_{\text{dep.}} < 100$ MeV in the fiducial volume, yielding a $\sim 90\%$ detection efficiency below 100 MeV (recall Figure 3.22 in chapter 3). Figure 5.12 shows the

localization of BNB ν_μCC vertices in the west T300 module, based on whether they triggered the standard majority-5, the adders in global-OR but not the majority-5, or neither of them, in the active volume. According to Monte Carlo calculations, the adders should be able to recover most of the low-energy events localized near the upstream and downstream non-instrumented walls of the cryostat, even if mostly outside of the fiducial volume. The global-OR signal would recover 4 out of the 8 low-energy non-triggering events in the fiducial volume (recall Figure 3.22), increasing the event recognition efficiency for BNB ν_μCC interactions below 100 MeV to $\sim 95\%$.

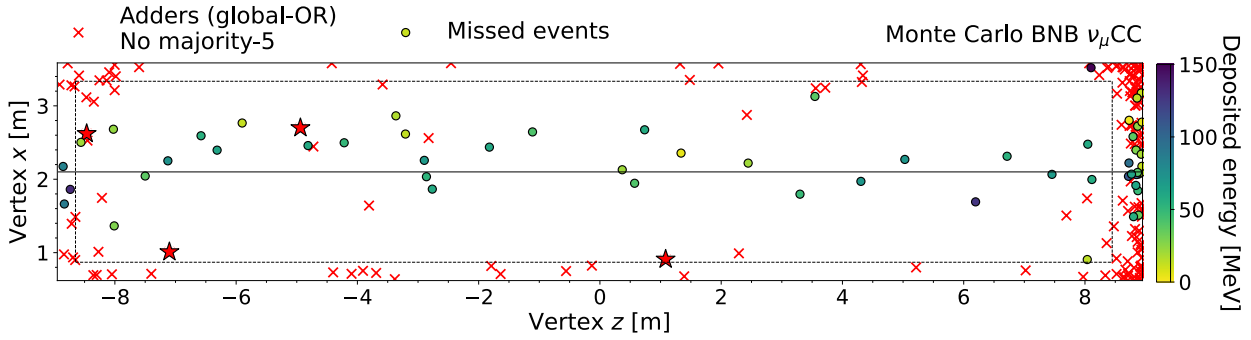

Figure 5.12: View of the West ICARUS T300 module from the top, with the cathode in the middle. Distribution of Monte Carlo BNB ν_μCC event vertices. Events that did not trigger the majority-5, but fired the corner-adder trigger are shown in red. Missed events are highlighted and colored with respect to their deposited energy. The star markers represent recovered events contained in the fiducial volume, and the latter is highlighted with dashed lines.

Detection of Out-of-time Cosmic Rays (MC) Monte Carlo calculations (chapter 3) and studies on Run2 data (chapter 4) showed that a strict majority-8 condition used for the detection of out-of-time cosmic rays presents $\sim 20\%$ inefficiencies to tracks crossing the corners of the detector or too close to the anode plane, where few PMTs collect most of the light and the multiplicity requirement is not met. According to the Monte Carlo, the trigger based on corner adders would be able to recover nearly half of them, increasing the recognition efficiency to $\sim 90\%$, even if using only 4 out of the 12 available adder boards in the T300 module (Figure 5.13).

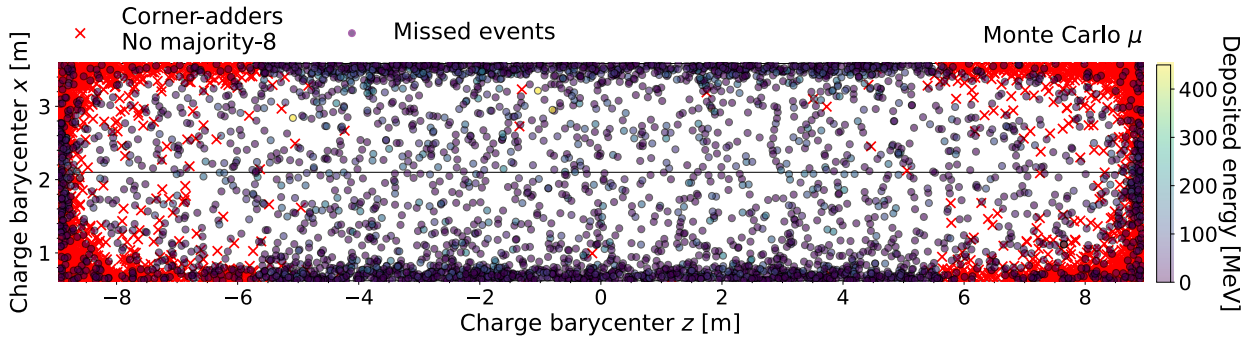

Figure 5.13: View of the West ICARUS T300 module from the top, with the cathode in the middle. Distribution of Monte Carlo cosmic muon charge barycenters. Events that did not trigger the majority-8, but fired the corner-adder trigger are shown in red. Adders are discriminated at a 16 PEs threshold. Missed events are highlighted and colored with respect to their deposited energy.

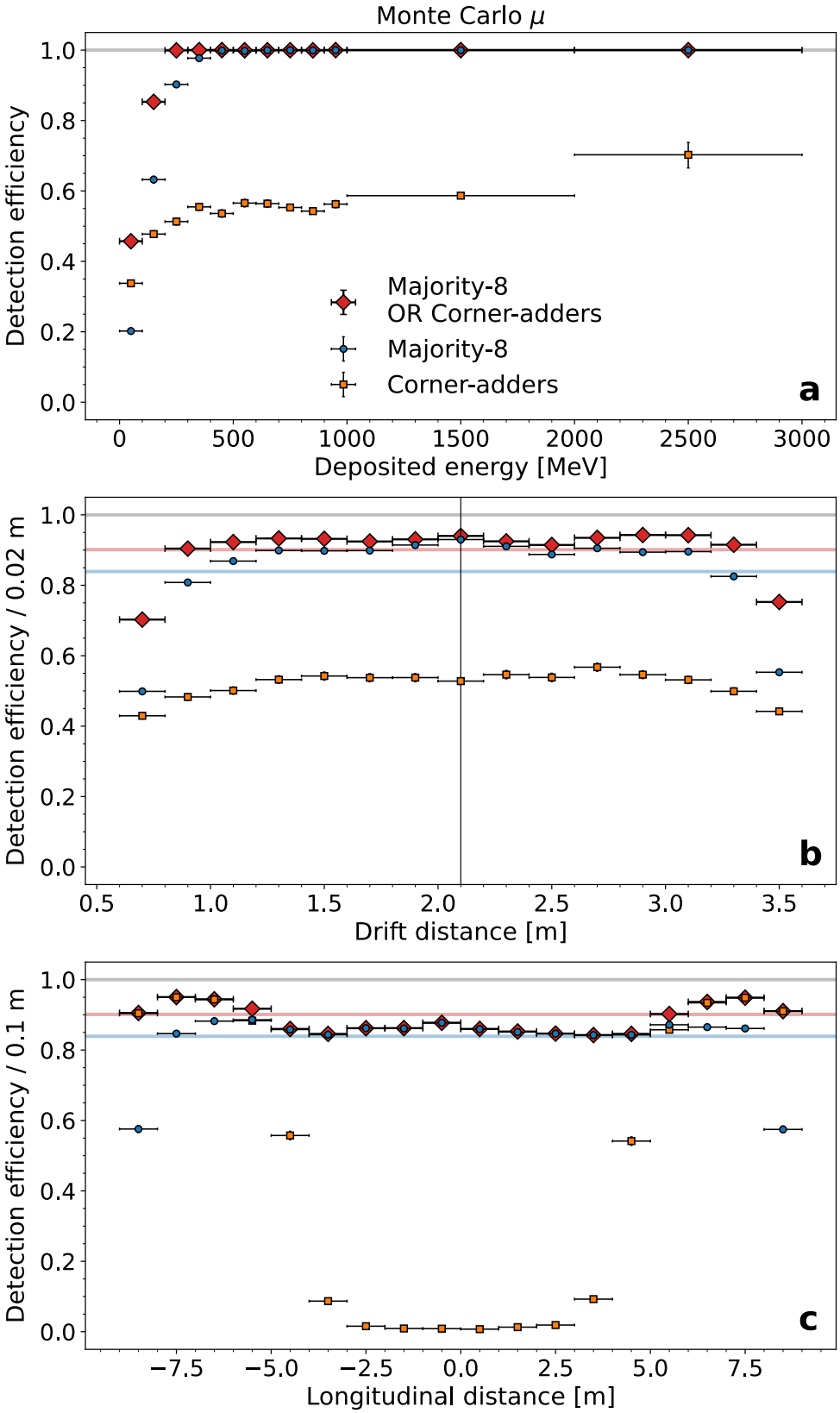

Figure 5.14: Trigger efficiency with majority-8, corner adders and their OR combination predicted with Monte Carlo cosmic muons, with respect to the deposited energy (a), drift (b), and longitudinal (c) coordinate of the tracks' charge barycenters. Adders are discriminated at a 16 PEs threshold. Energy bins are 100 MeV and 1 GeV wide. The average efficiencies for the majority-8 and its or with the corner adders are shown. The cathode is drawn along the drift direction.

Figure 5.14 shows the predicted trigger efficiencies for Monte Carlo cosmic muons with respect to the deposited energy, the drift, and the longitudinal coordinates of the deposited charge barycenter in the TPC. The efficiency is shown for the majority-8 trigger, the stand-alone corner-adders trigger, and their OR combination. In particular, events with very low deposited energy are usually tracks crossing the corners, where the adders give the strongest contribution: as a result, the efficiency for $E_{\text{dep.}} < 400$ MeV roughly doubles (Figure 5.14, a). While the efficiency saturates at $E_{\text{dep.}} > 500$ MeV with the standard PMT-majority trigger, the combination with the adders leads to the efficiency saturating at $E_{\text{dep.}} > 300$ MeV. The overall average recognition efficiency increases from 84% with the mj-8 to 90% when including the logic OR with the corner adders. Similarly, Figure 5.14(b) shows that the combined efficiency with respect to the drift distance improves in uniformity with respect to the majority, with smaller dips near the anode planes linked to small tracks in the bulk of the detector, far from the four adders at the corners. This is evident when looking at the efficiency with respect to the longitudinal position (Figure 5.14, c): the improvement from the corner adders is localized at the corners, and the efficiency far from the boards is essentially the same as with the PMT-majority. This explains visually how the corner-adders trigger is complementary to the majority.

5.3 Preliminary Out-of-time Trigger Evaluation from Data

The evaluation of the efficiency of the corner-adders trigger for out-of-time cosmic rays detection with respect to the PMT-majority trigger should be based on the minimum bias data, where the adder electronics chain is properly emulated. As previously mentioned, the full adder trigger emulation was not ready at the time of writing. As an alternative, data was collected by setting up the corner-adders trigger and analyzed by emulating the PMT-majority logic: events that don't meet the majority requirements are the ones that adders were able to recover. As described in chapter 4, tracks are selected by requiring a match between CRT and TPC with DCA < 30 cm to obtain a reliable track time around which the PMT-majority trigger can be emulated. Figure 5.15(a) shows the reconstructed length spectrum of cosmic muons in three corner-adders trigger runs with no neutrino beam, collected with different adder discrimination thresholds set on the CAEN DT1081B module.

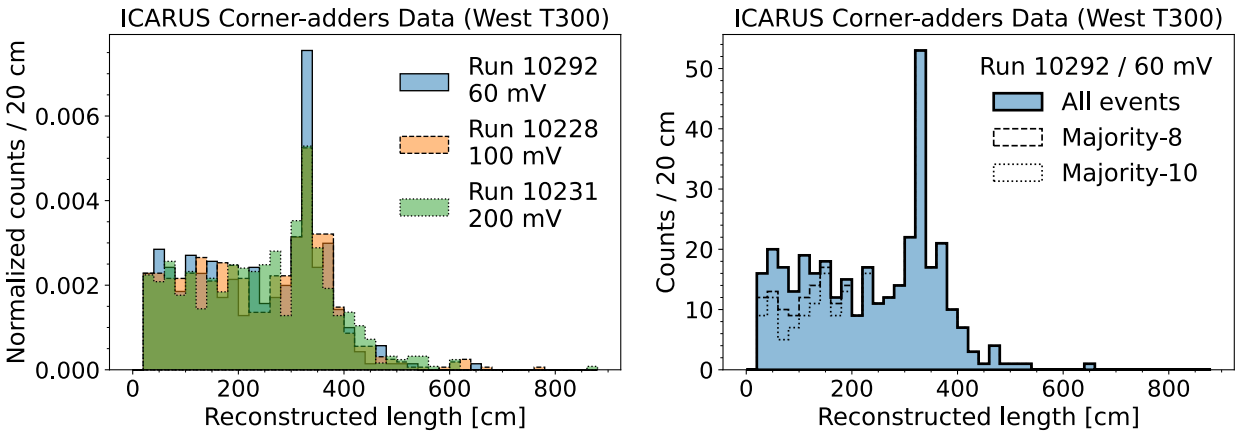

Figure 5.15: (left) Distribution of cosmic muon reconstructed lengths for three corner-adders trigger runs with the $(60, 100, 200)$ mV adder discrimination thresholds. Histograms are normalized to the area. (right) The distribution with the 60 mV threshold is shown, by also selecting the mj-8 and mj-10 requirements. No normalization is applied.

The lower the threshold, the higher the number of tracks in the highest peak, corresponding to vertical tracks crossing the whole vertical detector length, which are reported to always trigger the emulated PMT-majority logic. Indeed, tracks with smaller lengths (i.e., the continuum of muons crossing the detector in the corners) that by design may be recovered with adders are preserved even with thresholds as high as 200 mV. This opens up the feasibility of using a discrimination threshold higher than 60 mV to meet the DAQ requirements, lowering the trigger rate while preserving the adders' detection capabilities. This is confirmed by the length spectrum, selecting events that fired the mj-8 (Figure 5.15, b): the majority is fired for all the tracks in the peak, while shorter tracks are missed consistently. Overall, roughly 10% of the muons collected with the corner-adders trigger did not meet a majority-8 requirement.

Figure 5.16 shows the distribution of the muons' charge barycenters in West ICARUS T300 with respect to the emulated majority-8. Events that are recovered with the adders are shown to be localized at the corners of the detector, and three of them are displayed along with the reconstructed PMT flash barycenter, which matches the track position well. Interestingly, the corner adders were able to recover a short stopping muon track (event 315). The track is identified to be stopping inside the TPC by the increased $\mathrm{d}E/\mathrm{d}x \sim 10$ MeV/cm energy loss at its last hits.

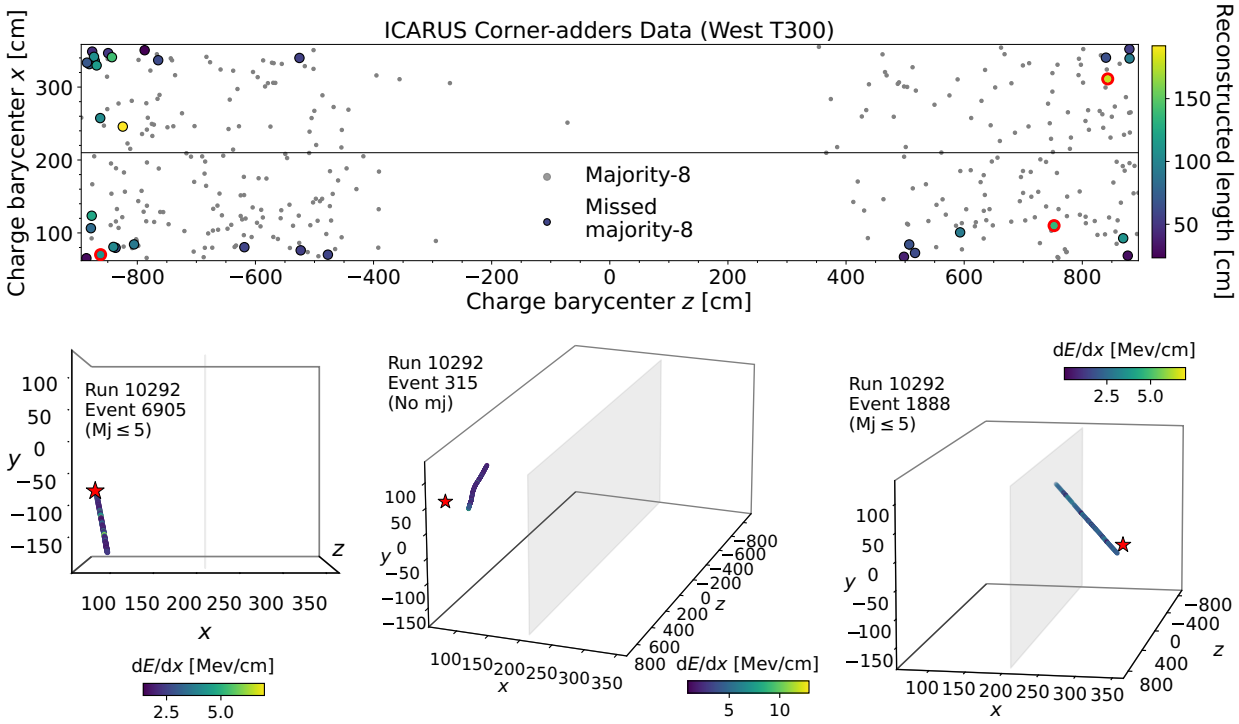

Figure 5.16: (top) View of the West ICARUS T300 module from the top, with the cathode in the middle. Distribution of cosmic muons' charge barycenters, for the corner-adders trigger run with a 60 mV discrimination threshold. Events that did not trigger a majority-8 are colored with respect to the reconstructed length. (bottom) Event display of reconstructed space points for three events that did not trigger the PMT-majority and are hence recovered with adders. The reconstructed light barycenter is highlighted.

5.3.1 PMT-majority Conditional Probability

The PMT-majority detection efficiency computed on data collected with the corner-adders trigger can be interpreted as a conditional probability. In particular, the majority-8 is chosen as a reference to show the promising event recognition efficiency with adders for off-beam triggers. Figure 5.17(left) suggests that the PMT-majority is inefficient at the detector corners for cosmic muons with reconstructed lengths $L < 3$ m, i.e. non-vertical tracks crossing the corners, independently of the threshold. The probability estimation for tracks with $L < 0.5$ m is likely biased by the fact that the CRT-TPC matching request tracks with lengths larger than 20 cm, hence the bump in the mj-8 efficiency with respect to the second length-bin. The complementary quantity to the mj-8 efficiency (Figure 5.17, right) quantifies the detection capabilities of the corner-adders trigger with respect to the PMT-majority, with up to a 50% recovering probability for tracks with $L < 1.5 - 2$ m.
Finally, it is shown that it may be convenient to consistently increase the adder discrimination threshold from the 60 mV reference value, with two considerations:

- the trigger rate decreases, and it may eventually be possible to introduce other adder boards in the trigger logic. Conveniently, it was observed that this decrease mainly involves longer tracks, which would have triggered the PMT-majority anyway, while the number of adder-triggering shorter tracks remains roughly constant (Figure 5.15);
- the event detection capabilities of the corner-adders trigger is predicted to remain consistently high even with a 200 mV discrimination threshold (Figure 5.17, right).

While the conditional probability is a convenient way of predicting the capabilities of the corner-adder trigger, it is planned to complete the development of the full adder emulation chain, validate it with digitized adder waveform, and finally evaluate the adder performance on MinBias data.

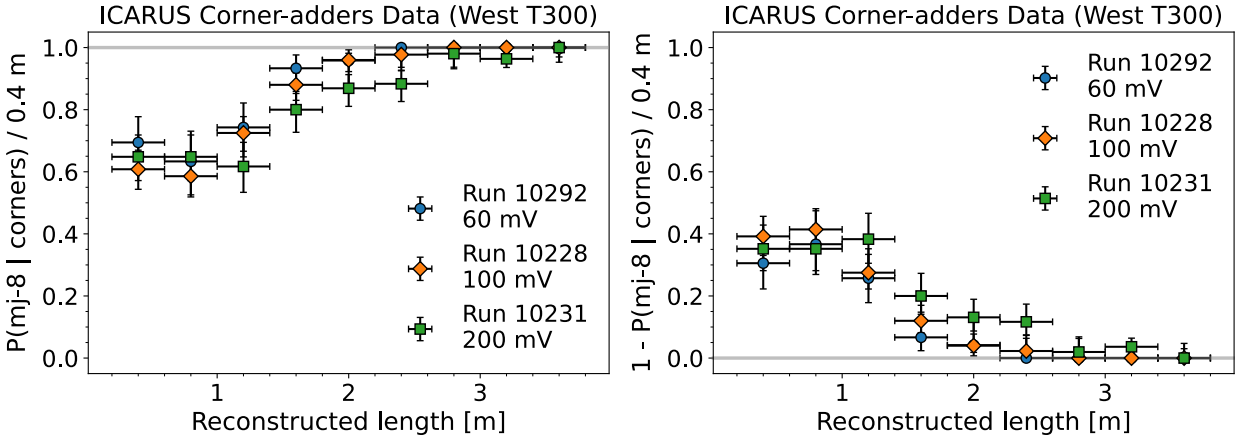

Figure 5.17: (left) Conditional probability of triggering an emulated majority-8 computed on runs collected with the corner-adders trigger, with respect to the reconstructed track length, for three adder discrimination thresholds. (right) Complementary quantity to the conditional probability.

Finally, note that this preliminary study is promising not only for cosmic rays but also for beam neutrinos below 100 MeV deposited energies, which lead to localized energy depositions, different than higher-energy

neutrino interactions. In this sense, the study of cosmic rays with adders can be instructive for low-energy neutrinos as well.

Conclusions

Several neutrino oscillation anomalies have been reported at short baselines, possibly hinting at the existence of additional "sterile" neutrino states, even if tensions arise between different oscillation channels and experiments. The ICARUS T600 detector is installed at a shallow depth at Fermilab as the far detector of the Fermilab Short Baseline Neutrino (SBN) program, based on three Liquid Argon Time Projection Chamber (LArTPC) detectors at different distances from the Booster Neutrino Beam (BNB) target. The combination of near and far detectors enables a direct neutrino event comparison at different baselines, minimizing the systematic uncertainties in a definitive search for eV-scale sterile neutrinos with short-baseline ν_e-appearance and ν_μ-disappearance oscillations at BNB. Moreover, ICARUS foresees stand-alone searches of a Neutrino-4-like short-baseline anomaly in the ν_μ-disappearance and ν_e-disappearance channels at BNB and with the off-axis neutrinos from the Neutrinos at the Main Injector (NuMI) beam. The high-intensity neutrino beams will be exploited to perform high-statistics measurements of the ν-Ar cross-sections with all neutrino flavors, at energies of interest for future long-baseline argon-based experiments. The ICARUS detector is exposed to a large flux of cosmic rays crossing its active volume during the $\sim$ 1 ms drift of ionization electrons to the TPC wire planes, which have to be recognized and rejected in order to reconstruct pure neutrino interactions.

This work was dedicated to the development of an optimal trigger logic, needed to select the neutrino event rate, and to the evaluation of its performance with recent ICARUS data.
In the initial phase of the experiment, a trigger based on the detection of scintillation light in liquid Argon with 180 PMTs in each T300 module in coincidence with the proton extraction at BNB and NuMI has been deployed. A data-driven Monte Carlo simulation framework was developed, to define an effective trigger logic using BNB neutrinos and cosmic muons events. Accounting for the typical $\sim$ 1 GeV energies of BNB and NuMI neutrinos and for the event dimension of $\sim$ 4 m along the BNB direction, scintillation light signals are recognized inside five overlapped 6 m windows along the 18 m T300 length, containing 60 PMTs each, front-facing between the two TPCs. To trigger on BNB and NuMI neutrinos, a multiplicity of 5 PMT pairs in at least one of the five windows ("majority-5") is requested. Corresponding Monte Carlo calculations indicate an almost full event recognition efficiency with charged-current interactions inside the fiducial volume of the detector, with inefficiencies related to events with deposited energy below 100 MeV. To recognize cosmic muons traversing the apparatus outside of the beam gates and during the $\sim$ 1 ms drift of ionization electrons in the TPC ("out-of-time" triggers), a majority-10 was initially chosen and tested with Monte Carlo, predicting a $\sim$ 77% efficiency.

Hints by the Monte Carlo were confirmed by studies on recent ICARUS data collected without imposing any requirement on the scintillation light and processed by matching the cosmic ray tracks reconstructed in the TPC with the Cosmic Ray Tagger (CRT) system. The trigger response was then emulated for each track using the collected PMT waveforms. An event selection procedure was developed to clean the sample with respect to any TPC reconstruction issue, and the out-of-time trigger efficiency was estimated to be $\sim 79\%$ with a majority-8 condition, which was proved to be manageable by the DAQ. A selection on straight clean vertical tracks with localized energy depositions was then developed to estimate the on-beam trigger efficiency, compared with truth-level Monte Carlo predictions for BNB ν_μ and ν_e charged-current interactions. Data shows that the ICARUS beam trigger is at full efficiency above deposited energies of 200 MeV, and at $\sim 90\%$ in the $100-200$ MeV range. The established mj-5 beam trigger rejects non-physical events with a factor ~ 30 while maintaining a high efficiency to neutrino interactions. In the near future, the PMT-majority trigger efficiency measurement will be finalized with the inclusion of systematic errors, inherited from the detector and the reconstruction algorithms. The event recognition efficiency maps will hence serve as input for early ICARUS physics analyses.

An ancillary trigger system based on the detection of the total scintillation light collected in each event rather than the multiplicity of fired PMTs has been studied to address low-energy events and short tracks close to the anode planes or the corners of the detector. For this purpose, 24 adder boards (12 per T300 module) that receive signals from 15 adjacent PMTs, split them into two 95%/5% lines, and sum the 5% outputs, were installed and their functionality checked in terms of counting rate and event detection efficiency with respect to the standard PMT-majority trigger. As a result, the 12 adders in each module could be integrated with the established majority-5 to improve the neutrino event recognition below 200 MeV deposited energy, as suggested by Monte Carlo evaluation, without overcrowding the DAQ. Furthermore, the signals from the 4 adders installed in the corners of each module ("corner-adders trigger") can also be combined with the established majority-8 trigger, to improve the out-of-time cosmic recognition during the ~ 1 ms drift of ionization electrons in the TPCs with an expected limited impact on the DAQ bandwidth. This corner-adders trigger was tested with cosmic rays and compared with the emulated PMT-majority. Even if biased, this successful test suggests that the corner-adders can recover $\sim 50\%$ of the cosmic rays traversing the detector during the ~ 1 ms e^--drift but not meeting the majority-8 requirement, as suggested by the Monte Carlo. The full adder-chain emulation is being wrapped up, and the performance of the proposed adder-based trigger system will be evaluated on data collected in an unbiased way without imposing any light requirement. In this way, the combination of the PMT-majority and the PMT-adders triggers will be tuned, optimizing the global neutrino trigger in terms of efficiency and fake events rejection.

Bibliography

[1] Pauli, W. *Dear radioactive ladies and gentlemen* Dec. 1930 (cit. on p. 3).

[2] Ellis, C. D. & Wooster, W. A. The average energy of disintegration of radium E. *Proceedings of the Royal Society of London. Series A, Containing Papers of a Mathematical and Physical Character* **117,** 109–123 (1927) (cit. on p. 3).

[3] Wilson, F. L. Fermi's theory of beta decay. *American Journal of Physics* **36,** 1150–1160 (1968) (cit. on p. 3).

[4] Reines, F. & Cowan Jr, C. Detection of the free neutrino. *Physical Review* **92,** 830 (1953) (cit. on p. 4).

[5] Neddermeyer, S. H. & Anderson, C. D. Note on the nature of cosmic-ray particles. *Physical Review* **51,** 884 (1937) (cit. on p. 4).

[6] Danby, G. *et al.* Observation of high-energy neutrino reactions and the existence of two kinds of neutrinos. *Physical Review Letters* **9,** 36 (1962) (cit. on p. 4).

[7] Decamp, D. *et al.* A precise determination of the number of families with light neutrinos and of the Z boson partial widths. *Physics Letters B* **235,** 399–411 (1990) (cit. on pp. 4, 14, 18).

[8] Kodama, K. *et al.* Observation of tau neutrino interactions. *Physics Letters B* **504,** 218–224 (2001) (cit. on p. 4).

[9] Gaillard, M. K., Grannis, P. D. & Sciulli, F. J. The standard model of particle physics. *Reviews of Modern Physics* **71,** S96 (1999) (cit. on p. 4).

[10] Goldhaber, M., Grodzins, L. & Sunyar, A. W. Helicity of neutrinos. *Physical review* **109,** 1015 (1958) (cit. on p. 4).

[11] Albajar, C. *et al.* Studies of intermediate vector boson production and decay in UA1 at the CERN proton-antiproton collider. *Zeitschrift für Physik C Particles and Fields* **44,** 15–61 (1989) (cit. on p. 4).

[12] Jones, R. S. *Muon-neutrino disappearance with multiple liquid argon time projection chambers in the Fermilab Booster neutrino beam.* PhD thesis (U. Liverpool (main), University of Liverpool, Liverpool U., 2021) (cit. on p. 5).

[13] Athar, M. S., Fatima, A. & Singh, S. Neutrinos and their interactions with matter. *Progress in Particle and Nuclear Physics,* 104019 (2022) (cit. on p. 6).

[14] Formaggio, J. A. & Zeller, G. P. From eV to EeV: Neutrino cross sections across energy scales. *Reviews of Modern Physics* **84,** 1307–1341 (July 2012) (cit. on p. 7).

[15] Langacker, P. & London, D. Lepton-number violation and massless nonorthogonal neutrinos. *Physical Review D* **38,** 907 (1988) (cit. on p. 8).

[16] Davis Jr, R., Harmer, D. S. & Hoffman, K. C. Search for neutrinos from the sun. *Physical Review Letters* **20,** 1205 (1968) (cit. on pp. 8, 12).

[17] Haines, T. *et al.* Calculation of atmospheric neutrino-induced backgrounds in a nucleon-decay search. *Physical review letters* **57** (1986) (cit. on p. 8).

[18] Nakahata, M. *et al.* Atmospheric neutrino background and pion nuclear effect for KAMIOKA nucleon decay experiment. *Journal of the Physical Society of Japan* **55,** 3786–3805 (1986) (cit. on p. 8).

[19] Fukuda, Y. *et al.* Evidence for oscillation of atmospheric neutrinos. *Physical review letters* **81,** 1562 (1998) (cit. on p. 8).

[20] Apollonio, M. *et al.* Limits on neutrino oscillations from the CHOOZ experiment. *Physics Letters B* **466,** 415–430 (1999) (cit. on pp. 8, 13).

[21] Ahn, M. *et al.* Indications of neutrino oscillation in a 250 km long-baseline experiment. *Physical Review Letters* **90,** 041801 (2003) (cit. on p. 8).

[22] Michael, D. *et al.* Observation of muon neutrino disappearance with the MINOS detectors in the NuMI neutrino beam. *Physical review letters* **97,** 191801 (2006) (cit. on p. 9).

[23] Agafonova, N. *et al.* Final results of the OPERA experiment on ν_τ appearance in the CNGS neutrino beam. *Physical review letters* **120,** 211801 (2018) (cit. on p. 9).

[24] Ahmad, Q. R. *et al.* Measurement of the Rate of $\nu\ e^+\ d \rightarrow p^+\ p^+\ e^-$ Interactions Produced by B 8 Solar Neutrinos at the Sudbury Neutrino Observatory. *Physical review letters* **87,** 071301 (2001) (cit. on pp. 9, 12).

[25] Hampel, W. *et al.* GALLEX solar neutrino observations: Results for GALLEX IV. *Physics Letters B* **447,** 127–133 (1999) (cit. on pp. 9, 12, 13, 16, 19).

[26] Abdurashitov, J. *et al.* Measurement of the solar neutrino capture rate with gallium metal. III. Results for the 2002–2007 data-taking period. *Physical Review C* **80,** 015807 (2009) (cit. on pp. 9, 12, 13, 16, 19).

[27] Murayama, H. Origin of neutrino mass. *Progress in Particle and Nuclear Physics* **57,** 3–21 (2006) (cit. on p. 9).

[28] Maki, Z., Nakagawa, M. & Sakata, S. Remarks on the unified model of elementary particles. *Progress of Theoretical Physics* **28,** 870–880 (1962) (cit. on p. 9).

[29] Giunti, C. in *Particle Physics in Laboratory, Space and Universe* 35–44 (World Scientific, 2005) (cit. on p. 10).

[30] Wolfenstein, L. Oscillations among three neutrino types and CP violation. *Physical Review D* **18,** 958 (1978) (cit. on p. 10).

[31] Barger, V., Whisnant, K., Pakvasa, S. & Phillips, R. Matter effects on three-neutrino oscillations. *Physical Review D* **22,** 2718 (1980) (cit. on p. 10).

[32] Mikheev, S. & Smirnov, A. Y. Resonance amplification of oscillations in matter and spectroscopy of solar neutrinos. *Yadernaya Fizika* **42,** 1441–1448 (1985) (cit. on p. 10).

[33] Denton, P. *Accelerator Neutrino II: Flavor mixing, CP violation, and Unitarity (Theory)* June 2022 (cit. on p. 12).

[34] Nakajima, Y. *et al. Recent results and future prospects from Super-Kamiokande* in *Presentation at the XXIX International Conference on Neutrino Physics and Astrophysics (Neutrino 2020)* (2020) (cit. on p. 12).

[35] Aharmim, B. *et al.* Combined analysis of all three phases of solar neutrino data from the Sudbury Neutrino Observatory. *Physical Review C* **88,** 025501 (2013) (cit. on p. 12).

[36] Bellini, G. *et al.* Precision measurement of the Be 7 solar neutrino interaction rate in Borexino. *Physical Review Letters* **107,** 141302 (2011) (cit. on p. 12).

[37] Gando, A. *et al.* Constraints on θ_{13} from a three-flavor oscillation analysis of reactor antineutrinos at KamLAND. *Physical Review D* **83,** 052002 (2011) (cit. on p. 12).

[38] Abe, K. *et al.* Atmospheric neutrino oscillation analysis with external constraints in Super-Kamiokande I-IV. *Physical Review D* **97,** 072001 (2018) (cit. on p. 12).

[39] Aartsen, M. *et al.* Measurement of atmospheric neutrino oscillations at 6–56 GeV with IceCube DeepCore. *Physical review letters* **120,** 071801 (2018) (cit. on p. 12).

[40] Abe, K. *et al.* T2K measurements of muon neutrino and antineutrino disappearance using 3.13×10^{21} protons on target. *Physical Review D* **103,** L011101 (2021) (cit. on p. 13).

[41] Constraint on the matter–antimatter symmetry-violating phase in neutrino oscillations. *Nature* **580,** 339–344 (2020) (cit. on p. 13).

[42] Acero, M. *et al.* First measurement of neutrino oscillation parameters using neutrinos and antineutrinos by NOvA. *Physical review letters* **123,** 151803 (2019) (cit. on p. 13).

[43] Abe, K. *et al.* Improved constraints on neutrino mixing from the T2K experiment with 3.13×10^{21} protons on target. *Physical Review D* **103,** 112008 (2021) (cit. on p. 13).

[44] Acero, M. *et al.* Improved measurement of neutrino oscillation parameters by the NOvA experiment. *Physical Review D* **106,** 032004 (2022) (cit. on p. 13).

[45] Abe, Y. *et al.* Indication of reactor ν_e disappearance in the Double Chooz experiment. *Physical Review Letters* **108,** 131801 (2012) (cit. on p. 13).

[46] Double Chooz θ_{13} measurement via total neutron capture detection. *Nature Physics* **16,** 558–564 (2020) (cit. on p. 13).

[47] Adey, D. *et al.* Measurement of the electron antineutrino oscillation with 1958 days of operation at Daya Bay. *Physical review letters* **121,** 241805 (2018) (cit. on p. 13).

[48] Bak, G. *et al.* Measurement of reactor antineutrino oscillation amplitude and frequency at RENO. *Physical Review Letters* **121,** 201801 (2018) (cit. on p. 13).

[49] Abe, S. *et al.* Precision measurement of neutrino oscillation parameters with KamLAND. *Physical review letters* **100,** 221803 (2008) (cit. on p. 13).

[50] Athanassopoulos, C. *et al.* Evidence for $\nu_\mu \to \nu_e$ oscillations from the LSND experiment at the Los Alamos Meson Physics Facility. *Physical Review Letters* **77,** 3082 (1996) (cit. on pp. 13, 14, 19).

[51] Barinov, V. *et al.* Search for electron-neutrino transitions to sterile states in the BEST experiment. *Physical Review C* **105,** 065502 (2022) (cit. on pp. 13, 16, 19).

[52] Mention, G. *et al.* Reactor antineutrino anomaly. *Physical Review D* **83,** 073006 (2011) (cit. on pp. 13, 16).

[53] Pontecorvo, B. Conservation of lepton charge. *JETP* **5,** 1297 (1957) (cit. on p. 14).

[54] Armbruster, B. *et al.* Upper limits for neutrino oscillations $\nu_\mu \to \nu_e$ from muon decay at rest. *Physical Review D* **65,** 112001 (2002) (cit. on pp. 14, 19).

[55] Seto, R. *BNL E776: A Search for neutrino oscillations* in *AIP Conference Proceedings* **176** (1988), 957–963 (cit. on p. 14).

[56] Dydak, F. *et al.* A search for ν_μ oscillations in the Δm^2 range $0.3 - 90$ eV^2. *Physics Letters B* **134,** 281–286 (1984) (cit. on p. 14).

[57] Eskut, E. *et al.* The CHORUS experiment to search for $\nu_\mu \to \nu_\tau$ oscillation. *Nuclear Instruments and Methods in Physics Research Section A: Accelerators, Spectrometers, Detectors and Associated Equipment* **401,** 7–44 (1997) (cit. on pp. 14, 19).

[58] Astier, P. *et al.* Search for $\nu_\mu \to \nu_e$ oscillations in the NOMAD experiment. *Physics Letters B* **570,** 19–31 (2003) (cit. on pp. 14, 19).

[59] Adamson, P. *et al.* Search for sterile neutrinos mixing with muon neutrinos in MINOS. *Physical review letters* **117,** 151803 (2016) (cit. on p. 14).

[60] Aguilar-Arevalo, A. *et al.* Significant excess of electronlike events in the MiniBooNE short-baseline neutrino experiment. *Physical review letters* **121,** 221801 (2018) (cit. on p. 15).

[61] Antonello, M. *et al.* Search for anomalies in the ν_e appearance from a ν_μ beam. *The European Physical Journal C* **73,** 1–6 (2013) (cit. on p. 15).

[62] Abratenko, P. *et al.* Search for an excess of electron neutrino interactions in MicroBooNE using multiple final-state topologies. *Physical review letters* **128,** 241801 (2022) (cit. on p. 15).

[63] Giunti, C., Li, Y., Ternes, C., Tyagi, O. & Xin, Z. Gallium Anomaly: critical view from the global picture of ν_e and $\overline{\nu}_e$ disappearance. *Journal of High Energy Physics* **2022,** 1–34 (2022) (cit. on p. 16).

[64] Serebrov, A. *et al.* Search for sterile neutrinos with the Neutrino-4 experiment and measurement results. *Physical Review D* **104,** 032003 (2021) (cit. on pp. 17, 20, 41).

[65] Antonello, M. *et al.* Experimental search for the "LSND anomaly" with the ICARUS detector in the CNGS neutrino beam. *The European Physical Journal C* **73,** 1–9 (2013) (cit. on pp. 19, 20, 25).

[66] Agafonova, N. *et al.* Limits on muon-neutrino to tau-neutrino oscillations induced by a sterile neutrino state obtained by OPERA at the CNGS beam. *Journal of High Energy Physics* **2015,** 1–13 (2015) (cit. on p. 19).

[67] Conrad, J. & Shaevitz, M. Limits on electron neutrino disappearance from the KARMEN and LSND ν e-carbon cross section data. *Physical Review D* **85,** 013017 (2012) (cit. on p. 20).

[68] Serebrov, A., Samoilov, R., Chaikovskii, M. & Zherebtsov, O. The result of the Neutrino-4 experiment, sterile neutrinos and dark matter, the fourth neutrino and the Hubble constant. *arXiv preprint arXiv:2302.09958* (2023) (cit. on p. 20).

[69] Alekseev, I. *et al.* Search for sterile neutrinos at the DANSS experiment. *Physics Letters B* **787,** 56–63 (2018) (cit. on p. 20).

[70] Achkar, B. *et al.* Search for neutrino oscillations at 15, 40 and 95 meters from a nuclear power reactor at Bugey. *Nuclear Physics B* **434,** 503–532 (1995) (cit. on p. 20).

[71] Ko, Y. *et al.* Sterile neutrino search at the NEOS experiment. *Physical review letters* **118,** 121802 (2017) (cit. on p. 20).

[72] Collaboration, P. *et al.* First search for short-baseline neutrino oscillations at HFIR with PROSPECT. *Physical review letters* **121,** 251802 (2018) (cit. on p. 20).

[73] STEREO neutrino spectrum of 235U fission rejects sterile neutrino hypothesis. *Nature* **613,** 257–261 (2023) (cit. on p. 20).

[74] Böser, S. *et al.* Status of light sterile neutrino searches. *Progress in particle and nuclear physics* **111,** 103736 (2020) (cit. on pp. 21, 22).

[75] Acciarri, R. *et al.* A proposal for a three detector short-baseline neutrino oscillation program in the Fermilab booster neutrino beam. *arXiv preprint arXiv:1503.01520* (2015) (cit. on pp. 23, 25, 34, 35, 37, 39, 40, 41).

[76] Abratenko, P. *et al.* ICARUS at the Fermilab Short-Baseline Neutrino program: initial operation. *The European Physical Journal C* **83,** 467 (2023) (cit. on pp. 23, 25, 29, 30, 31, 32, 38).

[77] Amerio, S. *et al.* Design, construction and tests of the ICARUS T600 detector. *Nucl. Instrum. Meth. A* **527,** 329–410 (2004) (cit. on pp. 25, 27).

[78] Acciarri, R. *et al.* Long-Baseline Neutrino Facility (LBNF) and Deep Underground Neutrino Experiment (DUNE): Conceptual Design Report, Volume 1: The LBNF and DUNE Projects. *arXiv preprint arXiv:1601.05471* (Jan. 2016) (cit. on pp. 25, 34, 39, 41).

[79] Acciarri, R. *et al.* Long-Baseline Neutrino Facility (LBNF) and Deep Underground Neutrino Experiment (DUNE): Conceptual Design Report, Volume 2: The Physics Program for DUNE at LBNF. *arXiv preprint arXiv:1512.06148* (Dec. 2015) (cit. on pp. 25, 34, 39, 41).

[80] Rubbia, C. The Liquid Argon Time Projection Chamber: A New Concept for Neutrino Detectors (May 1977) (cit. on pp. 26, 28).

[81] Menegolli, A. The Long Journey of ICARUS: From the LAr-TPC Concept to the First Full-Scale Detector. *Universe* **9,** 74 (2023) (cit. on p. 26).

[82] Diwan, M., Potekhin, M., Viren, B., Qian, X. & Zhang, C. A novel method for event reconstruction in Liquid Argon Time Projection Chamber. *Journal of Physics: Conference Series* **762,** 012033 (Oct. 2016) (cit. on p. 26).

[83] Amoruso, S. *et al.* Study of electron recombination in liquid argon with the ICARUS TPC. *Nuclear Instruments and Methods in Physics Research Section A: Accelerators, Spectrometers, Detectors and Associated Equipment* **523,** 275–286. ISSN: 0168-9002 (2004) (cit. on pp. 27, 81).

[84] Farnese, C. *Some recent results from ICARUS* in *AIP Conference Proceedings* **1666** (2015), 110002 (cit. on p. 28).

[85] Antonello, M. *et al.* Experimental observation of an extremely high electron lifetime with the ICARUS-T600 LAr-TPC. *Journal of Instrumentation* **9,** P12006 (2014) (cit. on pp. 29, 80).

[86] Bagby, L. *et al.* Overhaul and installation of the ICARUS-T600 liquid argon TPC electronics for the FNAL Short Baseline Neutrino program. *Journal of Instrumentation* **16,** P01037–P01037 (Jan. 2021) (cit. on p. 29).

[87] Ali-Mohammadzadeh, B. *et al.* Design and implementation of the new scintillation light detection system of ICARUS T600. *Journal of Instrumentation* **15,** T10007–T10007 (Oct. 2020) (cit. on pp. 30, 31).

[88] Bonesini, M. *et al.* An innovative technique for TPB deposition on convex window photomultiplier tubes. *Journal of Instrumentation* **13,** P12020 (Dec. 2018) (cit. on pp. 30, 47).

[89] Bonesini, M. *et al.* The laser diode calibration system of the ICARUS T600 detector at FNAL. *Journal of Instrumentation* **15,** C05042–C05042 (May 2020) (cit. on p. 30).

[90] Babicz, M. *et al.* Linearity and saturation properties of Hamamatsu R5912-MOD photomultiplier tube for the ICARUS T600 light detection system. *Nuclear Instruments and Methods in Physics Research Section A: Accelerators, Spectrometers, Detectors and Associated Equipment* **936,** 554–555 (2019) (cit. on p. 31).

[91] Abratenko, P. *et al.* First Measurement of Inclusive Muon Neutrino Charged Current Differential Cross Sections on Argon at $E_\nu \sim 0.8$ GeV with the MicroBooNE Detector. *Physical Review Letters* **123** (Sept. 2019) (cit. on pp. 34, 41).

[92] Aguilar-Arevalo, A. A. *et al.* Neutrino flux prediction at MiniBooNE. *Physical Review D* **79** (Apr. 2009) (cit. on pp. 34, 36, 37, 41).

[93] Adamson, P. *et al.* The NuMI neutrino beam. *Nuclear Instruments and Methods in Physics Research Section A: Accelerators, Spectrometers, Detectors and Associated Equipment* **806,** 279–306 (Jan. 2016) (cit. on p. 34).

[94] Backfish, M. *MiniBooNE resistive wall current monitor* tech. rep. (Fermi National Accelerator Laboratory (FNAL), 2013) (cit. on p. 35).

[95] Aguilar-Arevalo, A. *et al.* Dark matter search in nucleon, pion, and electron channels from a proton beam dump with MiniBooNE. *Physical Review D* **98** (Dec. 2018) (cit. on pp. 35, 36).

[96] Group, P. D. *et al.* Review of Particle Physics. *Progress of Theoretical and Experimental Physics* **2022.** 083C01. ISSN: 2050-3911 (Aug. 2022) (cit. on p. 35).

[97] Catanesi, M. G. *et al.* Proposal to study hadron production for the neutrino factory and for the atmospheric neutrino flux (Nov. 1999) (cit. on pp. 36, 46).

[98] Apollonio, M. *et al.* Large-angle production of charged pions with incident pion beams on nuclear targets. *Physical Review C* **80,** 065207 (2009) (cit. on pp. 36, 46).

[99] Ayres, D. S. *et al.* The NOvA Technical Design Report (Oct. 2007) (cit. on p. 38).

[100] Machado, P. A., Palamara, O. & Schmitz, D. W. The Short-Baseline Neutrino Program at Fermilab. *Annual Review of Nuclear and Particle Science* **69,** 363–387 (Oct. 2019) (cit. on pp. 39, 40, 41).

[101] Serrano, J. *et al.* The White Rabbit Project (Nov. 2009) (cit. on p. 45).

[102] Snider, E. & Petrillo, G. *LArSoft: toolkit for simulation, reconstruction and analysis of liquid argon TPC neutrino detectors* in *Journal of Physics: Conference Series* **898** (2017), 042057 (cit. on p. 46).

[103] Agostinelli, S. *et al.* GEANT4–a simulation toolkit. *Nucl. Instrum. Meth. A* **506,** 250–303 (2003) (cit. on pp. 46, 47).

[104] Andreopoulos, C. *et al.* The GENIE neutrino Monte Carlo generator. *Nuclear Instruments and Methods in Physics Research Section A: Accelerators, Spectrometers, Detectors and Associated Equipment* **614,** 87–104 (Feb. 2010) (cit. on p. 46).

[105] Andreopoulos, C. *et al.* The GENIE neutrino Monte Carlo generator: physics and user manual. *arXiv preprint arXiv:1510.05494* (2015) (cit. on p. 46).

[106] Heck, D., Knapp, J., Capdevielle, J. N., Schatz, G. & Thouw, T. CORSIKA: A Monte Carlo code to simulate extensive air showers (Feb. 1998) (cit. on p. 47).

[107] Abele, H. The neutron. Its properties and basic interactions. *Progress in Particle and Nuclear Physics* **60,** 1–81. ISSN: 0146-6410 (2008) (cit. on p. 50).

[108] Cousins, R. D., Hymes, K. E. & Tucker, J. Frequentist evaluation of intervals estimated for a binomial parameter and for the ratio of Poisson means. *Nuclear Instruments and Methods in Physics Research Section A: Accelerators, Spectrometers, Detectors and Associated Equipment* **612,** 388–398 (2010) (cit. on p. 58).

[109] Acciarri, R. *et al.* The Pandora multi-algorithm approach to automated pattern recognition of cosmic-ray muon and neutrino events in the MicroBooNE detector. *The European Physical Journal C* **78,** 1–25 (2018) (cit. on pp. 70, 71).

[110] Bettini, A. *et al.* A study of the factors affecting the electron lifetime in ultra-pure liquid argon. *Nuclear Instruments and Methods in Physics Research Section A: Accelerators, Spectrometers, Detectors and Associated Equipment* **305,** 177–186 (1991) (cit. on p. 80).

[111] Antonello, M. *et al.* Study of space charge in the ICARUS T600 detector. *Journal of Instrumentation* **15,** P07001 (2020) (cit. on p. 80).